Measurement of Cerebral Blood Flow in Humans Using MRI with Arterial Spin Labelling

Jonna Aleide Wiersma

Wellcome Department of Imaging Neuroscience
University College London

Submitted for the Degree of Doctor of Philosophy
University of London

June 2002

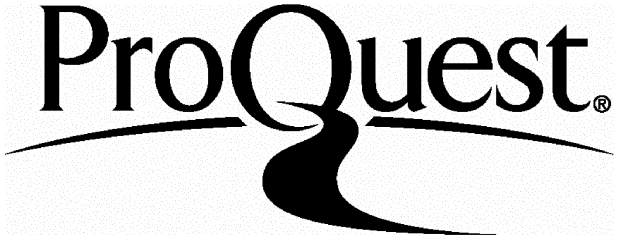

Science

I am but a grateful tourist
enjoying the sights
the perspective
charting the landscape
taking pictures

life looks in my eyes
and smiles
its beauty more
in detail

I am humbled
I fly; nothing
in the universe
love the buzz

4/5/99

And what is good, Phaedrus,
And what is not good —
Need we ask anyone to tell us these things?

Robert Pirsig, *Zen and The Art of Motorcycle Maintenance*

Abstract

Cerebral blood flow (CBF) is an important marker for tissue well-being and brain function. Traditionally, CBF has been measured with invasive methods using exogenous tracers. With the introduction of arterial spin labelling (ASL) MRI techniques, non-invasive, quantitative CBF mapping in humans became feasible. The aim of the work described in this thesis was to implement, optimise and validate an ASL MRI technique for measuring CBF in humans. Furthermore, the utility of this technique for longitudinal studies was to be evaluated.

FAIR, a pulsed ASL technique, was successfully implemented. A data acquisition and analysis protocol was proposed after an extensive survey of acquisition and quantification issues such as rf pulse profiles, static subtraction error, voxel partial voluming, volunteer movement and choice of CBF quantification models.

Fitting for CSF fraction resulted in an improved goodness-of-fit when compared to the standard fit model. It was also derived that it is necessary to analyse the magnitude of the FAIR data to avoid erroneous results. Furthermore, it was shown that the inflow delay has to be included in the fit model for an accurate CBF value. Two image realignment protocols were proposed and evaluated.

The CBF measurement was validated by comparing baseline and parametric CBF results with literature values. Finally, the technique was applied in a study of CBF, inflow delay, BOLD signal and cerebrovascular reactivity (CR) over the course of a day. The findings were used to propose upper limits to diurnal changes in these parameters.

The standard deviation of a CBF measurement was found to be satisfactory for functional experiments, but not for longitudinal studies where small CBF changes are of interest. It was argued how FAIR could be made more suitable for longitudinal studies by applying 3D-realignment to whole brain FAIR, acquired preferably at a higher magnetic field strength.

Contents

List of Figures

List of Tables

Acknowledgements

Firstly, I would like to thank my supervisor, Bob Turner, for his ideas and optimism that underlie this PhD project. His door was always open for me and I've much appreciated that. My thanks also goes out to my second supervisor, Roger Ordidge, and to other great physicists working around Queen Square: David Thomas, Fernando Calamente and Alan Connelly. I have learnt a lot about ASL techniques and scientific methods in general from discussions with them. Alan Connelly has also been a very helpful and diligent proofreader of this thesis for which I am very grateful.

Within the FIL, I owe a great deal to the physics group: Alistair Howseman, Oliver Josephs, Ralf Deichmann and Chloe Hutton have been incredibly helpful and supportive over the years. Ralf Deichmann, especially, meticulously proofread this thesis and also contributed significantly to the project with bottom-up derivations of complicated CBF quantification formula. I thank John Ashburner for many informative discussions about data analysis and realignment procedures, Peter Aston for building head repositioning gear and helping with the setup for the hypercapnia experiment and Chris Freemantle, Ric Davis and Rachael Maddock for crucial computer support. I owe a great thanks to all my volunteers and to my external collaborators, Doug Corfield and Leanne McKay from the Charing Cross Hospital, who set up and operated the breathing circuits required for my hypercapnia studies. Leanne, especially, has been a wonderful, dedicated and fun collaborator, who sacrificed nine weekends of her free time to perform the longitudinal experiment with me. Finally, I am deeply grateful to Richard Frackowiak, who was incredibly helpful and supportive when I needed it most.

I would like to thank my friends in London, especially Chloe, Nash, Lindsey, Becky, Liz, Damien, Jocelyn, Carien, Fiona and Maddy and my friends at home, in particular Lauri, Edith, Simone, Steph and Pauline. A special thank you to Lesley and Kamala Devi, to my parents, Douwe and Jary, my sister Vera, my brother Sî-man, the Ninaber family and finally, most importantly, Alex Ninaber, my husband.

1 Introduction

Nuclear magnetic resonance (NMR) is one of the most powerful examples of the translation of fundamental research into successful applications. Isidor Rabi measured the magnetic moment for the first time in 1939 (Rabi et al., 1939); could he ever have imagined magnetic resonance becoming the standard clinical tool that it is today?

What drew me to NMR as an undergraduate chemistry student was its elegance and flexibility: while X-ray diffraction could only elucidate protein structure in crystals, NMR spectroscopy allowed one to study both protein structure and dynamics in solution, with a seemingly endless range of experiments available to the researcher.

And thus I ended up studying Haloalkane Dehalogenase, a protein from the bacterium Xanthobacter autotrophicus that is responsible for the first step in the bio-degradation of toxic haloalkanes. This natural garbage man can be found in many waste dumps and industrial surroundings. Unfortunately, it is very slow, breaking down only 6 haloalkanes per second. It was hoped that knowledge of the molecular basis behind its rate limiting step could be used to accelerate the breakdown process.

By measuring the structural changes during a titration with bromide (a substrate), I could demonstrate the two slowly exchanging conformations of the protein in the presence of the substrate. This confirmed kinetics studies that had found an activation barrier in the binding and release of the substrate that had to be surmounted, resulting in the slow breakdown process. Surprisingly, I found that the same two slowly exchanging protein conformations were present during a pH titration, suggesting that the protonation of the active site histidine induced the same conformational change as substrate binding. Without knowledge of my later research field, I described these experiments in my Masters thesis as 'functional NMR'.

The step from functional NMR to functional MRI was larger than one would expect from two techniques both centred around the proton spin. Even though the BOLD effect is in its basis molecular (the disappearance of the net magnetic moment of iron in hemoglobin when oxygen is bound), its application is in brain function and physiology on a scale which covers brain areas in the cm range rather than single protein molecules.

When I first heard of functional MRI in 1995, the first application of BOLD fMRI in humans was only three years old. The concept of this non-invasive brain mapping tool was incredibly exciting. And again, like NMR for molecular studies, MRI is a very flexible technique: apart from looking at brain function using the BOLD effect, it can also be used to study tissue structure, diffusion and perfusion.

The first quantitative, non-invasive perfusion measurements using MRI, continuous arterial spin labelling (ASL), were reported in 1992 by Detre and colleagues (Detre et al, 1992). The first pulsed ASL techniques, EPISTAR and FAIR, were reported by Edelman (Edelman et al, , 1994) and Kim (Kim et al., 1995) in 1994 and 1995. I started my PhD project soon after that, in September 1996.

The potential of ASL techniques was clear from the start: to provide the traditional 'PET parameter', CBF, with the non-invasiveness and high resolution of MRI. ASL methods should be eminently suited for longitudinal studies of brain function and physiology, because of this non-invasiveness and the transparency of the CBF parameter. The BOLD fMRI measurement is also non-invasive, but (changes in) the BOLD data are much harder to interpret. Finally, a CBF scan could be incorporated easily in existing clinical MRI protocols.

This PhD thesis describes an implementation, optimisation and validation of an ASL technique with the aim of measuring CBF in humans. The potential for its application in longitudinal studies is evaluated in a study of CBF over the course of a day.

1.1 PhD project aims

The aims of this PhD project were:

- to implement a non-invasive, quantitative ASL method for use in cognitive neuroimaging
- to optimise pulse sequence design to neuroscientific demands
- to develop an accurate model for CBF quantification
- to validate CBF results by comparison with another technique and/or literature values
- to apply the ASL method in a longitudinal neuroscientific experiment

1.2 Thesis summary

This thesis describes the implementation, optimisation and application of a non-invasive, quantitative perfusion MRI method, FAIR, a member of the family of arterial spin labelling techniques.

Chapter 1 gives the background and motivation for this project. The thesis aims are also listed.

Chapter 2 describes the general theory of MRI from basic NMR principles to rf pulses and pulse sequences.

Arterial spin labelling methods are reviewed in **Chapter 3**. A range of quantification issues relevant for the work described in this thesis is explored from different perspectives in the literature.

Following on from suggestions in the literature that inversion and readout pulse profiles are important for the accuracy and sensitivity of FAIR, **Chapter 4** describes pulse simulations and experiments that establish the optimal inversion and readout pulse combination. It is found that this is a HS inversion and a spin echo readout with 5-lobed Hamming filtered sinc pulses. FOCI pulses do have better inversion profiles, but for the relevant inversion/readout slice thickness ratio they are not better than standard HS pulses. Moreover, the FOCI pulses require more complicated sequence programming to allow for off-resonance slice selection.

The implementation of the FAIR pulse sequence with the optimised rf pulses is documented in **Chapter 5**. Human FAIR data are analysed with a standard CBF quantification model. Then a range of quantification issues is explored including CSF partial voluming, the static subtraction error, macroscopic flow spoiling and subject motion. A formal model selection is performed. The time efficiency of the FAIR acquisition is increased by reducing the repetition time and introducing global saturation. An optimal CBF quantification model is formulated and applied to volunteer data. The mean CBF and

inflow delay values and their errorbars are established for single voxels and grey and white matter segments.

In **Chapter 6**, a parametric hypercapnia experiment is described that allows for a validation of the FAIR results with literature values. Furthermore, baseline CBF and inflow delay values are determined for a sample of 11 volunteers.

Chapter 7 reports an application of the FAIR technique in a longitudinal experiment on a group of volunteers. In this experiment CBF, inflow delay, baseline BOLD and Cerebrovascular Reactivity (CR) are measured repeatedly from the morning to the evening. Few studies have been reported regarding the variability of CBF, inflow delay, BOLD and CR over the course of a day; this work contributes to the discussion of the utility of these parameters in (longitudinal) research.

The thesis finishes with **Chapter 8**: a chapter of general discussion and conclusions regarding the strengths and limitations of measuring CBF in humans using this arterial spin labelling technique.

2 Magnetic Resonance Imaging

2.1 Magnetic resonance: microscopic description

Depending on the composition of its nucleus, an atom can have a net nuclear angular momentum P. This angular momentum is characterised by a so-called spin quantum number, or spin, I. Nuclei with an odd total number of protons and neutrons (mass number) have a half-integral spin; nuclei with an even mass number but an odd charge number (total number of protons) have an integral spin. The angular momentum is then characterised by its length and by a projection along an (arbitrary) z-axis:

$$P = \hbar\sqrt{I(I+1)} \tag{2.1}$$

$$P_z = m\hbar \tag{2.2}$$

With $\hbar = h/2\pi$ and h is Planck's constant. The variable m is allowed 2I+1 values, going from I, I-1,....,–I. The proton, for instance, has a spin ½ and therefore two possible P_z values: -½ ħ and +½ ħ. Nuclei with a net angular momentum - in short: spins - have a magnetic moment μ:

$$\mu = \gamma P, \tag{2.3}$$

with γ the gyromagnetic ratio, a constant that depends on the type of nucleus. For a proton its value is $2.675 \cdot 10^8$ radians·s^{-1}·T^{-1}.

In the classical description, a magnetic moment μ interacts with an external magnetic field **B**, that is measured in T [1]. It then has a potential energy, which depends on the magnetic moment's angle with respect to **B** (Zeeman effect). Given a magnetic field **B** along z, called B_0 by definition, the energy of the magnetic moment is:

---

[1] B is in fact the magnetic flux density, which includes the magnetization M in a medium. B is defined by $B=\mu_0(H+M)$, where the magnetic field strength H and the magnetization M are given in A/m and the magnetic permeability μ_0 is given in H/m. Following convention, I will call B the magnetic field from now on.

(2.4) $$E = -\boldsymbol{\mu} \cdot \mathbf{B} = -\mu_z B_0 = -\gamma \hbar m B_0$$

The same result may be obtained quantum mechanically. In this case, μ is the expectation value of the magnetic moment of an ensemble of spins and μ_z is the expectation value of the z component of the magnetic moment.

The selection rule governing transitions between states is $\Delta m = +/-1$, resulting in emission and absorption, respectively. For a proton, for instance, its two allowed magnetic moment orientations ($m = -½, +½$) have an energy of $+½\gamma\hbar B_0$ and $-½\gamma\hbar B_0$ respectively. The energy difference and the resonance frequency of the transitions can then easily be derived (here for absorption):

(2.5) $$\Delta E = \gamma \hbar B_0$$

Using Planck's equation for the energy of one photon:

(2.6) $$\Delta E = h\nu ,$$

gives the resonance frequency ν:

(2.7) $$\nu = (\gamma / 2\pi) B_0 ,$$

and the angular frequency $\omega = 2\pi\nu$:

(2.8) $$\omega = \gamma B_0$$

Equation (2.8) is the principal equation of nuclear magnetic resonance. It is called the Larmor equation and ω is also known as the Larmor frequency. Transitions from low to high energy states (excitation) can be induced by applying electromagnetic radiation at the Larmor frequency. The Larmor frequency depends on the gyromagnetic ratio and thus the type of nucleus. For conventional field strengths B_0 the Larmor frequencies will lie within

the radiofrequency band. The oscillating field B_1 used for spin excitations is therefore often referred to as the radiofrequency (rf) field.

In the rest ('equilibrium') state, the spins are distributed over the available states depending on the energy in the system, i.e. following the Boltzmann distribution. For a proton system this is described by:

$$\frac{N^-}{N^+} = \exp(-\Delta E/kT) \quad , \tag{2.9}$$

with k the Boltzmann constant, N^- the number of spins with m=-½, N^+ the number of spins with m=+½.

For nuclear magnetic resonance the energy differences between the states are very small compared to the thermal energy in the system and therefore the population differences between the states are very small. For a proton it is only ~1 in 10^4-10^5; this limits the net absorption and thus the sensitivity of the technique. This is the motivation for the movement towards higher magnetic field strengths: they increase the energy difference between the states, the equilibrium population difference and thus the sensitivity.

2.1.1 Chemical shift

A useful microscopic magnetic effect is the so-called chemical shift. In the same applied magnetic field, spins can experience a different effective magnetic field due to their chemical environment. Surrounding electrons, atoms and atomic bonds shield the nucleus from the main magnetic field. The resulting effective magnetic field can be written as:

$$B_{0,\text{eff}} = B_0(1-\sigma), \tag{2.10}$$

with σ the shielding constant. Following the Larmor equation, this different magnetic field will result in a different resonance frequency. The shift in resonance frequency is measured with respect to an (arbitrary) reference, for protons usually Tetramethylsilane $(CH_3)_4Si$ (TMS), and then divided by the resonance frequency of the reference. The chemical shift is

thus defined in parts per million (ppm) of the resonance frequency. In this way chemical shift is independent of applied field strength.

Chemical shift forms the basis for nuclear magnetic resonance (NMR) Spectroscopy. Using NMR spectroscopy, one can study the chemical environment of spins and thus the structure and function of the molecules they form a part of.

2.2 *Magnetic Resonance: macroscopic description*

When studying a large ensemble of spins, the magnetization $\mathbf{M}(\mathbf{r},t)$ is observed, which is defined as the net sum of nuclear magnetic moments in a volume V divided by V. With a magnetic field B_0 along z, a population difference will exist between states with m= + ½ and m=- ½. A net macroscopic magnetic moment M_0 parallel to B_0 is the result. The size of M_0 depends on the strength of B_0, the temperature and the local spin density of the medium. At equilibrium there is no net alignment of magnetic moment components in the xy-plane. They are distributed randomly and average out over the ensemble. This is the start situation for every MRI experiment.

Now I will describe magnetic resonance on a macroscopic level more generally, using the expectation value of the magnetic moment $\boldsymbol{\mu}(\mathbf{r},t)$ and the total magnetic field $\mathbf{B}(\mathbf{r}, t)$, with $\mathbf{r}$ =(x,y,z) being a point in the laboratory coordinate system of reference. A magnetic moment in a magnetic field experiences a torque given by:

(2.11) $$\mathbf{L}(\mathbf{r},t) = \boldsymbol{\mu}(\mathbf{r},t)\times\mathbf{B}(\mathbf{r},t)$$

The torque $\mathbf{L}(\mathbf{r},t)$ is equal to the rate of change of the angular momentum $\mathbf{P}(\mathbf{r},t)$:

(2.12) $$\mathbf{L}(\mathbf{r},t) = \frac{d\mathbf{P}(\mathbf{r},t)}{dt},$$

Combination of equations (2.3), (2.11) and (2.12) yields

(2.13) $$\frac{d\boldsymbol{\mu}(\mathbf{r},t)}{dt} = \gamma\boldsymbol{\mu}(\mathbf{r},t)\times\mathbf{B}(\mathbf{r},t)$$

By summing up the magnetic moments in an infinitesimal volume element and dividing by the volume one obtains the so-called Bloch equations:

$$\frac{d\mathbf{M}(\mathbf{r},t)}{dt} = \gamma \mathbf{M}(\mathbf{r},t) \times \mathbf{B}(\mathbf{r},t), \tag{2.14}$$

Equation (2.14) describes a precession of $\mathbf{M}(\mathbf{r},t)$ around $\mathbf{B}(\mathbf{r},t)$ with the angular frequency $\omega=\gamma \cdot B(\mathbf{r},t)$. It is now assumed that $\mathbf{B}(\mathbf{r},t)$ contains a radiofrequency field, which rotates with a frequency ω_0 in the xy-plane. For convenience, this problem is described in a coordinate system which rotates with the same frequency. In this so-called rotating frame of reference the radiofrequency component is static and has an amplitude B_1 that may be time dependent. In the rotating frame, equation (2.14) remains unchanged and $\mathbf{B}(\mathbf{r},t)$ is given by

$$\mathbf{B}(\mathbf{r},t) = \mathbf{B}_1(t) + [B_0 - \frac{\omega_0}{\gamma}] \cdot \mathbf{z}, \tag{2.15}$$

with $\mathbf{z}$ the unit vector in the z-direction.
If ω_0 is identical to the Larmor frequency γB_0, the precession of $\mathbf{M}(\mathbf{r},t)$ around B_0 can be ignored. B_0 is effectively removed from $\mathbf{B}(\mathbf{r},t)$. This rotating frame convention will be used from now on in this work. $\mathbf{B}_1(t)$ is now the only field acting on $\mathbf{M}(\mathbf{r},t)$. The result of applying $\mathbf{B}_1(t)$ to $\mathbf{M}(\mathbf{r},t)$ is a precession of $\mathbf{M}(\mathbf{r},t)$ around $\mathbf{B}_1(t)$ with the angular frequency γB_1. The magnetization, which was in the beginning aligned in the z-direction, is tilted by a tip angle θ given by:

$$\theta = \gamma \int B_1(t) dt \tag{2.16}$$

B_1 can thus create a M_{xy} component. It is at its maximum for a tip angle of $\pi/2$ radians (a 90° pulse), when the whole magnetization vector $\mathbf{M}$ is rotated into the xy-plane. After the excitation, the M_{xy} component will precess around B_0 in the laboratory frame with the Larmor frequency. This produces an oscillating magnetic field, which can be picked up by a receiver coil. Its frequency content can be analysed by performing a Fourier transform on

the receiver signal. Apart from generating M_{xy} magnetization, the B_1 pulse can also invert the magnetization. Using a 180^0 pulse (a tip angle of π radians) all magnetization is put along the –z-axis. This is called inversion.

When magnetic field gradients are used, a gradient term $\mathbf{B}_{gradient}(\mathbf{r},t)$ is added to equation (2.15). The net magnetization will now precess around a new axis $\mathbf{B}_{gradient}(\mathbf{r},t) + \mathbf{B}_1(\mathbf{r},t)$ in the rotating frame. A z-gradient can thus be used for slice selection: as one moves away from the centre of the gradient, the tilt of the precession axis out of the xy-plane increases. While a 90° pulse will lead to the magnetization M_0 being rotated into the xy-plane for spins in the centre of the gradient, moving away from the centre of the gradient the magnetization will be less and less tipped towards the xy-plane until the point that the magnetization is completely unaffected by the rf pulse: the spins are off-resonance.

2.3 Relaxation; spin echo experiment

After the perturbation of the magnetization under the influence of $\mathbf{B}_1(t)$ has ended, $\mathbf{M}$ will relax back to its equilibrium state ($+M_z$). This relaxation process can be separated into two components: spin-lattice and spin-spin relaxation.

The spin-lattice or T_1-relaxation pertains to the re-growth of the magnetization vector along the positive z-axis. This magnetization is also called the longitudinal magnetization.

$$\frac{dM_z}{dt} = \frac{M_0 - M_z}{T_1}, \tag{2.17}$$

with t the time and M_0 the equilibrium magnetization. This process is characterised by the constant T_1. T_1 relaxation concerns the return to Boltzmann equilibrium and involves a loss of energy of the spins to their surroundings (the 'lattice'). In the same way that the oscillating $\mathbf{B}_1$ field induces transitions between spin states, any magnetic field with components in the xy-plane that oscillates at the resonant frequency can induce transitions. Oscillating magnetic fields are generated in the surroundings by the motion of nearby

magnetic moments in other nuclei. The dominant contributor to T_1 relaxation for protons in biological systems is the rotational and translational motion of nearby spins (dipoles).

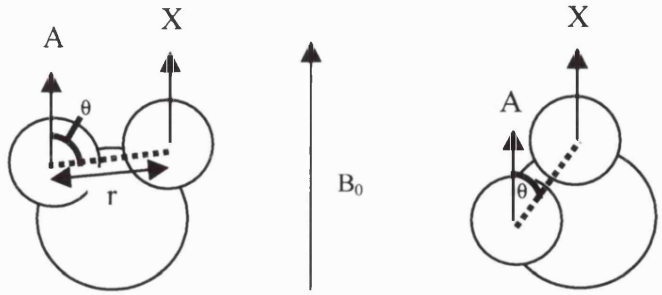

Figure 2-1 Two dipoles A and X within a molecule. The field at spin A due to the spin X depends on the angle θ and the distance r between the dipoles (adapted from Gadian, 1995).

For two dipoles as illustrated in Figure 2-1 the magnetic field component at spin A in the xy-plane is

$$B_{xy} = \frac{3}{2}\sin\theta\cos\theta\frac{2\pi\gamma}{hr^3} \tag{2.18}$$

The spin-lattice relaxation rate depends on the size of the magnetic field component B_{xy} and the tumbling motion of the molecule. This tumbling motion is characterised by its frequency distribution, the spectral density $J(\omega)$, which under many circumstances is given by:

$$J(\omega) = \frac{\tau_c}{1+\omega^2\tau_c^2}, \tag{2.19}$$

with τ_c the correlation time. This correlation time is approximately the root-mean-square of the rotational frequency (in radians/s). This dipole-dipole spin-lattice relaxation mechanism contributes to T_1 relaxation in the following way:

(2.20) $$\frac{1}{T_1} \propto B_{xy}{}^2 \frac{\tau_c}{1+\omega_0{}^2\tau_c{}^2}$$

This relaxation mechanism is most effective when $\tau_c=1/\omega_0$, i.e. when the characteristic frequency of molecular motion ($1/\tau_c$) is equal to the Larmor frequency. Note that the dipole-dipole interaction falls off rapidly with distance: $\sim 1/r^6$.

Spin-spin or T_2-relaxation is used to describe the decay of the net M_{xy} component- the transverse magnetization:

(2.21) $$\frac{dM_{xy}}{dt} = -\frac{M_{xy}}{T_2}$$

This process is characterised by the constant T_2. It arises purely from spin-spin interactions, and involves no transitions between ground and excited states. It is energy neutral- and is therefore sometimes called entropic.

T_2 relaxation is a consequence of the microscopic non-homogeneity of the sample under study: the individual spins experience a slightly different effective B_z depending on their surroundings. This means the magnetic moments will precess around B_0 in the xy-plane with slightly different Larmor frequencies. This leads to dephasing of the magnetic moments and thus a decrease of the resultant M_{xy}.

As the T_2-relaxation determines the rate of dephasing of spins in the xy-plane, it thus determines the line shape of the resonance frequency. This line shape is broadened around the Larmor frequency ν_0 by a frequency width $\Delta\nu_{1/2}$ – in Hz – following:

(2.22) $$\Delta\nu_{\frac{1}{2}} = \frac{1}{\pi T_2},$$

where $\Delta\nu_{1/2}$ is the frequency width at Full Width Half Max (FWHM) of the resonance peak. There is an inherent uncertainty in the resonance frequency $\Delta\nu_{T1}$ due to the lifetime of the excited state that is limited by T_1:

(2.23) $$\Delta\nu_{T_1} = \frac{1}{2\pi T_1}$$

This lifetime broadening gives a lower limit to $\Delta\nu_{1/2}$ and thus an upper limit to T_2 ($< T_1$).

Looking at T_2 relaxation at the molecular level, again the dipole-dipole interactions prove to be the dominant relaxation mechanism. The sources of T_2 relaxation through this mechanism are magnetic fields in the z-direction:

(2.24) $$B_z = \frac{1}{2}(3\cos^2\theta - 1)\frac{2\pi\gamma}{hr^3},$$

with θ and r defined in Figure 2-1. This component of the T_2 relaxation can be written as

(2.25) $$\frac{1}{T_2} \propto B_z{}^2\tau_c$$

The relaxation rate will be highest for long correlation times, i.e. slow tumbling motions.

Macroscopic magnetic field inhomogeneities also contribute to a loss of coherence in the xy-plane. These magnetic field inhomogeneities can be caused by magnet imperfections, non-optimal magnetic field shimming or by changes in magnetic field susceptibility over the sample. The mechanism of relaxation due to macroscopic magnetic field inhomogeneities is comparable to the microscopic T_2 relaxation mechanism due to different magnetic environments: if spins experience slightly different magnetic fields in time they will dephase with respect to each other in the xy-plane, which will lead to a reduction in the net M_{xy}. When macroscopic magnetic field inhomogeneities are included one speaks of T_2^* relaxation with

(2.26) $$\frac{1}{T_2^*} = \frac{1}{T_2} + \frac{1}{T_2'},$$

T_2' being the result of the macroscopic magnetic field inhomogeneities.

As these macroscopic inhomogeneities are static in time, their dephasing effect can be reversed in time. This is done with a so-called spin echo experiment. At a time τ after spin excitation, the n fast spins (i.e. spins experiencing a higher B_0) have a lead $\Delta\varphi_n$ over the slowest spins in the xy-plane. When a 180° pulse is applied at $t=\tau$ their lead $\Delta\varphi_n$ will become a lag, they now have a phase $-\Delta\varphi_n$. At a time 2τ the fast spins will again have traversed an extra $\Delta\varphi_n$ compared with the slow ones. They started with a phase of $-\Delta\varphi_n$ at $t=\tau$, traversed an extra $\Delta\varphi_n$ during the second τ interval and thus have $\Delta\varphi_n=0$ at $t=2\tau$. All spins will now be in phase, which constitutes the spin echo. This is why a 180° spin echo pulse is also called a 'refocussing' pulse.

Other less prevalent T_1 and T_2 relaxation mechanisms are chemical shift anisotropy (where the chemical shift of the nucleus and thus the local field depends on the orientation of its molecular environment in B_0), spin rotation (relaxation due to electrons that produce a local magnetic field at the nucleus, the size of which depends on the molecular rotational movement), scalar coupling (spin-spin coupling interaction) and electric quadrupole relaxation (the interaction of electric quadrupole moments with local electric field gradients).

Finally, an especially strong cause of relaxation is the presence of paramagnetic molecules. Paramagnetic molecules have unpaired electron spins, which results in magnetic moments a factor 1000 bigger than nuclear magnetic moments. The spin-lattice relaxation rate will depend on the square of the magnetic moment (2.20), and will thus be increased dramatically. The paramagnetic molecules also induce local magnetic field inhomogeneities (due to their different magnetic susceptibility) which will lead to an enhanced T_2^* relaxation.

2.4 Radiofrequency pulses

2.4.1 Slice selection; pulse simulations

An important principle in MRI is slice selection. The idea is to apply a B_1 pulse together with a magnetic field gradient. The resonance frequency of the spins will now depend on

their position along the gradient axis. The rf pulse will only be felt by a slice of spins that are not too far from resonance; the thickness of this slice is determined by the bandwidth of the pulse and the strength of the slice selective gradient. Thus a slice of spins can be selectively excited/inverted, leaving the rest of the sample unaffected. The performance of the rf pulse at a range of frequency offsets now becomes of interest. The slice profile is the projection of the slice along the slice selective axis. Ideally it is a perfect rectangle: full excitation/inversion within the desired slice, zero excitation/inversion outside. As explained in section 2.2, this is not likely to happen, as the rotation axis tilts when moving away from resonance. The rotation angles will thus gradually decrease. The slice profile can be optimised by shaping the B_1 pulse in time.

To predict the slice profile of rf pulses, one can simulate their effect by integrating the differential Bloch equation (2.14) over time and space. This is done by numerically integrating the equation using spherical polar coordinates and coordinate transformations, to arrive in a reference frame in which the change in magnetization from step to step can be easily calculated (Mansfield and Morris, 1982; Bottomley and Hardy, 1987). The equations and transformation matrices are given below:

(2.27) $$\mathbf{M}(t+dt) = \mathbf{R}_\phi \cdot \mathbf{R}_\theta \cdot \mathbf{S} \cdot \mathbf{R}_\theta^{-1} \cdot \mathbf{R}_\phi^{-1} \cdot \mathbf{M}(t),$$

with

(2.28)

$$\mathbf{R}_\phi^{-1} = \begin{bmatrix} \cos\phi & -\sin\phi & 0 \\ \sin\phi & \cos\phi & 0 \\ 0 & 0 & 1 \end{bmatrix}; \quad \phi = \arctan\left(\frac{\mathbf{B}_y}{\mathbf{B}_x}\right)$$

$$\mathbf{R}_\theta^{-1} = \begin{bmatrix} \cos\theta & 0 & -\sin\theta \\ 0 & 1 & 0 \\ \sin\theta & 0 & \cos\theta \end{bmatrix}; \quad \theta = \arctan\left(\frac{\mathbf{B}_{xy}}{\mathbf{B}_z}\right)$$

$$\mathbf{S} = \begin{bmatrix} \cos\alpha & \sin\alpha & 0 \\ -\sin\alpha & \cos\alpha & 0 \\ 0 & 0 & 1 \end{bmatrix}; \quad \alpha = \gamma \mathbf{B}_{eff}(t)dt$$

The required transformation is split up in 5 steps: the transformation $\mathbf{R}_\phi^{-1}$ puts the B_{xy} component along x. The subsequent $\mathbf{R}_\theta^{-1}$ transformation puts the vector sum of all field components $\mathbf{B}_{eff}$ along z. Then the change of **M** is a simple nutation about $\mathbf{B}_{eff}$ with an angle $\alpha = \gamma \cdot B(t) \cdot dt$ in a rotating frame, which is implemented by the rotation matrix **S**. After the nutation, the system is transformed back into the starting frame by the transformations $\mathbf{R}_\theta$ and $\mathbf{R}_\varphi$. The effect of a slice selective rf pulse can be simulated as follows: starting with $\mathbf{M}=\mathbf{M}_0$, the transformations of equation (2.27) are repeated for multiple time steps (covering the length of the rf pulse) and multiple positions in space (steps along the slice selective gradient). The time and position steps need to be sufficiently small that the rf pulse and the slice selective gradient values are constant over that interval.

The slice profile is approximately equal to the Fourier transform of the rf pulse shape. Sinc rf pulses give rectangular profiles and vice versa. But this is only an approximation: the transformation from input pulse to output profile is non-linear as the formula above have shown.

The presence of the slice selective gradient during excitation results in a dephasing of spins in the xy-plane. The amount of dephasing $\Delta\varphi$ depends on the gradient G(t,z) and the spins' position along the gradient axis z :

$$\Delta\varphi(z) = \int G(t,z)dt \tag{2.29}$$

This dephasing is refocussed by applying a gradient of the opposite sign after the slice selective excitation. The strength and duration of this gradient is tweaked experimentally for maximal signal recovery. For a typical 90° pulse the integral of the rephasing gradient over time will be approximately half of that integral of the dephasing gradient.

2.4.2 Adiabatic pulses

Adiabatic pulses have the special property that they are insensitive to variations in B_1 amplitude once the adiabatic equation is satisfied (see below). This is very useful when working with surface coils that exhibit a large B_1 inhomogeneity. The other advantage of

adiabatic pulses is that they can give sharp inversion profiles. This is the reason they are used in the work described in this thesis.

The principle of adiabatic pulses is illustrated in Figure 2-2. Adiabatic pulses have both a time varying $\mathbf{B_1}$ field as well as a time varying field offset $\Delta\mathbf{B_0}$. In the rotating frame, this means the resultant field, $\mathbf{B_{eff}}$, is the vector sum of $\mathbf{B_1}(t)$ and $\Delta\mathbf{B_0}(t)$. By changing the relative contributions of $\mathbf{B_1}$ and $\Delta\mathbf{B_0}$, the direction of $\mathbf{B_{eff}}$ can be changed and $\mathbf{B_{eff}}$ can be rotated during a pulse from, for instance, +z to –z. The net magnetization vector **M** will follow $\mathbf{B_{eff}}$ provided $\mathbf{B_{eff}}$'s rotation frequency $d\alpha/dt$ is much smaller than the frequency with which **M** rotates around $\mathbf{B_{eff}}$:

$$\left|\frac{d\alpha}{dt}\right| << |\gamma B_{eff}(t)| \tag{2.30}$$

This is called the adiabatic equation. This means excitation and inversion can now be achieved by rotating $\mathbf{B_{eff}}$ following the adiabatic equation. When $\mathbf{B_{eff}}$ has been rotated into the xy-plane ($\Delta\mathbf{B_0}$=0), **M** will be aligned with $\mathbf{B_1}$ and lies thus in the xy-plane. This is an excitation independent of the size of $\mathbf{B_1}$. When $\mathbf{B_{eff}}$ is rotated to end up along the –z-axis ($\mathbf{B_1}$=0), again the size of $\mathbf{B_1}$ is irrelevant: **M** will reach full inversion despite any B_1 inhomogeneities.

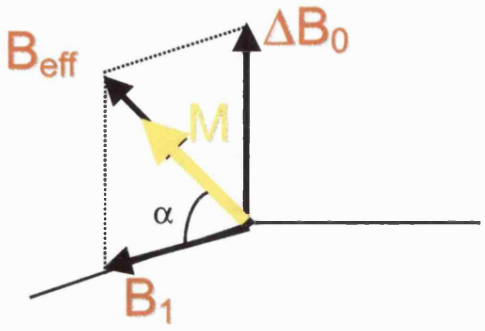

Figure 2-2 The principle of adiabatic pulses.

An elegant in-vivo implementation of adiabatic inversion is the so-called adiabatic fast passage (AFP) described by Dixon and colleagues (Dixon et al., 1986). When a low power, constant rf field is combined with a magnetic field gradient along the arterial flow direction, blood spins are inverted as they flow through the magnetic field gradient. This inversion relies on the linearity of bulk blood water flow. The gradient and rf fields have to be chosen to satisfy the adiabatic condition for the flow rates of the spins.

Many types of pulses can be designed that satisfy the adiabatic equation. A well-known adiabatic inversion pulse is the Hyperbolic Secant (HS) pulse (Silver et al., 1985). This pulse is an exact solution to the Bloch equations. It is given by:

(2.31) $$B_1(t) = \Omega_0 \mathrm{sech}(\beta t)$$

(2.32) $$\Delta B_0(t) = -\frac{\mu\beta}{\gamma}\tanh(\beta t),$$

with

(2.33)
$$\sinh x = \frac{\exp(x)-\exp(-x)}{2}; \cosh x = \frac{\exp(x)+\exp(-x)}{2}; \tanh x = \frac{\sinh x}{\cosh x}; \mathrm{sech}(x) = \frac{1}{\cosh(x)}$$

The t variable is related to the time of the pulse (Tp) by $t \in [-Tp/2 , +Tp/2]$.
This pulse is adiabatic under the following conditions:

(2.34) $$\Omega_0 \geq \mu\beta$$

and

(2.35) $$\mu \geq 2$$

Under these conditions the HS pulse will result in a localised inversion of a bandwidth

(2.36) $\Delta\omega = \pm\mu\beta$

2.4.2.1 FOCI pulses

Recently, Ordidge and colleagues (Ordidge et al., 1996) reported Frequency Offset Corrected Inversion (FOCI) pulses that are an extension to the HS pulses and perform even better. Their profiles are more rectangular and the FOCI pulse also leads to less chemical shift errors. Chemical shift errors arise when two species with different chemical shifts (for instance, fat and water) undergo the same slice selective pulse. Because of the different effective magnetic fields they feel, their resonance frequencies are different (2.1.1). A rf pulse will always give the same frequency profile for the two species, but due to their different resonance frequencies this will result in two different spatial profiles. An on-resonance slice selective pulse for water, for instance, will lead to a slightly shifted inversion profile for fat, as its 'on-resonance' field strength lies further along the slice selective gradient.

It had been discovered previously that using a higher slice selective gradient for a rf pulse leads to a sharper profile and less chemical shift errors, as every voxel along the gradient now spans a wider bandwidth. However, such a pulse requires a higher bandwidth, shorter pulse time and thus higher peak power. Using simulations, Ordidge et al. show that spin inversion of the profile edges occurs mostly at the beginning and end of the pulse. To improve the slice profile, they therefore increase the field gradient only at the beginning and end of the pulse, reducing the gradient back to its original value in the centre of the pulse. The same modulation function that is applied to the gradient shape is then also applied to the rf and field offset shapes to keep the adiabatic sweep unaffected. By choosing a modulation function that is large at the beginning and end but unity at the centre of the pulse, the maximum required B_1 remains the same. Ordidge et al. describe different types of modulation functions that differ in shape and thus extent of the gradient increase. All

modulation functions are unity at the centre of the pulse and do not exceed 10 anywhere, as above a tenfold increase the adiabaticity of the pulse starts to break down.

Examples of a HS pulse and a so-called FOCI C-shape version of it are given in Figure 2-3. The pulse parameters are μ=5 radians, β=1500 s^{-1}. The minimum B_1 peak amplitude used for the HS pulse (2.34) stays the same for the FOCI pulse, as does the pulse bandwidth ($\Delta\omega_0$ goes from –7500 radians/s to +7500 radians/s). The modulation applied to the gradient waveform is the same as the one applied to the field offset and rf fields. Using pulse simulations as described in section 2.4.1, the expected pulse profiles for a slice selective HS pulse and a FOCI pulse with these parameters are given in Figure 2-4. The inversion slice thickness is 15 mm, the field of view is 20 mm, the pulse time is 8 ms and 800 simulation points have been used for the time and space steps.

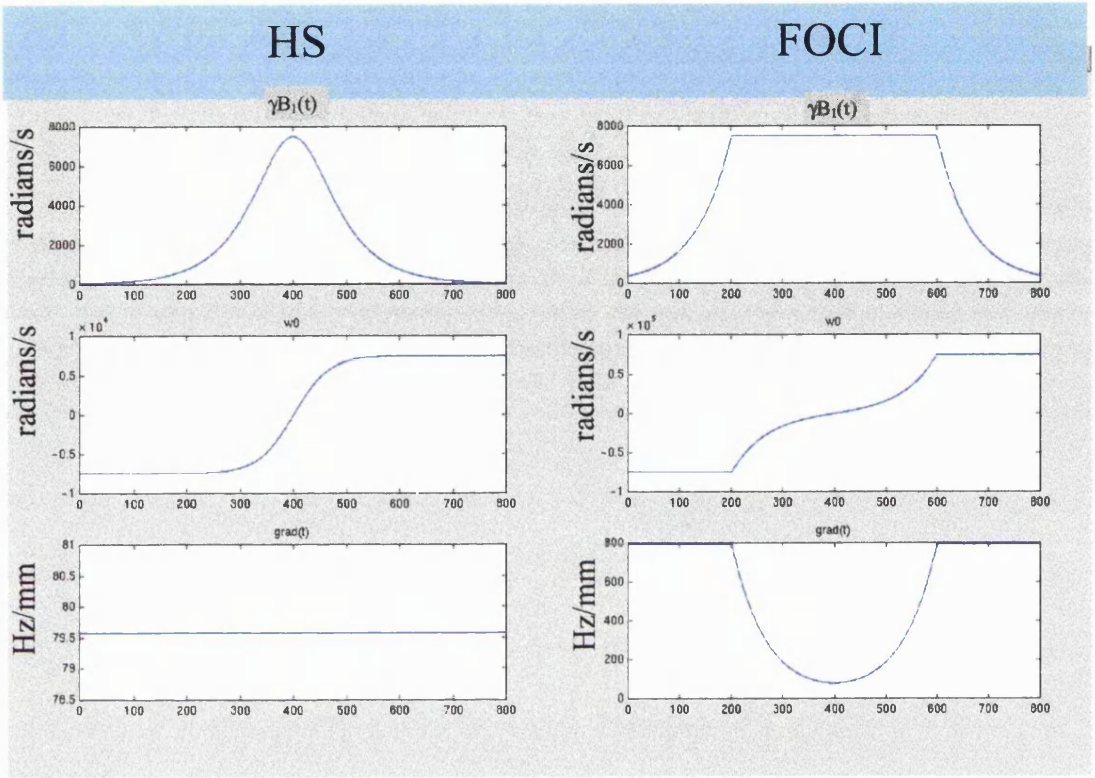

Figure 2-3 HS and FOCI pulses: rf (top) in radians/s, Δω(middle) in radians/s and gradient shapes (Hz/mm) for HS (left) and FOCI C-shape pulse (right).

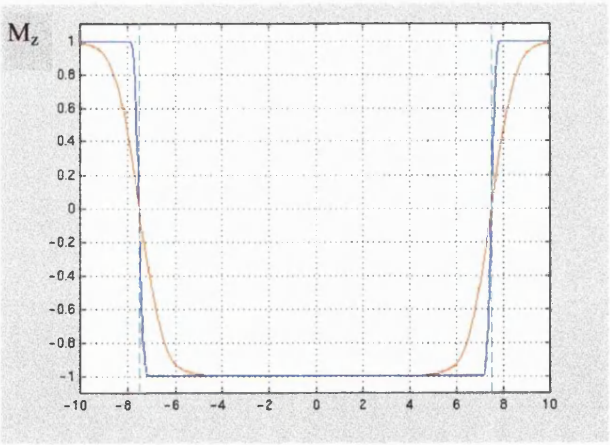

Figure 2-4 Simulated profiles of HS and FOCI pulses as described in the text. HS: red line, FOCI: dark blue line, striped light blue line gives –7.5 mm, +7.5mm inversion boundaries of a perfect pulse.

2.4.3 A standard imaging experiment

The use of magnetic field gradients is pivotal to MRI. Their use in slice selective excitation and inversion was briefly discussed earlier in this chapter. Magnetic field gradients have many applications, because they allow the observation and manipulation of spins depending on their spatial position, i.e. position encoding.

When turning on a magnetic field gradient, the spins' Larmor frequency becomes dependent on their position. If one excites a whole object and then turns on a gradient during the signal acquisition, a Fourier transform of the receiver signal will give a projection of the object along the gradient direction. This is because a spin's resonance frequency is determined by its position and the amplitude of that frequency is determined by the number of spins at that position. This spatial encoding by using a gradient during the readout is called frequency encoding. Lauterbur (Lauterbur, 1973) first published this principle, which constituted the birth of MRI.

Spatial encoding in the second dimension is achieved by a so-called phase encoding: depending on their position along a second (perpendicular) axis, the spins are given a different phase. This is achieved by temporarily switching on a gradient along the second axis. After this phase encoding gradient has been switched off the phase differences between the spins are conserved. At a point y along the second axis the phase shift $\Delta\varphi$ acquired after a phase encoding gradient of length t is given by:

$$\Delta\varphi(y) = \gamma y \int_0^t G_{ph}(t)dt \tag{2.37}$$

By repeating the same experiment [excitation-> phase encode -> frequency encoded readout] with different strengths of the phase encoding gradient, a two dimensional matrix is built up with position information encoded in both dimensions. (The collection of phases for different gradient strengths characterises the position dependent Larmor frequency induced by the applied second gradient). A two-dimensional Fourier transform will now give the position dependent spin density in two dimensions.

A typical MRI experiment using slice selection, phase encoding and frequency encoding is given in Figure 2-5. The spins are excited by a slice selective pulse and the dephasing caused by the slice selective pulse is rephased. The excitation pulse is often a 90° pulse, which rotates **M** fully into the xy-plane. However, if the sequence repeats are run very rapidly after each other such that $TR < T_1$, the maximum signal is the result of a balance between T_1 recovery and the number of sequence repeats. The signal to noise ratio (SNR) can be optimised by using the Ernst excitation angle α:

$$\cos\alpha = \exp(-TR / T_1) \tag{2.38}$$

Optimal rapid imaging thus involves a short TR and a low excitation flip angle. When the sequence is run in this manner it is called a Fast Low Angle Shot (FLASH) sequence (Haase et al., 1986). It has the following features:
Phase encoding: the gradient is stepped through *m* different values for each sequence repetition.
Readout: in this case a so-called gradient echo is shown: the spins are first dephased to give a gradient echo in the middle of the readout period. The signal is sampled with *n* sample points. The time from the middle of the excitation pulse to the maximum of the echo is the echo-time TE, the time from the excitation to the next in the subsequent sequence repeat is the repetition time TR.

A three-dimensional data set can be collected by acquiring multiple slices after each other or by adding a third perpendicular (phase encoding) axis. This basic type of sequence can be extended to the aforementioned spin echo experiment by adding a 180° refocussing pulse after the excitation pulse. The time from excitation to 180° pulse should then be equal to the time from the 180° pulse to the half of the readout gradient and will be equal to TE/2. Such a spin echo experiment is requires a longer TR due to the extra (refocussing) pulse and the echo time.

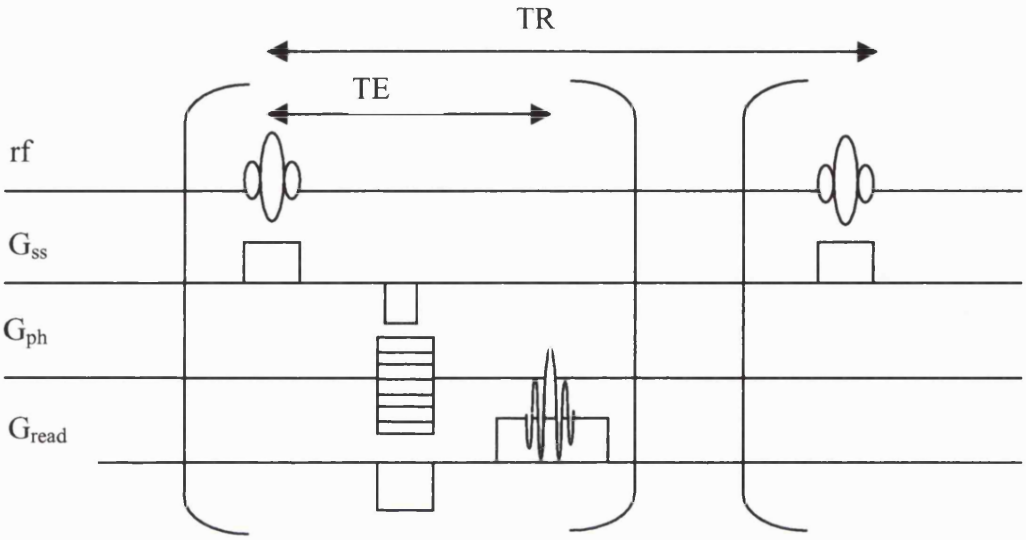

Figure 2-5 Basic MRI experiment. G_{ss}: slice selective gradient, G_{ph}: phase encoding gradient, G_{read}: readout/frequency encoding gradient. TE: echo time, TR: repetition time.

The sample that is being imaged is thus divided into small volumes, or voxels, by the slice selection, phase encoding (*m* points) and readout gradient (*n* points). The signal of a voxel is the sum of all spin contributions in it, and spins in a voxel can not be distinguished from each other. The size of a voxel defines the resolution of the image. When spins of a very different nature are together in a voxel (for instance CSF and grey matter) the resultant signal might be misleading. This is called a partial volume effect. The final resolution chosen in an image is a trade-off between SNR, partial volume effects and time.

The sequence as depicted in Figure 2-5 is called a multi-shot sequence, as it takes multiple sequence repeats to acquire the data required for an image. There are also single-shot techniques, that acquire all the required information after one excitation. To describe how these work, it is necessary to first introduce the concept of k-space.

2.4.4 K-space

The MRI signal due to the precession of **M** in the rotating frame in presence of a readout gradient can be written as:

$$S(t) = \int_x M \exp(i\omega(x_{read})t)dx, \tag{2.39}$$

with $\omega(x_{read})$ the Larmor frequency depending on the position x along the read gradient. Using equation (2.37) this can be re-written as:

$$S(t) = \int_x M \exp(i\int_0^t \gamma x_{read} G_{read}(t)dt)dx \tag{2.40}$$

Inserting k as defined by:

$$k = \int_0^t \gamma G_{read}(t)dt, \tag{2.41}$$

gives

(2.42) $$S(k) = \int_x M \exp(ikx_{read})dx$$

The signal S is now described as a function of k, the spatial frequency with units radians/m. Equation (2.42) is the Fourier transform of the magnetization M. Completely analogously the effect of the phase encoding gradient on the observed signal can be described in terms of a Fourier transform involving spatial frequencies along the phase encoding direction. A two-dimensional Fourier transform thus connects the object signal M with the time signal S.

A new perspective arises from realising that the multiplication and integration of M with exp(ikx) is an interrogation of the extent to which the spatial frequency k is present in M: for k=0, equation (2.42) reduces to the integral of M, the basic signal intensity. For higher values of k, equation (2.42) results in the integral of a positional dependent phase shift with M: the higher the k value, the faster the phase will change with position. Therefore the integral will yield how much of this frequency is present in M. By acquiring data with a range of k-values (different gradient values) we sample which spatial frequencies are present in the object, i.e. gather information to characterise the object. The k-space data of an object are like a diffraction pattern: it has the low frequency information in the centre and higher and higher frequency information as one moves away from the centre along the k_x (read) or k_y (phase encoding) axis. It is now obvious one needs data with sufficiently large gradient strengths in read and phase encoding directions to characterise the high frequency components of the object under study. The final resolution of the object λ_{min} in m is linked to the maximum acquired k-value by:

(2.43) $$\lambda_{min} = \frac{2\pi}{k^{x,y}_{max}}$$

When sampling a signal with interval dt, the maximum frequency bandwidth $\Delta\nu$ that can be distinguished is given by the Nyquist limit $\Delta\nu=1/(2dt)$. Analogously, the Field of View

(FOV) is connected to the size of the k-space increments (that are determined by the gradient samples m and n) by:

$$\text{FOV}_{x,y} = \frac{2\pi}{\Delta k_{x,y}} \tag{2.44}$$

By describing a MRI experiment in terms of data acquisition in k-space, more efficient gradient schemes can be devised to acquire the desired data.

2.4.5 Echo Planar Imaging

A FLASH sequence acquires one k-space line per repeat: by incrementing the phase encoding gradient from shot to shot the k-space data from the second dimension are gathered. This sampling scheme is illustrated in Figure 2-6.

A more efficient way of sampling k-space is given in Figure 2-7, this is the Echo Planar Imaging (EPI) sampling scheme (Mansfield, 1977). All the k-space lines are acquired in one go after the excitation pulse. This is achieved by a train of alternating readout gradient pulses with blips of the phase encoding gradient at the end of each readout lobe. An EPI pulse sequence is given in Figure 2-8. A pre-dephasing lobe both for the readout and phase encoding gradients moves the spin system to the outer edge of k-space. Subsequent readout lobes move k along the k_x axis, the phase encoding blips move from one k_y value to the next at the end of a k_x line.

EPI is very fast: it can acquire a whole slice in ~ 50ms. A FLASH sequence takes ~ 600 ms for the same image matrix. The great advantage of this fast EPI sequence is that it is less motion-sensitive than conventional sequences. However, it is much more demanding on the gradient hardware due to the rapid gradient switching. Furthermore, it suffers from image distortion and signal dropout in areas with magnetic field inhomogeneities. These inhomogeneities arise at boundaries with large magnetic field susceptibility changes, for instance at tissue-air interfaces. The reasons that EPI is so sensitive to these are the following: firstly, due to its long readout window compared to conventional sequences (typically ~30-100 ms vs 5-15 ms) the bandwidth along the phase encoding direction is quite small. An external gradient can thus easily disturb the phase encoding.

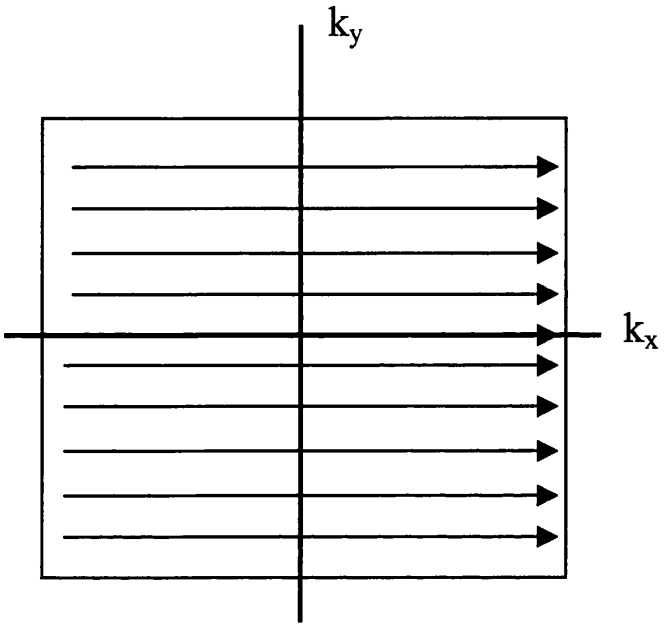

Figure 2-6 K-space sampling scheme for a FLASH sequence: one k-space line per excitation.

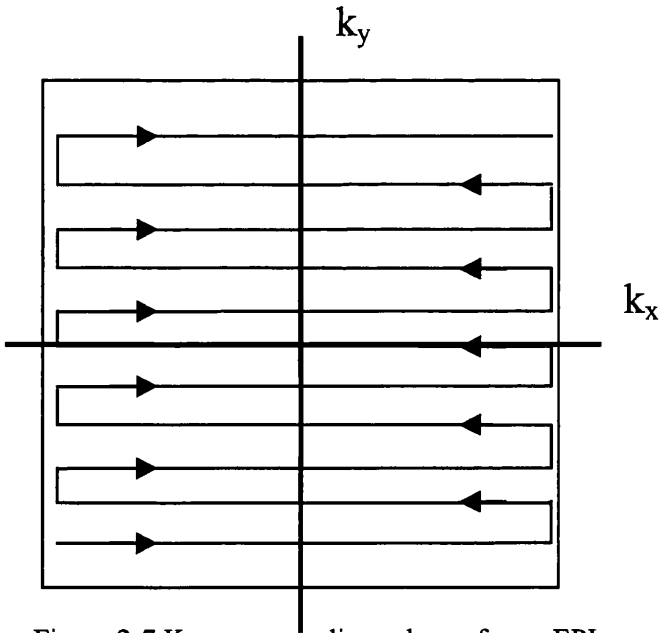

Figure 2-7 K-space sampling scheme for an EPI sequence: all k-space lines are acquired after one excitation.

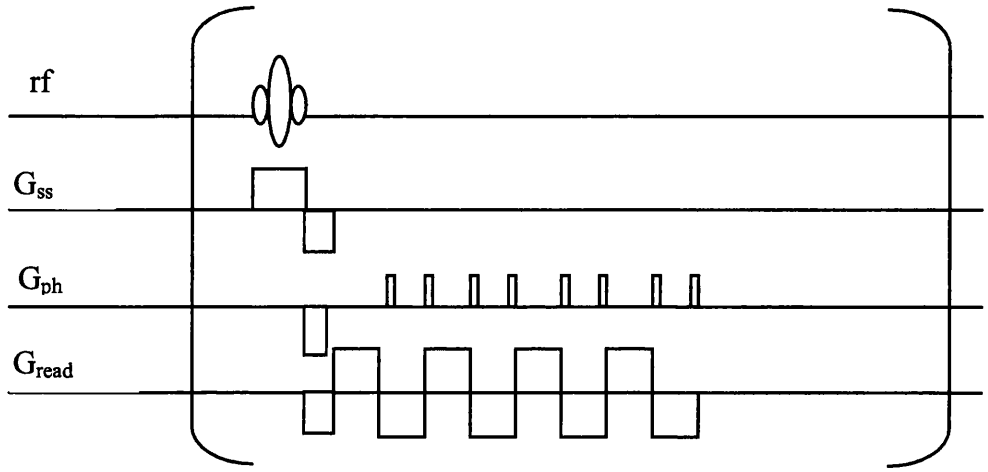

Figure 2-8 EPI pulse sequence.

A change in position of signal due to inhomogeneities leads to image distortion. Along the readout direction, a shift out of the acquisition window leads to signal dropout. Dephasing within a voxel due to field inhomogeneities will also have this effect.

The phase encoding direction is the one that is the most sensitive to artefacts and signal loss. Blurring along the phase encoding direction can occur due to the T_2^* decay during the readout, as the higher frequencies are not sampled completely. Chemical shift artefacts arise because the resonance frequency differs for spins at the same position along a gradient if they have a different chemical shift: the signal from these spins will be shifted into another voxel. For fat this can be a large shift, ~ 28 voxels. This is why the fat is usually suppressed by a single or composite saturation pulse at the beginning of the pulse sequence.

Finally, Nyquist or N/2 ghosting is a typical EPI problem. It arises as follows: the data in an EPI sequence are acquired by traversing k-space alternately from right-to-left and left-to-right by changing the polarity of the readout gradient. In the analysis the second lines are reversed to account for the opposite traversal of k-space in time. One assumes that right-to-left and left-to-right acquisitions are completely equivalent, but this is often not the case. Background susceptibility gradients, imperfections in the gradient pulses or gradient-induced eddy-currents can result in small mismatches between the even and odd lines. The small shift Δk every two lines constitutes an oscillation at the highest frequency that can be sampled. In the image domain this leads to an extra image, shifted by FOV/2 to the edge of image space. The larger the shift Δk, the larger the relative amplitude of this second shifted image becomes with respect to the normal image.

Nyquist ghosts can be minimised by optimising gradient hardware, minimising eddy currents and so forth. They can be corrected by acquiring so-called Navigator echoes at the beginning of the sequence: the phase encoding gradient is switched off and odd and even echoes are acquired. The differences between these echoes can be used to correct the rest of the data acquired thereafter.

2.5 Image weighting

Image data can be sensitized to a range of MRI parameters and physiological processes.

2.5.1 Proton density, T_1, T_2 and T_2* weighting

If the signal in the final image depends only on the proton density at each voxel, the image is proton density weighted. These are images that may have little contrast between tissue types. By making use of the different relaxation properties, much higher contrast can be achieved between tissues and other compartments such as CSF.

Sequences can be optimised to be most sensitive to differences in T_1, T_2 or T_2* relaxation. An inversion recovery sequence, for instance, is used to highlight differences in T_1. The speed of the M_z recovery is determined by the T_1 for each object constituent. By choosing the inversion time (the time from the middle of the inversion pulse to the middle of the excitation pulse) appropriately, the difference in signal between the T_1 species can be optimised. Another way of achieving T_1 contrast is by scanning with a short TR. Each T_1-species will reach a different steady state magnetization depending on the balance between their relaxation rate and the TR. The different steady state magnetizations are again a source of contrast.

T_2 weighting can be achieved with a spin echo experiment. The signal differences between tissue types can be maximised by using long echo-times. For long TE the contrast is maximal but the signal to noise is very low; a trade-off has to be made.

Gradient echo experiments (like EPI) without 180° spin echo pulses are T_2* weighted. As for T_2 weighting, the longer the echo-time, the larger the T_2* weighting and the smaller the signal. T_2* sequences are by definition sensitive to magnetic field inhomogeneities. This has many disadvantages such as the aforementioned image distortion and dropout. However, T_2* is also an alternative source of image contrast. Together with T_2, it can be used to measure levels of brain iron, which is accumulated in the course of ageing and in some neurodegenerative diseases such as Parkinson's disease and multiple sclerosis (Vymazal et al., 1995).

This sensitivity of T_2* to iron is exploited further in the so-called Blood Oxygen Level Dependent (BOLD) effect, which is the difference in T_2* weighted MRI signal of

deoxyhemoglobin versus oxyhemoglobin (Ogawa et al., 1990; Turner et al., 1991; Kwong et al., 1992). Deoxyhemoglobin has a net magnetic moment due to unpaired electrons on the iron in its heme groups; it is paramagnetic. In oxyhemoglobin oxygen is bound to the heme groups, the iron has no unpaired electrons and it therefore has no net magnetic moment. Brain activity results in a local *increase* in oxyhemoglobin and thus in an increase of local MRI signal due to the decrease in the paramagnetic deoxyhemoglobin. The BOLD effect is thus a marker for brain activity.

The intrinsic parameters T_1, T_2 and T_2* can be influenced dramatically by contrast agents. These contrast agents are often paramagnetic elements such as Gadolinium (Gd3+). These agents affect their surroundings by speeding up the spin relaxation. Their distribution and uptake appears readily on an appropriately weighted scan and shows if, for instance, the Blood Brain Barrier is disrupted.

2.5.2 Perfusion

Cerebral perfusion –known as cerebral blood flow or CBF - is a measure of blood supply at the tissue level. An adequate blood supply at this level is essential, as it is here at the capillaries with their slow blood flow and thin vessel walls, that the exchange of oxygen, nutrients and waste products between the blood and the brain cells takes place. Because CBF is defined at the capillary level, it is non-directional and has the units ml per 100g of tissue per minute (ml/100g/min). Normal CBF reported for grey matter is ~ 50-80 ml/100g/min, in white matter ~ 20-30 ml/100g/min (Calamante et al., 1999).

Perfusion is an important indicator for tissue health. Together with diffusion, it is one of the important clinical and scientific parameters for the study of (patho)physiology. Acute stroke, for instance, can be detected within minutes of the event with perfusion and diffusion methods. This is not possible using conventional MRI scans (T_1, T_2, T_2^*, proton density). Diffusion and perfusion MRI are thus important methods in the study of cerebral ischemia. Issues of interest are, for instance, the identification and characterization of the ischemic penumbra and finding the (combination of) perfusion and diffusion parameters that can predict long-term outcome for the affected tissue. Physiological parameters such as cerebrovascular reserve and cerebrovascular reactivity are also accessible using perfusion

methods. Furthermore, perfusion methods can be used in the study of brain tumors, as they have deviant CBF patterns. Apart from the observation and characterization of cerebrovascular disease, perfusion methods can allow therapeutic evaluation: assessing how well the tissue responds to medical intervention.

Besides the study of (patho)physiology, there is another reason why perfusion is of great interest to neuroscientists: perfusion is linked to brain activation. As early as 1890 Roy and Sherrington reported a link between brain metabolism and cerebral blood flow (Roy and Sherrington, 1890). When a brain area becomes active, local cerebral blood flow increases. This is the so-called hemodynamic response. The aforementioned BOLD effect is linked to this cerebral blood flow increase. By measuring the BOLD effect or the cerebral blood flow throughout the brain over time, one can therefore follow brain activation. This principle is the basis for the field of 'functional brain mapping', a systematic charting of brain function.

The measurement of CBF is different from methods used in angiography. This is because the parts of the vasculature that are observed in a CBF measurement are the smallest vessels (capillaries) with the slowest blood flow. The vessels themselves can not be visualised directly. CBF is measured indirectly by observing the amount of label arriving in a slice of interest.

Clearance methods observe the clearance of external tracers from the head after they have been injected into the bloodstream or inhaled. Nitrous oxide, krypton, xenon, hydrogen and microspheres have been used for this purpose. Positron Emission Tomography (PET) is the most successful approach; it is relatively safe and practical for use in animals and humans. The radioactive tracer it uses to measure CBF is labelled water ($H_2{}^{15}0$).

One of the advantages of MRI perfusion methods is that they can easily be combined with other MRI methods (diffusion-weighted imaging, metabolite spectroscopy, BOLD fMRI) to give a broader picture of brain physiology and function. Common invasive

MRI perfusion methods use contrast agents such as Gadolinium in so-called bolus tracking approaches (Villringer et al., 1988; Rosen et al., 1990). This class of techniques is called Dynamic Susceptibility Contrast (DSC) MRI. The contrast agent (~ 0.1 - 0.3 mmol/kg body weight) is injected in the blood stream, and the passage of the bolus through the brain is tracked by rapid acquisition of T_2 or T_2* images. Fast acquisition of the MRI signal is of great importance as the transit time of the bolus through the tissue is only a few seconds. The aim is to observe the first bolus passage with good temporal resolution.
The effect of the bolus passage on the T_2/T_2* MRI signal is a signal loss due to the spin dephasing effect of the contrast agent. Although the tracer is limited to the vascular space (~ 5% of the total tissue volume) its susceptibility effect extends far beyond the vasculature into the tissue. From the passage data the perfusion can be calculated using the principles of tracer kinetics for nondiffusable tracers (Zierler 1962, Axel 1995, Østergaard 1996)

This model assumes an intravascular tracer, which means the Blood Brain Barrier must be intact. The model gives for a voxel of interest (VOI): the CBF, Cerebral Blood Volume (CBV) and the Mean Transit Time (MTT), which is the average time needed for any particle of tracer to pass through the tissue after an ideal bolus injection. The latter parameter is especially interesting for the study of cerebrovascular disease where transit times can become very long.

Three time-dependent functions are defined to describe the movement of the tracer through the volume of interest. First, the Transport function, h(t), is a probability density function of transit time t through the VOI following an instantaneous unit bolus injection. This function characterizes the distribution of transit times through the VOI. This distribution depends on the vascular structure and the blood flow. Second, the Residue function, R(t), which is the fraction of tracer left in the VOI at a time t after an instantaneous unit bolus injection. The Residue and the Transport function are related, as all of the tracer that has passed through is subtracted from the Residue function. The Residue function at t=0 is per definition one. Finally, the Arterial input function (AIF), $C_a(t)$, is the concentration of contrast agent in the feeding vessel to the VOI at time t.

The concentration of tracer in a volume of interest, C_{VOI}, at a time t after bolus injection can be written as

(2.45) $$C_{VOI}(t) = \frac{\rho}{k_H} CBF(C_a(t) \otimes R(t)) = \frac{\rho}{k_H} CBF \int_0^t C_a(\tau) R(t-\tau) d\tau$$

ρ is the density of brain tissue and k_H is a scaling factor that accounts for the difference in haematocrit between capillaries and large vessels, as the tracer can only access the plasma volume. The concentration of tracer in a volume of interest is deduced from the T_2/T_2^* data using the relation (Villringer et al., 1988; Fisel et al, 1991)

(2.46) $$C_{VOI}(t) = \kappa_{VOI} \Delta R_2 = -\frac{\kappa_{VOI}}{TE} \ln\left(\frac{S_{VOI}(t)}{S_0}\right),$$

with $R_2 = 1/T_2$ or $1/T_2^*$, S_0 the baseline signal before bolus injection and $S_{VOI}(t)$ the signal intensity in the VOI at time t. κ_{VOI} is a constant and TE is the echo time of the pulse sequence.

A full quantification is in principle possible by measuring S_0 and $S_{VOI}(t)$ and using equation (2.46) to get $C_{VOI}(t)$. Equation (2.45) then has to be deconvolved to calculate CBF. Many approaches have been developed for this deconvolution. They have recently been reviewed by Calamante et al. (Calamante et al., 1999). An accurate arterial input function $C_a(t)$ is very important for the modelling. It can be measured empirically most accurately by measuring it close to the volume of interest; this is due to the delay and dispersion of tracer that occurs on the way from the artery to the volume of interest.

The CBV can be determined using

(2.47) $$CBV = \frac{k_H}{\rho} \frac{\int C_{VOI}(t) dt}{\int C_a(t) dt}$$

The normalisation by the arterial input function serves to make CBV independent of the amount of tracer injected. Relative CBV (relCBV) is independent of the arterial input function and has therefore been a popular physiological parameter to measure with DSC MRI.

A third physiological parameter that can be measured is the mean transit time, MTT. It can be calculated using

$$\text{MTT} = \frac{\text{CBV}}{\text{CBF}} \tag{2.48}$$

This model requires a number of assumptions: (1) The Blood Brain Barrier is intact, i.e. the tracer is intravascular; (2) The CBF is constant during the measurement, i.e. the brain is in a steady state; (3) The contrast agent is a true tracer: it has no effect on CBF and no significant volume; (4) There is no significant contribution of a second bolus passage to the data; (5) The tracer does not effect T_1 relaxation; (6) No significant delay or dispersion occur from the point of the measured arterial input function to the volume of interest. This last assumption might not be valid in all cases of cerebrovascular disease, which would lead to an underestimation of the perfusion.

Full quantification of CBF, CBV and MTT is non-trivial. A major problem is that the amount of contrast that a particular injection gives depends on the local vascular architecture. A T_2* weighted acquisition will give signal from the whole arterial tree, not just the capillary bed. One can't 'spoil' large vessel signal. Also, the arterial input function is determined away from the site of interest so there might be a different AIF locally due to, for instance, clots in downstream branches. Also, assumption (3) – that there is no significant contribution of a second bolus passage to the data – might become especially problematic in clinical cases where the bolus passage distributions are even broader than normally.

A way around quantification problems is to calculate relative CBF, CBV and MTT values. Easier, less robust approaches have also been adopted commonly. The use of summary parameters, for instance, does not require extensive modelling. Examples of these parameters are time-to-peak (TTP), bolus arrival time (BAT), maximum peak (MP), full-width-half-maximum and peak area. These parameters relate in a complex way to CBF, CBV, MTT, bolus volume and shape, injection rate and cardiac output. They are therefore not easily interpretable or reproducible. This makes the summary parameters unreliable for

use in longitudinal or comparative studies. They can be useful as a quick and easy single-session measure to find local physiological abnormalities. DSC MRI can thus readily give useful data, but a true CBF, CBV and MTT quantification is difficult and is therefore not commonly performed.

Another issue is that bolus tracking is non-diffusable: the label stays within the vasculature at all times. Strictly speaking, it does not really tell you what arrives in the tissue. If the blood goes straight from the arterial to the venous system (an A-V shunt) the DSC technique will overestimate the perfusion to the local tissue.

A final drawback of DSC MRI is its invasiveness, which limits its application in (repeated) studies on normals.

Non-invasive MRI perfusion techniques use water itself as a freely diffusible, endogenous tracer. The blood water is labelled by an inversion or saturation pulse and then detected as it moves into the slice of interest. These techniques are known as arterial spin labelling (ASL) or arterial spin tagging (AST). Both CBF and transit time can be fully quantified reproducibly. Because these techniques are non-invasive, they allow repeated studies on normals. They are the focus of this thesis and are therefore reviewed extensively in the next chapter.

3 Introduction to ASL Methods and BOLD fMRI

3.1 Arterial spin labelling

Non-invasive, quantitative CBF methods have become feasible in MRI with the conception of arterial spin labelling (ASL)[2] methods. The first ASL method was reported by Detre and colleagues (Detre et al, 1992). ASL methods monitor CBF by following labelled arterial blood spins into the tissue or, alternatively, fresh blood spins into labelled tissue. The labelling is achieved with a selective inversion or saturation pulse on the blood or on the slice of interest. The exchange between fresh and labelled spins occurs at the capillary level, where blood and tissue compartments communicate. Water is thus used as an endogenous, freely diffusable tracer. The final tissue concentration of labelled spins depends on CBF and the T_1 relaxation of the label. ASL MRI acquires images sensitized to the CBF label. A full quantification of CBF is possible by fitting the CBF weighted data to a perfusion model. This procedure often requires knowledge of other parameters such as λ, the brain/blood partition coefficient for water, the T_1 value of arterial blood, the labelling efficiency α_0 and the tissue equilibrium magnetization M_0.

A range of ASL techniques has been developed over the last decade. The techniques differ in how and where they label the water, how they can be used to quantify perfusion and which problems they are trying to solve or minimise. A useful categorisation of ASL methods is into continuous and pulsed techniques.

3.1.1 Continuous ASL methods

The continuous methods were the first to be developed. Detre and colleagues used a train of rf pulses to continuously saturate blood water spins flowing through the neck. This procedure eventually leads to a steady state in the slice of interest of saturated blood spins exchanging with fresh tissue spins (Detre et al., 1992). An improvement to this paradigm uses the aforementioned adiabatic fast passage inversion (Williams et al., 1992) to invert

[2] These techniques are also known as arterial spin tagging (AST), but I shall refer to them only as arterial spin labelling (ASL).

blood spins in the neck selectively and continuously. For both labelling methods the data of the slice of interest are acquired in a steady state of blood and tissue spins exchanging. A control image is acquired by labelling equidistantly from the imaging slice on the other side, to control for any effects of the labelling pulses on the imaging slice (see Figure 3-1). The effects of the CBF on the measured signal from the slice of interest can be calculated by modifying the Bloch equations, taking into account the in- and outflow of spins.

$$\frac{dM_z(t)}{dt} = \frac{M_b^0 - M_z(t)}{T_1} + fM_a(t) - fM_v(t), \tag{3.1}$$

with $M_z(t)$ the longitudinal magnetization of brain tissue per unit mass, $M_b{}^0$ the magnetization of fully relaxed brain tissue per unit mass, T_1 the longitudinal relaxation time of brain tissue water, M_a the arterial magnetization per volume of blood and M_v the equivalent of the latter for venous blood. f is the CBF (perfusion) in ml/100g/min. Assuming a good exchange at the capillary level ('a well mixed compartment'), the magnetic state of the venous outflow is equal to that of the water in the brain tissue. The venous magnetization can then be described by the tissue magnetization, scaled by a factor λ, that takes into account the differences in water concentration between blood and tissue.

$$\frac{dM_z(t)}{dt} = \frac{M_b^0 - M_z(t)}{T_1} + fM_a(t) - \frac{f}{\lambda}M_z(t), \tag{3.2}$$

with λ the brain/blood partition coefficient for water defined as (quantity of water/g of brain)/(quantity of water/ml of blood). Under fully relaxed conditions at t=0, inflow = outflow:

$$fM_a^0 = f\frac{M_b^0}{\lambda} \tag{3.3}$$

Given an inversion efficiency α_0 and a continual inversion/saturation of arterial spins, the arterial magnetization M_a can be written as:

(3.4) $$M_a(t) = (1-2\alpha_0)M_a^0$$,

with α_0 the inversion efficiency (0.5 for saturation, 1 for inversion).
Inserting (3.3) and (3.4) in (3.2) gives:

$$\frac{dM_z(t)}{dt} = \frac{M_b^0 - M_z(t)}{T_1} + (1-2\alpha_0)\frac{f}{\lambda}M_b^0 - \frac{f}{\lambda}M_z(t)$$

(3.5)

All time dependent terms have now been rewritten in terms of the tissue magnetization $M_z(t)$. Equation (3.5) can now be solved to give a single exponential decay with a constant T_{1app}:

(3.6) $$\frac{1}{T_{1app}} = \frac{1}{T_1} + \frac{f}{\lambda}$$

The equations can be solved for perfusion (f) OR ΔM to give:

(3.7)

$$\begin{cases} f = \dfrac{\lambda}{T_{1app}}\left(\dfrac{M_b^0 - M_b^{ss}}{\alpha_0 2M_b^0}\right) \\ \Delta M = 2\alpha_0 \dfrac{f}{\lambda} T_{1app} M_b^0 \end{cases}$$

$\Delta M = M_b^0 - M_b^{ss}$

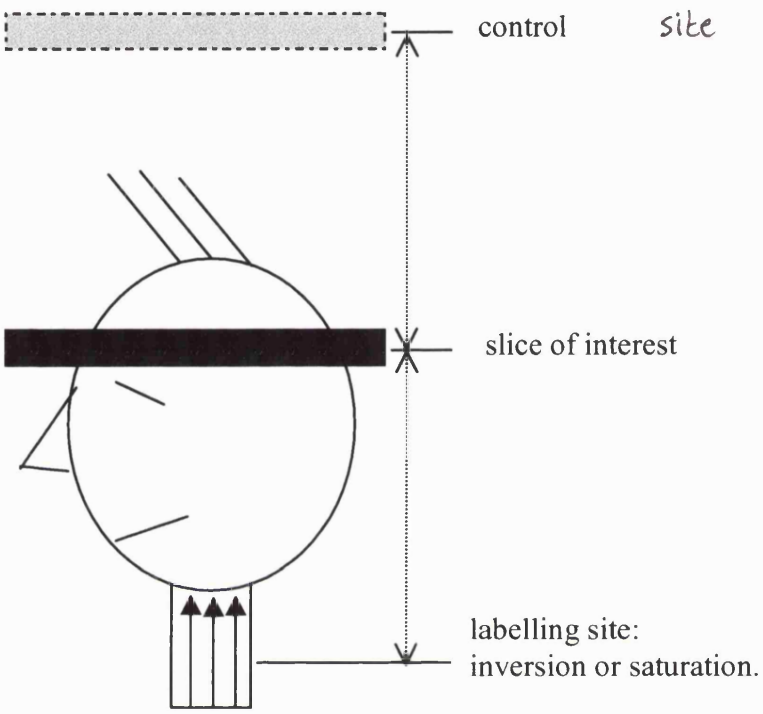

Figure 3-1 Schematic representation of basic setup continuous labelling ASL.

M_b^0 is measured during the control experiment and M_b^{ss} is the steady state tissue signal. The signal difference for the inversion experiment is twice as high as for saturation, which makes it a more sensitive technique. However, the rf deposition for the continuous labelling techniques is high, which requires a careful sequence and study design not to exceed patient safety limits.

There are two important issues affecting the reliability of this technique: magnetization transfer and transit time. These two points have motivated subsequent development of continuous ASL methods and their CBF quantification models.

3.1.1.1 Magnetization transfer effects

Long, off-resonance rf pulses of the order of several seconds are required for the continuous labelling schemes. A problematic side effect of these labelling pulses is the so-called Magnetization Transfer (MT) (Wolff and Balaban 1989). In the slice of interest the water is not affected by the rf pulses due to its narrow resonance bandwidth. Tissue macromolecules, however, have broad resonance peaks, and off–resonance saturation of macromolecules in the slice of interest will therefore occur. These macromolecules then attenuate the signal of the in-slice tissue water through magnetization transfer via dipole-dipole interactions.

The solution for these MT effects (a control acquisition equidistant on the other side of the slice of interest) can be implemented in two ways: by changing the sign of the frequency offset or by reversing the polarity of the labelling gradient. This assumes the magnetization transfer spectrum and the rf and gradient outputs are symmetric around zero. This does not have to be the case. To compensate for rf, gradient and MT spectrum asymmetries Pekar and colleagues suggested a four-step protocol, in which the gradient and rf polarities are alternated (Pekar et al., 1996). This form of MT compensation is complicated for multi-slice applications, however. Every slice needs its own control and slices need more and more off-resonance controls as they are further away from the labelling region. For these reasons other control methods were suggested: for instance a 2-coil approach in which labelling and readout are completely uncoupled (Silva et al., 1995). Because the labelling coil does not extend to the readout region, the macromolecules are

not saturated by the labelling process. This is a technically demanding setup, however. As the tagging and readout locations are far apart, transit time effects –discussed below- are a problem.

Recently, Alsop and Detre (Alsop and Detre, 1998) proposed an amplitude modulated rf method: the amplitude of the rf labelling pulse is modulated with a sine function of frequency ν. The modulation frequency and amplitude are chosen in such a way that the Fourier transform of the rf waveform with base frequency ν_0 gives a pair of inversion planes at frequencies $\nu_0 +/- \nu$. Spins that experience this pulse are inverted at the first plane and then uninverted at the second, thus resulting in the unlabelled control signal. The MT characteristics of the control pulse are equivalent to those of the labelling pulse and thus one control suffices for the whole head. This facilitates multi-slice acquisitions. Disadvantages of this approach are an increased rf power deposition and the fact that the double inversion is not perfect; the inversion efficiency will vary with flow speed and overall it is reduced compared to conventional adiabatic fast passage inversion schemes.

3.1.1.2 Transit time effects

The blood spins have to travel from the labelling site to the imaging site and from the vascular system into the tissue. The time this takes is called the transit time. A non-zero transit time leads to a loss in sensitivity due to label relaxation during the transit. The accuracy of the quantification can also be affected if the delay is not taken into account. The transit time problem is more severe in humans than in animals: transit times are longer in humans and humans tend to be scanned at lower fields where T_1 values are shorter.

When quantifying CBF, the loss of label due to transit time can be taken into account, but only for a mean transit time per voxel. The range of transit times that is likely to occur due to differences in local vascular architecture is harder to take into account. One approach advocated by Alsop and Detre (Alsop and Detre, 1996) is to introduce a delay after the continuous labelling before the acquisition. If the delay is longer than the transit time, the dependence of the difference between labelled and control signal on transit time is minimised:

$$M_z^{tag} - M_z^{control} = -T_{1app} \exp\left(-\frac{\Delta}{T_{1app}}\right)\exp\left(-\delta\left[\frac{1}{T_{1a}} - \frac{1}{T_{1app}}\right]\right)2\alpha_0 \frac{fM_b^0}{\lambda}, \quad (3.8)$$

with δ the transit time and Δ the delay, both in seconds. The difference between arterial and apparent tissue relaxation rates is small (~10% at 1.5 T) for grey matter. Thus the sensitivity to the transit time is minimised. For white matter, however, the relaxation rates are not so similar and this method is therefore not as effective.

This modification to the labelling process is a change from the continuous, steady state approach. Now the labelled blood acts as a bolus that travels from labelling to imaging site. The drawback of introducing this extra delay is a decrease in sensitivity due to the additional T_1 relaxation of the label during this time.

Another approach is to minimise the distance from labelling to imaging site, which reduces the transit time. The labelling site can be moved from the neck upwards somewhat, as long as the blood flow is still approximately linear (needed for AFP inversion to work).

Even so, the transit time for grey matter with continuous ASL can be as high as 0.7 seconds, for white matter it is even longer ~1.2 s (Ye et al., 1996). Ye and colleagues recommend not to assume one transit time for grey and white matter, as this can lead to a large underestimation of CBF of white matter.

3.1.2 Pulsed ASL methods

3.1.2.1 EPISTAR, PICORE AND FAIR

The high rf deposition, magnetization transfer and long transit times associated with continuous ASL methods motivated the development of pulsed ASL methods. With the pulsed methods short rf pulses are used to label the water spins and the labelling site is close to the slice of interest.

The first proposed pulsed ASL method was EPISTAR (Echo Planar Imaging and Signal Targeting with Alternating Radio frequency) by Edelman and colleagues. (Edelman et al., 1994). In EPISTAR the slice of interest is first saturated. Then the blood spins are labelled just below the slice of interest by a slice selective inversion pulse. The in-slice

saturation avoids the potential contamination of the slice signal by the wings of the inversion pulse. After a delay TI, the signal is acquired with an EPI readout. The control measurement is the same sequence with the label applied distal to the imaging slab.

Problems may occur with this approach due to the labelling of draining veins in the control acquisition. A later variant, PICORE, uses a control with the same off-resonance pulse but no slab selective gradient (Wong et al, 1997). This means that no water spins are inverted. The magnetization transfer effects are still present and the control can thus be used to subtract these effects from the data of interest. More recently, Edelman and Chen (Edelman and Chen, 1998) used a control with two 180° pulses to uninvert the spins. This can be set up in such a way that the MT effects for CBF and control scans are comparable.

The acquisition of CBF and control data can be interleaved for pulsed ASL techniques, which reduces sensitivity to motion. By changing the inversion time TI, one can selectively choose which part of the vascular tree one wants to focus on. To quantify, using the modified Bloch equations as described before, Calamante and colleagues (Calamante et al., 1996) show that the difference signal between flow sensitized and control data can be written as:

$$\Delta M = 2\alpha_0 M_0 TI \frac{f}{\lambda} \exp(-TI/T_1), \tag{3.9}$$

where α_0 is the degree of inversion and M_0 is the tissue equilibrium magnetization. It is worthwhile incorporating α_0, as this parameter takes into account inversion pulse profile imperfections. Ignoring these imperfections can lead to an underestimation of perfusion by up to 20% (Keilholz-George, S.D. et al., 2001). Equation (3.9) shows the subtraction signal is a factor of order $\exp(-TI/T_1)$ smaller than the expression derived in (3.7) for continuous labelling.

In the same paper, Calamante et al. show that the assumption that blood and tissue T_1's are equal can lead to substantial errors in CBF quantification: ~ 20% for grey matter, ~100% for white matter. When this T_1 difference and the imperfect inversion are taken into account, equation (3.9) changes into a bi-exponential equation:

$$\Delta M = 2\alpha_0 M_0 \frac{f}{\lambda}\left[\frac{\exp(-TI/T_{1app}) - \exp(-TI/T_{1a})}{1/T_{1a} - 1/T_{1app}}\right], \quad (3.10)$$

where T_{1a} is the T_1 for arterial blood. To quantify CBF, a range of measurements has to be made at different TI values.

Because the labelling and readout sites are closer to each other for EPISTAR than for the continuous techniques, the transit time will be shorter. An even shorter transit time can be achieved by labelling in the slice of interest. Flow-sensitive Alternating Inversion Recovery (FAIR) (Kim, 1995) labels the slice of interest with a slice selective inversion and measures CBF by observing the effect of inflow of fresh spins from outside the slice. The control image is a global inversion with the same readout. The control image is thus (practically) flow-insensitive as inverted spins in the tissue are exchanged with inverted spins from the blood (Figure 3-2). The idea of monitoring CBF by a slice selective inversion of the slice of interest had been proposed before (Kwong, 1992). The crux, however, is the control image that one needs to quantify CBF. Kwong and his colleagues finally extended their approach to arrive at the identical sequence as that of Kim (Kwong et al., 1995).

FAIR minimises transit time and has no MT effects. Moreover, it is sensitive to inflow from below and above as opposed to the methods discussed previously. The quantification is the same as for EPISTAR, described before in equation (3.10).
In the last couple of years, many more variations on pulsed ASL have been suggested (UNFAIR, BASE, TILT, ASSIST etc.). These methods are reviewed extensively by Calamante et al. (Calamante et al., 1999) and Barbier et al. (Barbier et al., 2001). More experimentation is needed to assess which of all the varieties will give practical and significant improvements in perfusion quantification.

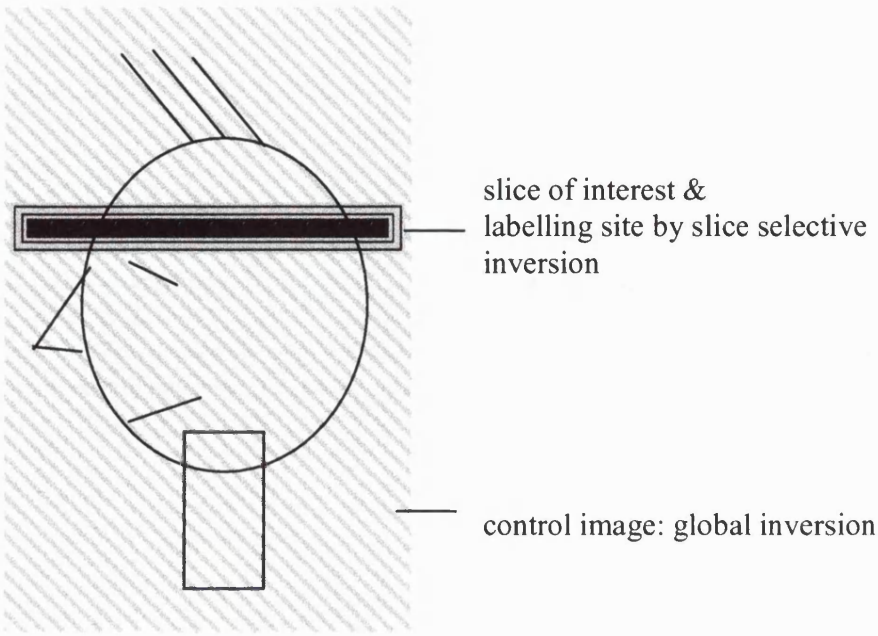

Figure 3-2 Schematic representation of basic setup FAIR, a pulsed labelling technique.

3.3.1 Static subtraction error, transit time, fresh inflow, QUIPSS

For all methods based on a subtraction between flow-sensitive and control images, it is very important to keep the flow-sensitized and control acquisitions as equal as possible, apart from the flow-sensitization. Subtraction images on a phantom (which has no flow) are a good test to see if the differences between the acquisitions are indeed only due to CBF. In practice there are always small non-zero subtraction differences on a phantom. This is called the static subtraction error (SSE).

The static subtraction error can be caused by eddy current differences between the two – labelling and control – pulse sequences. Kwong therefore suggested for FAIR to shift the slice selective gradient in time until after the inversion pulse in the global inversion sequence, to minimise the eddy current differences (Kwong et al., 1995).

Another source of static subtraction differences are pulse profile interactions between the labelling and readout pulses. To avoid any such interactions between the inversion and readout pulse profiles, an inversion to readout slice thickness ratio of 3:1 is commonly used in FAIR (Kim, 1995), and a saturation pulse twice the slice thickness is used for EPISTAR (Edelman, 1994). However, this does lengthen the transit time and decreases the sensitivity to slow flow. By improving the rf pulse profiles the gaps between the labelling and readout slices can be reduced (Frank et al., 1997). FOCI pulses have been advocated for this (Ordidge et al., 1996; Yongbi et al., 1999). Recently, Yongbi and colleagues (Yongbi et. al., 2000) suggested an *in vivo* method for assessing the static subtraction error and the minimum labelling-readout gap needed: by using Gd-DTPA in a calibration session on humans the blood T_1 will be dramatically reduced and this will give subtraction images that consist only of static subtraction signal.

Zhou and colleagues suggested another cause of the static subtraction error: radiation damping. Radiation damping is caused by the reaction of the induced current in the coil to the transverse magnetization inducing this current (Zhou et al., 1998). It leads to an apparent increase in T_1 relaxation. The extent of this increased longitudinal relaxation depends on the total equilibrium magnetization M_0. For global inversion the total magnetization will be much larger than for the slice selective inversion, leading to a

difference in T_1 relaxation which is not due to perfusion. Zhou et al. recommend a sequence ('FAIRER') with small gradients (~ 0.06 G/cm) that leave no large transverse magnetization at any time before the acquisition. Radiation damping depends on field strength, shimming and rf coil characteristics. It is less relevant at lower, clinical, field strengths.

More recently another approach to minimize the static subtraction error was reported: the SEEPAGE sequence (Blamire and Styles, 2000) avoids the need for image subtraction and thus the subtraction problems. All spins in the slice of interest are pre-saturated, followed by a train of non-selective inversion pulses interspersed with crusher gradients. The pulses, gradients and acquisition are timed in such a way that the slice of interest signal is 'trapped' at zero, while the unsaturated inflowing spins approach saturation with a time constant T_1. Thus an image can be obtained that only contains spins that have entered the slice after the initial saturation. This approach seems very promising; more experimental evaluation (e.g. sensitivity to pulse imperfections, etc.) will be required to establish it further.

Even though the transit times are reduced for pulsed techniques compared to continuous methods, they can still be substantial. As discussed before, transit time can be mimimized by optimal rf pulse design, which allows for a small gap between the readout and labelling slices. However, for multi-slice sequences where one wide inversion slab encompasses (FAIR, (Kim and Tsekos, 1997)) or lies below (EPISTAR, (Edelman and Chen, 1998)) all slices that are imaged, longer transit times for at least some of the slices are inevitable. To deal with the residual transit time after pulse sequence optimizations, it is possible to incorporate the transit time delay δt into the model: equation (3.10) can be expanded into (Thomas, D.L., 1999):

(3.11)

$$\Delta M = 0 \qquad t \le \delta t$$

$$\Delta M = 2\alpha_0 M_0 \frac{f}{\lambda}\left[\frac{\exp(-(TI-\delta t)/T_{1a}) - \exp(-(TI-\delta t)/T_{1app})}{1/T_{1app} - 1/T_{1a}}\right]\exp(-\delta t/T_{1a}) \qquad t \ge \delta t$$

This uses a mean transit time for the whole slice. This approach has been successfully implemented by Yang and colleagues (Yang et al, 1998).

Another problem highlighted by Calamante et al. (Calamante et al, 1996) is the physical width of a tag: in FAIR the global inversion only pertains to spins within the rf coil. After some time τ, fresh spins will move in. This will lead to an underestimation of CBF. Similarly in EPISTAR, the inversion slab is of a limited width determined by the inversion pulse and the slice selection gradient. Again, fresh spins will move in after some time τ, leading to an underestimation of calculated CBF.

One way around this is to ensure that the inversion times used are shorter than the fresh spin inflow time τ. On the other hand, the modelled T_1 decay of the label will also limit the range over which a fresh spin that started out fresh can be distinguished from a fresh spin that was inverted before. Yang et al. (Yang et al., 1998) studied this phenomenon: they increased the slice selective inversion width from 80-1000 mm using a body rf coil. They showed that spins further away than 300-400 mm did not contribute to the FAIR signal of the slice of interest at a TI of 1.2s due to the transit time and label decay. Hypothesizing this would not change dramatically for slightly longer inversion times, they proposed that using a standard rf coil of 300 mm diameter should not give any significant errors due to fresh inflow.

Buxton et al. (Buxton et al., 1998) describe the effects of transit times and the fresh inflow by considering the labelled spins as a bolus of finite width coming into the slice of interest. Their results reduce back to the formula above for standard ASL assumptions (plug flow of bolus, single compartment kinetics leading to a constant blood-brain partition coefficient λ and immediate extraction of water from vascular bed into tissue upon arrival in voxel).

Wong and colleagues (Wong et al., 1998) have specifically designed sequences with minimised sensitivity to transit time delays and fresh inflow. These are called QUIPSS and QUIPSS II. They solve the problem of the transit time variation and limited length of the tag by setting these parameters themselves. In QUIPSS I, after the labelling below the slice, a saturation pulse is applied to the slice of interest at a time TI_1 to remove all inflow history. The signal is then acquired at a time TI_2. If TI_1 is chosen larger than the longest transit time and TI_2 shorter than that transit time + the bolus length, then transit time and bolus length

disappear from the equations. QUIPSS II applies the saturation pulse to the *labelling* region after time TI_1 (< bolus width). This cuts off the tag at this point. The bolus of length TI_1 thus created can be followed into the slice and imaged at time TI_2 (> max transit time).

Again the equations become independent of transit time and tag width. QUIPSS II can easily be extended into multi-slice, whereas QUIPSS cannot. Obviously the timing of the saturation pulse and readout is crucial, and difficult to get right when a range of transit times is present. If one would want to characterise the bi-exponential curve completely, this would be a problem. Wong and colleagues approximate the effect of the bi-exponential with a correction factor q. In a later report (Luh et al., 1999) these researchers minimised pulse related quantification errors by optimising the saturation profile. The QUIPSS techniques have a lower signal difference compared to standard pulsed ASL methods due to label decay during TI_2 .

3.1.3 Intravascular signal

CBF quantification models assume that all spins that enter the imaging slice instantly exchange with tissue following the blood/brain partition coefficient λ. However, this exchange only takes place at the capillary level. Any spins in larger vascular structures in the slice will also contribute to the signal, without contributing to the CBF as defined and modelled. Both continuous and pulsed methods suffer from this problem. Calamante and colleagues (Calamante et al., 1999) point out that if blood water contributes to the signal, the different T_2 (or T_2*) values of blood and tissue will lead to a weighting towards the intravascular signal in EPI acquisitions. This might confound CBF quantification. This suggests using spin echo over gradient echo pulse sequences.

Ye et al. (Ye et al., 1997) report that in continuous ASL methods the intravascular signal can lead to an overestimation of CBF by a factor of two. Transit time effects result in an *under*estimation of CBF by a factor of two. The errors can thus counterbalance each other, which can explain why reasonable CBF values have been found even when these errors have not been accounted for. Ye and colleagues demonstrate how this intravascular signal can be reduced by applying bipolar crusher gradients. These gradients crush signal from spins moving faster than a given velocity, such as those in arteries or veins. The size

of the spoiling gradients required can be determined empirically: the spoiling gradients are increased until the signal difference ΔM does not reduce any more. Ye et al. advocate the use of spoiling gradients of b=5 s/mm^2, leading to a reduction of CBF signal (ΔM) of ~50%. This b-value was recommended previously by Le Bihan and Turner (Le Bihan and Turner, 1992). The application of crusher gradients lengthens the transit time, as only the signal from the last part of the arterial tree is seen. Ye and colleagues (Ye et al., 1997) report a change from 0.5 s to 0.9 s when spoilers are turned on.

There are different views regarding the degree of spoiling necessary. Buxton et al. (Buxton et al., 1998) argue that the blood signal should not be spoiled completely; they state that the blood in the voxel that is *ultimately* going to perfuse the voxel tissue should be included, even if it has not done so yet at the acquisition time. They propose a model that describes perfusion on the basis of blood spin magnetization $M_{0,b}$ as opposed to tissue magnetization M_0. The issue becomes one of the definition of perfusion: is it what arrives as blood in the voxel or what ends up in the voxel tissue? The difference between these is the water extraction fraction, which is close, but not equal to unity. It can vary significantly over voxels, and can be smaller than unity especially at higher flow values. The advantage of the Buxton model is that the assumption of a uniform water extraction fraction λ is replaced by a single measurement of the global scaling $M_{0,b}$ parameter. The difficulty is getting a good measurement of $M_{0,b}$ (in an 'arterial blood only' voxel). The assumption is that $M_{0,b}$ is constant over all voxels (i.e. no susceptibility effects).

3.2 BOLD fMRI

BOLD fMRI (Ogawa et al., 1990; Turner et al., 1991; Kwong et al., 1992) uses local deoxyhemoglobin concentration as the marker for brain activation. Local deoxyhemoglobin concentration depends on CBF, cerebral blood volume and oxygen consumption. Brain activation leads to a local decrease of deoxyhemoglobin: the increase in CBF overcompensates for the increased oxygen consumption.

Deoxyhemoglobin is a paramagnetic compound which reduces T_2* and (to a lesser extent) T_2. A local decrease of deoxyhemoglobin will thus result in an increase in MRI signal. BOLD fMRI uses T_2* weighted pulse sequences to image this effect. BOLD fMRI

is non-quantitative, although recent modelling work has progressed in characterizing the effect of CBF, CBV and oxygen consumption on the resulting BOLD signal (Buxton et al., 1998; Hoge et al., 1999).

3.3 Combining BOLD fMRI and ASL methods

When using a gradient echo acquisition, CBF data and BOLD data can be acquired simultaneously (Kim et al., 1997; Wong et al., 1997). The flow-independent controls can be used to measure BOLD. The BOLD effect will influence the flow-*de*pendent signal and has to be taken into account for CBF quantification (Kim, 1995).

By combining these measures, brain physiology can be investigated. Kim and Ugurbil (Kim and Ugurbil, 1997b) have used BOLD and CBF data –calculated from FAIR images– to estimate the relative Cerebral Metabolic Rate of Oxygen ($CMRO_2$) during visual stimulation. This oxygen consumption rate is a very important physiological parameter as it is directly coupled to neuronal activity.

Hoge and colleagues (Hoge et al., 1999) interleave short TE FAIR acquisitions with long TE BOLD acquisitions. The short TE of the FAIR acquisition minimises the BOLD contribution to FAIR data and thus ensures a clean separation of the two. Hoge and colleagues investigate the relationship between the BOLD signal, CBF and $CMRO_2$ by using graded hypercapnia and different levels of visual stimulation. Hypercapnia alters CBF but does not change brain activation in the visual areas. This means $CMRO_2$ will be constant too. Therefore the relationship between BOLD and CBF at constant $CMRO_2$ can be measured.

Previous models for BOLD, CBF and $CMRO_2$ (Mandeville et al., 1997; Davis et al., 1998; Ogawa et al., 1993) predicted a linear relationship for CBF increases up to 50%. For higher increases it would plateau to an asymptotic value. The data of Hoge and colleagues support this hypothesis. Hoge and colleagues research the effect of changes in $CMRO_2$ at constant CBF by matching perfusion levels during hypercapnia and visual stimulation. The BOLD signal during the visual stimulation was attenuated significantly compared to the BOLD signal in the hypercapnic state due to the increase in metabolic deoxyhemoglobin production. On the basis of these experiments and model simulations Hoge et al. propose a

quantitative model for the relationship between BOLD signal, CBF and $CMRO_2$ based on the concept of flow-dependent dilution of metabolically generated deoxyhemoglobin.

$$\frac{\Delta BOLD}{BOLD_0} = M\left(1-\left(\frac{CMRO_2}{CMRO_2|_0}\right)^{\beta}\left(\frac{CBF}{CBF_0}\right)^{\alpha-\beta}\right), \tag{3.12}$$

with

$$M = TE \cdot A \cdot CBV_0 [dHb]_{v_0}^{\beta} \tag{3.13}$$

$\Delta BOLD/BOLD_0$ represents the fractional change in the BOLD signal. The parameters at t=0 are indexed with a '0' subscript. A is a field strength and sample-specific proportionality constant, β is a constant that can range from 1-2 depending on the average blood volume within a tissue sample. α is a constant with an approximate value of 0.38. CBV is the cerebral blood volume and $[dHb]_v$ is the concentration of deoxyhemoglobin in venous blood. Hoge et al. find a coupling between relative changes in CBF and $CMRO_2$ of ~ 2:1. One criticism of this work is that the effect of inflow delay is neglected in the interpretation of the FAIR data. The extent to which this simplification can be made will be investigated further in this thesis.

4 Optimising inversion and readout pulses

4.1 Introduction

To minimise magnetization transfer problems, rf deposition and transit time, I decided to implement a pulsed ASL technique with in-slice labelling: FAIR. An added advantage is that FAIR measures CBF also from above and not just from below. The first element of the pulse sequence I chose to investigate was the inversion pulse. The inversion pulse is important as it determines the accuracy and degree of labelling.

Due to machine limitations, I had to work with a limited rf power (max B_1 amplitude ≅ 600-900 Hz). I therefore performed simulations to optimise the inversion pulse parameters for this special situation. Furthermore, I compared the Hyperbolic Secant (HS) and different types of FOCI pulses in their performance under these circumstances. Finally, I implemented the preferred FOCI and HS pulse to validate the results of the simulations.

A year later the limitations on the machine were removed, and I was able to use higher rf power levels (max B_1 amplitude ≅ 1600-2200 Hz). The low power work may still be of interest when low rf power deposition is desirable, for instance when working with children or when performing studies of very long duration.

As discussed in Chapter 3, the literature suggests an important role for slice profile *interactions* in the FAIR experiment. If the slice selective inversion and readout pulses interact, FAIR will give a non-zero subtraction signal on a static phantom. This 'static subtraction error' will confound perfusion data *in vivo*. I therefore set out to investigate slice profile interactions. This was done by simulating 1-dimensional FAIR experiments with different inversion pulses and a range of readout pulses as found on a standard clinical scanner. The static subtraction error was then calculated for a range of ratios of inversion and readout slice thicknesses. These simulations suggest which inversion and readout pulses work best together for sharp inversion and readout profiles and minimal slice profile interactions.

4.2 Inversion pulses at low power

4.2.1 Methods

Pulse simulations were done by evaluating the Bloch equations in time steps of 10 μs for a range of frequency offsets, as described in Chapter 2, paragraph 4.1. The required pulse simulation software was adapted from a C program (Wylezinska, personal communication) into MATLAB (MATLAB, The Mathworks 1994-2001).

The inversion pulse length was 8 ms, the maximum pulse amplitude ($\mu \cdot \beta$) = 3200 radians/s and μ=5, 4, 3.2, 2 radians. The inversion slice thickness was 15 mm. The maximum gradient value, which determines the maximum amplification factor for the FOCI pulses, was set at 25 mT/m, allowing an amplification factor A of 10 for all FOCI pulses at this slice thickness.

The FOCI modulation functions applied were the C-shape (constant maximum B_1 amplitude for most of the pulse), E-shape (exponentially shaped modulation function) and T-shape (trapezoidally shaped modulation function) (Ordidge et al., 1996).

The HS and FOCI C-shape pulse profiles were evaluated experimentally on a Siemens VISION 2T scanner using a standard spin echo sequence with the readout along the slice selection direction. This data was then normalised by dividing the profile by one acquired with the same sequence without the inversion pulse applied. Experimental parameters: pulse length = 8 ms, μ=3.2 radians, β = 1000 s^{-1}, slice thickness=10 mm and a maximum gradient strength of 25 mT/m. The amplification factor for the FOCI pulse was 10.

4.2.2 Results and Discussion

Figure 4-1 and Figure 4-2 show simulated HS and FOCI C-shape HS inversion profiles for the different μ values when the product $\mu \cdot \beta$, and therefore the power requirement, is kept constant. At this limited power, the μ value of 5 radians, which is normally used, is not optimal: the resulting β-value is too low to achieve full inversion. A lower μ allows a higher β which increases the inversion depth and rectangularity of the profile. However, for

μ=2 the inversion profile is demonstrably worse. Also, for FOCI pulses the frequency of the profile oscillations increases as μ is reduced. There is therefore a limit on the extent to which the μ value can be reduced. The inversion width and depth for the HS and the FOCI pulse at this low power turns out to be optimal for μ=3.2 radians. Note how the FOCI pulse performs much better than the HS pulse in terms of profile rectangularity, but its profile has high frequency oscillations.

Figure 4-3 compares the performance of the three FOCI modulation functions (E-shape, T-shape, C-shape; Ordidge et al., 1996) in a simulation of inversion pulses with the same μ and β, for a slice thickness of 15 mm. Their performance is very comparable, although the C-shape does give better results in terms of inversion width and constancy. It is not surprising that the C-shape pulse performs best, as the amplification factor A is maximal at every point of the C-shape rf pulse: for every point A is the inverse of the original rf amplitude with a maximum of A=10. (For A> 10 the pulse is not adiabatic anymore). The superiority of the C-shape FOCI pulse over HS and other FOCI pulses was also found at normal power levels using simulations (Ordidge et al., 1996) and experiments (Pyne et al, 1997).

Figure 4-4 shows the experimental data for the HS and the FOCI C-shape pulses for μ=3.2 radians and β=1000 s^{-1}. As predicted by the simulations, the FOCI pulse does significantly better in terms of rectangularity, although its profile has high frequency oscillations. Note the effect of T_1-relaxation across the profiles demonstrating the frequency sweep of the adiabatic pulses.

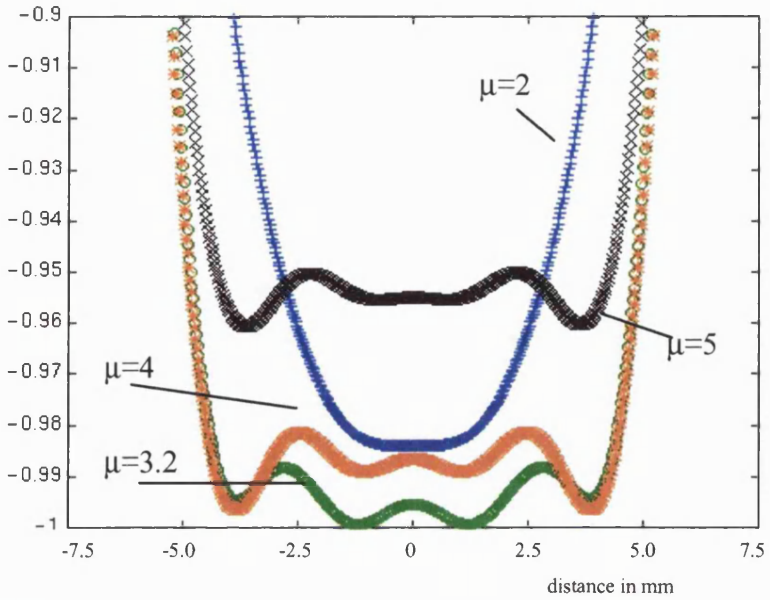

Figure 4-1 Inversion profiles for HS pulse, $\mu \cdot \beta$=3200 radians/s, μ=5 (black x), 4 (red *), 3.2 (green o), 2 (blue +) radians.

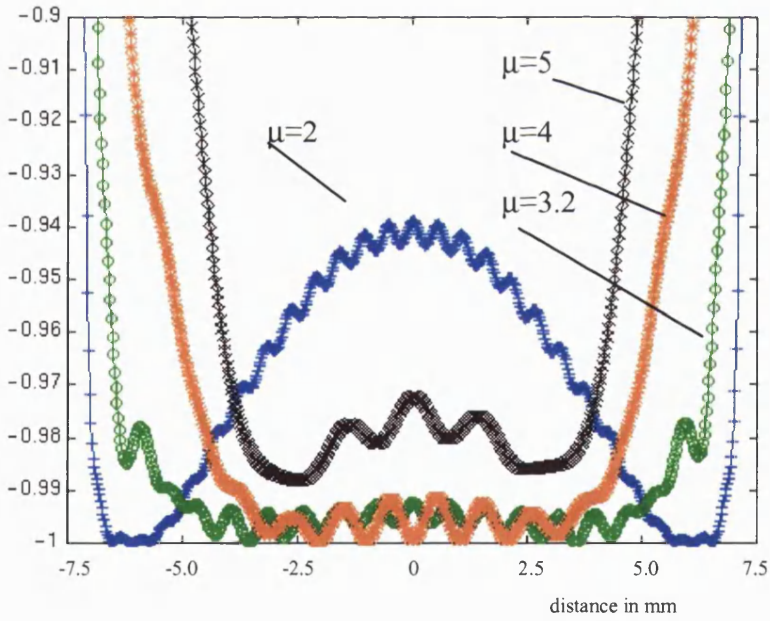

Figure 4-2 Inversion profiles for FOCI C-shape pulse, $\mu \cdot \beta$=3200 radians/s, μ=5 (black x), 4 (red *), 3.2 (green o), 2 (blue +) radians.

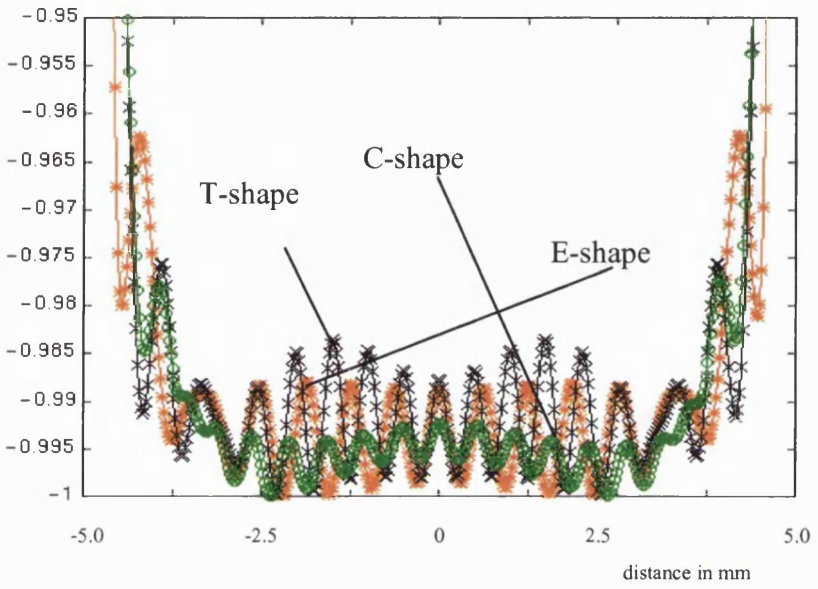

Figure 4-3 Inversion profiles of the different FOCI pulses compared.
$\mu \cdot \beta$=3200 radians/s: E-shape (red *), T-shape (black x), C-shape (green o).

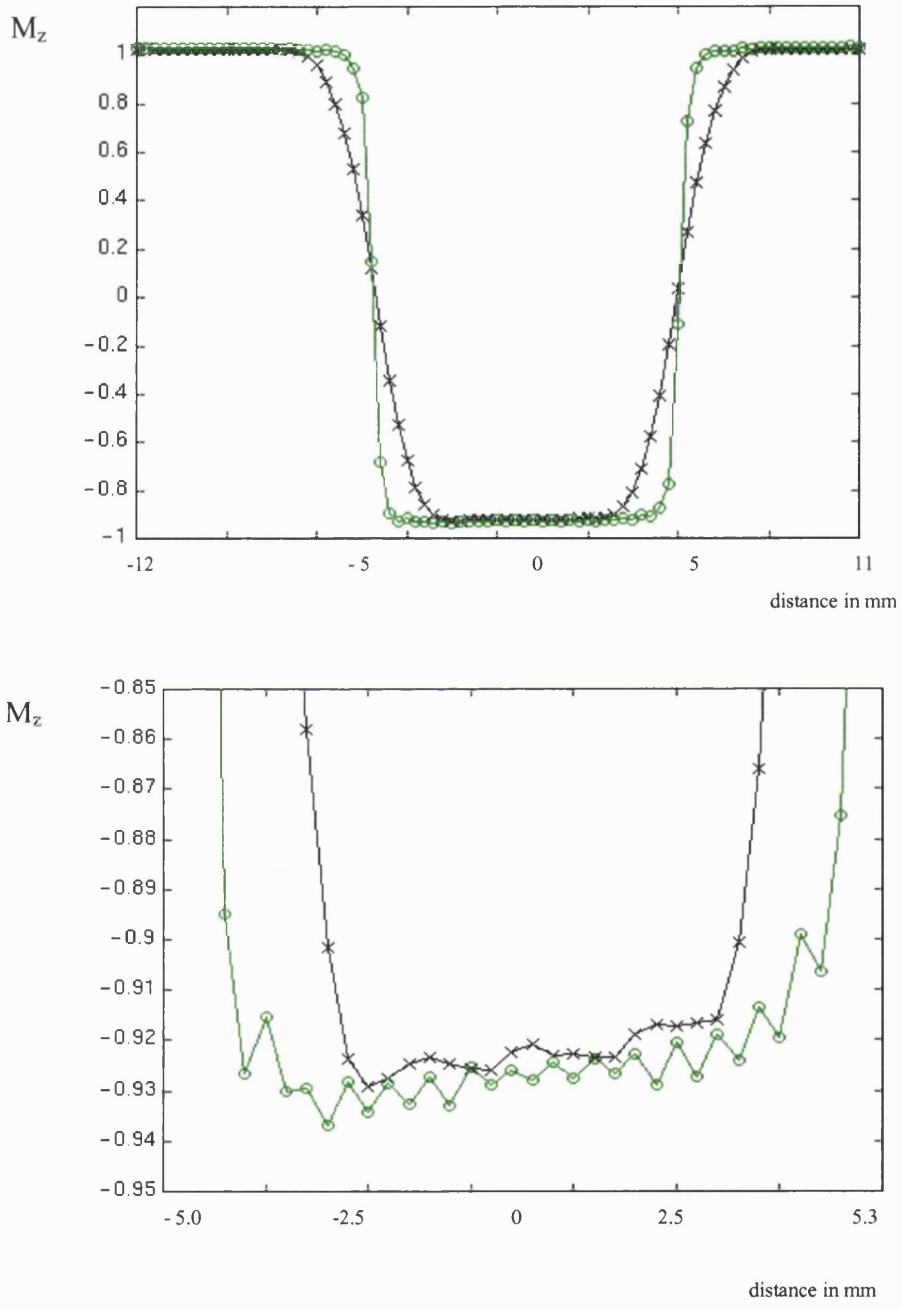

Figure 4-4 Experimental results for the HS (black x) and FOCI C-shape (green o) rf pulses: μ=3.2 radians, β=1000 s^{-1}, 10 mm slice thickness, 8 ms pulse. Above: whole profile, below zoomed-in.

4.2.3 Conclusions low power inversion pulse simulations

- The experimentally determined rf profiles confirm the predictions of the pulse simulations. Pulse profile simulations by integration of the differential Bloch equation are therefore a useful tool for the prediction of pulse behaviour.

- When working with low pulse powers, it is worthwhile to lower the μ value to allow for higher β-values. In this case choosing μ=3.2 radians instead of μ=5 radians allows for a higher β value and thus for a more deep and rectangular inversion profile, both for HS and FOCI pulses.

- The FOCI pulses give a wider and deeper inversion than the HS pulse at this low rf power. Both pulse profiles have oscillations; the FOCI profile oscillations are of a higher frequency.

- When comparing the three FOCI pulses, the C-shape FOCI pulse gives the best results in terms of inversion profile rectangularity. This can be understood when realising that the FOCI C-shape has the maximum allowed amplification factor A for every point in the rf pulse shape.

4.3 Pulse profiles and interactions of inversion and readout pulses at normal power

4.3.1 Methods

Inversion and readout pulses were simulated by integrating the Bloch equation as described previously. For a range of slice thicknesses [3.3, 4, 5, 6, 7, 8, 9, 10, 11 and 12 mm], the following inversion pulses were simulated:

- Standard Hyperbolic Secant (HS) pulse, μ=5 radians, β=1500 s^{-1}, Time Pulse = 8 ms
- FOCI C-shape pulse with the same pulse parameters, amplification factor A = 2

- FOCI C-shape pulse with the same pulse parameters, amplification factor A = 4.5
- FOCI C-shape pulse with the same pulse parameters, amplification factor A = 10

Then for a slice thickness of 3.3 mm the following readout pulses were simulated:

- Three-lobed 90° sinc pulse
- Five-lobed 90° sinc pulse
- Three-lobed 90°-180° sinc pulse pair
- Five-lobed 90°-180° sinc pulse pair
- Five-lobed 90°-180° Hamming filtered sinc pulse pair
  (as implemented on the Siemens Vision MRI scanner)

The time step for all simulations was 10 μs, the field of view was 20 mm and both the rf pulse shape and the field of view were sampled with 800 points.

Pulse profile interactions

The result of applying the inversion and readout pulses sequentially was simulated with a one-dimensional FAIR experiment. If a 90°-180° readout combination is used, gradients have to be applied before and after the 180° refocussing pulse to spoil unwanted magnetization of the 180° refocussing pulse. It is not feasible to simulate a true spoiler gradient, but its effects can be mimicked by adding up simulations with different phase shifts φ before and after the refocussing pulse.
Figure 4-5 illustrates this spin echo experiment; in Table 4-1 the required phase shift scheme is written out.

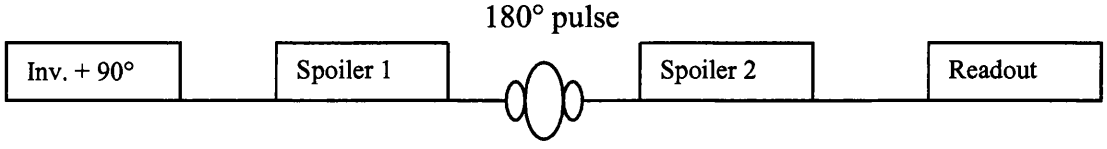

Figure 4-5 Illustration of a simulated one-dimensional spin echo FAIR experiment.

Phase shift to simulate spoiler	After inversion and 90° pulse	After first phase shift φ	After 180_x pulse: effective tip angle α	After second phase shift φ
φ = 0 radians **RUN 1**	$M_x \cdot \mathbf{x}$ M_y **y** $M_z \cdot \mathbf{z}$	$M_x \cdot \mathbf{x}$ $M_y \cdot \mathbf{y}$ $M_z \cdot \mathbf{z}$	$M_x \cdot \mathbf{x}$ $(M_y\cos\alpha - M_z\sin\alpha)\cdot \mathbf{y}$ $(M_z\cos\alpha + M_y\sin\alpha)\cdot \mathbf{z}$	$M_x \cdot \mathbf{x}$ $(M_y\cos\alpha - M_z\sin\alpha)\cdot \mathbf{y}$ $(M_z\cos\alpha + M_y\sin\alpha)\cdot \mathbf{z}$
φ = π radians **RUN 2**	$M_x \cdot \mathbf{x}$ $M_y \cdot \mathbf{y}$ $M_z \cdot \mathbf{z}$	$-M_x \cdot \mathbf{x}$ $-M_y \cdot \mathbf{y}$ $M_z \cdot \mathbf{z}$	$M_x \cdot \mathbf{x}$ $(-M_y\cos\alpha - M_z\sin\alpha)\cdot \mathbf{y}$ $(M_z\cos\alpha - M_y\sin\alpha)\cdot \mathbf{z}$	$M_x \cdot \mathbf{x}$ $(M_y\cos\alpha + M_z\sin\alpha)\cdot \mathbf{y}$ $(M_z\cos\alpha - M_y\sin\alpha)\cdot \mathbf{z}$
φ = + π/2 radians **RUN 3**	$M_x \cdot \mathbf{x}$ $M_y \cdot \mathbf{y}$ $M_z \cdot \mathbf{z}$	$-M_y \cdot \mathbf{x}$ $M_x \cdot \mathbf{y}$ $M_z \cdot \mathbf{z}$	$M_y \cdot \mathbf{x}$ $(M_x\cos\alpha - M_z\sin\alpha)\cdot \mathbf{y}$ $(M_z\cos\alpha + M_x\sin\alpha)\cdot \mathbf{z}$	$(-M_x\cos\alpha + M_z\sin\alpha)\cdot \mathbf{x}$ $M_y \cdot \mathbf{y}$ $(M_z\cos\alpha + M_x\sin\alpha)\cdot \mathbf{z}$
φ = - π/2 radians **RUN 4**	$M_x \cdot \mathbf{x}$ $M_y \cdot \mathbf{y}$ $M_z \cdot \mathbf{z}$	$M_y \cdot \mathbf{x}$ $-M_x \cdot \mathbf{y}$ $M_z \cdot \mathbf{z}$	$M_y \cdot \mathbf{x}$ $(-M_x\cos\alpha - M_z\sin\alpha)\cdot \mathbf{y}$ $(M_z\cos\alpha - M_x\sin\alpha)\cdot \mathbf{z}$	$(-M_x\cos\alpha - M_z\sin\alpha)\cdot \mathbf{x}$ $M_y \cdot \mathbf{y}$ $(M_z\cos\alpha - M_x\sin\alpha)\cdot \mathbf{z}$
SUM OF FOUR RUNS = SE-FAIR experiment			**SUM**	---------- + $(2M_x - 2M_x\cos\alpha)\cdot \mathbf{x}$ $(-2M_y + 2M_y\cos\alpha)\cdot \mathbf{y}$ $4M_z\cos\alpha \cdot \mathbf{z}$

Table 4-1 Illustration of phase shift scheme required for simulation one-dimensional spin echo FAIR experiment. To illustrate the effect of (imperfections in) the 180° refocussing pulse, the magnetization in x,y,z is calculated here for a perfect inversion and 90° pulse. The effect of the required spoiler gradient is mimicked by summing four experiments, each run with a different phase shift applied before and after the 180° refocussing pulse. By using different phase shifts φ of 0,π,-1/2π and 1/2π radians for the runs, the sum of the four simulations adds up to magnetizations without any contributions of the imperfections of the refocussing pulse. This is what is achieved *in vivo* by using spoiler gradients.

For a perfect 180° refocussing pulse this scheme will result in a final magnetization **M** of $(4M_x \cdot \mathbf{x}, -4M_y \cdot \mathbf{y}, -4M_z \cdot \mathbf{z})$. Spins that do not feel the pulse will be spoiled, as well as spins that are excited by it.

Once this basic simulation scheme is established, inversion and readout pulses of interest can be introduced and pulse interactions can be established. If only a 90° pulse was used for the readout (gradient echo experiment) these simulated 'spoiler gradients' were not employed.

The interaction of inversion and readout pulses is assessed by calculating the following:

$SL = \sum \mathbf{profile\_inversion} \bullet \mathbf{profile\_readout}$ slice selective inversion

$GL = \sum \mathbf{profile\_inversion}(\text{midpoint}) \bullet \mathbf{profile\_readout}$ global inversion

$FAIRr = 100\% * (SL - GL)/GL$

The one-dimensional FAIR experiment is the SL – GL subtraction. The relative FAIR signal (FAIRr) is the difference between SL and GL expressed as a percentage of GL. To disentangle the effects of imperfect readout and inversion pulses, interaction analyses were also performed with perfect (rectangular) inversion and readout profiles.

4.3.2 Results and Discussion

First, the inversion profiles were examined. Figure 4-6 shows simulated inversion profiles for the HS and FOCI pulses and the perfect rectangular profile. As shown before with the low rf power simulations, the FOCI pulses have a more rectangular profile than the HS pulse. As the amplification factor A increases, their profile more and more approaches the perfect rectangular profile.

Figure 4-7 shows the simulated readout profiles for the 3-lobed 90°, 5-lobed 90°, 3-lobed 90°-180°, 5-lobed 90°-180° and the Hamming filtered 5-lobed 90° and 90°-180° pulses. On inspection the first aspect that draws attention is the different effective slice thicknesses of the pulses. Although all the slice selective gradients are calculated on the basis of the first zero crossing of the sinc function, the effective slice thicknesses are significantly different. Their values are listed in Table 4-2.

A 90°-180° pulse combination leads to a reduction of the FWHM slice thickness and a removal of the 90° pulse profile side wings. Hamming filtering narrows the pulse in time, increasing the bandwidth and thus the slice thickness. The differences in all these effective slice thicknesses will affect the SNR of the measurement and the interactions with inversion pulses.

Pulse Name	Full Width Half Max (FWHM) in mm
3-lobed sinc 90° pulse	3.28
3-lobed sinc 90°-180° pulses	1.87
5-lobed sinc 90° pulse	3.25
5-lobed sinc 90°-180° pulses	2.43
5-lobed Hamming filtered sinc 90° pulse	4.68
5-lobed Hamming filtered sinc 90° - 180° pulses	3.47

Table 4-2 Effective slice thicknesses of simulated pulses.

The side lobes of 90° pulse profiles are important in pulse profile interactions as shown in Figure 4-8: performing the 1D-FAIR simulations with different readout pulses for a perfect (rectangular) inversion, the data demonstrate how the inversion pulse profile interactions with the 90°-180° profiles die down quickly (at an inversion slice thickness ~ 6mm) while the interactions with the 90° pulse profile oscillate around zero and persist much longer (inversion slice thickness ~ 8-12 mm). This is not just an effect of a different effective slice thickness of the readout pulses: the Hamming filtered 90°-180° readout combination [6-5] has a FWHM of 3.47 mm, which is comparable to that of the 3 and 5-lobed sinc 90° pulses, but the interactions die down much quicker.

The differences between these spin echo and gradient echo acquisitions are seen more clearly when the effective slice thicknesses are taking into account. Figure 4-9 shows the profile interactions of a perfect rectangular inversion profile with a 5-lobed 90° and a 5-lobed 90°-180° plotted against the ratio of inversion to *effective* readout slice thickness. The picture is focussed to highlight the +/- 0.1% signal difference boundary, which seems a reasonable requirement for the static signal differences (as the FAIR signal in vivo is ~ 1%). For this cut off point, a spin echo needs a 2:1 inversion to readout slice thickness ratio, for a gradient echo this ratio is 3:1. A spin echo readout is therefore preferable to a gradient echo experiment when considering pulse profile interactions.

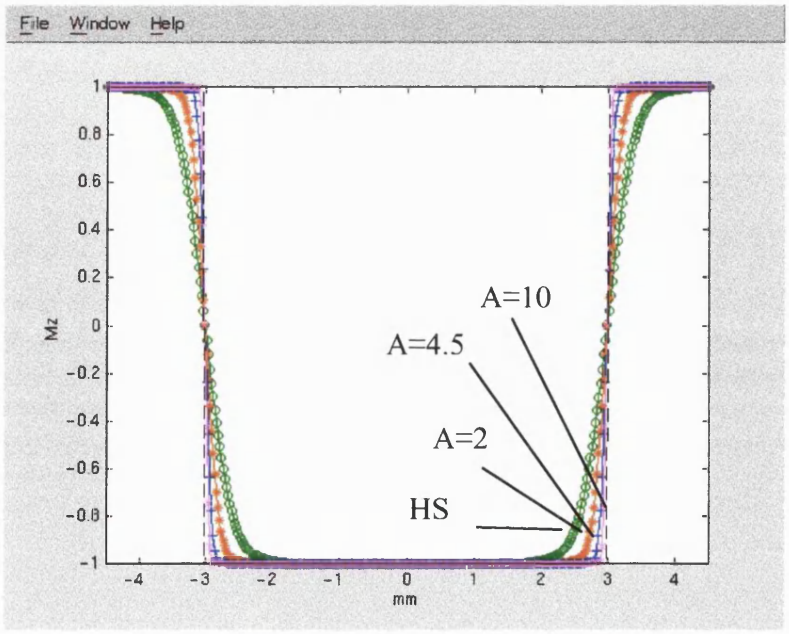

Figure 4-6 Inversion profiles: HS μ=5 radians, β=1500 s^{-1}, Time pulse = 8ms, slice thickness = 6mm (green o). FOCI same parameters, A=2 (red *), A=4.5 (blue +), A=10 (magenta x). Rectangular profile (black striped line).

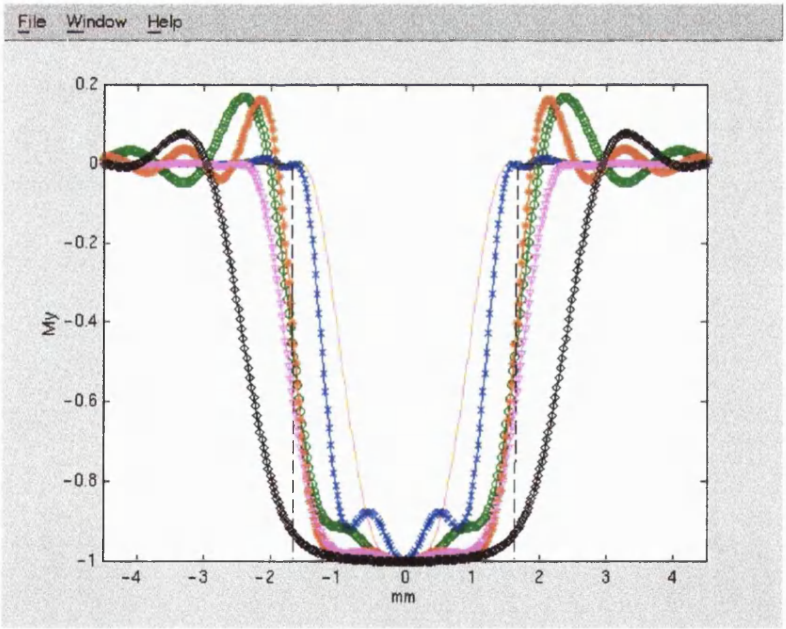

Figure 4-7 Readout profiles: 3-lobed sinc 90° (green o), 3-lobed sinc 90°-180°(yellow/pink stripe dot), 5-lobed sinc 90° (red *), 5-lobed sinc 90°-180° (blue x), 5-lobed Hamming filtered sinc 90° (black ◊), 5-lobed Hamming filtered sinc 90°-180° (magenta ∇). Rectangular profile (black striped line).

Figure 4-10 shows the profile interactions for a perfect rectangular readout pulse (again of 3.3 mm) and a range of different inversion pulses. Again, the FOCI pulses perform better than the standard HS. As the amplification factor A increases, the interaction becomes smaller. However, the differences are most prominent as long as the inversion slice thickness < 5 mm (i.e. the inversion: readout ratio < 1.5). After that, the differences become very small. Considering the readout pulse profile interactions examined before, even for a perfect inversion the minimum inversion width for this readout slice thickness should be ≥ 5 mm to compensate for readout imperfections. Readout imperfections therefore dominate the pulse profile interactions for the pulses considered here.

As the readout pulse performance is dominant for the pulse interactions, it is worthwhile investing the extra time for a 5-lobed pulse and a spin echo experiment. A potentially good readout combination is the Hamming filtered 90°-180° combination, as it gives very good readout profiles as shown in Figure 4-7.

In Figure 4-11 the pulse profile interactions for the Hamming filtered 5-lobed sinc 90°-180° readout are compared for a range of inversion pulses. For a maximum subtraction error of 0.10% an inversion slice thickness > 6 mm for the standard HS and > 7 mm for the FOCI pulses is needed. This amounts to inversion: readout ratios of 1.7:1 and 2.0:1 respectively. The FOCI pulse has a slight disadvantage over the standard HS here, probably because its inversion area is larger which can lead to a larger % difference between SL and GL for interactions with readout pulses that have imperfect profile edges.

Considering that the FOCI pulses will probably have worse eddy current effects as their gradients are much stronger, the differences between SL and GL in practice could be worse for FOCI compared to the standard HS for these pulses and slice thicknesses. Because this work focusses on single slice FAIR applications, the HS pulse will therefore be used, as the subtraction errors should be similar to the FOCI pulses and there is less risk of eddy currents with the lower gradient strengths required.

Experimental data from Yongbi and colleagues (Yongbi et al., 1998; Yongbi et al., 1999) show that the FOCI pulse does give a large improvement over HS pulses for multi-slice applications, as it is for wide slabs especially that the HS pulse profiles are much less sharp than the FOCI pulse profiles.

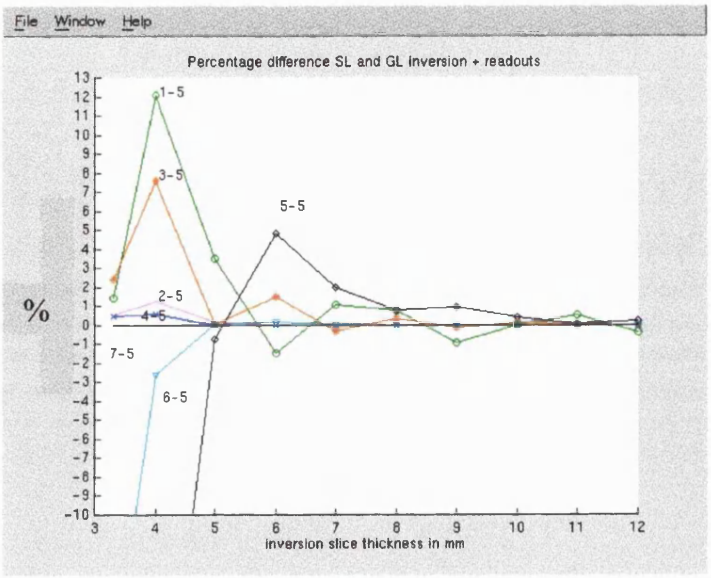

Figure 4-8 Percentage difference between SL and GL for a perfect rectangular inversion pulse and the following readout pulses: [1-5] 3-lobed sinc 90° (o), [2-5] 3-lobed sinc 90°-180°(line), [3-5] 5-lobed sinc 90° (*), [4-5] 5-lobed sinc 90°-180° (x), [5-5] 5-lobed Hamming filtered sinc 90° (◊), [6-5] 5-lobed Hamming filtered sinc 90°-180° (∇). [7-5] Rectangular profile: along x-axis. Pulse profiles for the readout pulses on their own are given in Figure 4-7.

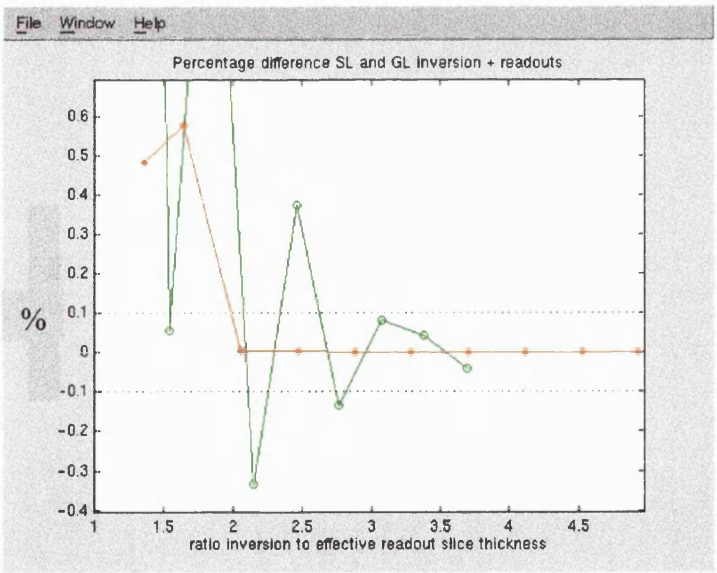

Figure 4-9 Comparing the 5-lobed 90° (o) and 5-lobed 90°-180° (*) for different ratios of inversion and effective readout slice thicknesses.

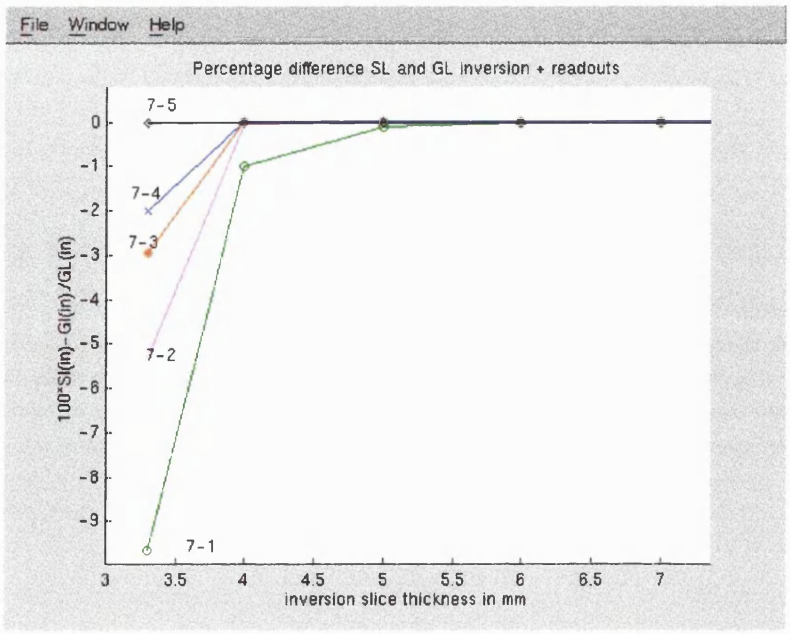

Figure 4-10 Percentage difference between SL and GL for a rectangular readout pulse of slice thickness 3.3mm and a range of inversion pulses: [7-1] HS μ=5 radians, β=1500 s^{-1} , Time pulse = 8ms (o). HS FOCI same parameters, [7-2] A=2 (line), [7-3] A=4.5 (*), [7-4] A=10 (x). [7-5] Rectangular profile (◊).

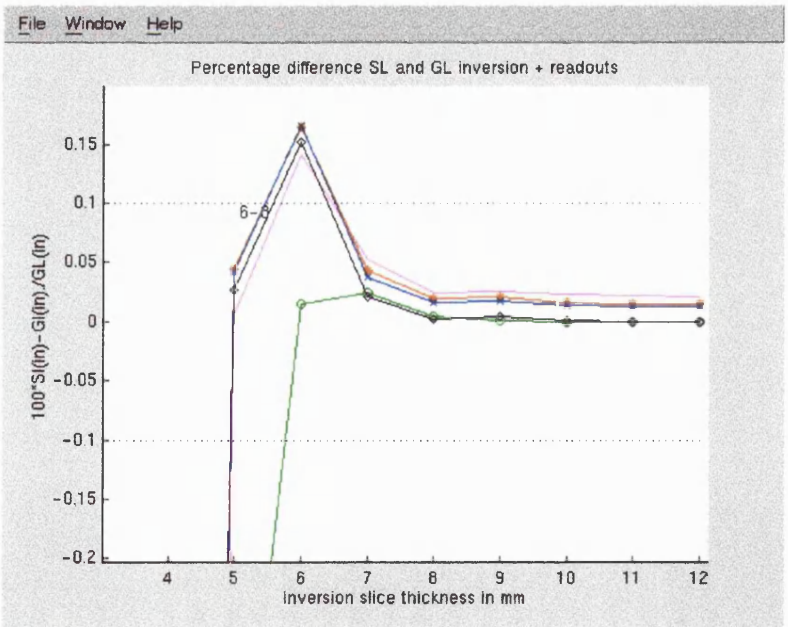

Figure 4-11 Profile interactions of Hamming filtered 5-lobed 90°-180° of slice thickness 3.3mm with standard HS (o), FOCI with A=2 (line), A=4.5 (*), A=10 (x) and a perfect rectangle (◊)

4.3.3 Conclusions regarding pulse profile interactions

- A spin echo readout leads to much smaller pulse profile interactions than a gradient echo readout. For a perfect inversion, a spin echo sequence needs an inversion: readout ratio of order 2:1, a gradient echo sequence a ratio of 3:1, to give a maximum static subtraction error of 0.10% of M_0. This difference between spin and gradient echo is due to the 'cleaning up effect' of the spin echo 180° pulse on the profile of the 90° pulse: the side wings disappear.

The readout pulses dominate pulse profile interactions between inversion and readout pulses for the simulated slice thicknesses. Even in the case of a perfect rectangular inversion the minimum required inversion slice thickness is substantially larger than the readout slice thickness due to the imperfections of the readout pulse profiles. The inversion slice thickness required leaves such a gap between the readout and the inversion edges, that the effect of different inversion pulse parameters as tested here becomes very small.

- FOCI pulses do not give an advantage over standard HS pulses for the inversion slice thicknesses minimally required for these readout pulses (> 2:1). Taking into account the higher gradient strengths required for the FOCI pulses, the static subtraction errors might be even larger due to eddy current effects. The superiority of the FOCI pulse will be most apparent in multi-slice FAIR applications (Yongbi et al., 1999), but this thesis focusses on single-slice FAIR quantification and the HS pulse will therefore be used henceforth.

SL	slice selective inversion
GL	global inversion
TI	inversion time
CBFD model	fitting for CBF and inflow delay
CBFO model	fitting for CBF only
ITM model	fitting for inversion, T_{1app} and M_0
TMF model	fitting for T_{1app}, M_0 and CSF fraction
SSE	static subtraction error

Explanation of commonly used abbreviations for modelling terms.

5 Measuring CBF with FAIR

5.1 Introduction

This chapter describes the implementation of the FAIR technique. The concepts behind the pulse sequence are clarified and strategic choices explained. FAIR data modelling and interpretation are first discussed for a basic experiment using standard fit models (Calamante et al., 1999). Then quantification issues such as partial voluming, macrovascular contributions, the static subtraction error, volunteer movement and fit model selection are explored further. The chapter ends with an outline of an experimental setup and data modelling optimised for steady state studies in humans. This is the basis for the analyses in the rest of this thesis.

5.2 FAIR pulse sequence implementation

FAIR was implemented on a 2.0 T Siemens Vision MRI scanner. The acquisition and data processing were optimised to maximise signal to noise and minimise systematic errors. Figure 5-1 gives the pulse sequence for FAIR. The global inversion is immediately followed by the gradient that is also used for slice selective inversion, to minimise the static subtraction error due to eddy currents (Kwong et al., 1995). Both inversions are followed by a spoiler in three directions to crush any transverse magnetisation generated by the inversion pulse.

A DANTE fat saturation pulse group is applied just before the 90° pulse to excite the fat spins; their signal is then crushed by the subsequent spoilers. The water spins are not excited.

The simulations described in Chapter 4 predicted no advantage for the FOCI pulse over the HS pulse, so a standard HS pulse has been implemented in the sequence. A practical advantage of the HS pulse is that it allows scanning at different slice shifts from the centre of the rf coil by changing the offset frequency. For the FOCI pulse this would require a rescaling of the pulse parameters for every slice shift.

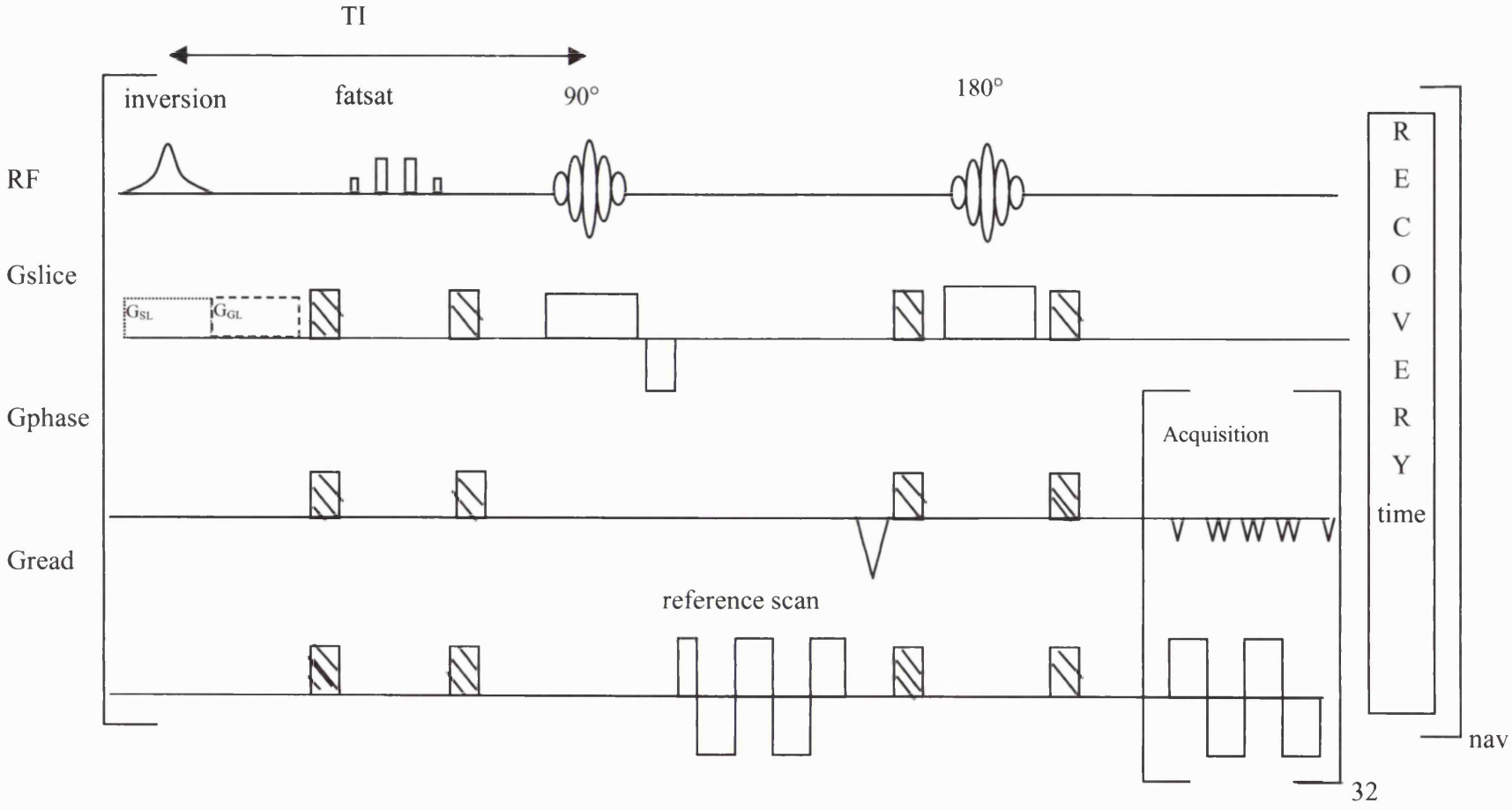

Figure 5-1 Pulse sequence for FAIR. G_{SL}: gradient for slice selective inversion; G_{GL}: gradient for global inversion. The slice selective and global inversions are alternated. Shaded pulses: spoiler gradients. RF: radiofrequency pulses. Gslice, Gphase, and Gread: respectively slice selective gradient, phase encoding gradient, read gradient. Fatsat: fat saturation. nav: number of averages.

The power available for the HS pulse was calculated on the basis of a square pulse. When the rf coil was loaded with a gel phantom, a 1 ms, 180° pulse specified by one hundred points used 67.36 V. The radial frequency was $\omega = \pi/(1*10^{-3}) = 3141.6$ radians/s. The maximum voltage available was 300 V, which for this coil loading comes down to 13992 radians/s. On a human, the voltages required for the same pulse are ~ 40% higher. Thus the maximum voltage available for humans is equivalent to ~10000 radians/s. A pulse was implemented at 80% of this maximum available rf amplitude, 8000 radians/s, with HS pulse parameters: μ=5 radians, β=1500 s^{-1} and the pulse length was 8 ms. The minimum rf amplitude this pulse needs is 7500 radians/s. The rf amplitude was set at 8000 radians/s to compensate for B_1 drop-off away from the centre of the coil.

The pulse profile of the HS pulse was measured using a one-dimensional pulse sequence with the readout along the slice selection direction. The inversion slice thickness was 30 mm. The same sequence without the inversion pulse was used to acquire M_0 data to normalise the profile.

Figure 5-2 gives the normalised pulse profile for the HS pulse at TI=50 ms and a slice thickness of 30 mm.

The inversion efficiency α_0 of the slice selective and global inversions was assessed with single shots of the FAIR sequence. The TI-values were [0.4, 0.5, 0.6, 0.7, 0.9, 1.1, 1.3, 2.0, 3.0, 4.0, 5.0 s]. These TI-data were fitted for the whole slice to the inversion recovery equation:

$$(5.1)\ SL(TI) = \left| M_0\left(1 - 2\alpha_0 \exp(-TI/T_{1app})\right)\right|$$

The modulus signs around the inversion recovery equation are necessary as the SL data are in magnitude mode. For the phantom T_{1app} is the same as T_1, as there is no CBF. The mean inversion efficiency over the slice was calculated for the SL and GL inversions. The fits for inversion efficiency for the FAIR SL and GL inversions resulted in the mean values α_0=0.987 +/- 0.006 for SL and α_0=0.988 +/- 0.005 for GL. Figure 5-3 (a) shows an example fit of slice selective inversion recovery data for one voxel.

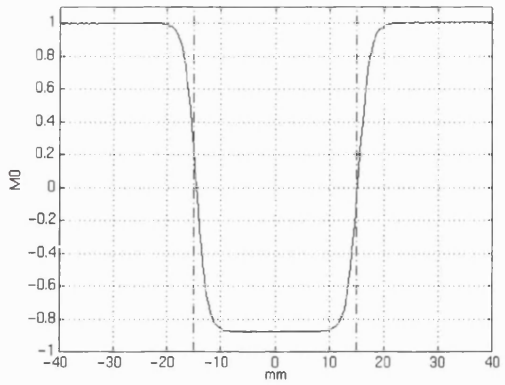

Figure 5-2 The normalised pulse profile of the HS pulse measured on a phantom. μ=5 radians, β=1500 s^{-1}; slice thickness =30 mm.

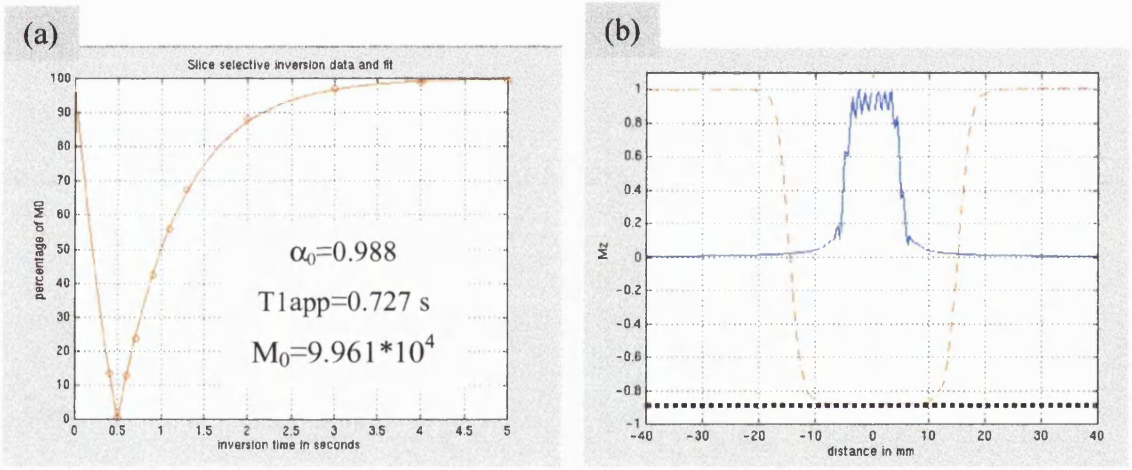

Figure 5-3 (a) Inversion recovery data ('o') and fit ('-') for the FAIR slice selective inversion for one voxel. (b) Pulse profile of 5-lobed Hamming filtered 90°-180° sinc pulses (blue); HS slice selective inversion profile (-.) and expected HS GL inversion profile (dotted) added.

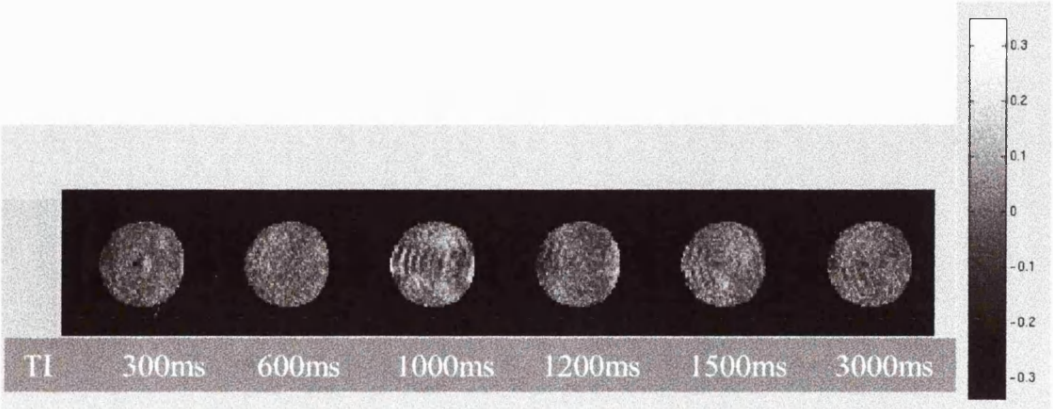

Figure 5-4 Static subtraction error as percentage of M_0 measured on a gel phantom.

On the basis of the recommendations of Chapter 4, a spin echo readout was implemented. This minimises the interactions between inversion and readout pulses. The spin echo readout also has the advantage of minimising dropout and any contributions from the BOLD effect. The disadvantage is a significantly longer minimum echo time and thus a lower signal to noise.

The simulations also suggested it was worthwhile spending the extra time on better readout pulses. Therefore the 5 ms 5-lobed Hamming filtered 90° and 180° sinc pulses from the Siemens Vision were used. The pulse profile of the 90°-180° readout for a 10 mm slice thickness was measured using a one-dimensional pulse sequence with the readout along the slice selective direction. The pulse profile of the 5-lobed Hamming filtered 90°-180° sinc pulses is given in Figure 5-3 (b).

Combining the readout pulses with the HS pulse described above, the pulse interaction can be calculated as described previously in Chapter 4.2:

$$SL = \sum \mathbf{profile\_HS} \bullet \mathbf{profile\_Hamming}_{90\_180}$$

$$GL = \sum \mathbf{profile\_HS}(\text{midpoint}) \bullet \mathbf{profile\_Hamming}_{90\_180}$$

$$FAIRr = 100\% * (SL - GL)/GL$$

FAIRr for the HS inversion and Hamming readout pulses was 0.14% of the GL signal (0.12% of M_0). This is higher than the result predicted in Chapter 4 using simulations for the same inversion to readout slice thickness ratio (3:1): there a FAIRr of ~ 0.01% of GL was found (0.01% of M_0) — see Figure 4-11. This difference in theoretical and experimental relative FAIR signal is probably a result of machine imperfections such as eddy currents.

In the FAIR pulse sequence, spoilers have been placed around the 180° pulse to remove the effects of pulse imperfections and to allow for flow spoiling. These gradients have been set to a value of 10 mT/m, which results in a b-factor of 1.6 s/mm^2. With the timings of this pulse sequence, the maximum possible b-factor is 10 s/mm^2.

The phase encoding dephasing lobe and the 90°-180° pulse timings have been set up in such a way that the centre of k-space is acquired a quarter through the acquisition. In this

way the signal to noise is maximised for the spin echo design. A further shift of the centre of k-space would lead to artefacts. The minimum echo time for this setup is 42 ms.

After the 90° pulse three lines of k-space are acquired without any phase encoding. These three k=0 lines are used as reference echoes, to correct for differences between odd and even k-space lines and thus for Nyquist ghosts.

The complex imaging data are acquired in a 64*64 matrix; each k-space line is acquired in 760 μs. The total sequence time for one half of the FAIR sequence (SL or GL) at a zero inversion time is 127 ms. In practise, the imaging time will be determined by the inversion time (~0.3-3.0 s) and the recovery time between the SL and GL subsequences (~3-6 s).

The data are processed with software written by Oliver Heid and Oliver Josephs (Heid, personal communication; Josephs, personal communication). The first and third acquired reference echoes are averaged to achieve reference data with effectively the same echo-time. The reference echoes are Fourier-transformed along the readout direction. The phase differences between even and odd echoes are calculated using complex division of the odd by the even projection. The phase differences are unwrapped and weighted by their amplitude. They are then fitted to a fifth order polynomial. The fitted phase differences are then applied to the even k-space lines after the first Fourier transform along the readout direction. The second Fourier transform is then applied along the phase encoding direction to yield the image.

The static subtraction error (SSE) – the SL-GL difference due to instrumental factors – was measured on a gel phantom (T_1=0.7 s). In Figure 5-4 it is depicted for inversion times TI (0.3, 0.6, 1.0, 1.2, 1.5 and 3.0 s) as a percentage of M_0. Some of the patterns in the SSE look like oscillations; it is possible that small oscillations still occur in the gel phantom. Still, this static error will be taken as the upper boundary for the static subtraction error that can be expected *in vivo*. The mean +/- sd SSE for the 6 TI points is given in Table 5-1.

SSE as % M_0 TI=300 ms	SSE as % M_0 TI=600ms	SSE as % M_0 TI=1000 ms	SSE as % M_0 TI=1200 ms	SSE as % M_0 TI=1500 ms	SSE as % M_0 TI=3000ms
–0.01+/-0.05	0.01+/-0.04	0.03 +/- 0.07	0.01 +/- 0.06	0.02 +/- 0.05	0.04 +/- 0.05

Table 5-1 Static subtraction error as percentage M_0 measured on a gel phantom for a range of inversion times TI.

5.3 A basic CBF quantification experiment

5.3.1 Data acquisition

A quantitative FAIR experiment was conducted on a human volunteer. To ensure a good SNR, a thick (10 mm) slice was selected. The inversion slice thickness was 30 mm. The head was positioned in the coil to get the imaging slice just above the corpus callosum, on resonance. Flow spoiling was applied (b= 1.6 s/mm^2) to reduce the contributions of large vessels. To ensure full relaxation of brain tissue between runs, a recovery time of 6 seconds ($\approx 5 * T_{1,\text{grey matter}}$) was inserted after every readout. Slice selective (SL) and global (GL) inversion acquisitions were interleaved. Fifty acquisitions of each were made for every inversion time TI. FAIR data were thus acquired for six inversion times ranging from 300-3000 ms. Short and long TI points were alternated to minimise the effects of any long term drifts on the CBF quantification. The duration of the whole experiment was 1 hour and 13 minutes. The imaging parameters are summarised below in Table 5-2.

TI values (in order acquisition)	300, 3000, 600, 1500, 1000, 1200 ms
averages of SL-GL per TI point	50 acquired; 44 used in analysis
recovery time	6 s
inversion/readout slice thickness	30 mm/10 mm
FOV	300 mm
acquisition matrix	64*64
b-value	1.6 s/mm^2
total duration experiment	1 hr 13 min

Table 5-2 Parameters for basic FAIR experiment.

The data were read into MATLAB and scaled to correct for different receiver gains used at the different inversion times. The first 5 acquisitions for all inversion times were discarded to reach a steady state for CSF. In this particular case the last acquisition for all inversion times was also removed, as the last image of the TI=3000 ms dataset was corrupted. For every TI point, 44 acquisitions thus remained.

The (magnitude) slice selective and global inversion data were then averaged separately for each TI point. These data are depicted in Figure 5-5. The SL and GL data appear to be identical, which is not surprising as the difference between them - the FAIR signal - should only be maximally ~1% of M_0 (Calamante et al., 1996). Grey-white matter contrast is clearly visible in the data; the white matter is nulled at shorter inversion times than the grey matter, which demonstrates its shorter T_1.

The FAIR data (SL-GL) are shown in Figure 5-6. The subtraction data build up from TI=50 ms to a maximum at TI=1.5 s. After that time the signal difference decreases due to the relaxation of the T_1-label. A striking aspect of the data is the negative FAIR signal — the voxels darker than the background noise. The negative FAIR signal is most apparent in areas where CSF is to be expected (at the edges of the brain and between the hemispheres). This negative FAIR signal is discussed further in sections 5.3.2.3 and 5.4.

Another interesting feature is the appearance of large vessels as bright dots in the FAIR images. The bright dot in the back of the brain disappears with increasing inversion time TI. This is a large vessel, the superior sagittal sinus, for which the label has washed through at long inversion times. There is another focal intensity point in a more medial-frontal area. The signal there seems to follow an inversion recovery trajectory. It is very unlikely that at an inversion time of 3 s a large vessel would still have label in it: the label should wash out quickly in large vascular structures. There is a more complex explanation for this focal signal, which will be formulated later in this chapter.

The contrast between grey and white matter in the FAIR data shows the difference in perfusion between these tissues (perfusion ratio grey matter: white matter ~ 3:1, Calamante et al., 1999).

Some signal from the skull appears in the image on the right side. This can be due to slow blood flow along the skull that is picked up. Alternatively, the static subtraction error can result in tissue and skull appearing in the subtraction data.

The signal-to-noise-ratio (SNR) of the maximum FAIR image at TI=1.5 s is ~ 90; the SNR for the maximum SL image at TI=3000 ms ~ 9800; the equilibrium magnetization M_0, if acquired, would then have a SNR of ~ 10800. The FAIR signal is thus ~ 0.8% of M_0. This magnitude of the FAIR signal is in accordance with predictions on the basis of CBF models (Calamante et al., 1996).

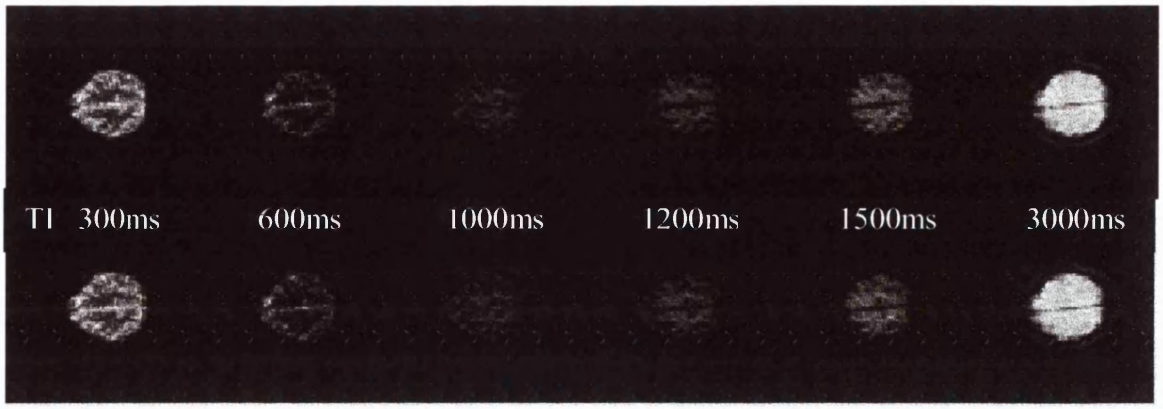

Figure 5-5 Slice selective (top row) and global (bottom row) inversion data over a range of inversion times TI.

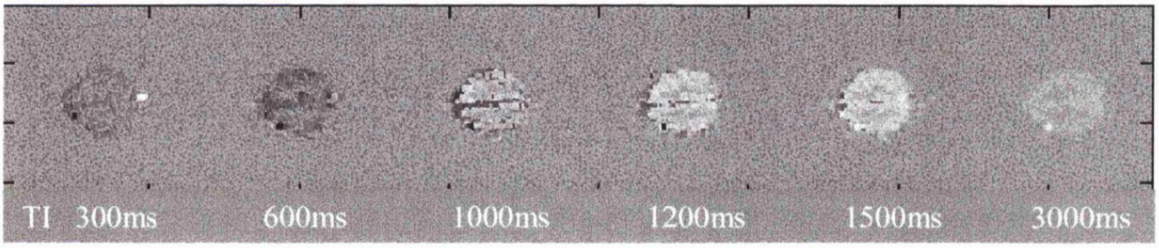

Figure 5-6 FAIR (subtraction) data over a range of inversion times TI.

5.3.2 Modelling the data

5.3.2.1 General modelling procedure

Fitting a model of n parameters to a data set constitutes a search through a n-dimensional landscape of possible parameter combinations. The search criterion used in this work is a minimal sum of squares difference between the data and the model.

In general, there is no guarantee that a found minimum is actually the *global* minimum, i.e. the best possible solution. Chances of finding a good solution are increased by using appropriate starting values for the fit parameters, i.e. by incorporating prior knowledge. It is also possible to limit the search by constraining the values of the fit parameters using prior knowledge.

Because of measurement noise, there is never an exact fit of the model to the data, even if the model is correct. To assess whether the model used is appropriate for the data, a goodness-of-fit test is performed. The question to be answered is: do the data points satisfy the functional relation assumed, taking into account the measurement errors? For this method the standard deviations on the data have to be known. First, the so-called chi-square value is calculated using:

$$\chi^2 = \sum_{i=1}^{N} \left(\frac{y_{data}(i) - y_{fit}(i; a_1 \ldots a_M)}{\sigma(i)} \right)^2 , \tag{5.2}$$

with $y_{data}(i)$ and $y_{fit}(i)$ the data and fit points, respectively; $\sigma(i)$ is the standard deviation of the data points; N is the total number of data points, M is the number of fit parameters $a_1 \ldots a_M$. The number of degrees of freedom, ν, is equal to N-M. For models that are linear in the parameters a, the probability of a value chi-square is given by the chi-square distribution for ν degrees of freedom. The distribution of chi-square, $p(\chi^2 | \nu)$, is normal for large numbers of degrees of freedom, with mean ν and standard deviation $\sqrt{2\nu}$. For lower

number of degrees of freedom $p(\chi^2|\nu)$ is a complex gamma function. The cumulative distribution function $p(\chi^2|\nu)$ and its complement $Q=1-p(\chi^2|\nu)$ are tabulated. As long as the noise is approximately gaussian, chi-square distributions also hold for non-linear models, and are therefore generally used for many models (Press et al., 1992; Ashburner, personal communication 1999).

If Q is a very small number for a particular data set and model, the differences between model and fit are unlikely to be chance fluctuations. This leaves three options: the model is wrong for the data, the measurement errors $\sigma(i)$ have been underestimated or the measurement errors are non-normally distributed. The last option is fairly common and therefore models with Q-values as low as 0.001 are generally still accepted (Press et al., 1992). Typically, truly wrong models will be expected to have Q values of $\sim 10^{-18}$.

If Q values are very high (i.e. close to unity) either the measurement errors have been overestimated or the data are too noisy for the model, i.e. the data are being overfitted by the model and the number of parameters in the model should be reduced.

The last step in a modelling procedure is the determination of the errors on the fit parameters. There are several methods to do this. The gold standard for establishing errorbars is by acquiring multiple repeats of the measurement ('repeated measures' method). The standard deviation of the parameter is the standard deviation on the mean of the parameter samples, i.e. the standard error of the repeated measurements. This method assumes that the parameter of interest is constant over the repeats, e.g. that CBF does not change significantly over the time of the repeats. If the parameter of interest is not constant over the repeats, the standard deviation on the fit parameter will be overestimated; this method therefore gives a conservative estimation of the standard deviation. As a rule of thumb, a minimum of 10 repeats is required for the multiple repeats method and the SNR of each of the repeats should be sufficient to give a converging and reasonable fit result. This is the most robust method of determining the standard deviation on the fit parameters, as it makes no assumptions about the fit model.

If there are not sufficient repeats available, another commonly taken approach is to use the Jacobian: this is a matrix with the partial derivatives of the fit parameters as columns. These partial derivatives are derived from the fit model. If the measurement errors

are normally distributed, these partial derivatives together with the standard deviation on the data points readily give a standard deviation for all fit parameters. This is how fitting programs calculate errorbars on fit parameters. This method does assume that the model is correct for the data, while the repeated measures method does not make any assumptions about the model.

The third method uses a ROI on the parameter map, e.g. the CBF map, and takes the variability of the parameter over the ROI as errorbar. This requires a ROI that encompasses enough voxels for a reasonable estimation of the variability. This method assumes that the mean value of the parameter over the ROI stays the same, i.e. that the ROI samples one distribution of the parameter.

If one wants to establish if it is worthwhile to add an extra parameter to the model, the extra-sum-of-squares test is applied. In this procedure, the sum of square differences, or residual error, between the data and model is compared for a model with and without the extra parameter. If the reduction in residual error for the extra parameter is not significantly larger than the residual error per degree of freedom of the full model, then the extra parameter can not be justified, as it might just be fitting noise fluctuations. In an equation:

$$F_{\delta f,N-npar} = \frac{(\varepsilon_R{}'\varepsilon_R - \varepsilon_F{}'\varepsilon_F)/\delta f}{(\varepsilon_F{}'\varepsilon_F)/(N-npar)}, \tag{5.3}$$

with $F_{\delta F, N-npar}$ the F-value of the model comparison, npar the number of parameters in the full model, δf the difference in degrees of freedom between the full (F) and reduced (R) model, N the total number of data points and $\varepsilon'\varepsilon$ the sum of squared differences between the data and the model. Using lookup tables, the F-values can be translated into p-values. For a low p-value ($p < 0.05$) it is unlikely that the null-hypothesis is true, i.e. it is unlikely that the reduction in residual error by adding the extra parameter is due to fitting noise.

5.3.2.2 The slice selective inversion data

The first step of the quantification procedure as commonly reported in the literature is to fit the slice selective inversion data (SL) to find the inversion efficiency (α_0), the apparent T_1

value (T_{1app}) and the equilibrium magnetization M_0 (Calamante et al., 1996). The relation is a simple inversion recovery following equation (5.1). This fitting was performed on the acquired human data set with unconstrained fit parameters. All background voxels were set to zero by applying a threshold mask. Then the fits were done on a voxel-by-voxel basis. The start value for α_0 was 0.99, the result of the HS inversion efficiency fitting on the gel phantom in section 5.2. The start value for T_{1app} was set to the T_1 of grey matter at 2 T, 1.2 s (Deichmann, personal communication). A start value of T_{1app} at the T_1 of white matter (0.7 s) was also tried, but this made very little difference. Finally, the initial M_0 value for each voxel was set to its value in the SL image with the longest inversion time: $SL_{TI=3000ms}$.

The results of the constrained SL fit, i.e. the parameter maps for the inversion efficiency α_0, the apparent longitudinal relaxation T_{1app} and the equilibrium magnetization M_0, are shown in Figure 5-7.

The fitted inversion efficiency varies throughout the brain and in CSF regions the inversion efficiency is even larger than the physically possible value of 1.0! So in these areas the model is obviously not optimal. The T_1 values expected at 2 T are 1.17 +/- 0.05 s for grey matter, 0.70 +/- 0.05 s for white matter and 4.65 +/- 1.20 s for CSF (Deichmann, personal communication). The T_{1app} values should be very similar to the T_1 as the effects of CBF on it are very small ~ 1%, see equation (3.6). The fitted T_{1app} values in Figure 5-7 (b) are a somewhat higher than the expected range: white matter voxels have T_{1app} values of ~ 0.8 s, grey matter regions have T_{1app} values of 1.2-1.4 s. In regions with CSF voxels (the edges of the brain and between the hemispheres) T_{1app} values are found somewhere between the T_{1app} of grey matter and the expected T_1 value for CSF. This is probably due to partial voluming of CSF with grey and/or white matter in these areas. The contrast demarcating grey and white matter boundaries in the T_{1app} and M_0 parameter maps is consistent with the contrast in the raw slice selective inversion data in Figure 5-5 and the perfusion dependent contrast in the FAIR data in Figure 5-6.

Examples of fits for white and grey matter voxels are shown in Figure 5-8 and Figure 5-9. The mean SL data +/- the standard error (se=sd/$\sqrt{}$nav) are depicted.

(a)

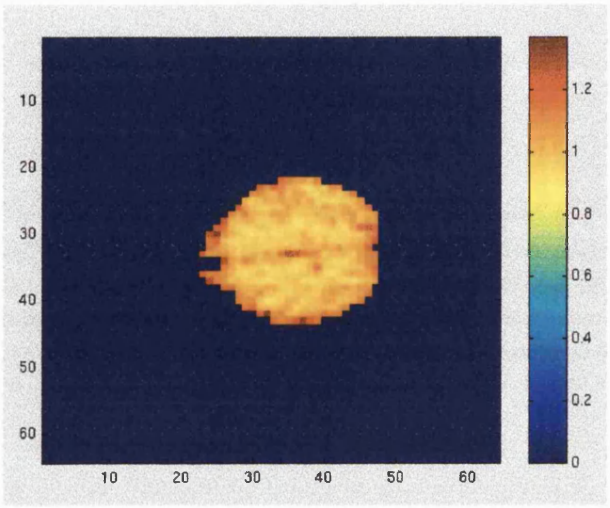

(b)

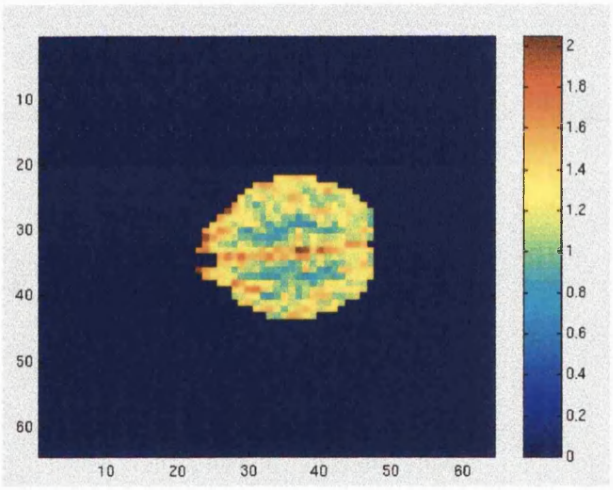

(c)

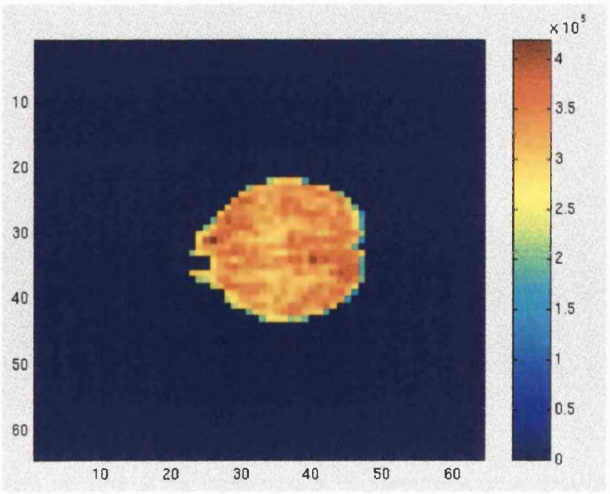

Figure 5-7 Results SL fit: (a) Inversion efficiency α_0, (b) T_{1app} in s, (c) M_0 in arbitrary units.

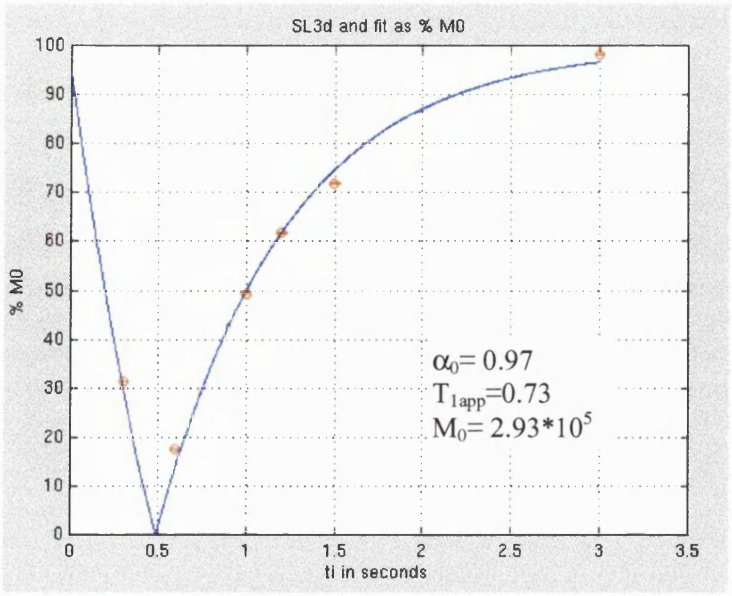

Figure 5-8 Mean SL +/- se and fit as percentage M_0 – white matter voxel

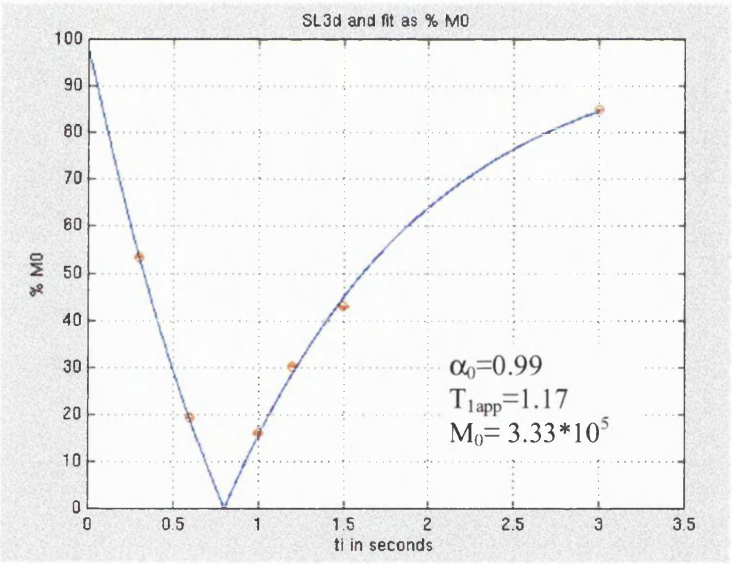

Figure 5-9 Mean SL +/- se and fit as percentage M_0 – grey matter voxel

To test if the slice selective inversion model is appropriate considering the data and the standard deviation on the data, a goodness-of-fit test was performed as described in section 5.3.2.1. As the SNR of slice selective inversion data is high, the goodness-of-fit test was performed using single average SL fits for each voxel (selected randomly from the 44 repeats acquired). This allows for the most accurate estimation of the standard deviation of the mean (the standard error, se), as for one acquisition this is estimated by the standard deviation of the sample of all repeats. In other words, in this way any instabilities – e.g. volunteer movement- that could lead to a non-gaussian averaging ($se > sd_{all\ repeats}/\sqrt{nav}$) do not influence the goodness-of-fit test. The chi-square values were thus calculated for all non-zero voxels using equation (5.2). Then the corresponding Q-values ($Q=1- p(\chi^2|\nu)$) were retrieved from online distribution tables. The percentage of all voxels that survived the $Q > 0.001$ goodness-of-fit threshold was only 15%. The physics of magnetization inversion recovery is well established, so in that sense there is no reason to doubt the model. The data does follow the inversion recovery model reasonably well (see Figure 5-8 and Figure 5-9), but the difference between the data and the model must be larger than was to be expected on the basis of the variability of the SL data.

To exclude the possibility of any machine or pulse sequence imperfections, an equivalent experiment was run on an agarose gel phantom. When its outer layer of voxels is excluded (as this is where partial voluming of glass and gel occurs) 85% of all remaining voxels pass the $Q > 0.001$ threshold. The inversion recovery model is therefore appropriate for data acquired with this pulse sequence on a homogeneous medium.

Two possible explanations for the disappointing goodness-of-fit results for the human data are partial voluming and volunteer movement. Partial voluming must be a contributor to the low Q values. It is unlikely that a 220 mm^3 voxel is pure in containing only one T_1 species (grey matter/white matter/CSF). Probably, a mix of two or three of these T_1 species will be present in one voxel. This partial voluming results in a signal that is a sum of the contributions of every T_1 species: the signal from an inversion recovery experiment will be a sum of each of the inversion recovery curves, each with their own T_{1app}. Trying to fit a single exponential recovery curve to such a signal will result in a less accurate fit, with a larger difference between the data and the fit than would be expected on the basis of the gaussian variability of the data.

Volunteer motion between the different inversion time points will also increase the difference between the data and the model; the repetition time for one SL-GL repeat is 2*(6 s + TI) and every inversion point is acquired 50 times, which therefore takes somewhere between 10-16 minutes. For the 6 inversion times acquired in this experiment, the total scanning time is 1h 13 min. This is a long scan time and significant subject motion effects are expected to occur.

Partial voluming and volunteer motion will be further explored in the 'Quantification issues' in section 5.4, but for now the results of this standard inversion recovery model will be used to establish a reference analysis with which the results of potential improvements can be compared.

Finally, the standard deviations on the SL fit parameters for the human data were calculated. As the number of repeats (44) was sufficient for the repeated measures method, this was the approach taken. Every one of the 44 repeats was fitted to the model separately. Individual data points that were too noisy to give a converging result in the algorithm were discarded. For every voxel a distribution for each fit parameter was thus calculated. The mean and standard deviation of the mean (standard error) for each fit parameter were derived from these distributions. For the inversion efficiency, T_{1app} and M_0 parameters the average sd of the parameters over the whole slice (with each voxel's sd as percentage of the voxel's parameter mean) were 0.1%, 0.2% and 0.2% respectively.

5.3.2.3 The FAIR data

The results of the slice selective inversion fit were inserted into the formula for CBF. For data acquired with a long repetition time – i.e. full relaxation of the spins at the beginning of each inversion – and negligible inflow delay, the FAIR data, dM, follows (Calamante et al., 1996):

(5.4) $$dM(TI) = 2\alpha_0 M_0 \frac{f}{\lambda}\left[\frac{\exp(-TI/T_{1app}) - \exp(-TI/T_{1a})}{\frac{1}{T_{1a}} - \frac{1}{T_{1app}}}\right],$$

with f the CBF in ml/100g/min, λ the brain/blood partition coefficient for water (in ml/g) and T_{1a} the T_1 of arterial blood. If an inflow delay, or transit time, is taken into account this changes into (Thomas, 1999):

(5.5)

$$dM(TI) = 0 \qquad TI \le \delta t$$

$$dM(TI) = 2\alpha_0 M_0 \exp(-\frac{\delta t}{T_{1a}})\frac{f}{\lambda}\left[\frac{\exp(-(TI-\delta t)/T_{1app}) - \exp(-(TI-\delta t)/T_{1a})}{\frac{1}{T_{1a}} - \frac{1}{T_{1app}}}\right] \qquad TI \ge \delta t$$

With δt the inflow delay in seconds.

dM(TI) is the difference $M_z^{SL}(TI)$- $M_z^{GL}(TI)$, where $M_z^{SL}(TI)$ and $M_z^{GL}(TI)$ are the *longitudinal* magnetization values at the time TI after slice selective and global inversion, respectively. M_z^{SL} and M_z^{GL} can be both negative and positive due to the inversion. dM(TI) is obtained from the measurement by subtraction of the *magnitude* of the slice selective inversion data (SL) minus the *magnitude* of the global inversion data (GL). Strictly speaking, this is wrong if M_z^{SL}, M_z^{GL} or both values are negative: before the zero-crossing, the faster relaxing M_z^{SL} signal will be smaller in magnitude than the magnitude M_z^{GL} signal and the M_z^{SL}- M_z^{GL} subtraction will thus yield a negative FAIR signal. However, this zero crossing occurs at ~ 0.5 s for white matter and at ~ 0.8 s for grey matter. These values correspond to the literature values for the inflow delay (Ye et al., 1996), so for the critical TI range dM(TI) should be zero anyway.

These dM(TI) data were then masked with the same mask used for the slice selective inversion data and the remaining voxel data dM(TI) were fitted for perfusion alone or perfusion and inflow delay, on a voxel-by-voxel basis. For each voxel the inversion efficiency α_0, T_{1app} and M_0 were substituted from the slice selective inversion fit.

Unlike the slice selective inversion data, the FAIR data can have a very low SNR, especially in low CBF areas (white matter). To direct the fit and to avoid fitting noise, two extra procedures were applied:

- If a fitted delay or CBF is smaller than zero, the data are considered to be noise and the CBF and delay results are set to zero.
- If a fitted delay is larger than/equal to the second largest inversion time (e.g. fitted delay $\geq$ 1.5 s for TI=[0.3 0.6 1.0 1.2 1.5 3.0] s), the data are considered to be noise and the CBF and delay results are set to zero.

Voxels whose CBF and delay results were set to zero, were excluded from all following analyses. The start value for CBF was 50/ml/100g/min (a value between grey and white matter CBF), for the inflow delay the start value was 0.7 s. The results of fitting the data without and with inflow delay are given in Figure 5-10. Three voxels with very high CBF values (> 200 ml/100g/min) were set to zero; the location of these voxels coincided with the bright spots in Figure 5-6, and these voxels are therefore most probably large vessels.

Fitting for the inflow delay has a large effect on the final CBF values: without fitting it (Figure 5-10 (a)), grey matter CBF values do not exceed 50 ml/100g/min, far below grey matter literature values of ~ 80 ml/100g/min. If the inflow delay is included in the model, CBF values fall within the literature range (with white matter ~ 30 ml/100g/min).

The fitted delay is significantly non-zero, ~ 0.6 s in grey and white matter areas. This inflow delay is in accordance with the literature: if no flow spoiling is used, inflow delays of ~ 0.5 seconds have been found (Ye et al., 1997). This inflow delay increases with increasing flow crushing, to a maximum of 0.9 s (values for grey matter). Yang et al. (Yang et al., 2000) find a mean inflow delay over 6 volunteers of 0.65 s using a FAIR technique with similar flow spoiling as used in this experiment (inflow delay for whole slice).

(a)

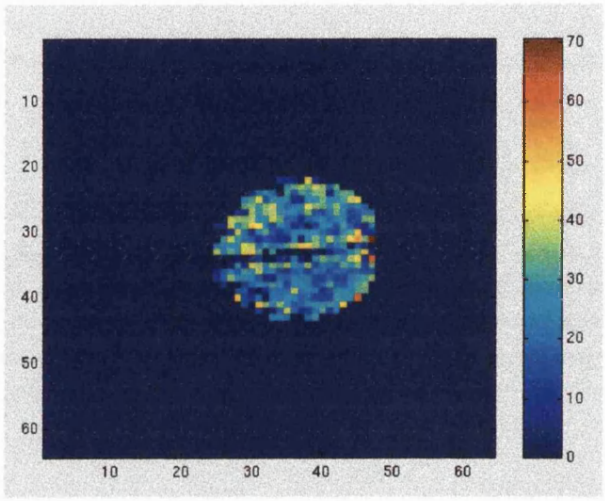

(b)

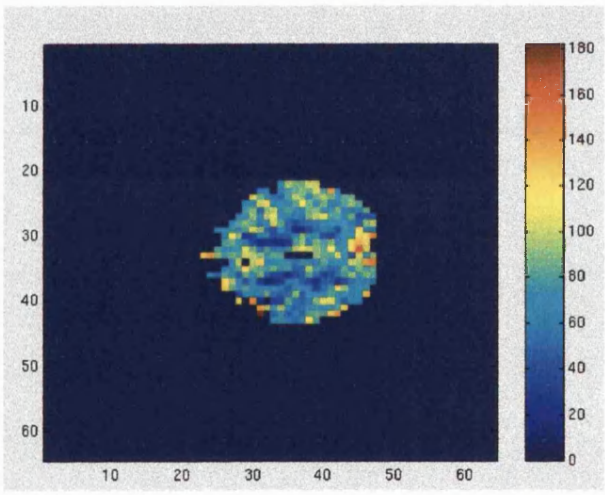

(c)

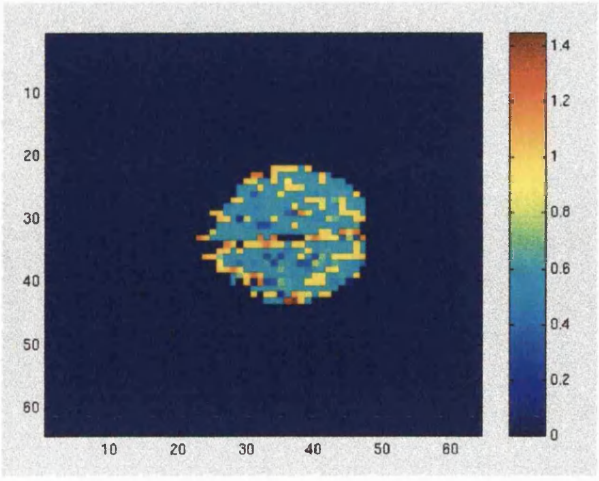

Figure 5-10 CBF in ml/100g/min, without (a) and with (b) fitting for delay, (c) fitted delay in s

Examples of CBF and delay fits for white and grey matter voxels are shown in Figure 5-11 and Figure 5-12. The mean FAIR data +/- the standard error is plotted. These fits do not look very good. For short inversion times negative FAIR signal is very prominent. This negative signal will be explored further in the Quantification issues of section 5.4.

A second observation is how the last TI=3000 ms data point falls below the model for both grey and white matter voxels. This could be a result of the finite width of the head coil: the global inversion only affects spins within the head coil. Spins outside the head coil that do manage to reach the slice of interest within these long inversion times will therefore not be affected by either inversion and thus do not contribute to the subtraction, i.e. the FAIR signal. This effect leads to an underestimation of the FAIR signal at long inversion times (Calamante et al, 1996). Yang and colleagues (Yang et al., 1998) have demonstrated that for inversion times < 1.2 s and a head coil with a length of 300 mm this 'global inflow' effect will not occur. The length of the head coil used in this experiment is also 300 mm, so for the data acquired at inversion times TI of 1.5 and 3.0 s, this effect *is* expected to be present.

To test formally if the two CBF models are appropriate considering the data and the standard deviation on the data, goodness-of-fit tests were performed. The FAIR data are too noisy to use single average data for this, so instead the mean +/- se FAIR data for each voxel were used. The standard error on the FAIR data was derived from the standard deviations on the SL and GL data and the number of repeats. For the model that fits for CBF and the inflow delay (CBFD model), 35% of all voxels passed the Q>0.001 threshold; for the CBF only fit (CBFO) 21% passed. The same issues as for the SL goodness-of-fit test apply here too: both partial voluming and volunteer movement between inversion time points will negatively influence the results of this test. However, as the goodness-of-fit test takes the number of fit parameters into account, this result is an indication that the CBFD model is the better model. The formal model selection for the FAIR data will be described in section 5.4.4.2.

(a) (b)

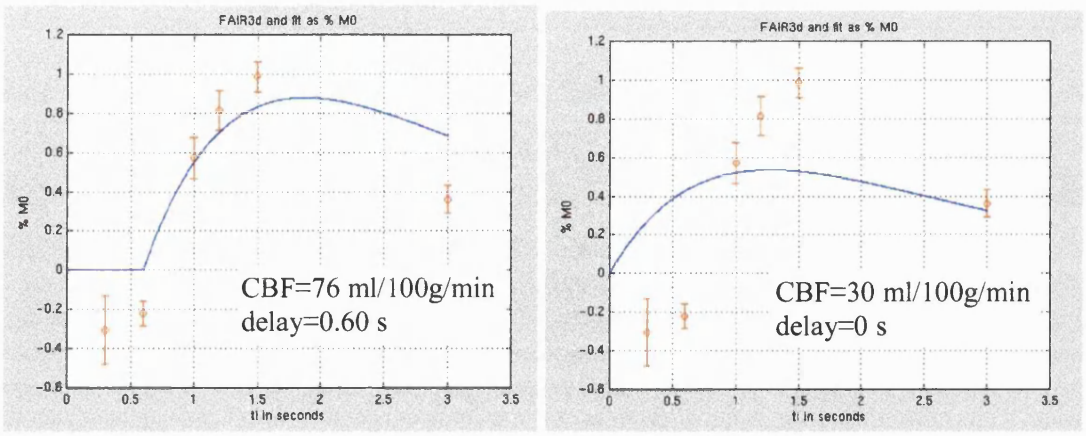

Figure 5-11 Mean FAIR +/- se and CBF fit as percentage of M_0 with (a) and without (b) delay fitted – grey matter voxel

(a) (b)

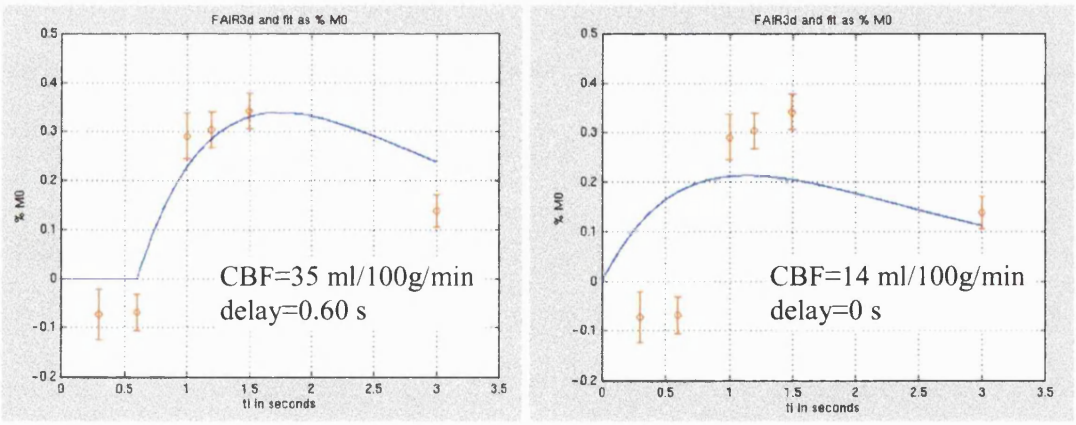

Figure 5-12 Mean FAIR +/- se and CBF fit as percentage of M_0 with (a) and without (b) delay fitted – white matter voxel

Finally, the standard deviations on the CBF and delay fit parameters were calculated with repeated measures approach. Each of the 44 repeats was fitted to the model separately. Individual data points that were too noisy to give a converging result in the algorithm were discarded. For every voxel a distribution for each fit parameter was thus calculated. The mean and standard deviation of the mean for each fit parameter were derived from these distributions. For the CBFD model, the mean sd values for CBF and the inflow delay over the whole slice (with each voxel's sd as percentage of the voxel's mean parameter value) were 10% and 18% respectively. For the CBFO model sd for CBF was 9%.

This calculation ignores the errorbars on the inversion efficiency, T_{1app} and M_0; these SL fit parameters are inserted as constants into the FAIR model. The effect of ignoring these contributions can be estimated using the general error propagation formula. For a function $f(a_1,a_2....a_n)$, the error df follows from the errors da_i according to:

$$(5.6) \quad (df)^2 = (\frac{\delta f}{\delta a_1})^2 da_1^{\ 2} + (\frac{\delta f}{\delta a_2})^2 da_2^{\ 2} .....(\frac{\delta f}{\delta a_n})^2 da_n^{\ 2}$$

So the additional error terms due to inversion efficiency, T_{1app} and M_0 simply add up to the errors already derived. For standard deviations on inversion efficiency, T_{1app} and M_0 of 0.1%, 0.2% and 0.2% respectively as found in the SL fitting, the derived mean standard deviation for CBF and delay change by $\leq 0.01\%$ when the standard deviations of the SL fit parameters are included in the error calculation. Because the errorbars on the SL fit parameters are so small, it is indeed safe to ignore them.

If for a particular voxel the errorbar is too large for the sensitivity required, averaging over a ROI of voxels will decrease the errorbar, at the price of a decreased resolution. The highest sensitivity can be achieved by averaging over a whole grey or white matter mask. This is the topic of the next paragraph.

5.3.2.4 Results for grey and white matter masks

Following the methods of Ye et al. (Ye et al., 1997), images were segmented into grey and white matter by applying T_{1app} masks. Using similar T_{1app} bandwidths but taking into

account the higher field strength of 2T, the grey matter T_{1app} bandwidth used here was 1.17 +/- 0.10 seconds, for white matter it was 0.82 +/- 0.10 seconds. These limited T_{1app} bandwidths exclude many voxels, but the aim is to get relatively pure grey and white matter without significant partial voluming.

The thus constructed grey matter mask contained 160 voxels (41% of total) and the white matter mask 29 voxels (7% of total). The T_{1app} bandwidth used for grey matter is in accordance with previously measured T_1 values at 2 T (Deichmann, personal communication), however, the white matter T_{1app} values used here are higher than the literature value (0.70 +/- 0.05 s). When using literature values for the white matter mask, only one voxel was found. It seems the fitted white matter T_{1app} values here are somewhat higher than the literature values. The bandwidth for the white matter mask was therefore determined by observing for which T_{1app} values the voxels formed clusters in the white matter areas. One explanation for the higher T_{1app} values found in this study is partial voluming of white matter with grey matter and/or CSF. The results for CBF and delay for these masks are listed in Table 5-3.

	grey matter mask – 160 voxels (41%)	white matter mask – 29 voxels (7%)	ratio CBF grey/white
T_{1app} in seconds	1.17 +/- 0.06 (5%) med. 1.17	0.86 +/- 0.04 (5%) med. 0.86	--
$CBF_{CBFD\ model}$ in ml/100g/min	78.92 +/- 18.43 (23%) med. 76.96; SE 1.46 (2%)	31.53 +/- 13.02 (41%) med. 32.37; SE 2.42 (8%)	2.50 +/- 0.20
$delay_{CBFDmodel}$ in seconds	0.62 +/- 0.10 (16%) med. 0.60;SE 0.0083 (1%)	0.57 +/- 0.26 (46%) med. 0.53; SE 0.0049 (1%)	--
$CBF_{CBFO\ model}$ in ml/100g/min	30.86 +/- 8.27 (27%) med. 30.46; SE 0.65 (2%)	13.70 +/- 6.48 (47%) med. 13.38; SE 1.20 (9%)	2.25 +/- 0.20

Table 5-3 Results for grey and white matter masks: T_{1app}, CBF and delay values. All values are listed in the following format: mean +/- standard deviation (% mean); median (% mean). For CBF values the standard error (SE) is also given. The standard deviations on the CBF ratios were calculated using the standard errors.

The results of the CBFD model are in very good accordance with the literature. However, the errorbars on CBF and delay over the masks (23% and 16% resp. for grey matter, 41% and 46% for white matter) are quite a lot larger than the mean individual sd values calculated before over all voxels (10% and 18% resp.). This can be explained

considering the standard deviation over the mask also includes the variability of CBF over that distribution of voxels. It is therefore expected to be larger than the standard deviation on an individual voxel.

It is obvious the CBFO model is not sufficient for the data: grey matter CBF is underestimated by ~ 60% when compared to literature values of ~80 ml/100g/min (Calamante et al., 1999). A more extensive discussion of the choice between the CBFD and CBFO models will be given in the model selection section (section 5.4.4.2). For now, only the CBFD model will be further discussed as the CBFO results are so obviously wrong.

The ratio between grey and white matter CBF (2.50) falls within the range reported in the literature, although the 'gold standard' value is considered to be 3.0 (Calamante et al, 1999). However, any grey matter partial voluming within the white matter will lower the calculated grey-white matter CBF ratio and considering the slightly elevated T_{1app} values of the white matter mask this might well be the case here.

5.3.2.5 The good, the bad and the ugly: conclusions from the basic quantification experiment

The aim of this basic CBF quantification experiment was to acquire and analyse CBF data in ways commonly reported in the literature. This serves firstly to compare results of the implemented ASL technique with the literature. Secondly, a critical appraisal of the results thus obtained points to issues that should be further explored. So what conclusions can be drawn from the results of this experiment?

Firstly, the analyses in section 5.3.2.4 for grey and white matter masks have shown that it is essential to include the inflow delay in the FAIR modelling (the CBFD model). If this inflow delay is not included, CBF values are underestimated by up to ~ 60%. Until the more extensive FAIR model selection as described in section 5.4.4.2, the CBFD model will be the only model discussed from now on.

Using the CBFD model and the grey and white matter masks defined in section 5.3.2.4, the measured CBF values, the inflow delay and the CBF ratios all fall well within the range of literature values (for a review see Calamante et al., 1999). However, the goodness-of-fit results for both the SL and the FAIR fits are not very good: only 15% of all

voxels pass the Q>0.001 threshold for the SL fit and only 35% of voxels for the FAIR fit. This casts doubts on the validity of the fit results, despite the fact that the numbers 'come out right'.

One issue that must contribute to the disappointing goodness-of-fit results is partial voluming. For the 10 mm slice thickness used, all voxels will suffer from partial voluming (of CSF, grey and/or white matter) to lesser or greater extent. This partial voluming seems to be a major problem: for a homogenous gel phantom 85% of all voxels pass the SL goodness-of-fit test, in a human this drops to 15%. The location of the 'trouble areas' with the worst fits also supports the partial voluming hypothesis: they are at the edges of the brain and between the hemispheres, the areas with significant CSF partial voluming. It is to be expected that partial voluming with CSF will be the most problematic, as the T_1 value of CSF is much larger than the T_1 value of grey or white matter. Fitting a single exponential to a multi-exponential inversion recovery signal will therefore give the worst results for partial voluming with CSF. Partial voluming is the first topic to be further investigated in the 'Quantification issues' in section 5.4.

The second area of concern is the static subtraction error. There is very prominent negative FAIR signal in the data (Figure 5-12 and Figure 5-11) which could be a result of the SL – GL magnitude subtraction, but it could also be due to the static subtraction error. The negative FAIR signal and the static subtraction error will be discussed further in section 5.4.

The effect of flow spoiling on the data will be discussed in section 5.4.2. Because the CBF quantification model assumes an exchange of spins in the vasculature with the voxel's tissue according to the blood/brain partition coefficient λ, it is important to crush all contributions from the larger vascular structures that will not deliver spins to the tissue.

Taking all the issues discussed above into account, what is the optimal model for the SL and FAIR data? This question will be addressed in the model selection section 5.4.4.

Waiting between acquisitions for full relaxation of the spins is not a very efficient acquisition strategy. Moreover, the long time needed for the full relaxation will exacerbate movement effects; furthermore, chances of CBF being stable over the acquisition time are reduced. It is therefore worthwhile optimising the time efficiency of the measurements, and this will be described in section 5.4.5.

The issue of motion correction is introduced in section 5.4.5 and realignment procedures are proposed and evaluated.

The final proposal for an optimised experimental setup and analysis will be given in 5.4.7. This is the approach that will be taken in all experiments to follow in this thesis.

5.4 Quantification issues

5.4.1 Partial voluming

The issue of partial voluming is not new: Kwong already pointed out this problem in his first FAIR paper; he simulated the effects of partial voluming with CSF and calculated that a voxel consisting of 50% grey matter and 50% CSF could result in an underestimation of perfusion values by 70% (Kwong et al., 1995).

Not much progress has been made beyond this early diagnosis. Ye et al. (Ye et al., 1997) use the different magnetization transfer properties of CSF to exclude voxels with significant CSF partial voluming from the analysis. But this can also be done by applying a T_1 mask with a small bandwidth around the 'pure' grey and white matter T_1 values as described in section 5.3.2.4. The voxels with large CSF partial voluming are not hard to find, but what about the more subtle effects of, say, a 10-20% CSF fraction in a grey matter voxel? The size of the error introduced by grey and white matter partial voluming has also not been established as yet. As CSF partial voluming is expected to have the most detrimental effect on CBF quantification, this is the first focus of this section.

5.4.1.1 CSF partial voluming

Although Kwong's simulation was very important in signalling the partial voluming problem, the model he employed to arrive at the 70% CBF underestimation is not optimal. In his simulation he calculated the expected SL signal for a 50%-50% grey matter-CSF voxel, given a CBF of 100 ml/100g/min for the grey matter and of 0 ml/100g/min for the CSF. He then fitted a single T_1 value to the resulting double exponential to get the T_{1app} fit value. The CBF values were calculated using the difference between the known T_1 value and the fitted T_{1app} using equation (3.6). This so-called T_1 difference approach is not often

used anymore. Zhou and colleagues have shown it is not as robust as the approach used in this thesis (the CBFD model), because the effect of transit time is hard to incorporate in it (Zhou et al., 1999).

So what sort of errors on CBF are to be expected if a similar simulation is carried out using the standard models of section 5.3.2? A partial voluming simulation was performed using the parameters listed in Table 5-4. Literature values were used for the T_1, CBF and delay values; the model and the settings of the fit algorithms were the same as for the basic CBF quantification experiment in section 5.3.2.

grey matter T_1	1.17 s
grey matter CBF	80 ml/100g/min
grey matter inflow delay	0.7 s
CSF T_1	4.65 s
fractions CSF	[0:0.05:1] ; 21 fractions
inversion efficiency	0.99
M_0	1
T_{1a}	1.4 s
λ	0.9 ml/g
TI	[0.3 0.6 1.0 1.2 1.5 3.0] s

Table 5-4 Partial voluming simulation parameters. All other unmentioned simulation settings are the same as used in the data analysis of section 5.3.2.

The equilibrium magnetization M_0 was set to 1 for convenience. The fraction of CSF in the voxel ranged from 0-1 in steps of 0.05.

For every fraction of CSF the total SL and GL signals were calculated as the sum of the grey matter and CSF fractions. Due to the inflow delay, the equations for SL and GL are more complicated than a simple inversion recovery (Zhou et al., 1999). The formula for SL and GL for the grey matter and CSF fraction are given in equation (5.7) .

$$SL_{grey} = (1-\text{fraction})[M_0(1-2\alpha_0 \exp(-TI/T_{1app}))$$
$$+2\alpha_0 M_0 \frac{CBF}{\lambda} \frac{1}{(\frac{1}{T_{1app}}-\frac{1}{T_{1a}})}(\exp(-TI/T_{1app})-\exp(-\delta t/T_{1a})\exp(-(TI-\delta t)/T_{1app}))]$$

(5.7) $$GL_{grey} = (1-\text{fraction})[M_0(1-2\alpha_0 \exp(-TI/T_{1app}))$$
$$+2\alpha_0 M_0 \frac{CBF}{\lambda} \frac{1}{(\frac{1}{T_{1app}}-\frac{1}{T_{1a}})}(\exp(-TI/T_{1app})-\exp(-TI/T_{1a}))]$$

$$SL_{CSF} = GL_{CSF} = \text{fraction} \cdot M_0(1-2\alpha_0 \exp(-TI/T_{1CSF}))$$

Fraction is the relative contribution of the CSF compartment to the signal for completely relaxed spins. The equation for SL is only valid for $TI \geq \delta t$, the inflow delay. For $TI < \delta t$, $SL_{grey} = GL_{grey}$. The difference between SL_{grey} and GL_{grey} is the aforementioned equation for the FAIR signal with an inflow delay, equation (5.5). For a SL *fit* on real data, the simple inversion recovery model (equation (5.1)) that was used in section 5.3.2.2 suffices (the additional CBF related terms are 1-3% of the SL signal). In this simulation, the aim was to derive the FAIR signal from the *calculated* SL and GL data and therefore the complete formula are necessary.

The SL_{grey}, GL_{grey}, SL_{CSF} and GL_{CSF} were calculated for a range of fractions of grey matter and of CSF. The total SL and GL signals were calculated as the magnitude of the sum of the grey matter and CSF contributions to SL and GL.

The total SL signal was fitted for inversion efficiency, T_{1app} and M_0 — in short, the ITM model. The FAIR signal was then calculated as the difference SL-GL. Using the parameters fitted from the SL data, the FAIR signal was then fitted for CBF and inflow delay. The modelling thus assumes a single T_1 underlying the SL data (grey matter or CSF) while actually the SL data are the result of the sum of two inversion recovery processes, each with their own T_1.

The results for the CBF, inflow delay, inversion efficiency, T_{1app} and M_0 are given in Figure 5-13 (a)-(e). The correct values considering the grey and CSF fractions are plotted in black dashed lines. It should be noted that the theoretical values for the CBF refer to the

perfusion of a voxel containing grey matter and CSF. Thus, the CBF decreases linearly with increasing CSF fraction. For CSF fractions from 0-20%, the fitted CBF and delay values are correct, even though the SL fit parameters (α_0,T_{1app}, M_0) are already starting to deviate from their correct values. As CSF partial voluming is expected to be quite prevalent *in vivo*, it is good news that the fitted CBF value exhibits a certain degree of immunity to it. Having said that, if the fraction of CSF in the voxel is unknown, it will not be possible to determine if CSF partial voluming or a locally depressed perfusion is the cause of the lowered CBF value found. Still, the found CBF value for CSF fractions of 0-20% will be a correct reflection of the amount of blood delivered to that voxel.

For CSF fractions of 25-50% this is not the case, as the resulting CBF values are overestimated by 40-50% and the inflow delay will be overestimated by up to 70%. For the CBFD model, the effects of partial voluming are therefore quite different from Kwong's reports; he predicted a 70% *under*estimation of CBF for a 50%-50% grey matter-CSF voxel using the T_1 difference method.

For CSF fractions > 50% the exclusion criterion is soon reached (fitted delay < 1.5s to avoid fitting noise) and the results are set to zero. But this last group is not very interesting anyway, as these are CSF voxels that will be easily excluded by a T_1 mask (T_1 > 1.7) or by using the different MT properties of tissue and CSF (Ye et al., 1997).

An interesting point to make, is the effect of constraining the fit parameters during the fit procedures. This is a very tempting thing to do, as one can assure physically sound values of all fit parameters in this way. Exactly the same simulation was performed, but now with the fit parameters constrained ($\alpha_0 \in [0.8 ; 1.0]$, $T_{1app} \in [0.6 ; 5.0]$ s, $M_0 \in [0.5 \cdot SL_{TI=3000ms} ; 5 \cdot SL_{TI=3000ms}]$, CBF $\in [0 ; 320]$ ml/100g/min, delay $\in [0 ; 1.4]$ s). The CBF for this constrained analysis is shown in Figure 5-13 g(f). CBF is now actually much more sensitive to partial voluming. For a 20% CSF fraction, CBF is underestimated by ~25%, and for a 50% CSF fraction it is underestimated by ~60%. So constraining the fit parameters leads to a quicker deterioration of the CBF fitting and should be avoided.

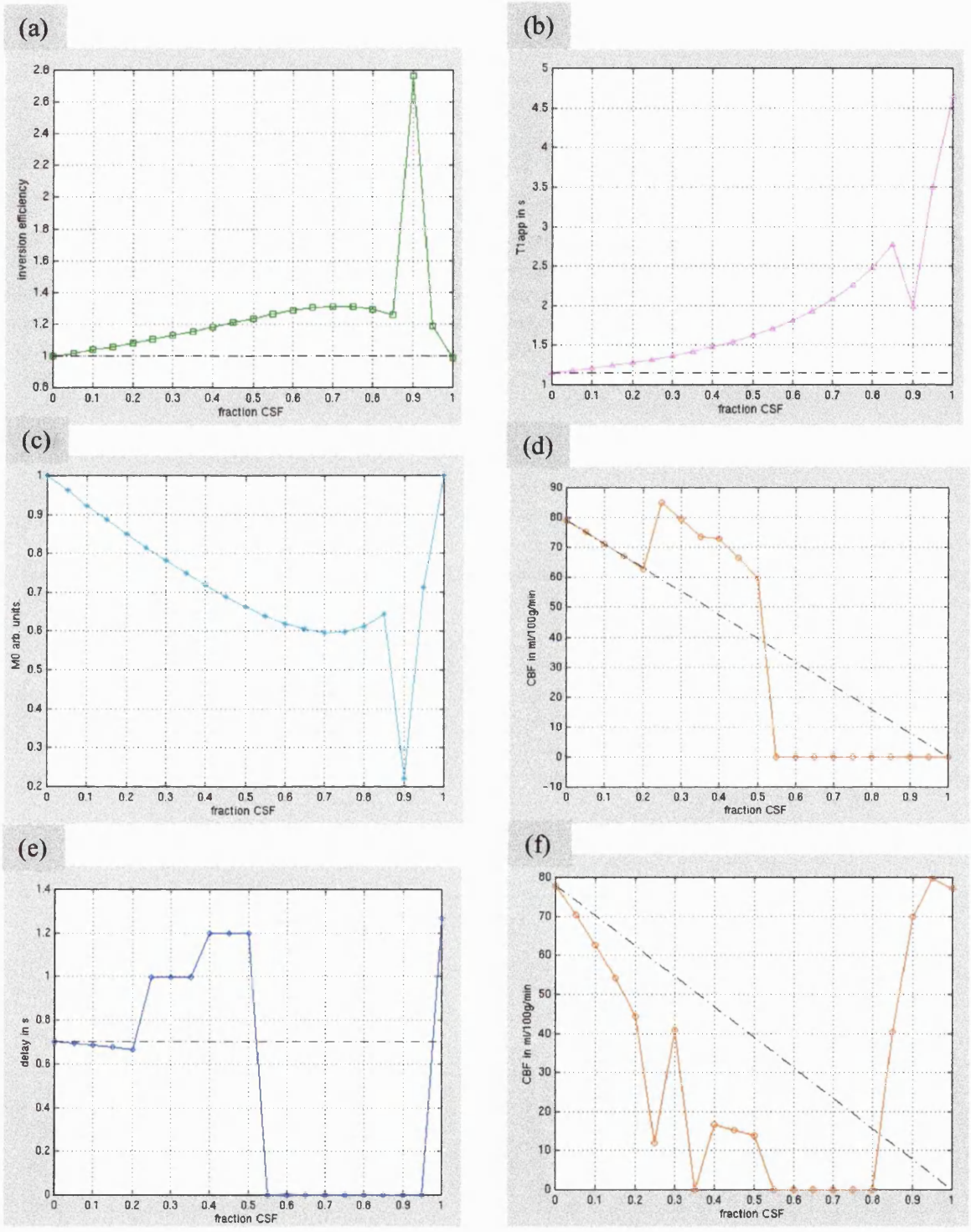

Figure 5-13 Partial voluming simulation, results grey matter with progressive CBF partial voluming: (a) inversion efficiency, (b) T_{1app}, (c) M_0, (d) CBF, (e) inflow delay, (f) CBF from *constrained* analysis

What insight do these simulations give about the experimental data from section 5.3? The first most striking connection is that of the inversion efficiency: the simulations predict an overestimation of α_0 in areas with CSF partial voluming. And indeed, the regions with inversion efficiency > 1 in Figure 5-7 (a) are exactly those areas where significant partial voluming with CSF is expected.

The predicted overestimation of T_{1app} compared to the literature value of 1.17 s is also seen in the experimental results: the voxels in grey matter areas tend to have elevated T_{1app} values of 1.2-1.4s, see Figure 5-7 (b). The T_1 mask applied in section 5.3.2.3 to exclude CSF partial voluming (T_{1app} > 1.4 s) thus, according to Figure 5-13 (b), excluded all voxels with a CSF fraction > 35% — assuming the voxel consists only of grey matter and CSF. Predictions from the simulations regarding the inversion efficiency and T_{1app} are thus supported by experimental data.

The effects of partial voluming on CBF are harder to assess with experimental data. It is here that the simulations are extremely useful in pointing out how large this CSF partial voluming problem actually is. If the applied T_1 mask only excludes voxels with CSF partial voluming > 35%, this means that all lower CSF partial voluming is still present in the masked data. Thus up to 40% overestimation of CBF can occur for these data according to Figure 5-13 (d). The crucial question is, is there anything that can be done about it?

The most obvious approach to take, is to try to fit for the CSF fraction in the voxel. The equation for the SL fit then becomes:

(5.8)

$$SL(TI) = \left| (1 - \text{fraction}_{CSF}) M_0 \left(1 - 2\alpha_0 \exp(-TI / T_{1app})\right) + \text{fraction}_{CSF} M_0 \left(1 - 2\alpha_0 \exp(-TI / T_{1CSF})\right) \right|$$

The fraction_{CSF} is the fraction of the M_0 *magnitude*, not a spin fraction — this would require taking the spin densities into account. This model was implemented as a 3-parameter model, fitting SL for T_{1app}, M_0 and the fraction of CSF — in short, the TMF model. The inversion efficiency was set as a constant at 0.99 — the measured inversion efficiency on a phantom. After the SL fitting, the simulated FAIR data were modelled using

the CBFD model and the parameters from the TMF model. Both the FAIR data as well as M_0 were scaled with (1-fraction$_{CSF}$) before the fitting. The results for T_{1app}, M_0, CSF fraction, CBF and inflow delay are given in Figure 5-14. The correct results, taking into account the CSF partial voluming, are depicted with the black dashed line.

In contrast with the results from the ITM model (fitting for α_0, T_{1app}, M_0; Figure 5-13) the fitted T_{1app} and M_0 parameters are now very accurate –with only tiny deviations from ideal–, without using any parameter constraints. The algorithm also finds the correct fraction of CSF, although it slightly overestimated it for small CSF fractions.

However, the CBF and delay values are still overestimated and, interestingly enough, are practically identical to the results of the ITM model (Figure 5-13 (d),(e)). This means, that even though the parameters α_0, T_{1app} and M_0 are not fitted correctly in the ITM model, their errors compensate each other in the final FAIR fit, as its CBF and delay results are the same as for the TMF model with correct α_0, T_{1app} and M_0 values. It is this self-compensation that will be disturbed by constrained fitting. So the issue of elevated inversion efficiency and T_{1app} values has been resolved by fitting for the CSF fraction; however, the problem of the overestimation of CBF and delay has not.

A great insight into the latter problem comes from looking at the simulated FAIR signal for a range of CSF fractions. As Figure 5-14 (f) demonstrates, for CSF fractions ≥ 25%, the FAIR signal becomes negative! A negative FAIR signal will be set to zero by the model, which means longer fitted delays and thus a higher CBF value. And indeed, the fitted delays in Figure 5-14 (e) match the TI values in Figure 5-14 (f) where dM becomes positive. For the 55% CSF fraction, this TI-value exceeds 1.5 s, which for the inflow delay falls under the fit exclusion criterion. And consequentially, the fitted delay is zero from that fraction onwards. In conclusion, there is a clear connection between the CSF fraction and the fitted CBF and delay values.

Another worthwhile observation is how CSF partial voluming leads to an underestimation of dM for the TI=3000ms point: every 5% CSF leads to a ~5% reduction of dM. This might have a bearing on the undershoot of the FAIR data with respect to the model reported in section 5.3.2.3.

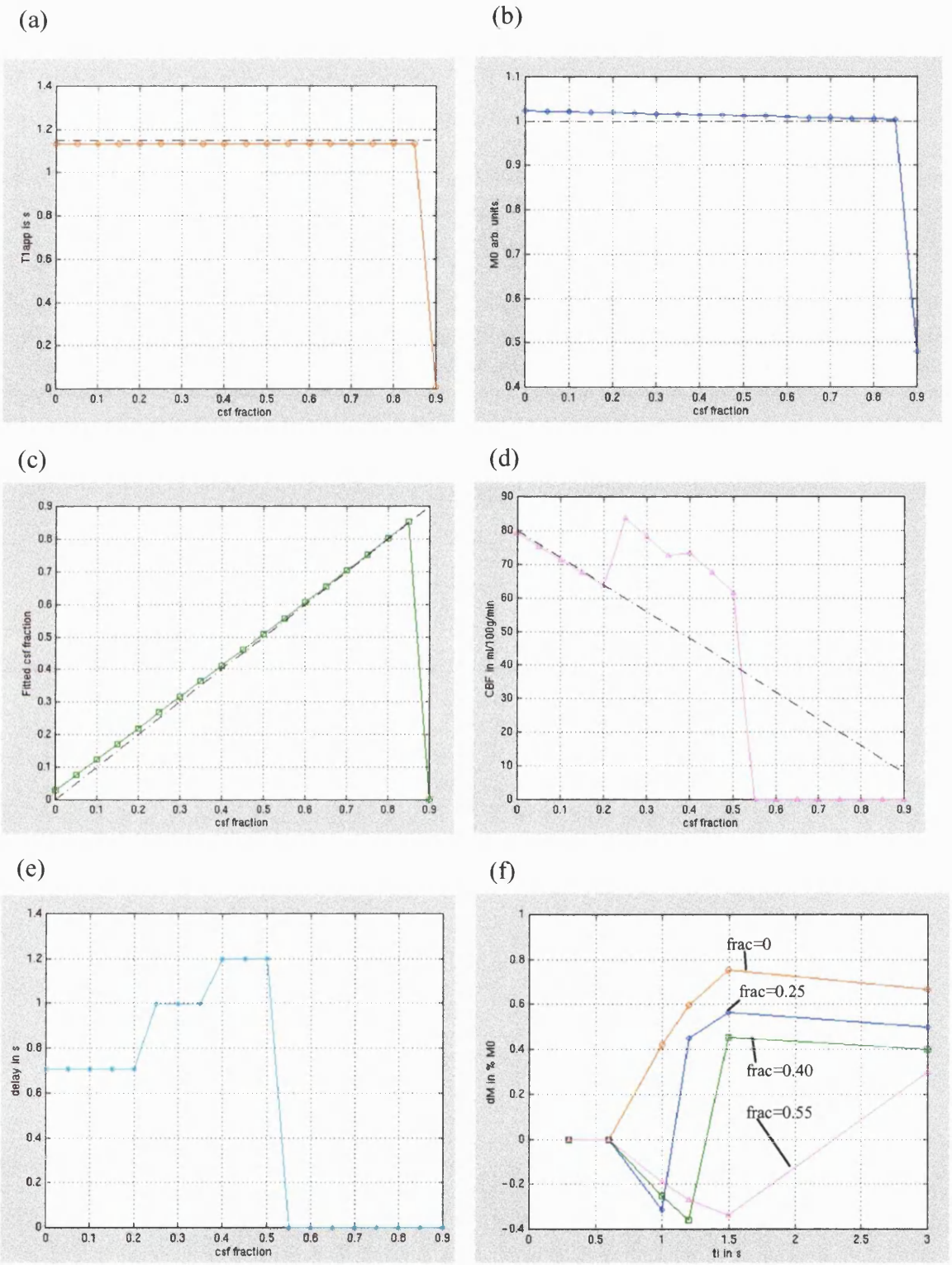

Figure 5-14 Partial voluming simulation, TMF model; results grey matter with progressive CBF partial voluming (α_0=0.99): (a) T_{1app}, (b) M_0, (c) fraction CSF, (d) CBF, (e) inflow delay, (f) FAIR signal for CBF=80 ml/100g/min and different CSF fractions.

The reason for negative FAIR data was already indicated in section 5.3.2.3: the magnitude subtraction. Ideally, the function $dM(TI)=M_z^{SL}(TI) - M_z^{GL}(TI)$ has to be measured. Since magnitude data are acquired, a different function dM'(TI) is observed:

$$dM'(TI) = \left|M_z^{SL}(TI)\right| - \left|M_z^{GL}(TI)\right| \quad (5.9)$$

There are 3 possibilities:

1) $M_z^{SL}(TI) > 0$ and $M_z^{GL}(TI) > 0$

In this case dM'(TI)=dM(TI).

2) $M_z^{SL}(TI) < 0$ and $M_z^{GL}(TI) < 0$

In this case dM'(TI)=- dM(TI).

3) $\text{sign}(M_z^{SL}(TI)) \neq \text{sign}(M_z^{GL}(TI))$

In this case the relationship between dM'(TI) and dM(TI) is unknown.

The problematic scenarios 2 and 3 are not expected to occur often for grey and white matter voxels. As explained before, the apparent relaxation times for SL and GL are almost identical. Thus, $M_z^{SL}(TI)$ and $M_z^{GL}(TI)$ have their zero-crossings at approximately the same TI and scenario 3 hardly occurs. Scenario 2 leads to the negative FAIR signal and aforementioned incorrect fitting. However, as pointed out before, $T_{1app} \approx 0.7\text{-}1.2$ s and the zero crossing will therefore be at ~0.5-0.8 s, which is in the range of the expected inflow delay for which dM(TI) is zero anyway.

In the case of CSF partial voluming, however, T_{1app} is increased considerably due to the contribution of T_{1CSF} (~5 s). The inversion recovery zero-crossing will shift to high TI values due to the contribution of the slowly recovering CSF signal (Figure 5-15 (b)). Now for a large range of inversion times TI up to the new zero-crossing, scenario 2 applies: dM'(TI)=-dM(TI) and dM'(TI) < 0, the negative FAIR signal (Figure 5-15 (c)).

CSF itself does not contribute to CBF in this simulation model and should therefore not contribute to the FAIR signal. However, it is the *interaction* of magnitude subtraction, non-zero CBF and partial voluming of CSF that results in this effect. When CBF is zero, SL and GL are the same (equation (5.7)), and the difference signal dM will be zero. If CBF

is non-zero, there is a difference between the SL_{grey} and GL_{grey}, while SL_{CSF} and GL_{CSF} are still equal. The FAIR signal for a voxel is the difference of the *total* SL and GL components which are the sums of SL_{grey}+ SL_{CSF} and GL_{grey} + GL_{CSF}, respectively. The presence of CSF signal will delay the $M^{SL}(TI)$ and $M^{GL}(TI)$ zero-crossings and lead to negative FAIR signal for a large range of TI values in a magnitude subtraction (scenario 2): dM'(TI)=-dM(TI)). Figure 5-15 (a) shows for a grey matter voxel with a CBF of 80 ml/100g/min and an inflow delay of 0.7 s how, in the absence of CSF partial voluming, there is no difference between dM'(TI) and dM(TI) and all FAIR signal is positive. Figure 5-15 (c) shows dM'(TI) and dM(TI) for the same grey matter voxel, but now with 25% CSF partial voluming: now dM'(TI) and dM(TI) are not the same and the erroneous negative FAIR signal appears.

So it is the combination of magnitude subtraction, non-zero CBF and CSF partial voluming that leads to negative FAIR signal at long inversion times, which in turn leads to elevated fitted CBF and delay values. This interaction is also a likely answer to the mystery of the inversion recovery-like focal medial frontal signal in the raw FAIR images of Figure 5-6: partial voluming of a vessel and CSF can explain the high focal signal that occurs even at the long inversion times.

The solution to the problem of this erroneous negative FAIR signal is taking the magnitude of the FAIR data before fitting. By doing this, the correct difference between SL and GL will be obtained irrespective if $M_z^{SL}(TI)$ and $M_z^{GL}(TI)$ are both positive or both negative (the aforementioned scenarios 1 and 2). Thus the effects of CSF partial voluming on the sign of the FAIR data are undone, as significant CSF partial voluming leads to both $M_z^{SL}(TI)$ and $M_z^{GL}(TI)$ being negative (scenario 2).

This method does not work if $M_z^{SL}(TI)$ and $M_z^{GL}(TI)$ have different signs (scenario 3), but this scenario will not occur often, as T_{1app} and T_1 and thus the zero-crossings for $M_z^{SL}(TI)$ and $M_z^{GL}(TI)$ are very similar.

The CBF and delay results as percentage of their correct values (resp. $fraction_{grey}$ · 80ml/100g/min, 0.7 s) for fitting the magnitude and non-magnitude FAIR data using the parameters from the TMF and ITM models are given in Figure 5-15 (d) and (e).

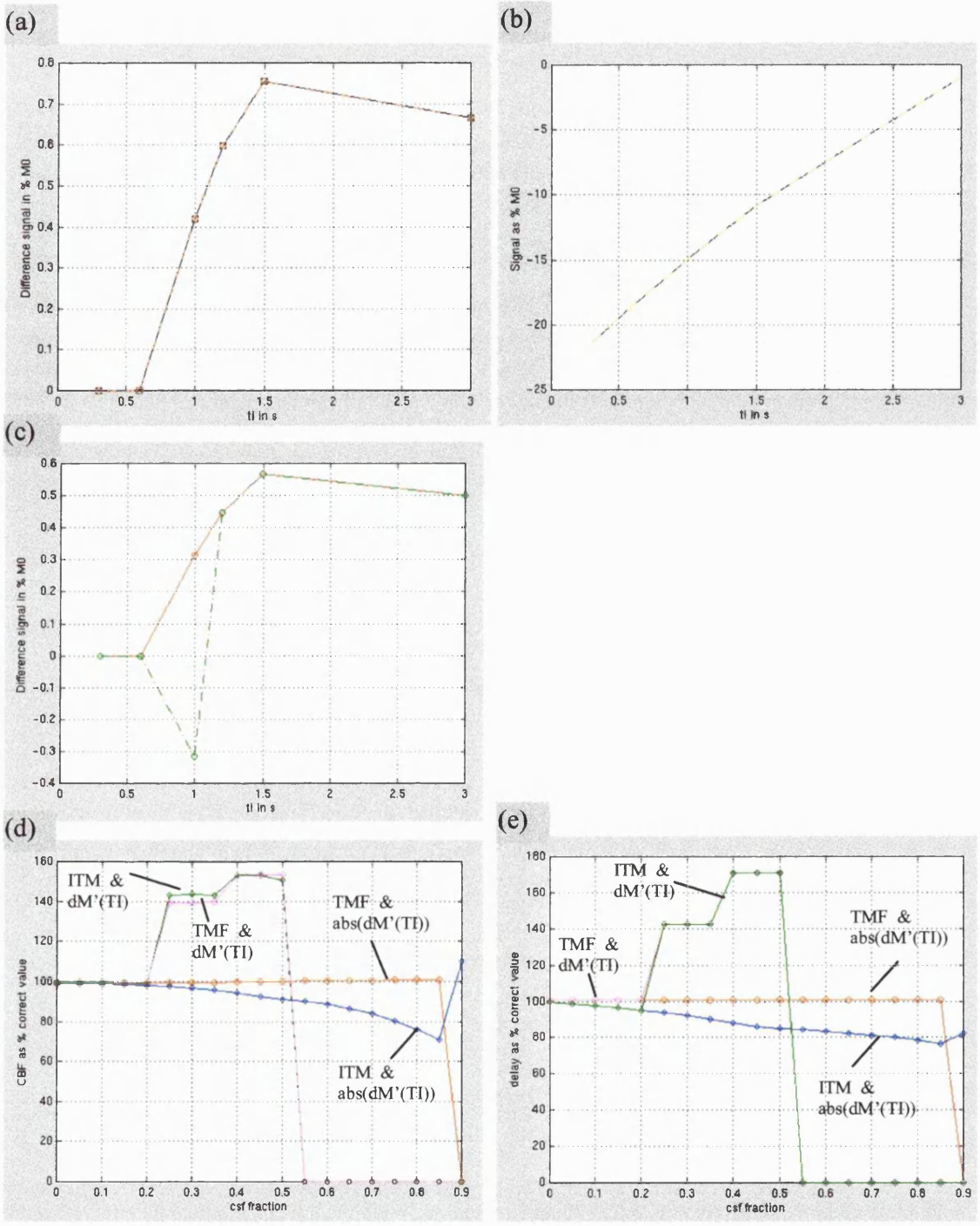

Figure 5-15 Explaining negative FAIR signal due to CSF partial voluming; evaluation of improved fitting models. For a grey matter voxel with a CBF of 80 ml/100g/min and an inflow delay of 0.7 s with/without CSF partial voluming. (a) No CSF: dM(TI) (black squares) overlaid on dM'(TI) (red circles). (b) Inversion recovery signal for CSF: $M_z^{SL}(TI)$ (yellow striped) and $M_z^{GL}(TI)$ (black striped) for a CSF fraction of 25% of M_0. (c) For a 25% CSF fraction: dM'(TI) for sum of grey matter and CSF fractions (green circles) overlaid on dM'(TI) for the grey matter fraction only (red circles). (d) CBF and (e) inflow delay as percentage of the correct value for TMF and ITM models, when fitting dM'(TI) and abs(dM'(TI)).

The TMF model combined with the magnitude FAIR data is the best model, with the correct CBF and delay values found all the way up to 90% CSF partial voluming. The ITM model (which does not take the CSF fraction into account), still does well when the magnitude FAIR data are fitted, underestimating the delay by ~10% and the CBF by ~15% for a 50% CSF fraction. This robustness with respect to CSF partial voluming is due to the aforementioned error self-compensation in the α_0, T_{1app}, M_0 parameters. The results for non-magnitude FAIR data are given as a reference. Taking the magnitude of the FAIR data thus results in a large improvement in accuracy for both models, with the TMF model being the most accurate. The only assumption that is made by this magnitude approach is that there are no other processes resulting in a negative FAIR signal. For the simulation, this is correct. For experimental data, this can not easily be established. The static subtraction error might well lead to negative FAIR signal. This issue will be discussed further in section 5.4.3. The final decision on the model to use for *in vivo* experimental data considering partial voluming and other issues will be made in the model selection section 5.4.4.

Partial voluming of CSF and white matter is a lot less likely to occur. The results for simulations of partial voluming of CSF and white matter are very similar to the above and will not be discussed further.

5.4.1.2 Grey and white matter partial voluming

As the T_1 values of grey and white matter are very similar, it is not feasible to fit for the grey and white matter fractions. What is useful, is to assess how well the fit algorithms can handle grey/white matter partial voluming: what happens to the fitted CBF and delay, and how is the fitted T_{1app} affected? The latter is interesting, as T_1 masks are used to select the voxels to include in masks for grey matter and white matter CBF.

The simulations were run again with white matter included for the ITM and TMF models, fitting the abs(FAIR) data with the CBFD model as described before. For the white matter the following parameters were used:

white matter T_1	0.70 s
white matter CBF	30 ml/100g/min
white matter inflow delay	0.7 s; 1.2 s

Table 5-5 Simulation parameters for white matter.

Two values for the inflow delay were used, one equal to the inflow delay of grey matter and one equal to the longest inflow delay value suggested for white matter in the literature (Ye et al., 1996). The results for inversion efficiency (ITM model only), T_{1app}, CBF and inflow delay are given in Figure 5-16.

For α_0 and T_{1app} the results are independent of white matter inflow delays, as the delay is not part of the fit model for the SL data. Both ITM and TMF models do reasonably well in finding the correct CBF values, they overestimate CBF slightly by ~10%. The white matter fraction will be unknown *in vivo*, so it will not be possible to derive pure white and grey matter CBF values from data with significant grey/white matter partial voluming. However, the absolute amount of blood delivered to these grey/white matter voxels as found by the fitting algorithms will be overestimated by only ~10%. This means that both models are quite robust in dealing with voxels that consist of 2 or 3 T_1 species, even though these T_1 species are not all included in the model — the ITM model only fits for one T_1 species, the TMF model assumes two.

The inflow delay is also fitted well by both models, it is only for CSF fractions $\geq$ 50% that the ITM model can underestimate inflow delay by up to 20%. The TMF model results only deviate very slightly ($\leq$ 10%) from ideal. It is interesting to note how the TMF inflow delay results for the CSF fractions 0%, 25% and 50% overlap. For this TMF model, the effect of grey/white matter partial voluming on inflow delay is therefore independent of CSF fraction.

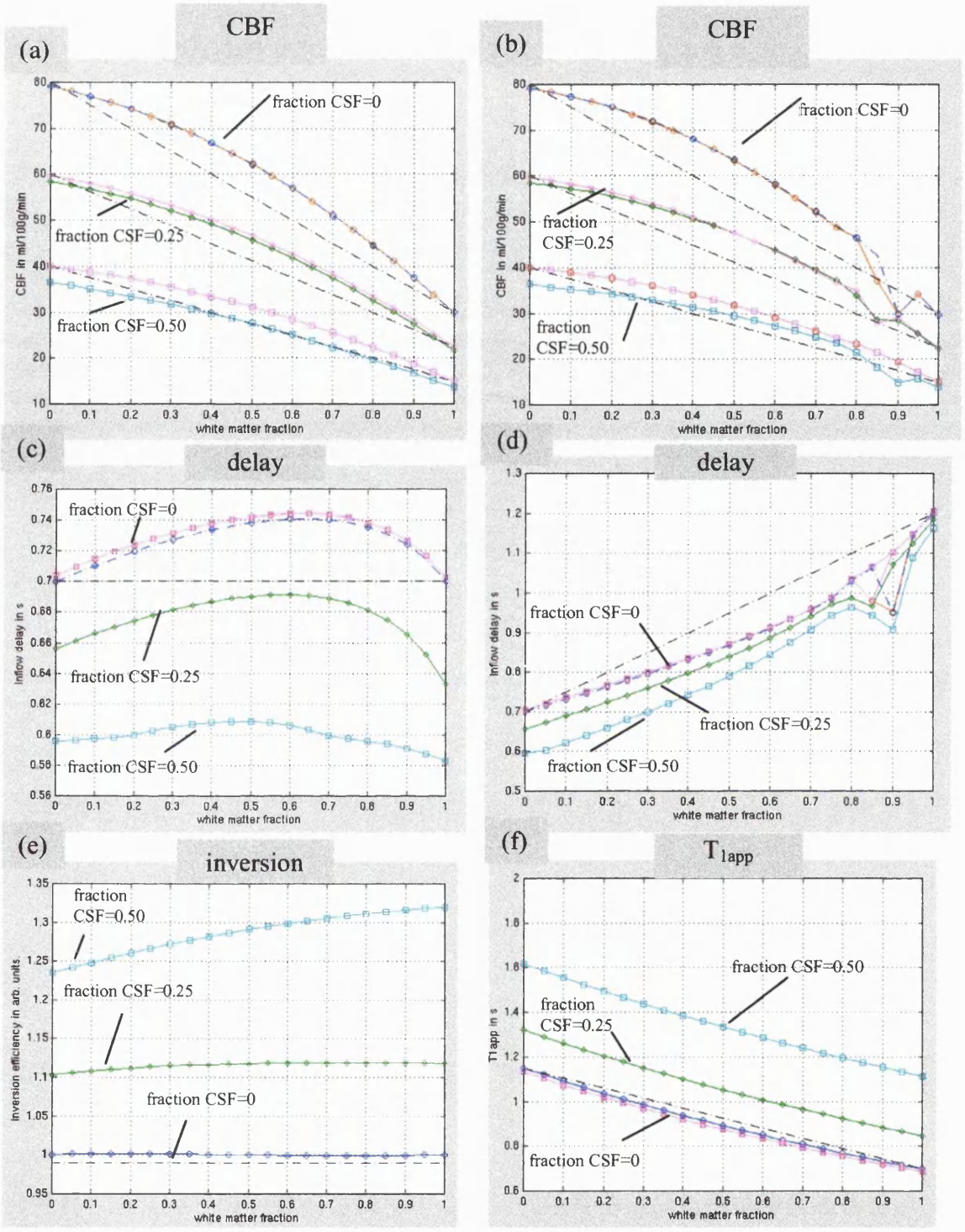

Figure 5-16 Grey/white matter partial voluming. Fitted parameter values for increasing white matter fraction and for different CSF fractions. Fraction CSF=0: ITM(blue), TMF (red); fraction CSF=0.25: ITM (green), TMF(magenta); fraction CSF=0.50: ITM(cyan),TMF(magenta). Correct values in dashed black lines. (a) Fitted CBF, delay of white matter is 0.7 s. (b) Fitted CBF, delay of white matter is 1.2 s. (c) Fitted inflow delay, (input) delay of white matter is 0.7 s* (d) Fitted inflow delay, (input) inflow delay white matter is 1.2 s * (e) Fitted α_0 – not fitted in TMF model (f) Fitted T_{1app}, linear relation between grey and white matter dotted.*

* the results for the 3 TMF fits overlap (magenta line), i.e. are independent of CSF fraction.

When looking at the results for the SL fit, the inversion efficiency —only fitted for in the ITM model— is sensitive to CSF fraction as demonstrated before. The added factor of grey/white matter partial voluming has a much smaller effect. The fitted T_{1app} values very nearly follow a linear relation from grey to white matter (even though, in fact, the grey and white matter each relax exponentially with their own T_{1app}). For the TMF model the results again overlap and are well described by a simple straight line between the T_{1app} of grey and white matter. The CSF fraction, again, has no influence on the results for the TMF model. The T_{1app} results for the ITM model are similar, but progressively shifted upwards under the influence of CSF partial voluming.

In conclusion, on the basis of these partial voluming simulations, the TMF model seems best in giving the most accurate results for CBF, inflow delay and T_{1app} under the circumstances of grey/white matter and CSF partial voluming. Deviations for CBF and inflow delay from the correct values are of the order ~10%. Irrespective of the CSF fraction, the T_{1app} changes from grey to white values almost linearly with white matter fraction. These simulated T_{1app} values can be used as a reference to choose the most optimal T_1 mask for grey and white matter masks. Of course the natural variability of grey matter and white matter T_1 *in vivo* has to be taken into account for this as well.

5.4.2 Macrovascular contributions: flow spoiling

In this basic CBF quantification experiment a b-value of 1.6 s/mm^2 was used. The bright dots in the raw FAIR data (Figure 5-6) and the resulting fitted CBF values > 200 ml/100g/min suggest this flow spoiling was not high enough to spoil the contributions of large vessels.

To explore the effect of flow spoiling on the FAIR data, an additional experiment was run on a human volunteer at one inversion point, TI=1200 ms, for b-values 0.6, 3, 5, and 10 s/mm^2. The magnitude FAIR data are depicted in Figure 5-17 (a), the mean +/- se of the FAIR signal over the slice is plotted for each b-value in Figure 5-17 (b). Voxels at noise level were excluded from this analysis. The effect of increasing flow spoiling is clear in the FAIR data: the bright spots fade and the global FAIR signal decreases. This is more clear in

the plot of the slice mean +/- standard error: starting at a b-value at 0.6 s/mm^2, the mean and standard error of the FAIR signal rapidly decrease to plateau for a b-value > 5 s/mm^2 at a signal ~ 65% of the signal without spoiling (value estimated through extrapolation). This is a slightly smaller signal reduction than the 50% reduction that Ye and colleagues report in their study for b-values 0-5 s/mm^2, however, they look at a grey matter ROI, while this study looks at all voxels above noise level.

Increasing the b-value therefore does seem advisable, as this experiment has shown that there is plenty of signal to spoil. The signal that is spoiled by crusher gradients is fast flow in larger vascular structures and not perfusion, which is slow. The next question is how far to increase the b-value. It is not necessarily the case that the higher the b-value the better; higher b-values make the pulse sequence more susceptible to movement artefacts and can increase the static subtraction error. Taking the latter considerations into account, the lowest b-value for which the FAIR signal starts to plateau (b=5 s/mm^2) was taken as the flow spoiling to apply in future studies. This b-value is also commonly used by other researchers in this field (Ye et al, 1997; Yang et al., 1998; Yongbi et al., 1999; Pell et al., 1999). Flow spoiling with a sufficiently large b-value is expected to lead to longer inflow delays, as it takes longer for the blood to reach the smaller vascular structures from which the signal is not spoilt.

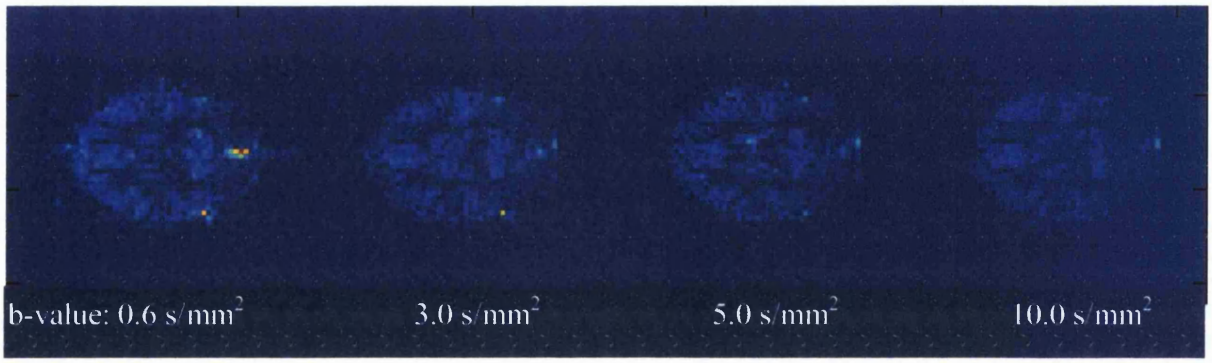

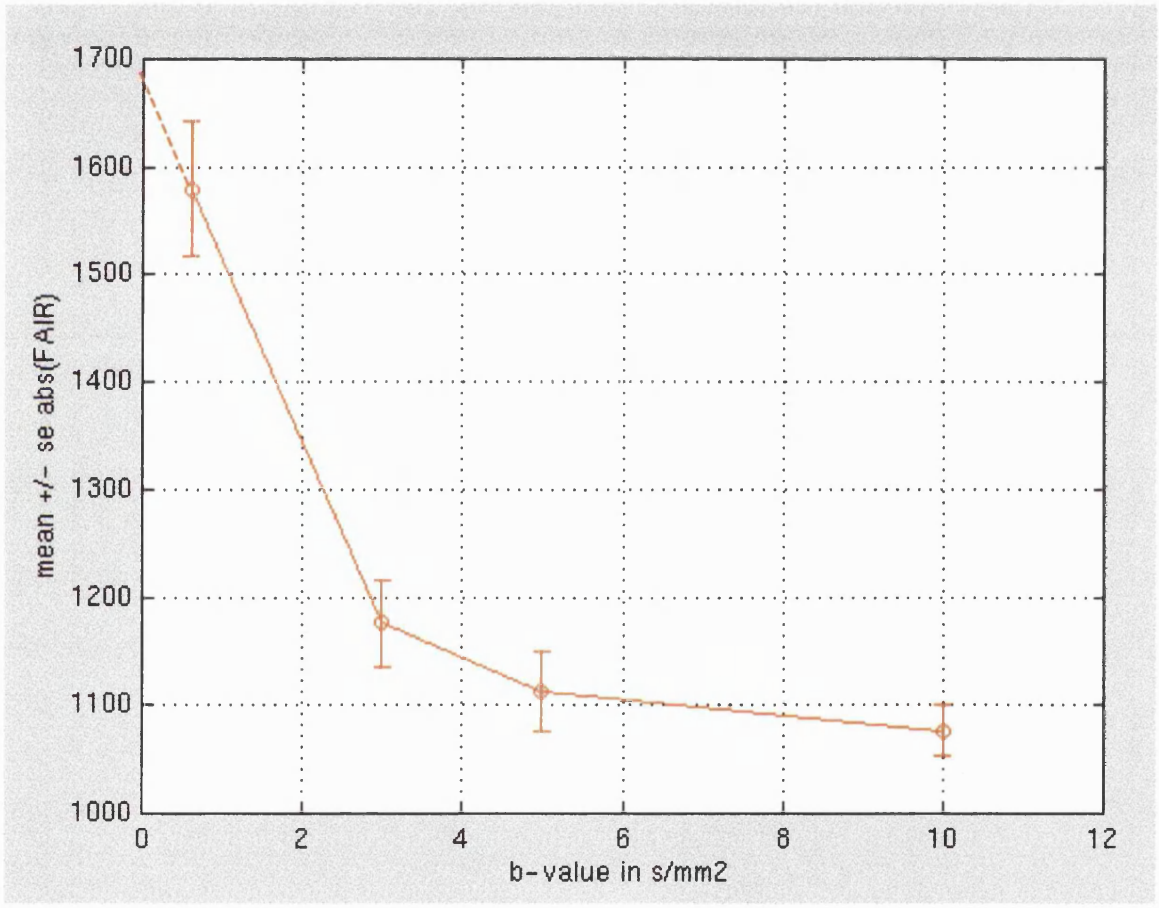

Figure 5-17 FAIR at TI=1200ms for a range of b-values. (a) Magnitude FAIR data. (b) Mean +/- se FAIR signal over slice (voxels at noise level not included).

5.4.3 The static subtraction error

As shown in section 5.2, the static subtraction error (SSE) as percentage of M_0 is very small, with an upper limit of ~0.03%. However, the expected *in vivo* FAIR signal for grey matter is very small too, ~1% of M_0. The upper limit of the static subtraction error is thus ~ 3% of the expected FAIR signal for grey matter in humans. For white matter the maximum FAIR signal is ~0.25% of M_0, so the SSE is ~12% of the white matter FAIR signal. The SSE is therefore expected to influence white matter results more.

The simulations described in the partial voluming section (5.4.1) were performed again, this time fitting the magnitude of the sum of the FAIR data and this static subtraction error. The FAIR fits were performed using the ITM as well as the TMF model parameters. The SSE does not influence the SL data and therefore the SL fits themselves were not repeated. The partial voluming scenarios most likely to be of interest for *in vivo* studies are grey matter/CSF voxels for CSF fractions < 50% and grey/white matter partial voluming all across the range of white matter fractions. The results for voxels with varying degrees of grey matter/CSF and grey/white matter partial voluming are depicted in Figure 5-18.

Starting with the TMF model, for a grey matter/CSF voxel the effect of the SSE is a progressive overestimation of the CBF and delay with increasing CSF fraction: for a 50% CSF fraction both CBF and delay are overestimated by ~7%. The effect of the SSE in the case of grey/white matter partial voluming without CSF is an overestimation of the CBF by up to 14% and of the delay by ~3%. These results also hold for a grey/white matter voxel with a 25% CSF fraction (data not shown). For a 50% CSF fraction and grey/white matter partial voluming CBF and delay are overestimated progressively with white matter fraction. The upper limit is reached for a 50%/50% white matter- CSF voxel for which the SSE will lead to an overestimation of CBF by ~30% and of delay by ~20% (data not shown). Such a voxel is not very likely to occur *in vivo*, apart from the edges of the corpus callosum and the ventricles. For the most likely partial voluming scenarios — predominantly two compartments, either grey matter/CSF of grey/white matter — the upper limit for the overestimation of CBF is therefore 14%, for the delay 7%.

The ITM model, interestingly, self-compensates its errors to a certain degree in this situation. The underestimation due to other errors in the model compensates partially for the overestimation due to the static subtraction error. For the grey matter/CSF voxels CBF is underestimated by up to ~4% for CSF fractions < 50% — without the SSE this underestimation is ~9%. The delay, normally underestimated by ~15%, is underestimated by only ~9% with the SSE. For the grey/white matter partial voluming the CBF results are the same as for the TMF model, an overestimation up to 14 %. The delay deviated from ideal by +/- 2% (without the SSE the delay is overestimated by up to 6%). For a 25% CSF fraction with grey matter/white matter partial voluming, the upper limit in CBF overestimation is the same, however, the inflow delay will be progressively underestimated with white matter fraction by up to 12% (data not shown). For a CSF fraction of 50% and grey/white matter voluming, the deviations of CBF and delay from ideal that occur are normally compensated partially by the SSE: CBF is overestimated by maximally 15% and delay underestimated by up to 10% for the delay. The upper limits for the most relevant situations — CSF /grey matter and white/grey matter partial voluming with up to 25% CSF — are thus an overestimation of CBF by up to 14% and an underestimation of delay by 12%. The ITM and TMF models therefore give very similar results under conditions of this static subtraction error.

The simulations thus give a good indication of the effect of this static subtraction error on the results for CBF and inflow delay. The crucial question: is it reasonable to assume that the static subtraction error will be the same for the human brain as for the gel phantom? Yongbi and colleagues have measured the static subtraction error both in a gel phantom and in humans using Gd-DTPA (Yongbi et al., 2000). Using FOCI pulses, they showed that for inversion to readout slice thickness ratios > 2, the static subtraction error is the same *in vivo* as in the gel phantom. For a slice thickness ratio > 2.4, Yongbi et al. have also shown that the HS and FOCI pulses have the same static subtraction error on a phantom (Yongbi et al., 1999). The latter is in accordance with the predictions made on the basis of HS and FOCI pulse simulations in Chapter 4 of this thesis.

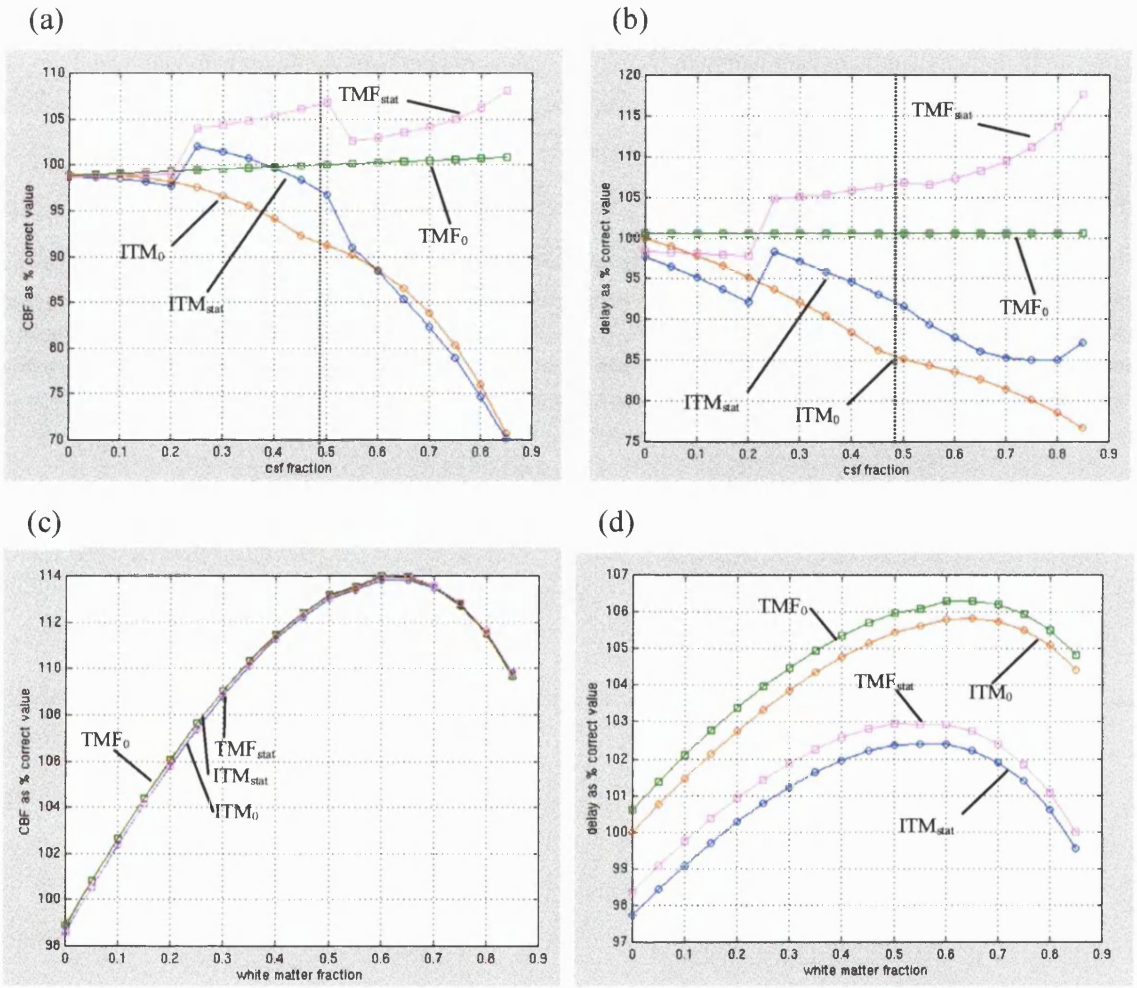

Figure 5-18 Simulations of the effect of the static subtraction error (SSE) on CBF and delay values for partial volumed data. TMF_0/TMF_{stat}: FAIR data without/with SSE, fitted with TMF model parameters. ITM_0/ITM_{stat}: FAIR data without/with SSE, fitted with ITM model parameters. (a) CBF as percentage correct value for grey matter/CSF partial voluming. (b) delay as percentage correct value for grey matter/CSF partial voluming (c) CBF as percentage correct value for white/grey matter partial voluming, fraction CSF is 0. (d) delay as percentage correct value for white/grey matter partial voluming, fraction CSF is 0.

Considering that the implemented FAIR technique described in this thesis uses an inversion to readout slice thickness ratio of 3:1, it indeed seems a reasonable hypothesis that the standard subtraction error in human brain will not be significantly different from the one measured in the gel phantom. This means that the simulation results using the phantom's static subtraction error also hold for the *in vivo* studies described in this thesis. On the basis of these simulations the upper limit of the overestimation in CBF and delay due to the static subtraction error *in vivo* is therefore predicted to be 14% and 7% (TMF model).

For experimental data the effect of the SSE is unlikely to depend strongly on the position of the voxel in the image, as its main cause are small differences in the inversion efficiency for SL and GL, that effect only the slice selective direction. However, its effects will depend on the voxel being predominantly white or grey matter: the CBF of white matter is likely to be overestimated more than that of grey matter due to white matter's intrinsic low SNR. This will result in a lowering of the grey/white matter CBF ratio. A careful selection of 'pure' grey and white matter voxels will minimise this effect.

5.4.4 Model selection

The simulations regarding the effects of partial voluming have lead to the proposal of two changes in the modelling of SL and FAIR data:

1) To fit for CSF fraction in the SL fit, while fixing the inversion efficiency — the TMF model.

2) To use the magnitude FAIR data to avoid the erroneous negative FAIR signal. This negative signal is a by-product of the magnitude subtraction of SL and GL data, an effect exacerbated by CSF partial voluming.

This section compares the results for the standard ITM model with the TMF model for experimental data. Furthermore, a formal model selection between the CBFD and CBFO model will be described.

5.4.4.1 Model selection for slice selective inversion data

The analysis of experimental data using the ITM model has been described in section 5.3. Next, the TMF model was implemented. For every voxel, one randomly selected average (of the 44) was used to fit for α_0, T_{1app} and M_0 using the ITM model. The mean α_0 value in the white matter (as defined by the white matter mask defined in section 5.3.2.4) was used as the value for the fixed α_0 in the TMF fit. This should be a reasonably accurate value, as chances of CSF partial voluming are slim in white matter and grey/white matter partial voluming on its own has very little influence on the fitted α_0 values, as derived in section 5.4.1.2. The mean SL data of the other averages were fitted for T_{1app}, M_0 and CSF fraction following:

$$SL(TI) = \left| (1-\text{fraction}) M_0 \left(1 + \left[(1-\exp(-\frac{\tau}{T_{1app}}))(1-2\alpha_0) - 1 \right] \exp(-\frac{TI}{T_{1app}}) \right) \right. \\ \left. + \text{fraction} \cdot M_0 \left(1 + \left[(1-\exp(-\frac{\tau}{T_{1CSF}}))(1-2\alpha_0) - 1 \right] \exp(-\frac{TI}{T_{1CSF}}) \right) \right| \quad (5.10)$$

fraction is the CSF fraction in the voxel.

Start values for T_{1app} and M_0 were as for the ITM model, the start CSF fraction was set to 0.20. The fitting algorithm was unconstrained, but for voxels for which the fit resulted in non-sensical negative CSF fractions, the fit was performed again with a reduced model of T_{1app} and M_0 only, with the CSF fraction set to zero. These voxels (9% of total) were automatically labelled as 'refitted', to allow the assignment of the correct number of degrees of freedom in the goodness-of-fit test. The results of the fit are displayed in Figure 5-19.

In accordance with the predictions from the CSF partial voluming simulation (Figure 5-13) the T_{1app} is lowered for the TMF model compared to the ITM model: the mean T_{1app} values in the T_1 mask defined in section 5.3.2.3, decrease from 1.14 s to 1.03 s for the TMF model. The M_0 is increased by 19% on average, supporting the predictions from the simulations that M_0 is underestimated for the ITM model in regions with significant CSF partial voluming. The TMF model assigns significant CSF fractions to the

expected places (between the hemispheres and around the edges of the brain), but also inside the brain CSF fractions of ~10-30% are found. This means that the CSF fraction fitting is also susceptible to noise.

The results for the goodness-of-fit test for the TMF and ITM models are summarised in Table 5-6. The improvement in the goodness-of-fit for the TMF model for all voxels is significant, the percentage of voxels that pass the test has increased by 40% of the original value.

The grey and white matter masks defined in section 5.3.2.4 were used to look at grey and white matter masks separately: 18% of grey matter voxels passed the threshold for the TMF model, compared to 9% for the ITM model. For the voxels in the white matter mask this was 0% and 7% respectively for the TMF and ITM models. So the TMF model is a clear improvement for the grey matter, but not so for the white matter. This is understandable, as the CSF partial voluming included in the TMF model is not expected to take place in white matter and the TMF model does not fit for α_0. However, this inversion efficiency should not vary over the slice, as it applies to the inversion by the rf pulse which is along the slice selective direction, perpendicular to the slice; if α_0 varies significantly over the slice it acts more as a 'fudge factor' for bad fits than fitting a physical reality.

SL fit	mask all voxels (416 voxels)	grey matter mask (160 voxels)	white matter mask (29 voxels)
TMF model	21%	18%	0%
ITM model	15%	9%	7%

Table 5-6 Results Goodness-of-fit test TMF vs ITM models for SL fit : percentage voxels in mask with $Q > 0.001$

The standard deviations on the fit parameters calculated for all converging voxels using the repeated measures method for both fit models are given in Table 5-7. The calculated standard deviations on the fit parameters (as mean percentage error per voxel) are very similar for M_0. For T_{1app} they are larger, but then again, the average T_{1app} value in the TMF fit is lower, so a higher relative error is expected. The standard deviation on the fraction CSF is an order of a magnitude larger than on the other TMF parameters; this can be understood by appreciating the difficulty of separating a double exponential inversion recovery curve into two separate exponentials.

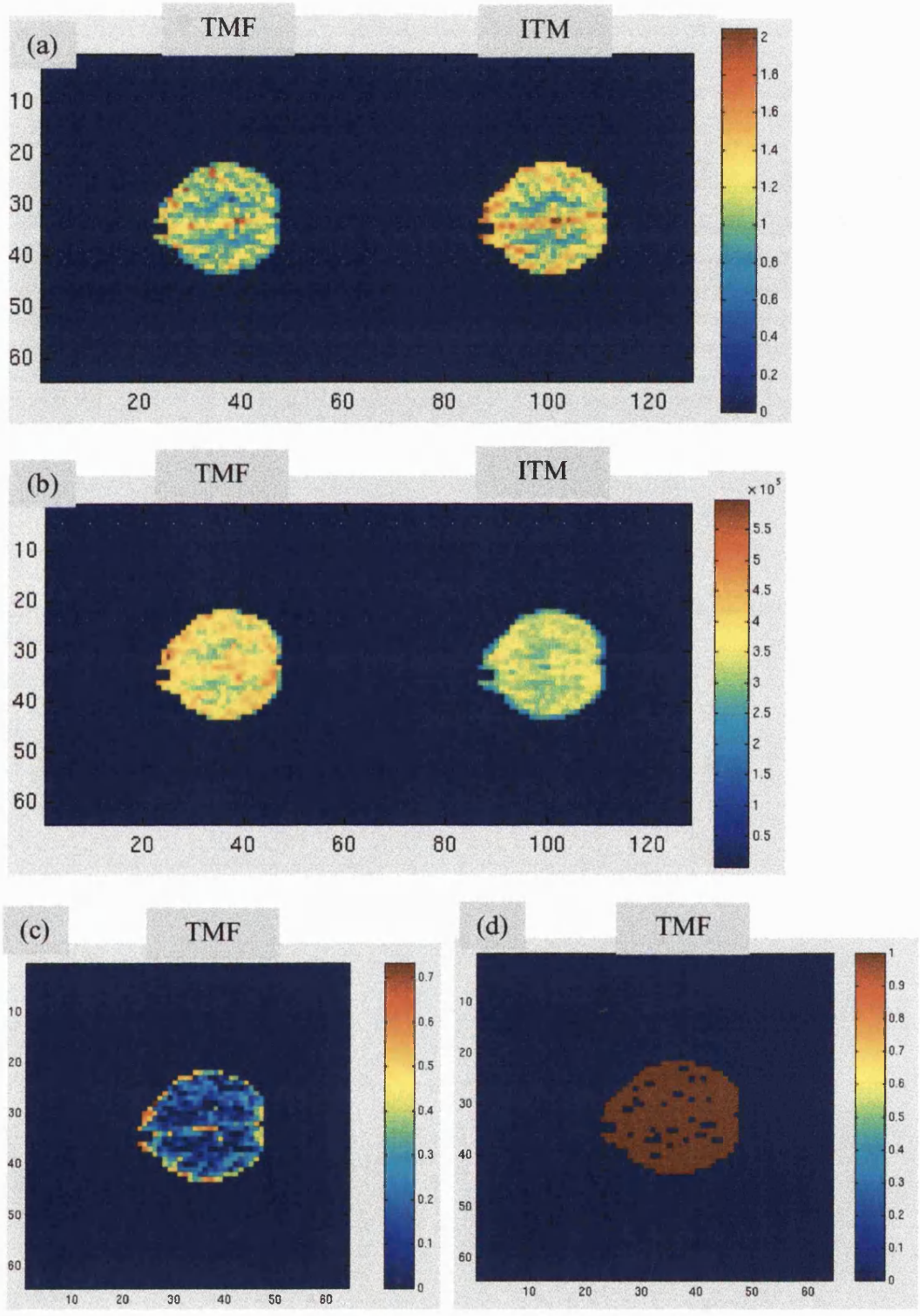

Figure 5-19 Fit results for TMF (left) and ITM models (right). (a) T_{1app} values in s. (b) M_0 values in arb. units. For TMF model only: (c) fitted CSF fraction (d) Voxels that were refitted for T_{1app} and M_0 only (blue); nulled for display reasons within the brain mask (red).

	α_0	T_{1app}	M_0	$frac_{CSF}$
TMF model	----	1.2%	0.5%	7.5%
ITM model	0.1%	0.2%	0.2%	----

Table 5-7 Comparing the mean sd as percentage mean value voxel for TMF and ITM models

Next the ITM and TMF model parameters were inserted into the formula for the FAIR fit —not taking the magnitude of the FAIR data — and the FAIR fits were run using the CBFD model. The results for the goodness-of-fit tests are given in Table 5-8. For the 'all voxels' mask a new mask was constructed which was the product of the masks of voxels converging in the fit; this is to assure the same voxel populations are compared for the two models and that all voxels included in the mask have actually given a converged fit result. The results are very similar for both models.

FAIR fit	mask all voxels (393 voxels)	grey matter mask (160 voxels)	white matter mask (29 voxels)
TMF model	39%	34%	93%
ITM model	35%	32%	90%

Table 5-8 Results goodness-of-fit test TMF vs ITM models in FAIR fit: % voxels in mask with $Q > 0.001$. Fitting of the magnitude FAIR data is evaluated in the next section.

Table 5-9 lists the mean +/- sd CBF, delay and CBF ratio values for the CBFD model fits using the ITM and TMF models. The results are very similar for both models.

	mask all voxels (393 voxels)	grey matter mask (160 voxels)	white matter mask (29 voxels)	ratio CBF grey/ white
CBF +/- sd in ml/100g/min TMF model	74.54 +/- 26.41	78.09 +/- 18.81	32.33 +/- 13.47	2.42 +/- 0.19
delay +/- sd in s TMF model	0.71 +/- 0.22	0.63 +/- 0.11	0.58 +/- 0.28	----
CBF +/- sd in ml/100g/min ITM model	74.90 +/- 26.06	78.92 +/- 18.43	31.53 +/- 13.02	2.50 +/- 0.20
delay +/- sd in s ITM model	0.70 +/- 0.22	0.62 +/- 0.10	0.57 +/- 0.26	----

Table 5-9 CBF, delay and CBF ratios for fitted FAIR data with TMF and ITM parameters. Fitting of the magnitude FAIR data is evaluated in the next section.

So which model to use for the SL fit? On the basis of the simulations, the TMF model is predicted to give physically correct parameter values for the SL fit, while the ITM is not, even though its errors largely self-compensate in the FAIR fit up until a 50% CSF fraction (for magnitude FAIR data). When applying both models to experimental data, findings from the simulations are replicated: in areas with expected CSF partial voluming the T_{1app} values are lower and the M_0 values are higher for the TMF model. As this is exactly what the simulations predicted to happen once the distorting effect of CSF partial voluming was taken into account, it is a reasonable assumption that the other predictions from the simulation are true: that the TMF model will result in more accurate SL parameter values than the ITM model. This is important when defining T_1 masks. Another strength of the TMF model is that it gives the CSF fraction, which will allow making the distinction between a lowered perfusion and CSF partial voluming in grey matter areas.

The goodness-of-fit results for SL and FAIR fits are better for the former and comparable for the latter when using the TMF fit model. The fact that the percentage voxels passing the goodness-of-fit test does not increase more for the TMF model signifies that the number of voxels with significant CSF partial voluming is limited, as one would expect, and means that other factors such as grey/white matter partial voluming or the volunteer motion dominate the goodness-of-fit results. Still, the TMF model is an improvement on the ITM model because it gives more accurate and relevant SL fit parameters and a comparable or better goodness-of-fit. Therefore, the TMF model will be used from now on in this thesis.

5.4.4.2 Model selection for FAIR data

In this section two FAIR modelling questions will be addressed:

1) What happens if the magnitude FAIR data are fitted as opposed to the normal subtraction data?

2) Is it really necessary to fit for the inflow delay? A formal model selection between the CBFO and CBFD model will be conducted.

The effect of fitting magnitude FAIR data was evaluated first. The magnitude FAIR data for a range of inversion times are given in Figure 5-20. The results of this fit compared with fitting the normal ('non-magnitude') FAIR data are depicted in Figure 5-21. The goodness-of-fit results for all converging voxels, and the grey and white matter masks are given in Table 5-10.

FAIR fit	mask all voxels (355 voxels)	grey matter mask (151 voxels)	white matter mask (24 voxels)
magnitude FAIR TMF model inputs	80%	74%	96%
Non-magnitude FAIR TMF model inputs	41%	38%	96%

Table 5-10 Results goodness-of-fit test magnitude vs non-magnitude FAIR fitting, using parameters from the TMF model: percentage voxels in mask with $Q > 0.001$

As before, the mask with all voxels is comprised out of all voxels that gave converging fit results for both fits that are compared here. The standard grey and white matter masks that were used before were corrected to exclude non-converging voxels. The goodness-of-fit is strongly improved when fitting magnitude data: the number of voxels passing the $Q > 0.001$ threshold is doubled. The goodness-of-fit therefore gives a clear answer that the magnitude FAIR model is appropriate and superior to non-magnitude fitting.

The mean standard deviations of the fit parameters as percentage of each voxel's mean is given in Table 5-11. The magnitude FAIR fitting leads to an increase in the relative errorbars.

mean sd as % mean	magnitude FAIR	non-magnitude FAIR
sd on CBF	14%	8%
sd on delay	16%	5%

Table 5-11 Comparing the relative errorbars -mean sd as percentage mean value voxel- for magnitude and non-magnitude FAIR fitting of experimental data, with TMF model inputs.

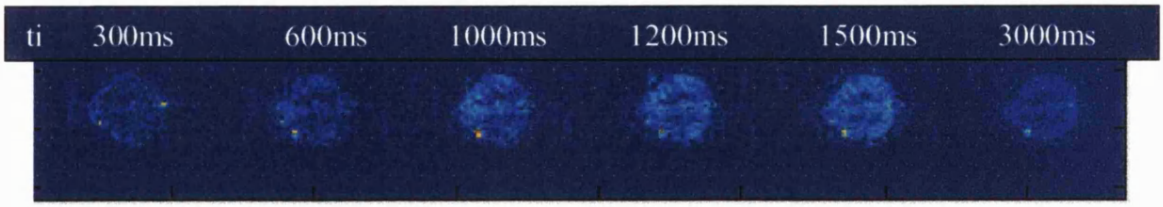

Figure 5-20 Magnitude FAIR data.

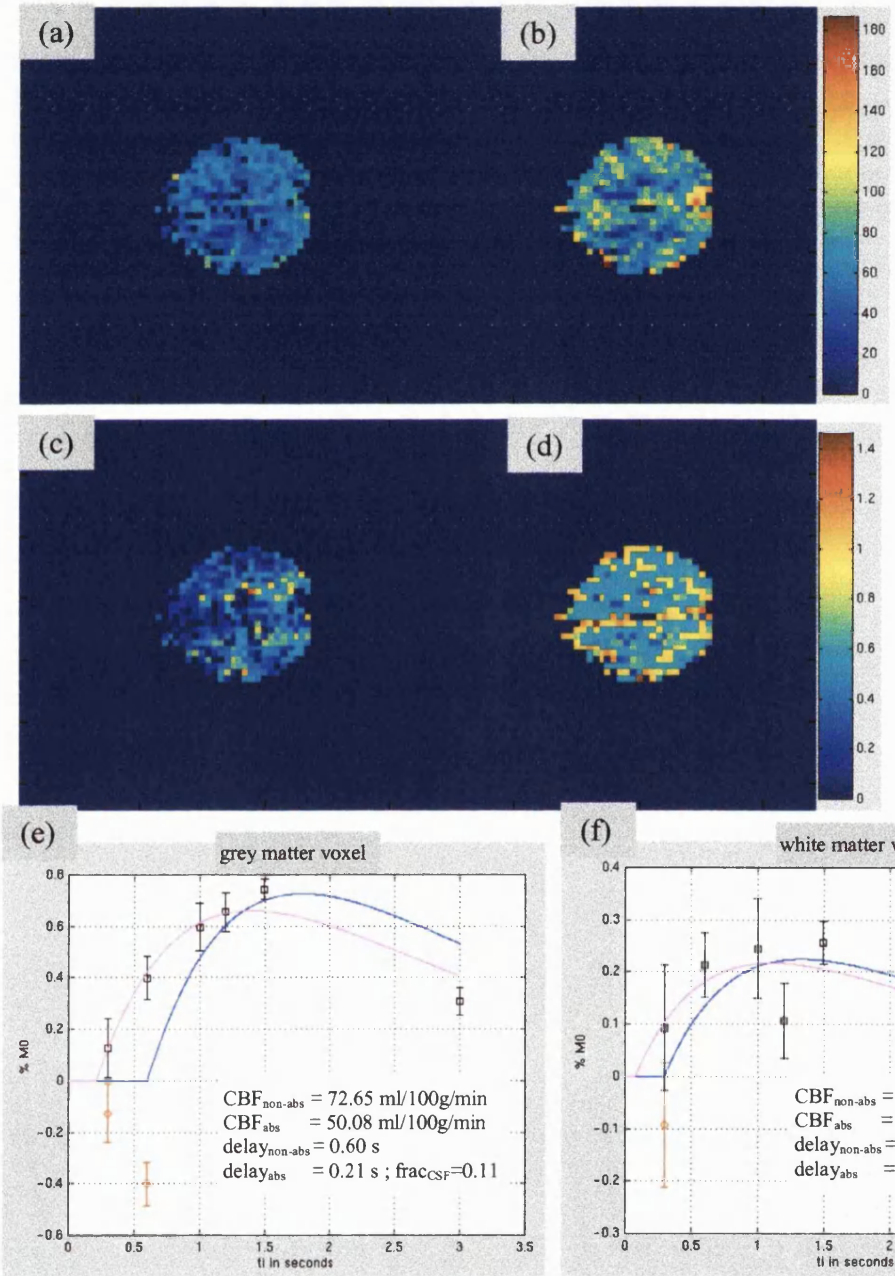

Figure 5-21 Results fitting magnitude FAIR data vs results standard non-magnitude FAIR fitting. CBF in ml/100g/min, delay in s. (a) CBF_{abs}, (b) $CBF_{non-abs}$, (c) $delay_{abs}$, (d) $delay_{non-abs}$, (e) Plot grey matter voxel fits, abs data (black squares), non-abs data (red circles), abs fit (magnenta line), non-abs fit (blue line). (f) Plot white matter voxel fits, abs data (black squares), non-abs data (red circles), abs fit (magnenta line), non-abs fit (blue line).

Because the reported mean sd values in Table 5-11 are based on the sd as a percentage of the voxel CBF or delay value, it is useful to be able to distinguish if changes in CBF or delay or changes in absolute sd values determine the increased percentage wise errorbars for magnitude FAIR fitting. The mean *absolute* errorbars are therefore given in Table 5-12. It is clear from this table, that the errorbars are very similar for magnitude and non-magnitude FAIR fitting. This means that the increased relative sd values of Table 5-11 are a result of a decrease in mean CBF for magnitude FAIR fitting.

mean sd (median)	magnitude FAIR	non-magnitude FAIR
	sd	sd
sd on CBF in ml/100g/min	6.63 +/- 3.36 m. 5.28	6.42 +/- 3.73 m. 5.14
sd on delay in s	0.04 +/- 0.01 m. 0.04	0.03 +/- 0.02 m. 0.03

Table 5-12 Comparing the absolute errorbars (in ml/100g/min or s) for magnitude and non-magnitude FAIR fitting of experimental data. The median value (m) is also given.

Table 5-13 lists the mean +/- sd CBF, delay and CBF ratio values for the CBFD model fits using magnitude and non-magnitude FAIR data.

	mask all voxels (355 voxels)	grey matter mask (151 voxels)	white matter mask (24 voxels)	ratio CBF grey/ white
CBF +/- sd in ml/100g/min magnitude FAIR	53.76 +/- 14.53	59.44 +/- 11.75	33.34 +/- 12.64	1.78 +/- 0.14
delay +/- sd in s magnitude FAIR	0.36 +/- 0.21	0.36 +/- 0.19	0.51 +/- 0.33	----
CBF +/- sd in ml/100g/min non-magnitude FAIR	74.61 +/- 25.72	77.88 +/- 18.86	35.22+/- 12.13	2.21 +/- 0.16
delay +/- sd in s non- magnitude FAIR	0.69+/- 0.20	0.62 +/- 0.11	0.58 +/- 0.26	----

Table 5-13 CBF, delay and CBF ratios for fitted magnitude and non-magnitude fitted FAIR data.

It is interesting how it is mostly the grey matter CBF that is affected by fitting magnitude data; the white matter CBF stays very similar. This is due to white matter's lower T_{1app} (the inversion recovery data goes through its zero-crossing earlier, so less chance of negative FAIR signal) and the fact that CSF/white matter partial voluming is much less likely to occur. Because of the lowering of the grey matter CBF the ratio of grey/white mask CBF is also lowered.

Looking at these results and at Figure 5-21, the magnitude FAIR results look more irregular and less ideal: CBF values in grey matter areas are reduced from ~80 ml/100g/min to 60-70 ml/100g/min. And consequentially, the grey/white matter contrast is less obvious. The inflow delays are shortened and vary significantly over the slice. However, the fact that the data looks less regular and thus less appealing, does not mean the standard non-magnitude FAIR fitting is better.

The key lies in the fitting of the inflow delay: if the fitted inflow delay is shorter, the resulting CBF values for the same dM curve will be lower. The non-magnitude FAIR fitting structurally finds longer inflow delays. In the CSF partial voluming section (5.4.1.1), it was predicted how negative FAIR signal would determine the fitted inflow delay: Figure 5-14 (e) and (f) predict how the longest TI value for which the FAIR signal is still negative will be equal to the fitted inflow delay. This means that that fitted inflow delay is a consequence of the erroneous negative FAIR signal and not a correct representation of the physical inflow delay.

To test if this effect also occurs in this modelling of *in vivo* data, the longest TI value for which the non-magnitude FAIR data were still negative was plotted for each voxel. When comparing this plot with the fitted inflow delay for the non-magnitude data, Figure 5-22, it immediately becomes clear that the erroneous negative FAIR signal is indeed the reason for the longer fitted delay values and consequently for the higher CBF values found when fitting non-magnitude FAIR data. Even though this error leads to more appealing results, which correlate very well with the literature, the results are wrong and non-magnitude FAIR fitting should not be performed. Magnitude FAIR data will be used from now on.

Magnitude subtraction, CSF partial voluming as well as the static subtraction error can all result in negative FAIR signal. By fitting magnitude FAIR data, erroneous negative

signal due to magnitude subtraction and CSF partial voluming is corrected. The effects of the static subtraction error will still be present in magnitude FAIR data, but they are limited: CBF and delay are overestimated by up to 14% and 7% respectively, as calculated in section 5.4.3.

The most probable reason why the grey matter CBF values for the magnitude FAIR fitting are so much lower than the literature values is partial voluming. The experimental data has been acquired for a slice thickness of 10 mm, which is thicker than the cortical sheet (~ 3-6 mm). The chances of getting pure grey matter voxels are not very high, and partial voluming with CSF or white matter will lower the CBF found. It is promising that with the magnitude FAIR fitting the inflow delay found for white matter is indeed longer than for grey matter, which is in accordance with the literature (Ye et al., 1996).

The second question to be addressed is if it is necessary to include the inflow delay in the model. In the basic analysis in section 5.3.2 the CBFO model underestimated CBF values by 40-60%; it is worthwhile to look at his issue again, now that magnitude fitting of the FAIR data is the new method of choice and the ssinv fitting models have changed. Figure 5-23 shows the CBF maps for magnitude FAIR data fitted with the CBFO (only CBF fitted) and CBFD (CBF and delay fitted) models. The goodness-of-fit results are compared for both models in Table 5-14.

FAIR fit	mask all voxels (355 voxels)	grey matter mask (151 voxels)	white matter mask (24 voxels)
CBFD model on magnitude FAIR	80%	74%	96%
CBFO model on magnitude FAIR	70%	60%	96%

Table 5-14 Results goodness-of-fit CBFO vs CBFD model in FAIR fitting: percentage voxels in mask with $Q > 0.001$

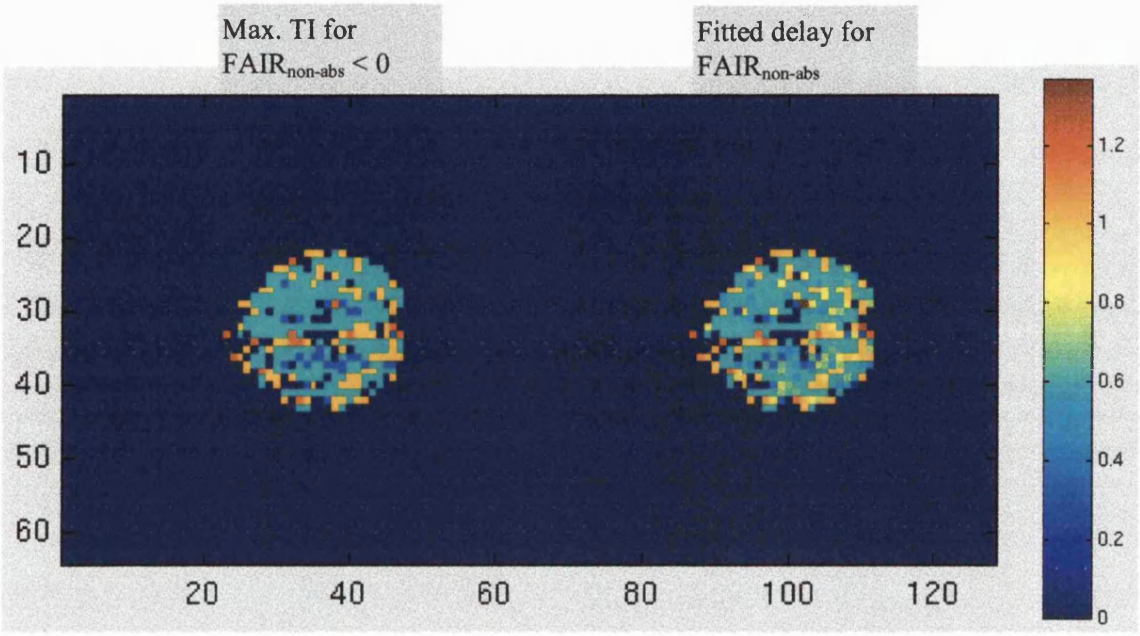

Figure 5-22 The effect of negative FAIR signal on delay fitting *in vivo*: (left) for each voxel, the longest TI value is given at which its FAIR signal is still negative; (right) the fitted delay for FAIR$_{non-abs}$.

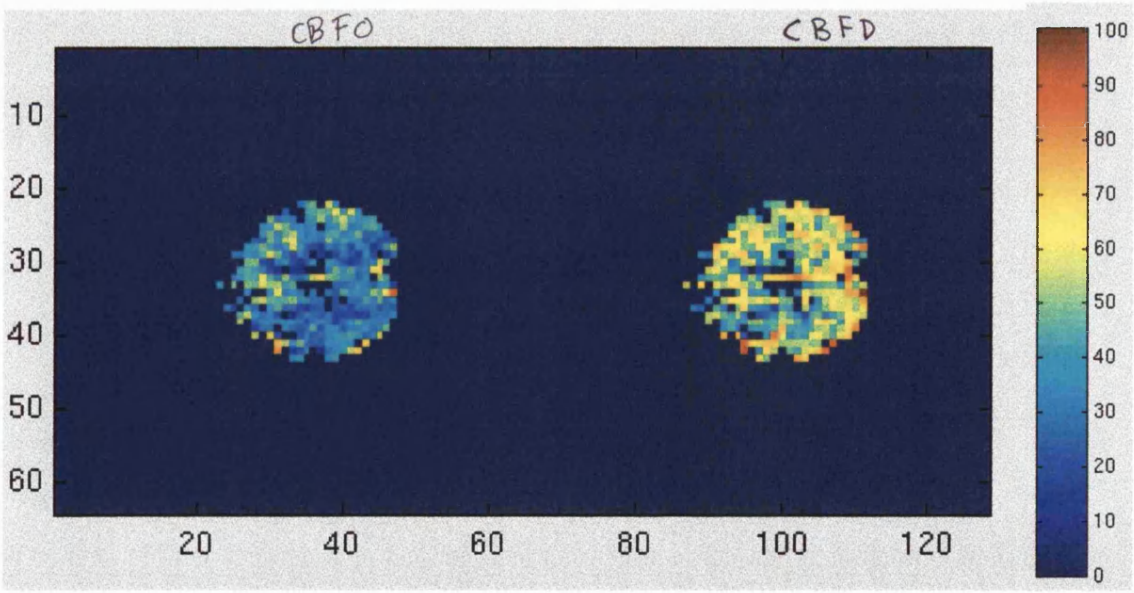

Figure 5-23

CBF in ml/100g/min as a result of fitting magnitude FAIR data for CBF and inflow delay (CBFD model) and for CBF only (CBFO model). TNF parameters from SL fit.

The goodness-of-fit test takes the number of degrees of freedom into account, so there is indeed an improvement for the fit when including the inflow delay in the model. A more formal way of comparing the two models is the extra-sum-of-squares test as described in the general modelling procedures of section 5.3.2.1. When using the extra-sum-of-squares test looking at all converged voxels, 20% experience a significant better fit when the inflow delay is included. When the grey matter mask is applied, 25% of the voxels experience a significant improvement in fit, for voxels in the white matter mask this is 8%. What about the accuracy of the results? In Table 5-15 the CBF values for the CBFD and CBFO models are compared.

	mask all voxels (355 voxels)	grey matter mask (151 voxels)	white matter mask (24 voxels)	ratio CBF grey/ white
CBF +/- sd in ml/100g/min CBFD model	53.76 +/- 14.53	59.44 +/- 11.75	33.34 +/- 12.64	1.78 +/- 0.14
CBF +/- sd in ml/100g/min CBFO model	35.96 +/- 12.35	39.44 +/- 11.20	12.52 +/- 6.34	2.25+/- 0.17

Table 5-15 CBF values and CBF ratios for FAIR data fitted with CBFO and CBFD models.

The goodness-of-fit test has shown a better goodness-of-fit for the CBFD model, which means it is not likely that the CBFD results are less accurate. Moreover, the grey matter CBF values from the CBFO model are far below the literature value of ~ 80 ml/100g/min (Calamante et al.,1999). Considering the thick imaging slice used here, it is very possible that partial voluming will lead to somewhat lower CBF values for the grey matter mask here used, as none of the voxels in that mask is likely to contain 100% pure grey matter. However, it is unlikely that this very low grey matter CBF value for the CBFO model can be explained by partial voluming alone.

It seems therefore that the CBF is underestimated when using the CBFO model. This is in line with expectations, as many groups have reported a non-zero inflow delay in *in vivo* data (Gonzalez-Atavales et al., 2000, Yang et al., 2000) and underestimating the inflow delay leads to an underestimation of CBF as discussed before. The results here give an indication of the size of this underestimation effect for *in vivo* data. Assuming the CBFD

model gives the correct CBF values, if the inflow delay is not included in the CBF quantification, CBF values are underestimated by ~ 30% in grey matter, by ~ 60% in white matter. This underestimation will become more severe for higher inflow delays, i.e. when flow spoiling is applied.

The large underestimation of CBF in the CBFO model therefore suggests that fitting for inflow delay in the CBF quantification is worthwhile. Moreover, the inflow delay parameter itself is of interest to clinicians (Chalela, et al., 2000) as it provides information regarding the state of the vasculature, which is especially interesting in cerebrovascular disease.

Most groups include inflow delay in their model when quantifying CBF using ASL techniques (Ye et al., 1997; Buxton et al., 1998b; Yang et al., 2000). However, several groups report results of single-shot, single-inversion time point FAIR data sets, for which transit time effects are ignored (Kim et al., 1997; Hoge et al., 1999). The here demonstrated effects of ignoring the inflow delay might have implications for those type of 'event-related' FAIR studies. When the CBF *changes* over the course of such a FAIR time series, the transit time is likely to change too. Taking FAIR measurements at the same inversion time for different inflow delays (i.e. the whole FAIR vs inversion time curve shifts to the right or to the left) might lead to erroneous results: a change in measured FAIR signal might be due to the different sampling point of the FAIR signal curve, not to a real change in CBF. The effect of ignoring the inflow delay will depend on the size of the delay, the change in the delay and the shape of the FAIR signal vs inversion time curve.

Recent studies support the hypothesis of the importance of the inflow delay: using continuous ASL Gonzalez-Atavales et al. (Gonzalez-Atavales et al., 2000) find significant inflow delay changes during visual and motor studies; Yang et al. (Yang et al. 2000) report a significant change in transit time of ~ 0.11 s (17%) during a sensorimotor task studied with FAIR. They calculate a possible error of 10-30% in perfusion if the *changes* in the inflow delay and also in the trailing delay (end of the spin label bolus) are not taken into account in the modelling of rest and activated sensorimotor states. Ye et al. (Ye et al., 2000) report a cross-validation of rCBF measurements in human with $H_2{}^{15}O$ PET: if a fitted mean inflow delay is used for all voxels in the ASL modelling, PET and ASL grey matter CBF values are in good accordance (no significant difference). However, white matter CBF

values of ASL are underestimated by ~ 20%, which Ye et al. attribute to the fact that white matter inflow delay values are in fact significantly larger (~ 1.2 s) than the used mean (grey matter) value (~ 0.93 s). The white matter inflow delays are hard to establish separately, however, due to the low SNR of white matter FAIR data. All these findings point towards the necessity of including the inflow delay into the perfusion quantification, but caution should be applied to use the *correct* inflow delay (rest vs activated states, grey vs white matter).

A systematic study of changes in CBF and inflow delay due to a hypercapnic challenge will be described in the next chapter. With these data one can calculate the error in CBF if the (change in) inflow delay is ignored for a CBF range that is relevant for cognitive and physiological studies.

5.4.5 Optimising the time efficiency of the CBF measurement

Running at full relaxation is not very efficient. The SNR for a given acquisition time is not optimised and because of the long duration of the acquisition, the data are more likely to be influenced by subject motion. Moreover, the CBF can change during the course of the measurement, decreasing the accuracy of the quantification.

To optimise the efficiency, the approach demonstrated by Pell and colleagues (Pell et al., 1999; Thomas, 1999) was followed: the repetition time tr was reduced after inserting global spin saturation into the pulse sequence just before the recovery time (Figure 5-1). This ensures that the longitudinal magnetisation in blood and tissue has the same starting value for SL and GL acquisitions. When the repetition time is reduced without this global saturation, inflowing blood during the SL acquisition following the GL acquisition will not be fully relaxed and CBF quantification is complicated. With the global saturation pulse, the FAIR equations are simplified. The SL and FAIR formula for a short tr setup with global saturation and inflow delay included become (Deichmann, personal communication; Thomas, 1999):

$$(5.11)\quad SL(TI) = \left| M_0 \left(1 + \left[(1 - \exp(-\frac{\tau}{T_{1app}}))(1 - 2\alpha_0) - 1 \right] \exp(-\frac{TI}{T_{1app}}) \right) \right|$$

(5.12)

$$dM(TI) = 0 \qquad TI \le \delta t$$

$$dM(TI) = 2\alpha_0 M_0 \exp(-\frac{\delta t}{T_{1a}})\frac{f}{\lambda}\left[\frac{\exp(-(TI-\delta t)/T_{1app}) - \exp(-(TI-\delta t)/T_{1a})}{\frac{1}{T_{1a}} - \frac{1}{T_{1app}}}\right][1 - \exp(-\tau/T_{1a})] \qquad TI \ge \delta t$$

The exact SL equation also includes terms dependent on CBF and inflow delay, but these terms are ~ 1% of the total SL signal and can therefore be ignored. δt is the inflow delay and τ is the recovery time between the global saturation and the inversion pulse. The SNR per unit time can be maximised by maximising the following function (Pell et al., 1999; Thomas, 1999).

$$(5.13) \quad \frac{\Delta M(TI,\tau)\sqrt{N_{av}}}{t_{total}} \propto \frac{\Delta M(TI,\tau)}{\sqrt{TI+\tau}},$$

with N_{av} the number of averages acquired. This was done for grey matter, with an inflow delay of 0.2 s and a CBF of 50 ml/100g/min. The optimal recovery time τ was found to be 2.65 s. The ratio of dM vs the square root of the repetition time (TR = TI + τ), where dM is given as a percentage of M_0, will change from 0.27%/√s to 0.32%/√s for this recovery time τ. The optimum recovery time τ will be slightly different for different CBF or inflow delay values, but as Figure 5-24 demonstrates, the SNR per √time ratio of equation (5.13) is a flat plateau for a large range of recovery times τ.

Maximum dM values will decrease due to the global saturation: for grey matter with an inflow delay of 0.2 s, a CBF of 50 ml/100g/min and a recovery time of 2.65 s, the maximum dM signal will decrease from 0.74% to 0.64% of M_0.

For a grey matter CBF value of 80 ml/100g/min, an inflow delay of 0.7 s and a recovery time of 2.65 s this maximum dM signal goes from 0.83% to 0.71% of M_0.

The maximum dM signal is thus expected to decrease slightly when using global saturation; the reward lies in an increased time efficiency in accumulating SNR for the dM measurement. A human data set acquired with global saturation in the pulse sequence, a reduced repetition time and all other acquisitions and analysis improvements discussed so far will be described in the final section 5.4.7.

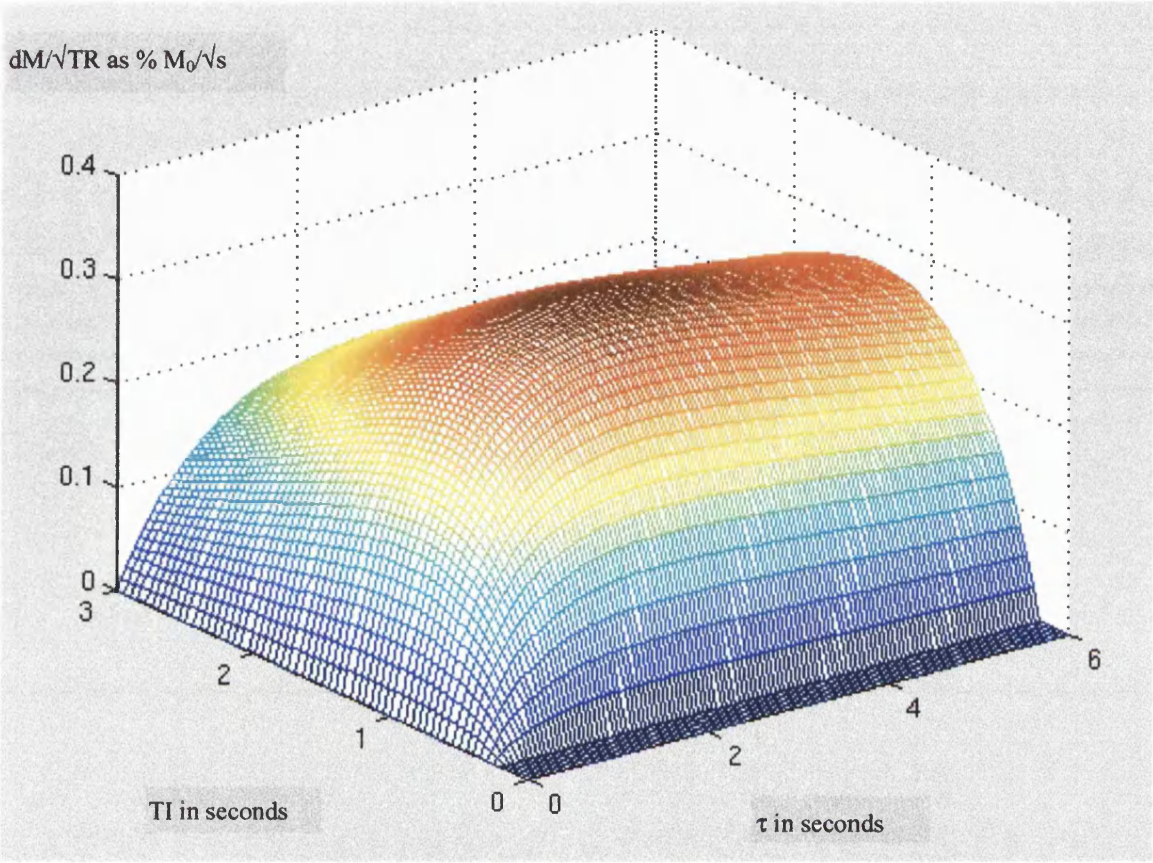

Figure 5-24 Optimising dM/√TR by choice of recovery time τ; TR=TI+ τ; dM/√TR given as percentage of $M_0/\sqrt{s}$.

5.4.6 Volunteer Motion; Realignment

For BOLD data, the necessity of motion correction has been well established (Hajnal et al., 1994; Friston et al., 1996). Image realignment has become a standard step in the BOLD data analysis and there are many software packages around that can do this, among which the well-known SPM package (SPM, 1999).

It is not hard to imagine the possible benefits of realignment for FAIR: if the head shifts > 1 voxel in a particular direction, the FAIR sequence could be measuring signal from white matter at one TI point and of grey matter for the next. A shift in and out of CSF areas will have even greater effects.

Standard realignment packages such as SPM(SPM, 1999) cannot deal with FAIR data for two reasons:

- FAIR only covers 1-10 slices and not a whole brain volume.
- The FAIR data has different contrasts for different inversion times. Realignment programs optimise for a minimal sum of squares difference between images which is not possible if the contrasts are different.

The first problem will become less and less important as the brain coverage of FAIR increases by using faster readout sequences. For the single-slice FAIR sequence implemented in this project, however, this is an issue, because it is based on a single slice acquisition. It means all movement correction is limited to in-plane motions as there is no data to establish and correct out-of-plane movement. The second problem is more general and applies to all multi-TI acquisitions. Two-dimensional realignment for repeat acquisitions of one inversion time is not a problem, realignment over multiple inversion times is.

Three different analysis approaches were developed for a standard FAIR dataset:
1) no realignment
2) realignment of repeat acquisitions of every inversion point TI ('intra-TI' realignment); this means that averaged images for different inversion times TI might still be misaligned with respect to each other.

3) realignment of repeat acquisitions within and between inversion points ('inter-TI' realignment).

The inter-TI realignment was implemented as follows:

- For each inversion time TI, before the acquisition of its nav repeats, a single shot, single slice M_0 image was acquired. These M_0 snapshots were realigned to the first acquired M_0 snapshot, thus giving the required in-plane image transformations at the beginning of each TI point. These image rotations were applied to the first image of the FAIR data at each inversion point. The other repeats (nav-1) were then realigned to the first image of each TI point series. This realignment scheme is illustrated below. By using the M_0 snapshots as reference scans, realignment across different contrasts is thus possible.

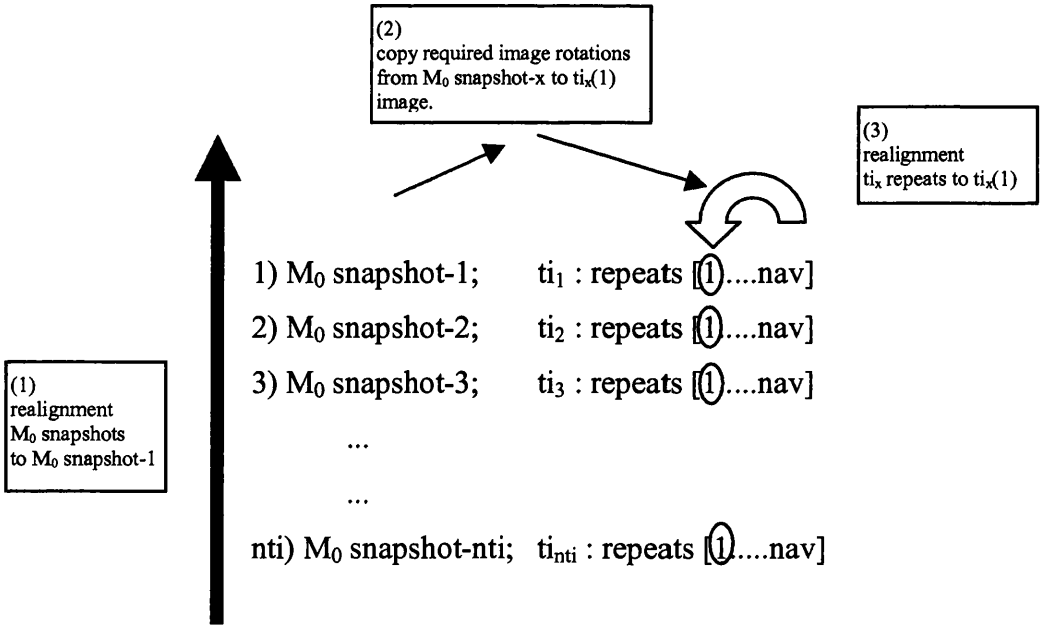

nti is the number of TI points, nav is the number of repeats for each TI point.

The 'intra-TI' realignment is simply the realignment of the nav averages for every inversion point TI. This method thus does not realign between inversion points TI and the M_0 snapshot data are therefore not used.

These realignment procedures were applied to a FAIR data set acquired with a slice thickness of 5 mm, a short tr of 2.65s (with global saturation in the pulse sequence) and a b-

factor of 5 s/mm^2. This experimental setup will be described more extensively in the next section. M_0 snapshots were also acquired immediately before the start of every TI-point acquisition. The standard deviation averaged over the slice and all TI points for FAIR data are given in Table 5-16. The standard deviation is given as a percentage of that of unrealigned data.

	Unrealigned	intra-TI realignment	inter-TI realignment
sd FAIR over slice	100%	91%	91%

Table 5-16 Effect of realignment on summed sd of FAIR data: mean sd over inversion points and over all voxels ($sd=\sqrt{\sum_i sd_i^2}$) as percentage of unrealigned sd.

The realignment procedure is indeed reducing the variability of the FAIR data. The reduction in the total standard deviation is 9%, and there is no difference for intra-TI and inter-TI realignment.

To see if the data has been realigned correctly, the different FAIR data sets (unrealigned, intra-TI realigned, inter-realigned) were fitted using the CBFD model, with inputs from a TMF fit of SL data. The percentage of voxels passing the $Q > 0.001$ threshold for the goodness-of-fit test on the CBFD results was 88%, 90% and 89% for the unrealigned, intra-realigned and inter-realigned data, respectively. So the realignment only has a small effect on the goodness-of-fit results. However, realigning repeats of one TI point will reduce the mean value's standard deviation and thus might *decrease* the chance of a voxel passing the goodness-of-fit test. More information comes from looking at the sum of squared differences between the data and the model. For the intra-realigned data, the sum of squared differences is reduced by 13%, and by 10% for the inter-realigned data. So both intra- and inter- realignment improve the fit. The intra-realignment seems to be a little better.

As the realignment procedures are weighted towards edges, a risk with inter-realignment is that the movements perpendicular to the slice can lead to a shift in the edges, which the algorithm tries to correct, thus potentially leading to an increase in the differences for voxels inside the slice. This is illustrated in Figure 5-25. The intra-

realignment can also suffer from this problem, but as the time scale for the intra-realignment is much shorter (18-36 acquisitions for one inversion point for intra-realignment vs 6*18 or 6*36 acquisitions for inter-TI realignment) the out-of-plane movements will generally be smaller for intra-realignment.

Because the intra- and inter-realignment both result in comparable improvements and the intra-realignment is less sensitive to out-of-plane movement, the intra-TI realignment will be used in this thesis. Inter-realignment will probably be the method of choice once whole brain FAIR data sets become available, as this method can reduce variability between TI-points, i.e. between subsequent CBF measurements.

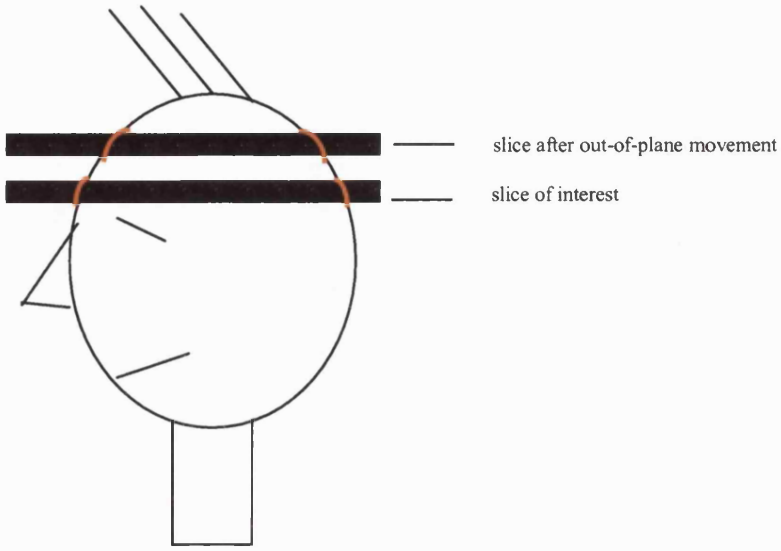

Figure 5-25 Effect of out-of-plane movement on slice edges.

5.4.7 Proposed optimised experimental setup and analysis

On the basis of the quantification issues previously discussed, the following optimised experimental setup and modelling is proposed for a CBF measurement using FAIR:

proposed experimental setup

- selection of a thin slice, 5 mm, to reduce partial voluming problems.
- inversion of a slice of 20 mm, to reduce the static subtraction error further.
- flow spoiling with a b-value of 5 s/mm^2 to reduce the influence of large vessels further.
- reduction of the longest TI from 3 to 2 seconds, to reduce the chance of non-inverted spins flowing in after the global inversion.
- introduction of a global saturation pulse followed by a gradient spoiler and a delay τ=2.65 s before each selective or non-selective inversion to reduce acquisition times.

proposed data analysis

- realigning the data following the intra-TI realignment procedure as described in section 5.4.6.
- fitting the SL data for T_{1app}, M_0 and CSF fraction (TMF model). The inversion efficiency is determined by fitting extra acquired SL data using the ITM model. The ITM model uses the short tr SL(TI) fit formula, equation (5.11). In the TMF model, a contribution of CSF is fitted following equation (5.10).
- fitting the magnitude FAIR data to avoid erroneous negative FAIR signal that can result from magnitude subtraction and CSF partial voluming.
- fitting for CBF and inflow delay in the FAIR modelling (CBFD model).

A FAIR data set was acquired and analysed following the proposals above. The inversion times TI were 0.3, 0.6, 1.0, 1.2, 1.5, and **2.0** s; the measurement for every TI point was repeated 18 times. After the FAIR acquisitions a separate SL data set was acquired for the inversion times TI 0.3, 0.6, 1.0, 1.2, 1.5, and **3.0** s, with 36 averages for every inversion point TI. Due to the global saturation preceding each SL and GL acquisition, no images needed to be discarded. An intra-TI realignment procedure as described in section 5.4.6 was

first performed. Then the separate SL data set was fitted for the inversion efficiency using the ITM model and equation (5.11). The longer TI_{max} of the SL data set allows for a better inversion efficiency fit. The fitted α_0 was 0.94. This value was inserted into the TMF model and the SL data derived from the FAIR data set were thus fitted for T_{1app}, M_0 and CSF fraction. The goodness-of-fit results for the ssinv fits are given in Table 5-17. As before, these goodness-of-fit tests were performed on single average data.

	separate SL fit (ITM model)	SL from FAIR fit (TMF model)
goodness-of-fit: % of voxels with Q>0.001	79%	87%

Table 5-17 Goodness-of-fit for SL fits using ITM and TMF models; final experimental setup.

The first striking result is the overall increase in percentage of voxels that pass the goodness-of-fit threshold: for the basic CBF quantification experiment described in section 5.3 this was only 15% of voxels for the ITM fit, here it is 79%; for the TMF model the percentage increases from 21% to 87%.

The realignment only decreases the total standard deviation by 9%, so it is not very likely that that has such a large effect. More likely, it was the thick slice and resulting large partial voluming that was the cause of the bad goodness-of-fit results of the basic quantification experiment in section 5.3. Both ITM and TMF models therefore now do adequately describe the SL data. Now that the use of these models has been justified with this slice thickness and experimental setup, the goodness-of-fit test will not be performed again for SL data acquired under these experimental conditions.

In Table 5-18 below, the errorbars are given for the TMF and ITM fits. Again, these were obtained by fitted all averages separately (repeated measures method).

mean sd as % voxel value	TMF model on SL from FAIR (18 averages)	ITM model on separate SL data (36 averages)
α_0	----	0.14%
T_{1app}	2.2%	0.30%
M_0	1.5%	0.19%
$frac_{CSF}$	8.6%	----

Table 5-18 The errorbars (mean sd as percentage mean value voxel) for TMF and ITM models on experimental data; final experimental setup.

The errorbars are larger for the TMF model than for the experiment of 5.4.4.1, but there a thicker slice of 10 mm was used and 44 instead of 18 averages used.

Next the FAIR data were modelled. The FAIR data were fitted for CBF and inflow delay using the fitted SL parameters α_0, T_{1app}, M_0 and CSF fraction. For the magnitude FAIR data 90% of all voxels passed the Q>0.001 goodness-of-fit threshold. The results are given in Figure 5-26. Voxels that have not lead to a converging fit result or have CBF values > 200 ml/100g/min have been nulled. The CBF and delay seem more in accordance with expectations (grey/white matter contrast, etc.) than for the thick slice using the TMF-CBFD model and the old experimental setup (Figure 5-21 (a), (c)). It is interesting to note how the fitted inflow delay is increased in white matter regions in this new setup.

mean sd as % voxel value	magnitude FAIR fitting -CBFD model
CBF	25%
delay	13%

Table 5-19 The errorbars (mean sd as percentage mean value voxel) for CBFD model on experimental data, SL inputs from TMF model; final experimental setup.

In Table 5-19 the standard deviations are given for the fitted CBF and delay. For the inflow delay the value is similar, but for CBF this is a substantial increase from the results with the thick slice and 44 averages, which was 14%.

The effect of the errors of the SL parameters α_0, T_{1app} and M_0 was also calculated using equation (5.6): when including these errors in the calculation, the errors on CBF and the delay were increased by less than 1%, so these contributions can be safely ignored.

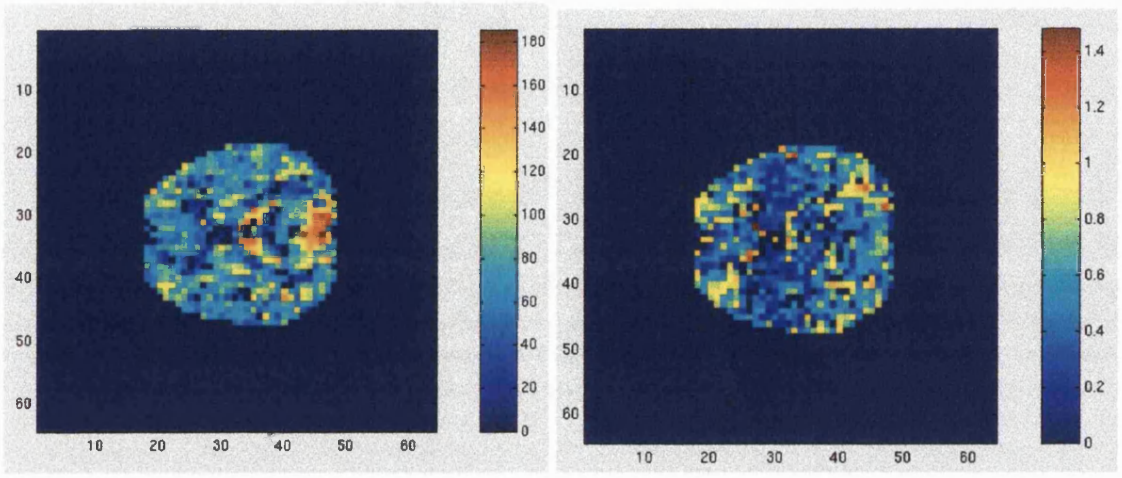

Figure 5-26 Results for optimised experiment: CBF in ml/100g/min (left) and delay in s (right).

Masks were generated to assess mean grey matter and white matter CBF and delay. As the TMF model fits for CSF fraction separately, a voxel with a very high CSF content can still be classified as 'grey matter' on the basis of the fitted T_{1app}. Therefore the following selection criteria were applied:

1) $T_{1app} \in$ <1.07; 1.27> s , for grey matter and <0.65; 0.75> s for white matter.

2) fitted CSF fraction < 0.50.

3) the voxel has given a converging fit for SL and FAIR data.

4) the fitted CBF < 200 ml/100g/min, to avoid contributions of large vessels.

The white matter boundaries are lower than used for the ITM fit in section 5.3.2.4, but that model overestimates T_{1app}. As the TMF model is more accurate, the boundaries have been based on the independently measured T_{1app} values for white matter, 0.70 +/- 0.05 s (Deichmann, personal communication). The CBF and delay results for grey and white matter masks are given in Table 5-20. An estimate of 'global' CBF and delay for the slice is also given. This is an average for *all* voxels that survive criteria (2)-(4) given above, and includes a much larger group of voxels than the grey and white matter masks.

	grey matter mask (85 voxels)	white matter mask (94 voxels)	global mask (522 voxels)	ratio CBF grey/ white
CBF in ml/100g/min	80.96 +/- 23.39(29%) med. 78.89; se 2.54	50.84 +/- 24.15(48%) med. 52.56; se 2.49	76.03 +/- 30.39(40%) med. 73.16; se 1.33	1.59 +/- 0.09
delay in seconds	0.43 +/- 0.23(54%) med. 0.44; se 0.03	0.67 +/- 0.33(49%) med. 0.59; se 0.03	0.48 +/- 0.27(56%) med. 0.47; se 0.01	----

Table 5-20 Results for global, grey and white matter masks for optimised experiment: CBF and inflow delay values. All values are listed in the following format: mean +/- standard deviation (% mean), median; standard error. The standard deviations of the CBF ratios were calculated using the standard errors.

Grey matter CBF values are now in the correct range as reported by the literature (Calamante et al., 1999), while for the thick 10 mm slice using the same models quite low values of 54 ml/100g/min were reported. The delay values for grey matter (0.43 s) are

somewhat shorter than expected: Ye and colleagues (Ye et al., 1997) report a transit time of 0.5 s in the absence of crusher gradients, and 0.9 s in the presence of gradients with b=4.5 s/mm^2. However, this is for a technique where the labelling occurs 3 cm below the slice. Because of the increased delay when spoilers are used, Ye et al. do suggest that there is a substantial delay, ~0.4 s, between the arrival of tagged blood in the imaging slice and the arrival of tagged blood at capillary exchange sites in the imaging slice. For FAIR the labelling occurs in slice and the blood only has to travel from the edge of the inversion slice to the edge of the readout slice (~ 5-10 mm). The rest of the transit time is then due to the transit from larger to smaller vascular structures within the slice. An inflow delay of a little more than 0.4 s would thus make sense. Alternatively, it could also be that inflow delays reported in the literature have been systematically overestimated due to the effect of negative FAIR signal due to subtraction of magnitude data and CSF/tissue partial voluming (section 5.4.1).

The white matter delay values are somewhat longer than for grey matter, which is what was expected on the basis of the literature. However, the CBF values of white matter seem very high: the literature value is ~ 20-30 ml/100g/min (Calamante et al., 1999). The white matter data are very noisy. For single voxel fits there is a large spread in the results: some voxels give results in accordance with the literature values, others far from it.

Averaging the data over all the voxels in the mask before fitting gives similar results: for the realigned data averaging over the 94 voxels in the white matter mask, it gives a CBF of 46.66 ml/100g/min and a delay of 0.65 s. The mean data and fits for the white and grey matter masks are given in Figure 5-27. An example of a good single voxel white matter fit is also given. Note how very noisy the data are for white matter for a single voxel, but also for the averaged white matter data in Figure 5-27 (b). The grey matter data, both for the single voxel and mean mask data, as shown in Figure 5-27 (a) and (d), have a much better SNR. The errorbars depicted are derived from the errorbars of the SL and GL data.

Possible influences that could explain the high white matter CBF values are partial voluming with grey matter and the static subtraction error. For every 10% partial voluming with grey matter, the fitted white matter increases by ~ 5 ml/100g/min (Figure 5-16 (a)). The static subtraction error can also lead to an overestimation of CBF: assuming the static

subtraction error is equal to the one measured on a phantom, it will lead to an overestimation of CBF by up to 14% (section 5.4.3), giving a corrected CBF for this white mask of matter of ~40 ml/100g/min. With a larger static subtraction error this overestimation could be bigger. The static error is expected to affect grey matter less, as it constitutes a smaller percentage of the grey matter signal. A static subtraction error as measured on the phantom and partial voluming of 10-20% grey matter could lead to an increase in white matter CBF values from the expected 30 ml/100g/min to 46 ml/100g/min, close to the value found here. Another contributing factor might be the noise: in the magnitude FAIR data random machine noise will appear as FAIR signal.

In conclusion, the low SNR of the white matter data makes the data very vulnerable to any artefacts and non-idealities. With white matter the here implemented FAIR technique thus reaches the boundaries of what it can reliably measure. Future studies at higher fields will help to increase the sensitivity of the FAIR technique to white matter and other regions with low CBF by lengthening the T_{1app} and allowing for thinner slices due to the increased SNR.

An important question is whether the overestimation of white matter CBF is an added constant to the correct CBF value or if it scales with CBF; if it is the former, relative changes of white matter CBF can be measured accurately. If the overestimation scales with CBF, white matter results from the current experimental setup and analysis can not be used reliably. This question will be addressed in the next chapter, in which the FAIR technique is further validated with a parametric hypercapnia experiment. The next chapter also gives baseline CBF and delay results for a group of volunteers to assess the variability of these parameters over subjects.

(a)

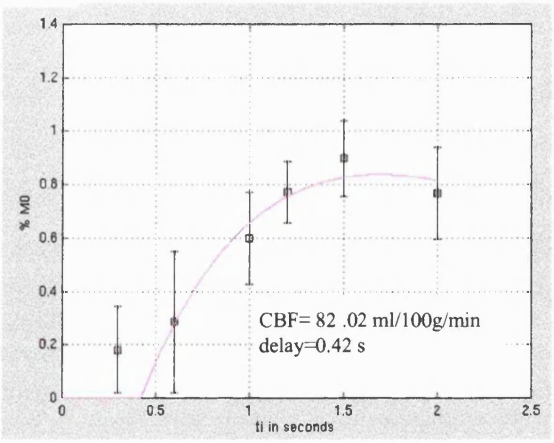

(b)

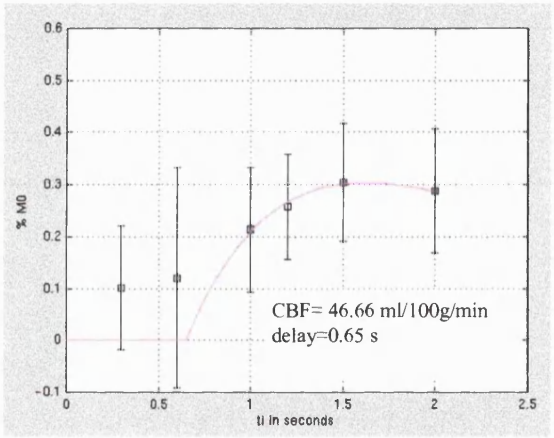

(c)

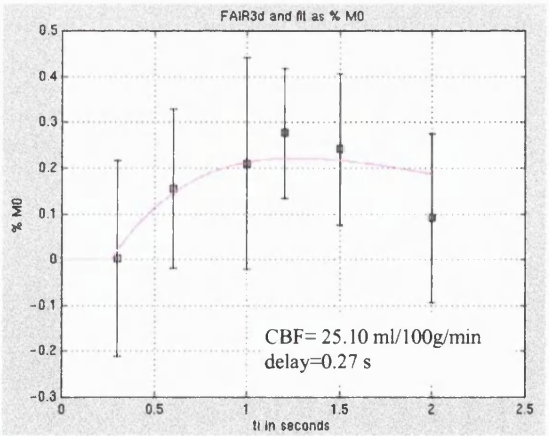

(d)

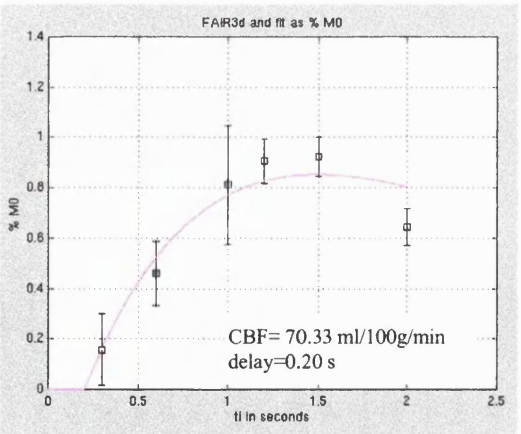

Figure 5-27 Data and fit for (a) mean of grey matter mask, (b) mean of white matter mask, (c) single white matter voxel, (d) single grey matter voxel. The mask data have been normalised by M_0 before averaging and fitting. All data have been realigned.

6 In vivo results: baseline and hypercapnic CBF and inflow delay in man

6.1 Introduction

In this chapter a parametric hypercapnia experiment is described that allows for a further validation of FAIR results with literature values. The well documented linearity of CBF for grey and white matter over the end-tidal CO_2 ($PetCO_2$) range used (Harper et al, 1990; Grubb et al. 1974) serves as a benchmark for the reliability of the implemented FAIR technique. Furthermore, the changes of inflow delay with increasing CBF are evaluated and the effects of ignoring the inflow delay discussed. Baseline BOLD MRI data are also acquired in each of the $PetCO_2$ states to look at the BOLD cerebrovascular reactivity and to allow for the comparison of BOLD with CBF data. Finally, baseline CBF, inflow delay values and their errorbars are determined for a sample of 11 volunteers.

6.2 A parametric hypercapnia experiment

6.2.1 Materials and Methods

6.2.1.1. Respiratory gas monitoring and control

The fractional concentrations of respired gases were determined from gas continuously sampled via a nasal cannula and analysed using a quadrupole mass spectrometer (MGA 900, Case Medical). The $PetCO_2$ was then determined from the expired CO_2 concentration. To control the fraction of inspired CO_2 and hence $PetCO_2$, a loose fitting mask was attached over the nose and mouth; through this a flow of air was maintained at approximately 40 l/min. The inspired CO_2 was then regulated by entraining CO_2 into this circuit. To allow for equilibration following each step change in CO_2, $PetCO_2$ was maintained constant for 5 minutes prior to any MRI measurement. Five different $PetCO_2$ states were transversed during the experiment, increasing $PetCO_2$ from the rest state by +0-20 mm Hg in steps of ~5 mm Hg. The ethics approval number for this work was 98/N050 and the volunteer studied gave informed consent to participate in this experiment.

6.2.1.2. MRI methods

FAIR data were acquired on a 2.0 T Siemens Vision MRI scanner following the procedures described in Chapter 5, section 5.4.7. The (axial) imaging slice was positioned above the corpus callosum. The inversion efficiency was determined by fitting SL data acquired in the rest state. Inversion times for these SL acquisitions were, as before, 300, 600, 1000, 1200,1500 and 3000 ms. There were 36 averages of SL data for each inversion time. FAIR data were acquired over 5 states of different expired (end-tidal) pCO_2 ($PetCO_2$), including the rest state. At each $PetCO_2$ state, the FAIR data were acquired at inversion times TI of 300, 600, 1000, 1200,1500 and 2000 ms, with 18 averages at each TI. For both SL and FAIR pulse sequences, the echo time was 42 ms, the b-factor was 5 s/mm^2, the inversion slice thickness was 20 mm, the readout slice thickness was 5 mm and the recovery time after each inversion-readout block was 2.65 s. Multi-slice BOLD data were also acquired at the end of each $PetCO_2$ state after the FAIR acquisitions: 48 slices of 5 mm centred around the FAIR slice were acquired, with 12 averages of each volume. The echo time was 40 ms. The SL, FAIR and BOLD data were all acquired at a FOV of 300mm, with a 64*64 acquisition matrix. The acquisition order of the inversion times and of the $PetCO_2$ states was interleaved, to minimise the effect of time on the results. The total duration of the experiment was ~ 2 ½ hours.

6.2.1.3. Data processing

The FAIR data were analysed per $PetCO_2$ state, following the procedures described in Chapter 5, section 5.4.7. The FAIR data were first realigned per TI point (intra-ti realignment) using the SPM package (SPM, 1999). The separately acquired rest state SL acquisitions were averaged and then fitted for inversion efficiency, T_{1app} and M_0 using the ITM model. The inversion efficiency was then inserted in the TMF model used to fit the mean SL data derived from the FAIR data for all $PetCO_2$ states. The results of this fit (T_{1app}, M_0 and CSF fraction) were inserted in the CBF model (equation 5.12), that is suitable for the short tr setup and includes the inflow delay. Grey and white matter segments were derived using the SL (TMF model) and FAIR (CBFD model) fit results. The segments were

defined by selecting voxels in appropriate T_{1app} ranges ($T_{1app} \in$ <1.07; 1.27> s, for grey matter and <0.65; 0.75> s for white matter) and for which their SL and FAIR fits had given convergent results. They were selected to have CSF fractions smaller than 0.5 and CBF values smaller than 200 ml/100g/min (to exclude vessels). The global segment was defined to encompass all voxels that passed the latter three criteria, irrespective of their T_{1app} values. These segments were used to calculate grey matter, white matter and global segment results.

The BOLD data were realigned (in a volume realignment) within and between all $PetCO_2$ states using SPM. This realignment also served to assess how much the volunteer had moved over the course of the study. The first 6 images were thrown away for saturation purposes; the remaining 6 BOLD images were then averaged to give mean BOLD volumes for all 5 $PetCO_2$ states. The slice of interest (the same slice as the FAIR slice) was selected from the volume and background voxels were removed using a mask.

The structural data and its grey and white matter segments were coregistered and resliced to the BOLD volumes. As the single slice FAIR and the multislice BOLD data could not be realigned to each other, the grey and white matter segments were derived for FAIR and BOLD data separately. The rational for this is that even though the exact voxels compared might not be the same, the characteristics of the segments (grey, white or global) would be. As the slices of BOLD and FAIR will be very close to each other, the chances of significant differences in grey/white or global segment CBF between the BOLD and FAIR slices are small. The grey and white matter masks for the BOLD data were derived from the structural segments: all voxels with > 0.9 grey or white matter fraction were contributed to the grey and white matter masks, respectively. A global mask was defined as all voxels with a CSF percentage < 50% and above background noise level.

6.2.2 Results and discussion

The $PetCO_2$ data for the FAIR and BOLD acquisitions are tabulated below.

$PetCO_2$ data				
	mean $PetCO_2$ +/- se (in mm Hg)		increase $PetCO_2$ from rest (in mm Hg)	
	FAIR	BOLD	FAIR	BOLD
State 1 (rest)	31.15 +/- 0.38	29.92 +/- 0.75	0	0
State 2	36.50 +/- 0.18	36.10 +/- 0.50	5.35	6.18
State 3	43.46 +/- 0.06	43.20 +/- 0.26	12.31	13.28
State 4	46.68 +/- 0.05	46.60 +/- 0.32	15.53	16.68
State 5	51.38 +/- 0.06	51.43 +/- 0.32	20.23	21.51

Table 6-1 $PetCO_2$ values for FAIR and BOLD data over all states.

The errorbars on $PetCO_2$ are very small and will therefore be ignored in further analyses. The raw FAIR data (after realignment) for all $PetCO_2$ states are given in Figure 6-1. The expected increase in CBF for the hypercapnic high $PetCO_2$ state is manifested in the progressively increasing FAIR signal with $PetCO_2$ for all inversion times. The raw FAIR signal increases by ~200-300% with the 20 mm Hg increase in $PetCO_2$. A similar, but smaller, effect of CBF increase on the BOLD signal is also noticeable: this is demonstrated in Figure 6-2, in which the raw realigned BOLD data are displayed for all $PetCO_2$ states. The mean BOLD signal changes by ~ 6% with the 20 mm Hg increase in $PetCO_2$.

A realignment of the BOLD data in three dimensions over all sessions showed only small volunteer movements over the whole study (extremes in out-of-plane (z) movement ~ +/- 1 mm), see Figure 6-3. As the movement over the course of the whole study is small with respect to the voxel size, it seems therefore a reasonable assumption that the FAIR masks (derived from rest state FAIR data) can be applied to the FAIR data of the other states.

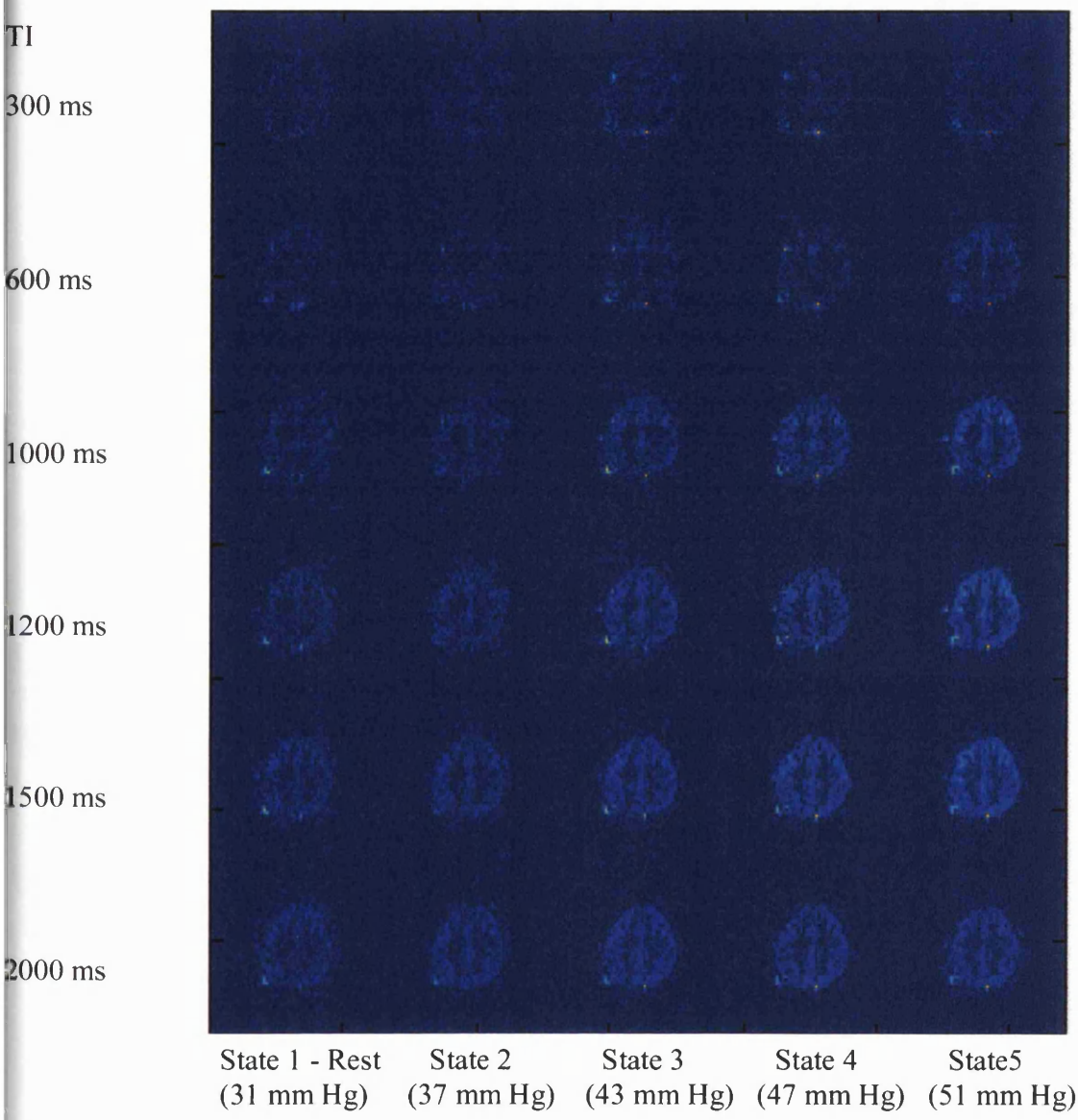

Figure 6-1 Raw magnitude FAIR data for all $PetCO_2$ states.

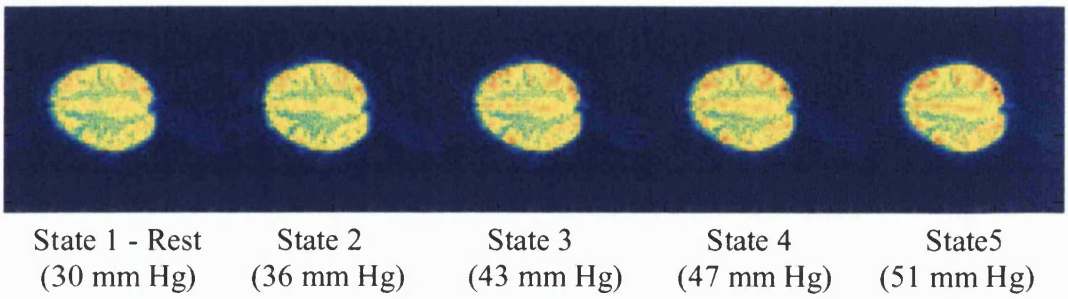

Figure 6-2 Raw BOLD data for all $PetCO_2$ states.

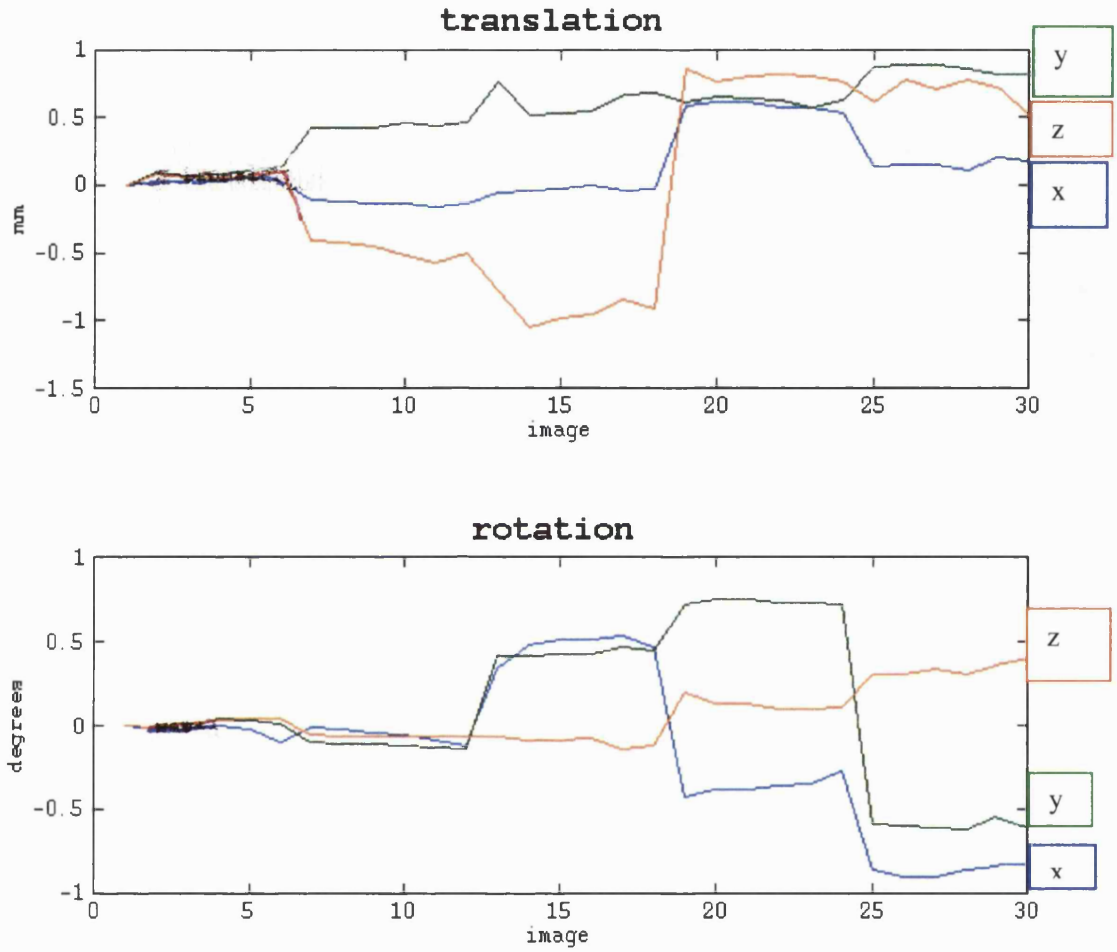

Figure 6-3 Realignment results for BOLD data, when 3d realignment is applied over all sessions. Translation in x, y and z and rotation around x, y and z axes.

The CBF and inflow delay parameters maps for each $PetCO_2$ state are given in Figure 6-4 and Figure 6-5. As the $PetCO_2$ increases, the CBF increases and the inflow delay *de*creases. There are two medial areas bilaterally with very low CBF in the rest state data: further analysis of these areas showed that the data there have a very low SNR; the voxels have white matter T_{1app} values or have a large CSF fraction. As the CBF increases with the parametric hypercapnia the SNR increases and the low CBF areas disappear.

The CBF and inflow delay results across all $PetCO_2$ states are given in Table 6-2 and Table 6-3 below for the grey matter, white matter and global segments.

CBF in ml/100g/min				
$PetCO_2$ in mm Hg	grey matter segment (51 voxels)	white matter segment (57 voxels)	global segment (321 voxels)	ratio CBF grey/white
31.15	45.41+/- 18.42(41%) med. 45.00; se 2.58	30.17+/- 15.13(50%) med. 27.48; se 2.00	38.05+/- 19.18 (50%) med. 35.22; se 1.07	1.51 +/- 0.13
36.50	59.93+/- 18.03(30%) med. 58.51; se 2.52	21.46+/- 20.02(93%) med. 21.10; se 2.65	41.34+/- 24.68 (60%) med. 45.84; se 1.38	2.79 +/- 0.36
43.46	70.78+/- 18.26(26%) med. 70.95; se 2.56	33.61+/- 22.64(67%) med. 31.55; se 3.00	51.82+/- 24.82 (48%) med. 54.11; se 1.39	2.11 +/- 0.20
46.68	73.63+/- 16.79(23%) med. 72.56; se 2.35	26.35+/- 18.66(71%) med. 25.63; se 2.47	52.03 +/- 27.470 (53%) med. 55.57; se 1.53	2.79 +/- 0.28
51.38	81.98+/- 30.06(37%) med. 80.53; se 4.21	42.24+/- 21.05(50%) med. 43.15; se 2.79	63.26+/- 28.03 (44%) med. 63.71; se 1.56	1.94 +/- 0.16

Table 6-2 Parametric hypercapnia experiment: CBF results for grey and white matter and global segments. All values are listed in the following format: mean +/- standard deviation (% mean); median; standard error. The standard deviations of the CBF ratios were calculated using the standard errors.

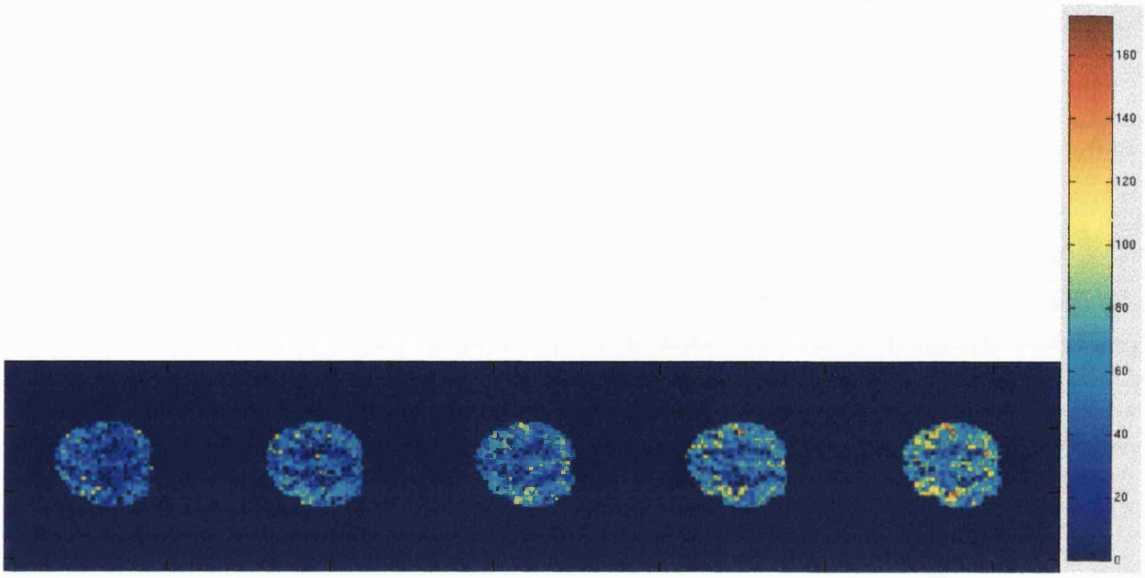

State 1 - Rest (31 mm Hg) | State 2 (37 mm Hg) | State 3 (43 mm Hg) | State 4 (47 mm Hg) | State5 (51 mm Hg)

Figure 6-4 CBF in ml/100g/min for all $PetCO_2$ states.

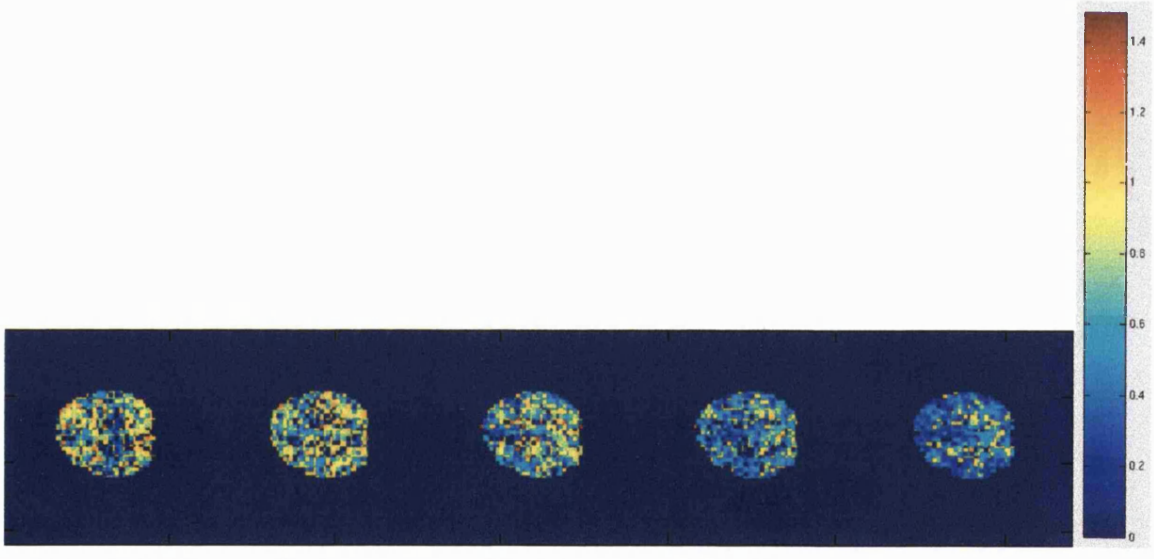

State 1 - Rest (31 mm Hg) | State 2 (37 mm Hg) | State 3 (43 mm Hg) | State 4 (47 mm Hg) | State5 (51 mm Hg)

Figure 6-5 Inflow delay in s for all $PetCO_2$ states.

Inflow delay in s			
$PetCO_2$ in mm Hg	grey matter segment (51 voxels)	white matter segment (57 voxels)	global segment (321 voxels)
31.15	0.56 +/- 0.29 (51%) med. 0.51; se 0.04	0.73+/- 0.32(43%) med. 0.75; se 0.04	0.64 +/- 0.33 (52%) med. 0.70; se 0.02
36.50	0.66 +/- 0.24 (37%) med. 0.65; se 0.03	0.41 +/- 0.36 (88%) med. 0.45; se 0.05	0.59 +/- 0.34 (58%) med. 0.65; se 0.02
43.46	0.56+/- 0.27 (48%) med. 0.55; se 0.04	0.61 +/- 0.39 (64%) med. 0.75; se 0.05	0.59 +/- 0.33 (55%) med. 0.55; se 0.02
46.68	0.46 +/- 0.17 (36%) med. 0.46 se 0.02	0.39 +/- 0.33 (83%) med. 0.41; se 0.04	0.44 +/- 0.26 (60%) med. 0.45; se 0.01
51.38	0.36 +/- 0.17 (47%) med. 0.37; se 0.02	0.51 +/- 0.32 (62%) med. 0.50; se 0.04	0.45+/- 0.26 (57%) med. 0.43; se 0.01

Table 6-3 Parametric hypercapnia experiment: inflow delay results for global and grey and white matter segments. All values are listed in the following format: mean +/- standard deviation (% mean); median; standard error.

The mean CBF and inflow delay for each segment is plotted against $PetCO_2$ in Figure 6-6 and Figure 6-7. Using linear regression, the correlations between CBF and $PetCO_2$ and between inflow delay and $PetCO_2$ were calculated; the linear regression results are drawn as straight lines in Figure 6-6 and Figure 6-7. Correlations with a p-value < 0.05 will be considered significant. There is a strong correlation between an increase in $PetCO_2$ and increases in CBF for the grey and global segments ($r \sim 0.98$; $p \leq 0.002$), for the white matter segment this correlation is moderate and not significant ($r=0.49$; $p=0.20$). For the global and grey matter segment, the decrease in inflow delay also correlates strongly with the increase in $PetCO_2$ ($r \sim -0.89$; $p < 0.03$), while for the white matter segment this is again a weaker correlation ($r = -0.57$; $p=0.16$). A goodness-of-fit test, which takes the errorbars on the data into account, shows how the linear model is a sufficient model for the grey and global segment CBF values ($Q=0.43$ and 0.02 resp.) and for the grey matter delay ($Q=0.002$). The white matter segment CBF and the white matter and global segment delays, however, give Q values of $1.3 \cdot 10^{-5}$, $2.6 \cdot 10^{-6}$ and $6.2 \cdot 10^{-6}$ resp., i.e. the simple linear model does not describe these data sufficiently. The slope of these fitlines does give an indication of the responsiveness of these parameters to CO_2, but it is not a reliable predictor or characterization of the responsiveness and should therefore be interpreted with caution.

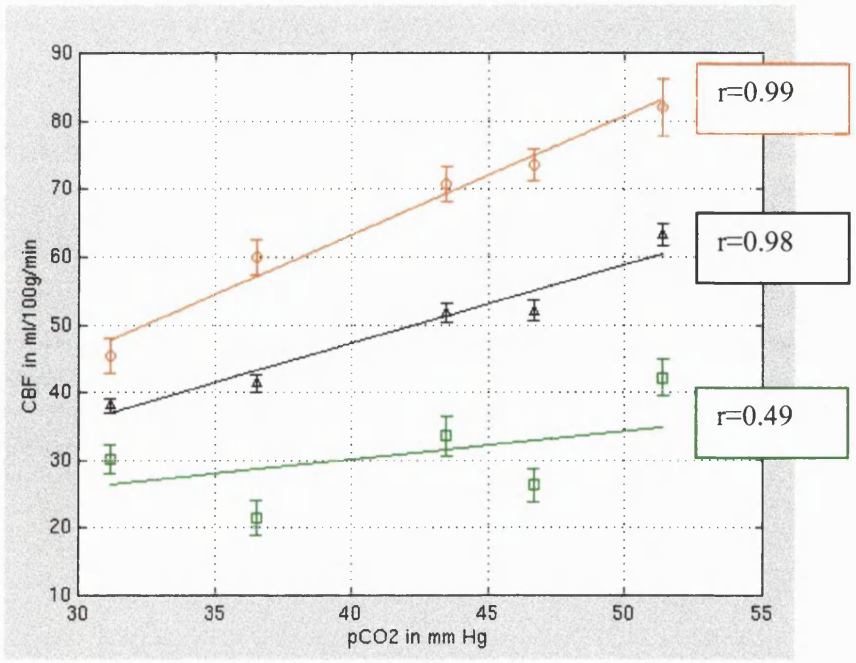

Figure 6-6 Mean CBF +/- se for global (black ^), grey matter (red o) and white matter (green square) segments. Linear regression plotted as line.

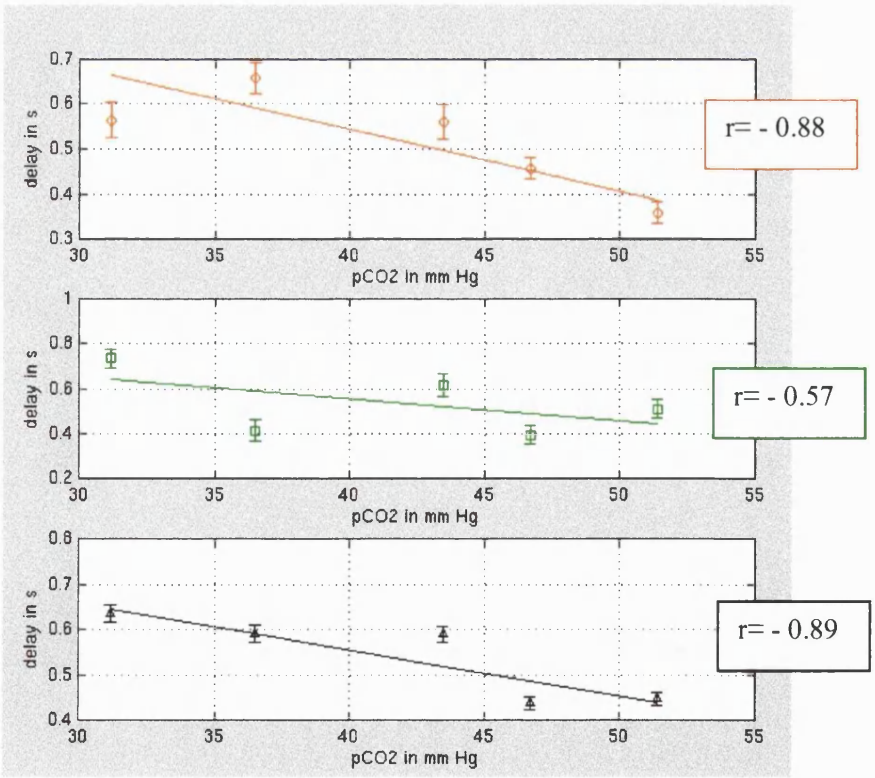

Figure 6-7 Mean inflow delay +/- se for global (black ^), grey matter (red o) and white matter (green square) segments. Linear regression plotted as line.

With these comments made, the slopes of the CBF and inflow delay regressions (the number of ml/100g/min increase in CBF per mm Hg increase in $PetCO_2$ - the cerebrovascular reactivity- and the number of seconds decrease in delay per mm Hg increase in $PetCO_2$) are given in Table 6-4. The results for which the linear model is valid, and the slope therefore a sufficient representation of the responsiveness, are marked with a cross.

segment	Cerebrovascular Reactivity		slope delay vs $PetCO_2$	
	(ml/100g/min / mm Hg)	% CBF change / mm Hg	(s / mm Hg)	% delay change / mm Hg
grey matter (51 voxels)	1.75 +/- 0.18 †	3.67 +/- 0.38 †	$(-1.40 +/- 0.20)\cdot 10^{-2}$ †	-2.08 +/- 0.29†
white matter (57 voxels)	0.41 +/- 0.15	1.55 +/- 0.55	$(-1.00 +/- 0.30)\cdot 10^{-2}$	-1.52 +/- 0.41
global (321 voxels)	1.17 +/- 0.08 †	3.15 +/- 0.22 †	$(-1.00 +/- 0.10)\cdot 10^{-2}$	-1.59 +/- 0.16

Table 6-4 Slopes of CBF vs $PetCO_2$ regression (cerebrovascular reactivity) and of delay vs $PetCO_2$.†linear model is sufficient for these data, Q value from goodness-of-fit test > 0.001.

Reich and colleagues have measured cerebrovascular reactivity (CR) using Xenon-133 by measuring CBF during rest and one hypercapnic state 5-10 mm Hg above rest level. They found CR values of 2.03 +/- 0.58 (for an age range 21-24) and 1.36 +/- 0.41 (for an age range 34-40) ml/100g/min/mm Hg for grey matter and 0.69 +/- 0.11 (for an age range 21-24) and 0.59 +/- 0.17 (for an age range 34-40) ml/100g/min/mm Hg for subcortical white matter (Reich et al, 1989). The volunteer in this study was aged 28 and his CR values for the grey and white matter segments are therefore in accordance with Reich's findings, although the here found white matter CR should be interpreted with caution as goodness-of-fit test has shown that the data are not sufficiently described by the linear model.

When using the whole $PetCO_2$ range the white matter segment CR results are in accordance with Reich's findings, but from one state to the next, the CBF change does not give a reliable prediction of the CR. For instance, from State 1(rest) to State 2 (+ 5.35 mm Hg) the mean CBF in the white matter segment *decreases* from 30 to 21 ml/100g/min,

suggesting of CR of ~ -1.63 ml/100g/min /mm Hg. It is well established that CBF in grey and white matter increases linearly over this range of $PetCO_2$ values (Harper et al, 1990; Grubb et al. 1974). This means that *relative* white matter CBF changes will not, like the absolute CBF values, be reliably measured with the presently implemented FAIR technique. Combining this finding with the results discussed in Chapter 5, section 5.4.7, this means that white matter CBF, both in absolute as relative terms, is out of reach of FAIR with the current implementation and field strength. Therefore from now on only grey matter and global CBF values will be reported. This finding also implies the FAIR technique implemented here is most suitable for studying normal and elevated grey matter and global CBF. It is less appropriate for looking at situations with lowered CBF, such as misery perfusion and stroke.

At this resolution (~ 110 mm^3 voxel) a wide range of expected CBF changes of 10-80% has been reported for typical visual and motor tasks (Gonzalez-At et al., 2000; Miller et al., (2001)). For BOLD a range of 0.5-1.5% change is to be expected at this resolution, for these sorts of tasks at this field strength (Miller et al., 2001). With this hypercapnia study, a cognitively relevant CBF and BOLD range has therefore been studied, as grey matter CBF changes with 81% and grey matter BOLD signal with 6% over the mm Hg increase.

Looking at our hypercapnia data, what is the minimum percentage CBF change for which we get a significant change in inflow delay? The mean +/- standard error of the rest state delay is 0.56 +/- 0.04 s for grey matter and 0.64 +/- 0.02 for the global segment, which means that a significant decrease of 3 times the standard error gives means smaller than 0.44 and 0.58 s, respectively. These delay values are reached after a $PetCO_2$ increase of roughly 6-9 mm Hg which means for CBF increases of ~ 20-30 % (calculated using Table 6-4; note the linear model for delay vs $PetCO_2$ is not a sufficient description of the data, so the slope is only a first approximation of the responsiveness). This rough calculation suggests that significant inflow delay changes will occur during the performance of cognitive tasks. This has also been reported recently by Gonzalez-At et al. and Yang and colleagues (Gonzalez-At et al., 2000; Yang et al., 2000).

The next important question is: what happens if the (change in) inflow delay is not taken into account in the data modelling? What sort of errors will be found for the fitted

CBF if the inflow delay is not part of the model? If the data are fitted without an inflow delay a drop in CBF values of 30-60% is observed for the global and the grey matter segments (Figure 6-8). The grey matter CBF slope (CR) drops 13% from 1.75 (r=0.97; p=0.001) to 1.52 (r=0.98; p=0.002) and the global segment drops 16% from 1.17 (r=0.98; p= 0.002) to 0.98 ml/100g/min/mm Hg (r=0.97; p= 0.004). The grey matter linear model is still valid for the CBFO data (Q=0.044 was 0.43), although the goodness of fit has decreased, and the linear model is not sufficient any more for the global segment ($Q=1.41*10^{-8}$ was 0.019). For grey matter, the slopes (CR) with and without delay included are therefore quite similar, even though the CBF values have shifted downwards significantly. For the global segment the slope (CR) also does not change very much, but the data are noisier and the linear model is not longer a sufficient description of the data.

If the inflow delay is assumed to be constant from rest to activated states, the CBF for the activated states (which in fact will have lower inflow delays) will be overestimated. When the grey matter inflow delay for the rest state (0.56 s) is used as a constant for the fitting of the + 20 mm Hg $PetCO_2$ state, the grey matter CBF is overestimated by 26% on average, compared to the situation where the correct lower inflow delay (0.36 s) is used for this hypercapnic state. Using an inflow delay that is appropriate for the activation/rest state is therefore important. This finding is supported by the work of Yang and colleagues (Yang et al., 2000) who calculated an error of 10-30% in CBF if rest state delays were used for the fitting of CBF in activated states.

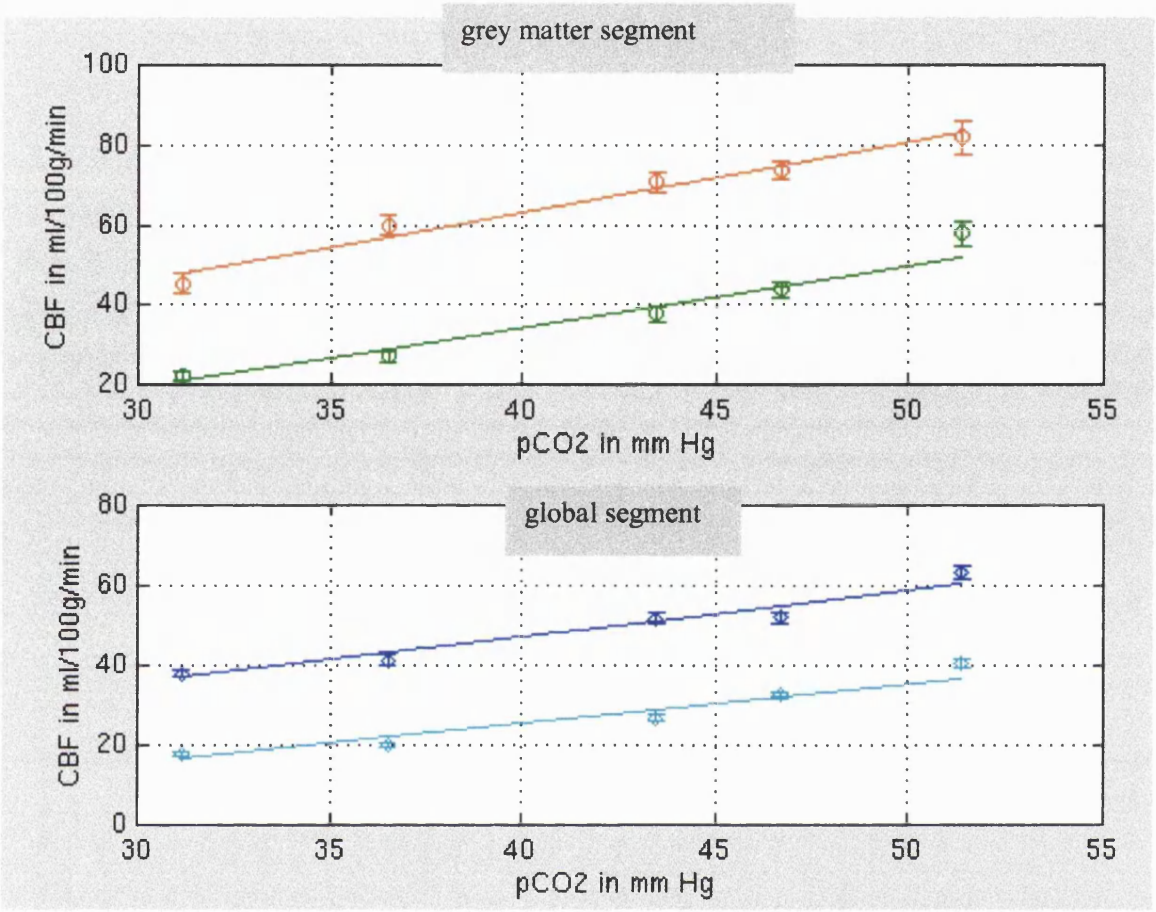

Figure 6-8 Comparing fitting with/without inflow delay: results for CBFD and CBFO models for grey matter and global segments. For both segments the lower line is the result of the CBFO fit.

Linear regression plots for the BOLD signal for the grey, white and global segments (defined on the basis of the structural scan) are given in Figure 6-9. The BOLD signal is very strongly correlated with the $PetCO_2$ values: r=0.96 (p=0.005), 0.96 (p=0.005) and 0.98 (p=0.002) for the grey, white and global segments respectively. A linear relation is indeed a sufficient model for these data as the goodness-of-fit test proves: for the grey, white and global segments Q-values of respectively 0.60, 0.19 and 0.10 were found. The slopes for these fitlines (in absolute and relative terms) are given in Table 6-5.

	change in BOLD(a.u.) /mm Hg	% change in BOLD/mm Hg
grey segment (57 voxels)	6.87 +/- 1.51†	0.32 +/- 0.07†
white segment (110 voxels)	4.03 +/- 0.51†	0.23 +/- 0.03†
global segment (620 voxels)	5.85 +/- 0.60†	0.30 +/- 0.03†

Table 6-5 Slopes for the regression of BOLD signal to $PetCO_2$ values. Data for which the linear model is sufficient are marked with a †.

The whole brain slope of 0.30 +/- 0.03%/mm Hg falls within the range of the 0.36 +/- 0.08 %/mm Hg reported by Davis et al. (Davis et al., 1998) and the 0.21 +/- 0.06 %/mm Hg reported by Kastrup et all (Kastrup et al., 2001); these two groups used smaller voxels, though, 70 and 18 mm^3 respectively, while the voxels in this study have a volume of 110 mm^3.

The relationship between relative BOLD and relative CBF changes for grey matter has been a topic of interest in the literature, some groups have reported a close to linear relationship between these two parameters (Hoge et al., 1999) while others find no correlation between the two (Kim et al., 1997). The percentage CBF change versus the percentage BOLD change is plotted in Figure 6-10. The r-value for this correlation is 0.93 (p=0.04) and the Q-value for the linear model is 0.86. For this data set there is therefore a linear relation between these two parameters, which suggests that the relative BOLD signal can be used as an indicator of relative CBF changes. In this analysis the errors in BOLD signal have been ignored, as they are much smaller than the errors in CBF. Furthermore the small difference in $PetCO_2$ values between the BOLD and CBF acquisitions are also not taken into account.

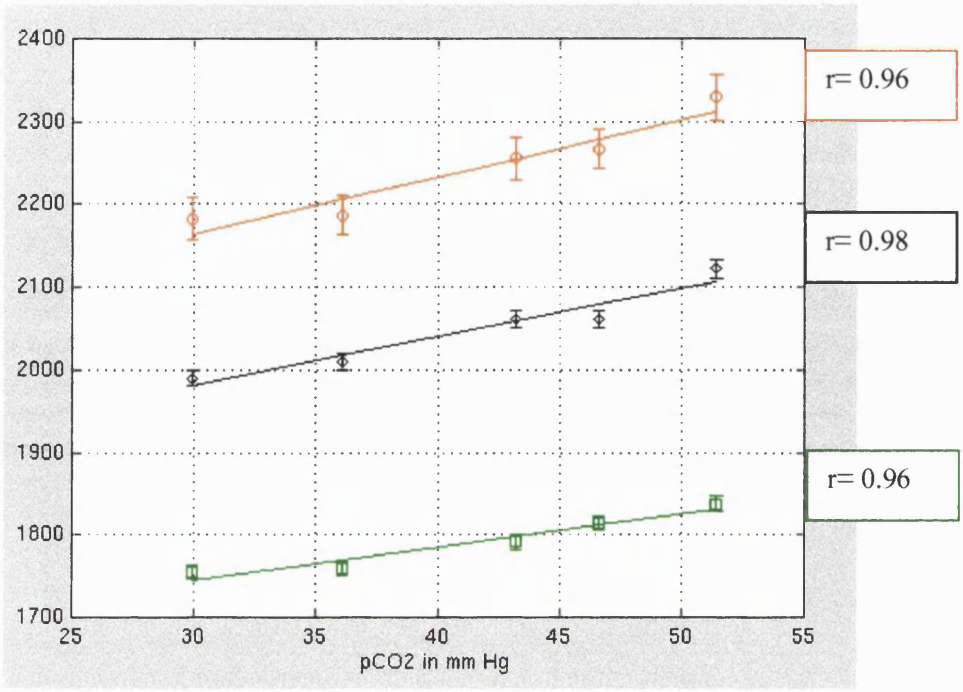

Figure 6-9 Mean BOLD signal +/- se for global (black ^), grey matter (red o) and white matter (green square) segments. Linear regression plotted as line.

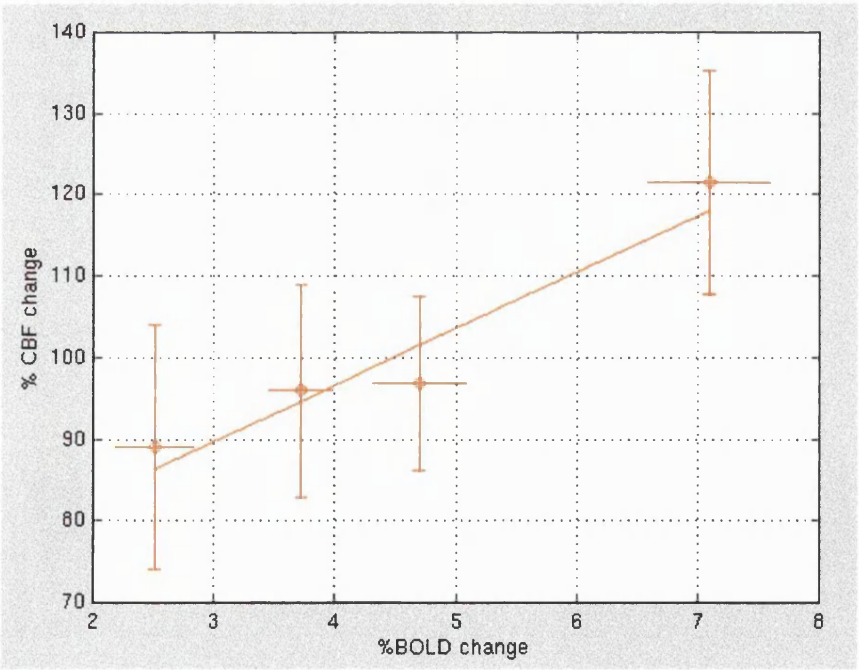

Figure 6-10 Percentage CBF change vs percentage BOLD change for grey matter. Straight line is result of linear regression.

6.3 Variability of CBF and inflow delay over 11 volunteers

6.3.3 Materials and Methods

Baseline CBF was measured using FAIR for a total of 11 volunteers. The baseline state consisted of watching a video of coral reef. In order to prevent loss of arousal, the volunteer was asked to push a button each time a particular colour (red, green, yellow or pink, randomised over volunteers) appeared in the video.

The volunteers were immobilised with padding on the sides of the head and by an arc around the top of the head, designed to minimise out-of-plane (z) movement along the magnet's bore. This immobilisation setup will be discussed more extensively in the next chapter.

FAIR data were acquired following the procedures described in Chapter 5, section 5.4.7. The (axial) imaging slice was positioned through the ventricles and top of the brainstem. The inversion efficiency was determined by fitting separately acquired SL data. Inversion times for these SL acquisitions were, as before, 300, 600, 1000, 1200,1500 and 3000 ms. There were 36 averages of SL data for each inversion time. The FAIR data were acquired at inversion times TI of 300, 600, 1000, 1200, 1500 and 2000 ms, with 18 averages at each TI. For both SL and FAIR pulse sequences, the echo time was 42 ms, the b-factor was 5 s/mm^2, the inversion slice thickness was 20 mm, the readout slice thickness was 5 mm and the recovery time after each inversion-readout block was 2.65 s. The SL and FAIR data were all acquired at a FOV of 300mm, with a 64*64 acquisition matrix. The acquisition order of the inversion times was interleaved, to minimise the effect of time on the results. The total duration of the experiment for each volunteer was ~ 30 minutes, 14 minutes for the FAIR acquisitions and 16 minutes for the SL acquisitions. For two volunteers (nrs 10 and 11) a lower rf pulse power was used due to rf coil problems. This resulted in a slightly lower inversion efficiency, but on careful examination this had no impact on the results nor the quality of the data.

6.3.4 Results and discussion

volunteer	grey matter segment		global segment	
	CBF in ml/100g/min	delay in s	CBF in ml/100g/min	delay in s
1	64.41 +/- 20.35 (32%) med. 62.55; se 2.09 # voxels = 95	0.47 +/- 0.20(43 %) med. 0.46; se 0.02 # voxels = 95	55.09 +/- 25.10(46%) med. 53.08; se 1.04 # voxels = 580	0.51+/- 0.28(54%) med. 0.49; se 0.01 # voxels = 580
2	80.96 +/- 23.39(29%) med. 78.89; se 2.54 # voxels = 85	0.43 +/- 0.23(54%) med. 0.44; se 0.03 # voxels = 85	76.03 +/- 30.39(40%) med. 73.16; se 1.33 # voxels = 522	0.48 +/- 0.27(56%) med. 0.47; se 0.01 # voxels = 522
3	62.75 +/- 16.79(27%) med. 62.16; se 1.77 # voxels = 90	0.45 +/- 0.24(53%) med. 0.45; se 0.03 # voxels = 90	54.25 +/- 21.78(40%) med. 54.62; se 1.03 # voxels = 445	0.53 +/- 0.28(53%) med. 0.51; se 0.01 # voxels = 445
4	65.95 +/- 29.06(44%) med. 61.31; se 2.84 # voxels = 105	0.57 +/- 0.28(48%) med. 0.53; se 0.03 # voxels = 105	55.26 +/- 29.26(53%) med. 52.78; se 1.34 # voxels = 478	0.60 +/- 0.31(52%) med. 0.54; se 0.01 # voxels = 478
5	59.80 +/- 22.13(37%) med. 55.78; se 2.40 # voxels = 85	0.37 +/- 0.24(65%) med. 0.26; se 0.03 # voxels = 85	50.26 +/- 23.50(47%) med. 48.62; se 1.11 # voxels = 450	0.40 +/- 0.28(70%) med. 0.39; se 0.01 # voxels = 450
6	80.73 +/- 29.29(36%) med. 75.29; se 3.10 # voxels = 89	0.38 +/- 0.15(41%) med. 0.39; se 0.02 # voxels = 89	65.18 +/- 32.25(49%) med. 63.03; se 1.47 # voxels = 480	0.44 +/- 0.24(55%) med. 0.43; se 0.01 # voxels = 480
7	61.75 +/- 17.79(29%) med. 63.15; se 2.14 # voxels = 69	0.47 +/- 0.26(55%) med. 0.45; se 0.03 # voxels = 69	53.62 +/- 24.01(45%) med. 52.03; se 1.12 # voxels = 461	0.51 +/- 0.29(57%) med. 0.48; se 0.01 # voxels = 461
8	82.56 +/- 24.47(30%) med. 83.35; se 2.83 # voxels = 75	0.41 +/- 0.19(46%) med. 0.41; se 0.02 # voxels = 75	68.94 +/- 29.54(43%) med. 68.27; se 1.37 # voxels = 467	0.44 +/- 0.26(59%) med. 0.43; se 0.01 # voxels = 467
9	77.68 +/- 35.74(46%) med. 68.04; se 3.59 # voxels = 99	0.47 +/- 0.25(54%) med. 0.44; se 0.03 # voxels = 99	62.48 +/- 31.09(50%) med. 59.08; se 1.45 # voxels = 461	0.49 +/- 0.28(57%) med. 0.46; se 0.01 # voxels = 461
10	63.92 +/- 22.48(35%) med. 59.77; se 3.03 # voxels = 55	0.50 +/- 0.27(54%) med. 0.46; se 0.04 # voxels = 55	54.89 +/- 25.29(46%) med. 54.09; se 1.34 # voxels = 356	0.47 +/- 0.29(62%) med. 0.45; se 0.02 # voxels = 356
11	67.90 +/- 18.39(27%) med. 68.99; se 2.32 # voxels = 63	0.40 +/- 0.23(57%) med. 0.40; se 0.03 # voxels = 63	58.56 +/- 21.99(38%) med. 57.58; se 1.03 # voxels = 460	0.44 +/- 0.27(61%) med. 0.43; se 0.01 # voxels = 460
MEAN +/- sd	**69.86 +/- 8.75(13%)**	**0.45 +/- 0.06(13%)**	**59.51 +/- 7.81(13%)**	**0.48+/- 0.05(11%)**

Table 6-6 CBF and delay results over grey and global segments for all volunteers. Listed in each cell: mean +/- sd (sd as % mean), median, standard error and number of voxels.

volunteer	grey matter segment		global segment	
	sd on CBF as mean over each voxels sd as % of its mean	sd on delay as mean over each voxels sd as % of its mean	sd on CBF as mean over each voxels sd as % of its mean	sd on delay as mean over each voxels sd as % of its mean
1	27.69 +/- 7.99(29%) med. 26.61; se 0.82 # voxels = 94	34.99 +/-11.07(32%) med 35.22; se 1.14 # voxels = 95	30.74 +/-10.39(34%) med. 29.21; se 0.44 # voxels = 570	36.69 +/-14.35(39%) med. 36.67; se 0.60 # voxels = 577
2	27.37 +/-10.72(39%) med. 26.45; se 1.16 # voxels = 85	32.75 +/-13.86(42%) med. 31.67; se 1.50 # voxels = 85	26.55 +/-11.39(43%) med. 25.31; se 0.50 # voxels = 517	32.69 +/-13.09(40%) med. 31.25; se 0.57 # voxels = 522
3	25.43 +/-11.07(44%) med. 25.26; se 1.18 # voxels = 88	32.38 +/-11.81(36%) med. 30.29; se 1.25 # voxels = 90	28.11 +/-10.58(38%) med. 26.59; se 0.51 # voxels = 435	34.90 +/-11.26(32%) med. 34.16; se 0.53 # voxels = 444
4	32.80 +/-12.39(38%) med. 30.62; se 1.24 # voxels = 100	39.66 +/-13.45(34%) med. 36.82; se 1.31 # voxels = 105	34.30 +/-12.94(38%) med. 32.55; se 0.60 # voxels = 466	40.77 +/-13.72(34%) med. 39.32; se 0.63 # voxels = 477
5	29.64 +/-11.09(37%) med. 28.29; se 1.22 # voxels = 83	37.57 +/-11.89(32%) med. 37.37; se 1.29 # voxels = 85	31.25 +/-12.36(40%) med. 29.18; se 0.58 # voxels = 448	38.79 +/-13.63(35%) med. 37.33; se 0.64 # voxels = 450
6	22.16 +/- 9.36(42%) med. 20.74; se 0.99 # voxels = 89	29.78 +/- 9.96(33%) med. 28.17; se 1.06 # voxels = 89	25.98 +/-11.22(43%) med. 24.37; se 0.51 # voxels = 477	33.79 +/-12.59(37%) med. 31.82; se 0.57 # voxels = 480
7	31.38 +/-13.88(44%) med. 27.63; se 1.67 # voxels = 69	36.82 +/-12.47(34%) med. 36.09; se 1.50 # voxels = 69	32.60 +/-12.48(38%) med. 30.72; se 0.59 # voxels = 453	39.42 +/-13.81(35%) med. 37.82; se 0.65 # voxels = 458
8	26.54 +/- 9.34(35%) med. 25.44; se 1.08 # voxels = 75	34.14 +/-11.40(33%) med. 33.52; se 1.32 # voxels = 75	27.81 +/-10.78(39%) med. 26.15; se 0.50 # voxels = 458	34.67 +/-13.41(39%) med. 33.92; se 0.62 # voxels = 462
9	27.04 +/-11.72(43%) med. 24.67; se 1.18 # voxels = 98	34.75 +/-12.50(36%) med. 31.97; se 1.26 # voxels = 99	28.97 +/-11.72(40%) med. 26.86; se 0.55 # voxels = 457	36.51 +/-13.26(36%) med. 34.63; se 0.62 # voxels = 461
10	35.31 +/-14.59(41%) med. 31.13; se 1.97 # voxels = 55	35.31 +/-14.59(41%) med. 31.13; se 1.97 # voxels = 55	31.85 +/-12.02(38%) med. 29.55; se 0.65 # voxels = 344	38.30 +/-13.96(36%) med. 37.49; se 0.75 # voxels = 349
11	26.64 +/- 7.58(28%) med. 24.89; se 0.96 # voxels = 63	33.29 +/- 9.58(29%) med. 31.98; se 1.21 # voxels = 63	28.81 +/- 9.14(32%) med. 27.53; se 0.43 # voxels = 456	36.09 +/-11.21(31%) med. 35.12; se 0.52 # voxels = 459
MEAN +/- sd	**28.36 +/- 3.68(13%)**	**34.68 +/- 2.71(8%)**	**29.72+/-2.62(9%)**	**36.60 +/- 2.51(7%)**

Table 6-7 Standard deviation on CBF and delay results over grey and global segments for all volunteers. Derived using repeated measures method. First the standard deviation for each voxel is calculated as percentage of it's mean and then this percentage is averaged over all voxels. Listed in each cell: mean +/- sd (sd as % mean), median, standard error and number of voxels.

The CBF values found fall within the range reported in the literature (for a review: see Calamante et al., 1999). As mentioned before, the delay values here are somewhat shorter than what some groups find (~0.8s; Ye et al. 1996; Yang et al. 1998), however, more recent studies have been reported that find similar inflow delays (Gonzalez-At et al., 2000). Factors contributing to the differences in inflow delay are the labelling site (in or under the slice of interest, here the latter is used) and the amount of flow spoiling applied, as the inflow delay increases with flow spoiling.

The global segment results are listed only as an indication of 'global' CBF and inflow delay, values often reported in the literature. As this segment contains grey and white matter voxels it is a sort of weighted mean of these – very different– segments and therefore of limited information value.

The standard deviation of CBF for grey matter that was derived using the repeated measures method should ideally be equal to the standard deviation over the ensemble of voxels in the grey matter segment. In practice, CBF will vary over grey matter voxels and the standard deviation of the grey matter segment is therefore somewhat larger than the standard deviation calculated with the repeated measures method. This can be seen when comparing the first value in each cell of Table 6-7 with the percentage value in brackets of Table 6-6. For the global segment this comparison is nonsensical, as this segment will contain both grey and white matter voxels, each with very different CBF and delay values.

Table 6-7 demonstrates how single voxel results have on average a large standard deviation: with sds of order ~30%, it would only just be possible to pick up the largest CBF changes that can occur in cognitive experiments for this voxel size, as these CBF changes are in the range of 10-80% (Gonzalez-At et al., 2000; Miller et al., (2001)). It is therefore useful to study an ensemble of grey matter voxels such as, for instance, the grey segment listed here. For this grey segment the standard deviation on CBF is ~5%, making it sensitive to CBF changes $\geq$ 12.5%. It is therefore possible to pick up the CBF changes in this grey matter segment over a cognitively relevant range.

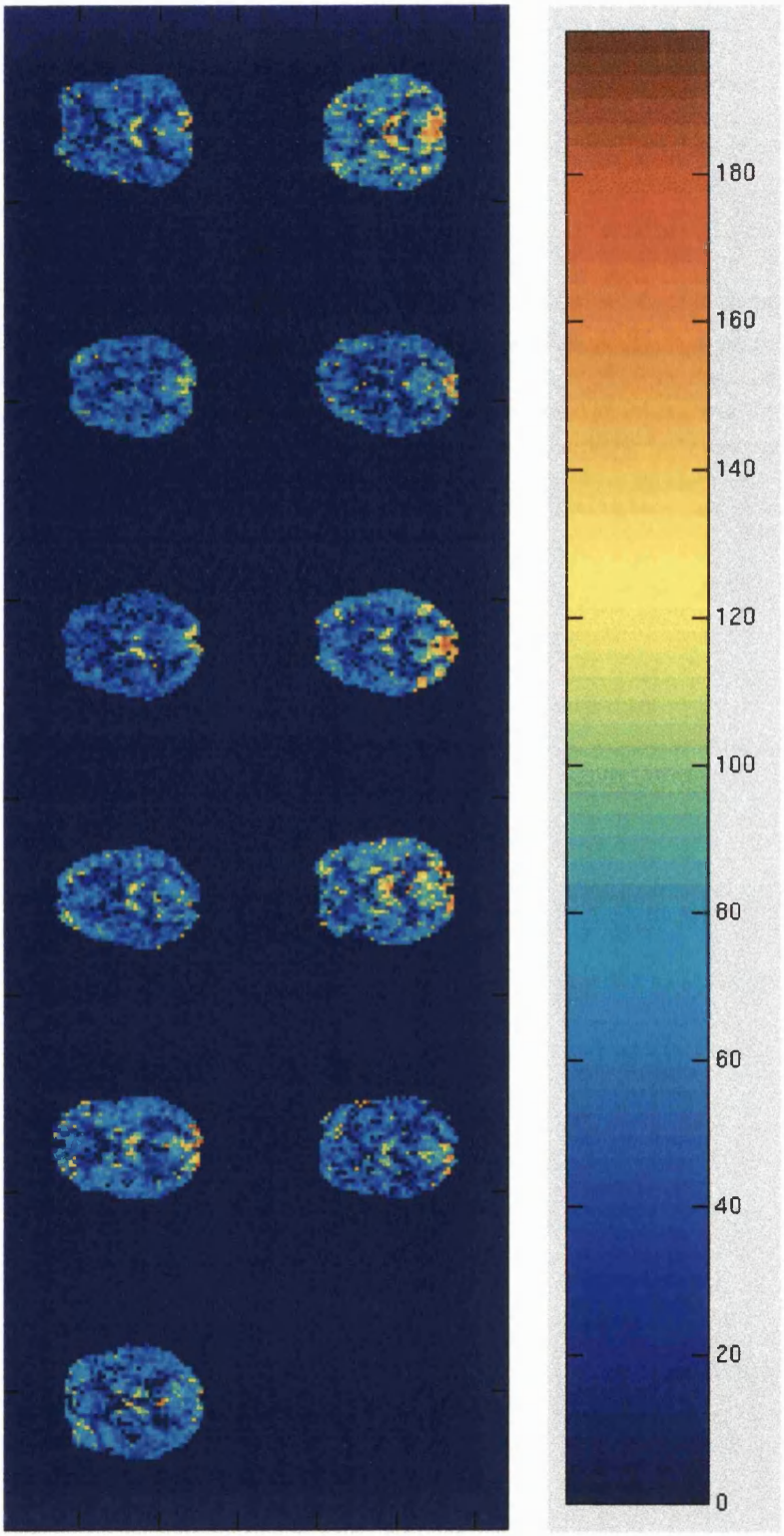

Figure 6-11 CBF maps for all 11 volunteers (plotted left to right, row by row).

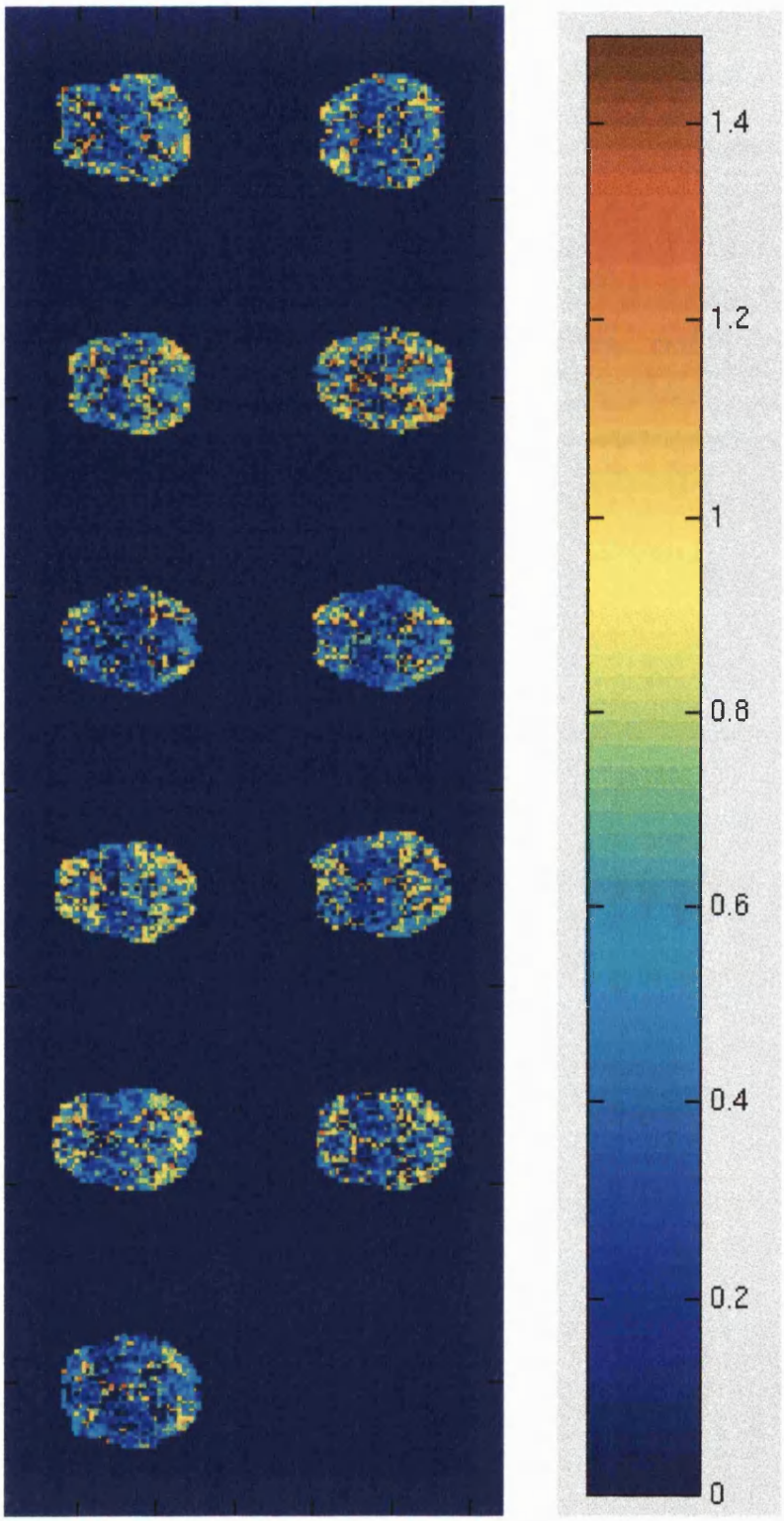

Figure 6-12 Inflow delay maps for all 11 volunteers (plotted left to right, row by row).

Interestingly, in all volunteers there are bilaterally medial areas in the inflow delay images with low inflow delay (~0.2s), while in the CBF images these areas have normal CBF. Low SNR for white matter voxels or voxels with a large CSF partial voluming can result in low inflow delay and CBF values as was the case for the rest state of the parametric hypercapnia experiment in section 6.2.2. However, for many of the voxels in the areas with lowered inflow delay this is not the reason. Their SNR is high and their fits are as good as for voxels with normal CBF and inflow delay (see Figure 6-13). The areas of lowered inflow delay encompass the thalamus and basal ganglia, as can be deduced from Figure 6-13 (a). These subcortical structures have a high CBF (Nakane et al. 1998; De Reuck et al., 1998). As a tentative hypothesis I propose that it is the different 'plumbing' of these regions that results in locally shortened inflow delays.

This chapter has demonstrated that baseline and hypercapnic CBF values measured with the FAIR technique implemented here are in accordance with the literature. This serves as a validation of the technique.

It was argued that white matter CBF, both in absolute as relative terms, cannot be measured reliably with FAIR with the current implementation and field strength. Therefore only grey matter and global CBF values will be reported from now on. The errorbars on the CBF measurement indicate that it is possible to detect cognitively relevant CBF changes in a grey matter segment.

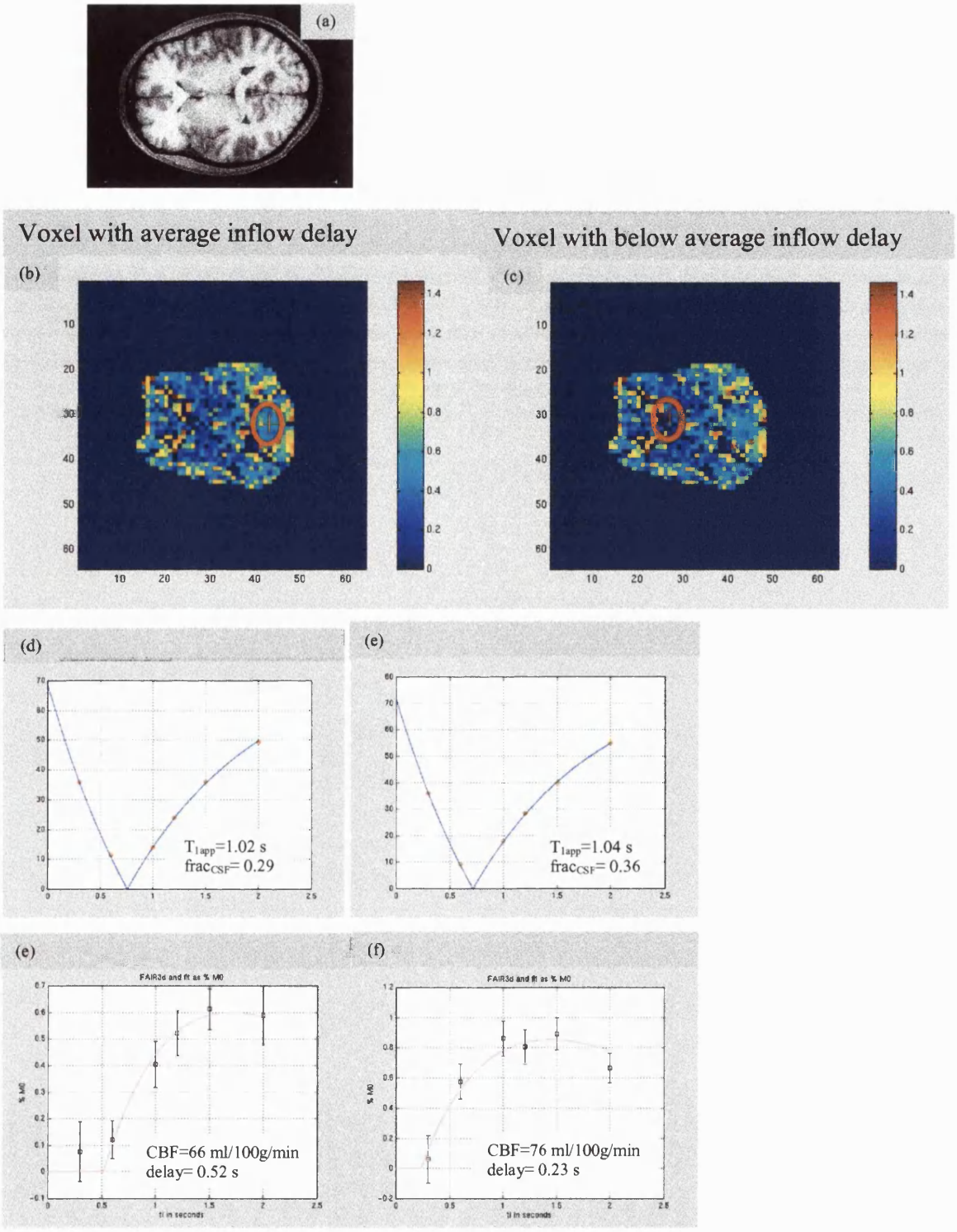

Figure 6-13 Results for a voxel with normal inflow delay (~0.5s), left, and for voxel with shortened inflow delay (~ 0.2s), right. (a) T_1 weighted structural scan of this slice. Second row (b), (c): inflow delay maps with red cross and circle marking the voxel, third row (d), (e): SL fit, bottom row (e), (f): fit of FAIR data. Note the scales are not equal for corresponding plots. Taken from data of volunteer number 1.

7 CBF, inflow delay, BOLD signal and cerebrovascular reactivity over the course of a day

7.1 Introduction

The aim of this experiment was to measure cerebrovascular reactivity (CR) and baseline CBF, inflow delay and BOLD signal in normals over the course of a day. Secondly, this experiment also served as a pilot study to evaluate the feasibility of longitudinal CBF studies using the FAIR technique.

Longitudinal CBF studies are only possible if the changes in the parameter of interest that occur from session to session are predominantly physiological and not determined by volunteer repositioning, machine drifts and such (the so-called 'session effects'). For a single-slice FAIR experiment, it is predominantly inter-session movement (repositioning errors) that results in session effects. A specially designed repositioning device was therefore used to minimise repositioning errors and volunteer movement in general.

The following questions are the basis for this study:

- What is the variation of CR and baseline BOLD, CBF and inflow delay over the course of a day?
- Are there any (obvious) patterns in the diurnal BOLD/CBF/inflow delay/CR fluctuations?

To my knowledge, there are no reports of baseline measurements of BOLD, CBF or inflow delay over the course of a day. PET, the main quantitative CBF technique so far, is limited in its utility for longitudinal studies due to the repeated radioactive label injections that would be required. This experiment is therefore of interest simply to establish the diurnal variability of these parameters.

The CR over the course of a day, however, has been the topic of several studies (Ameriso et al., 1994; Placidi et al., 1998; Qureshi et al, 1999). This is because the CR is seen as an indicator of vascular reserve, and a lowered CR as a warning signal for stroke.

Ameriso and colleagues (Ameriso et al, 1994) have reported a significant (25%) decrease in relative CR in the morning compared to the afternoon and evening. This measurement was done using transcranial Doppler. Their findings fit in nicely with the clinical observation that stroke occurs more often in the early hours of the morning.

Placidi and colleagues and Qureshi and colleagues have replicated this morning CR reduction for patient groups with sleeping disorders (snoring) that are thought to be more at risk for stroke. Placidi also studied a control group of normals, for which he did not find a significant reduction in relative CR. Placidi studied quite a small group (8 volunteers), while Ameriso studied 20 subjects. A tentative hypothesis for this study was therefore that there is a reduction in CR in the early morning session compared to the afternoon and evening. All three aforementioned studies were measuring relative CR with Doppler; for this diurnal study in which absolute CR was measured using FAIR, the sensitivity to changes in CR had yet to be established.

7.2 Inter-session movement effects

7.2.1 Minimising inter-session movement

A special re-positioning device was built in-house by Peter Aston. It was designed to minimise inter-session movement, i.e. repositioning errors and other volunteer motion. In particular, translations along the magnet bore and nodding were to be avoided, as these are out-of-plane movements for the axial slice of interest. This device is pictured in Figure 7-1.

The device is clamped to the rf coil at the back and fastened with screws. The top of the volunteer's head touches an arc so that repositioning errors and volunteer movement along the bore are minimised. A blunt pin touches the volunteer's forehead: a circle is drawn around this pin at the beginning of the first session. A black cross is then also drawn on the volunteer's forehead; this cross is defined by the scanner's slice positioning laser beams. At the beginning of each new session the head is repositioned until the pin falls within the circle again and the black cross and laser beams overlap. Furthermore, standard rf coil side-clamps are used to minimise movements sideways and the head rests in head-shaped black cushioning. The volunteer's chin is supported by a neck brace, to prevent nodding movements further.

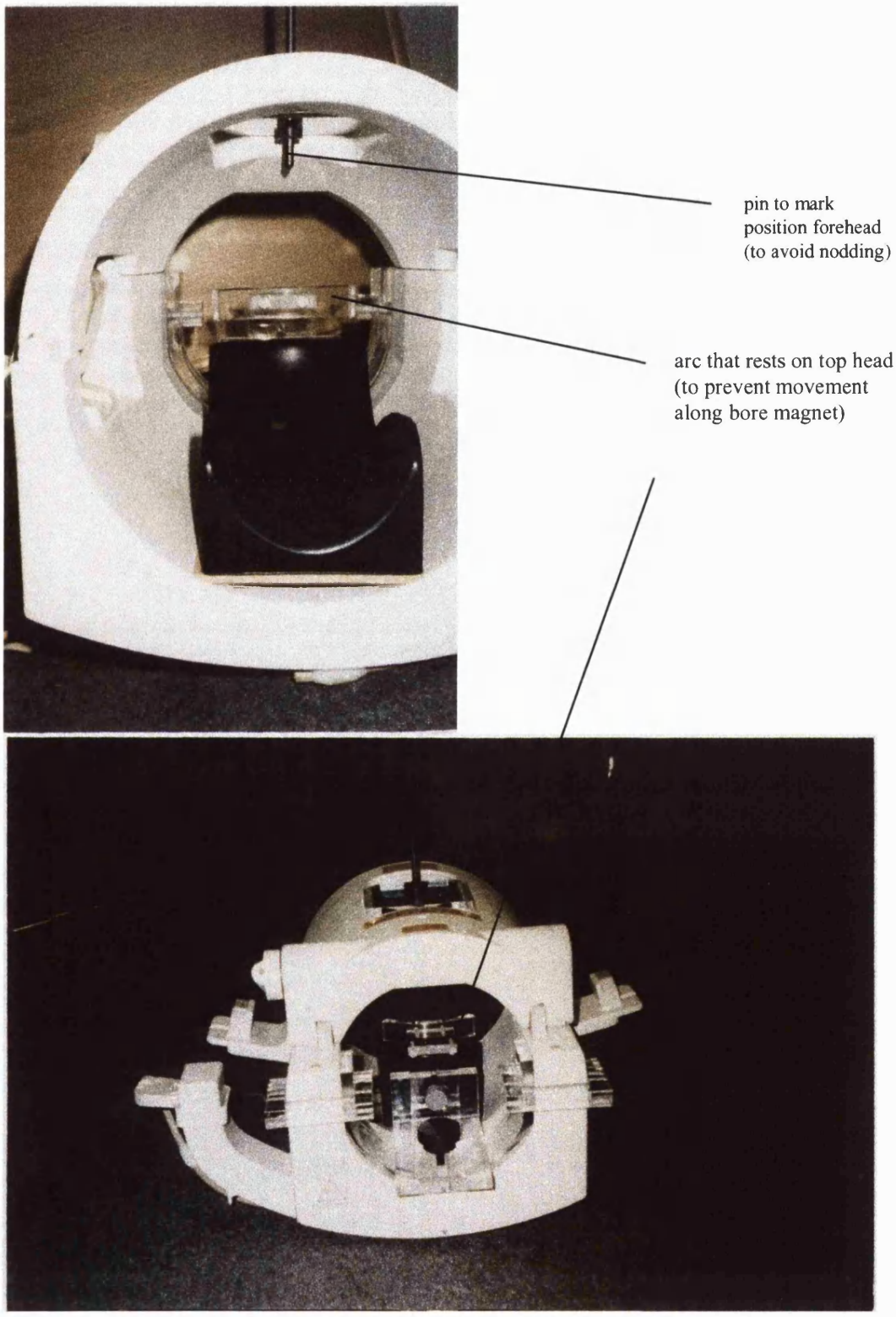

Figure 7-1 Minimising inter-session movement effects with a dedicated repositioning device.

7.2.2 The effects out-of-plane motion; choice of masks

The chances of significant out-of-plane movements are much larger for multi-session studies, mainly due to repositioning errors. As the FAIR technique implemented here only measures a single slice, a control experiment was performed to establish the effects of an out-of-plane shift. To that end, two volunteers were scanned following the imaging and analysis procedures of section 5.4.7. A rest state CBF measurement was made, the imaging slice was then shifted downwards by 5mm (= slice thickness) and the CBF was measured again for the new slice. Thus the effect of a repositioning error was mimicked, and a 'multi-session' data set generated with an exactly known out-of-plane shift between the two 'sessions'.

Assuming CBF to vary minimally over the two back-to-back CBF measurements (~ 45 minutes), the CBF values should be very similar for the first and second slice (the first and second 'session'), *if* the grey matter/white matter/CSF composition of the voxels in the masks of interest does not change dramatically over the 5 mm shift. Table 7-1 gives the absolute mean CBF and inflow delay differences (Δ) between the two sessions, for the global and grey matter masks. These global and grey matter masks were constructed for each 'session' following the criteria in section 5.4.7.

The global masks give smaller differences between sessions. This is to be expected, as any changes in partial voluming are more likely to average out over the large ensemble. The disadvantage of a global mask is that it will contain a mix of white and grey matter.

The grey matter masks are defined on the basis of their T_{1app} characteristics, CSF fraction and fit convergence as defined in section 5.4.7. These masks therefore use no prior knowledge of brain CSF and grey and white matter distributions. There is a way of incorporating this knowledge into the mask definition: by using information from segmented structural data, separately acquired. Using the sequence parameters listed in the 'Materials and methods' section below, whole brain structural and BOLD data were therefore also acquired for each session. If one coregisters the segmented structural data separately to each session's BOLD volume, a grey matter 'structural' mask can be defined per session consisting of voxels with a certain percentage grey matter. This method

assumes there is no significant motion between the FAIR and the BOLD acquisitions of each session, as these can not be coregistered to each other.

The results for these grey matter – structural ('grey-struc') masks are given in Table 7-2. The percentage of grey matter in each mask has been chosen in such a way as to give (close to) equal numbers of voxels to the standard grey matter masks used before, to facilitate comparisons. Voxels in the grey-struc masks that have not given converging fit results or have a fitted CBF > 200 ml/100g/min (vessels) were nulled, as is done by default for the standard grey matter masks.

	volunteer 1		volunteer 2	
	grey matter mask (85/106)	global mask (522/524)	grey matter mask (95/111)	global mask (580/601)
|Δ CBF| in ml/100g/min	8.46 (10%)	3.80 (5%)	1.22 (2%)	0.31 (1%)
|Δ inflow delay| in s	0.08 (19%)	0.06 (13%)	0.01 (2%)	0.03 (6%)

Table 7-1 Mimicking the effects of repositioning errors between sessions: changes in CBF and inflow delay for two volunteers after a 5 mm out-of-plane shift of the imaging slice. The number of voxels in each sessions's mask is given in brackets below the mask name. The difference in CBF or delay as percentage of its start value is given in brackets behind the difference.

	volunteer 1	volunteer 2
	grey-struc mask, 85% (100/96)	grey-struc mask, 87% (100/106)
|Δ CBF| in ml/100g/min	0.76 (1%)	4.00 (7%)
|Δ inflow delay| in s	0.01 (2%)	0.06 (13%)

Table 7-2 Using masks derived from structural scans, looking at the effects of repositioning errors between sessions: changes in CBF and inflow delay for two volunteers after a 5 mm out-of-plane shift of the imaging slice. The number of voxels in each session's mask is given in brackets below the mask name. The grey matter percentage in the mask name is derived from the structural segmentation results. The difference in CBF or delay as percentage of its start value is given in brackets behind the difference.

For these different masks, the changes in CBF for a 5 mm out-of-plane shift range from 1-10% and for inflow delay from 2-19%. The grey-struc masks are doing slightly better on average, with maximum changes in CBF of 7% and in inflow delay of 13%. These

measured CBF and inflow delay differences can be taken as an estimate of the minimum change in these parameters that is required before it can be considered to be physiologically significant. This estimate is valid only if out-of-plane shifts from session to session do not exceed 5 mm.

It is not immediately clear which is the optimal grey matter mask to use to minimise the impact of shifts, while still sampling a reasonably pure grey matter segment. Apart from minimising differences in CBF and delay for these two sessions (which is not a 100% reliable method, as that makes the assumption that the minimal CBF and delay difference is the correct one), it is also informative to look at GL inversion data over sessions.

GL data are independent of CBF and should therefore vary little over sessions. The mean sum of square differences between GL data over sessions for a mask is an indication of how well that mask keeps the mean voxel intensity constant. Considering this analysis includes GL intensity data over the whole TI range, this means this favours masks that select voxels with similar voxel T_{1app} values over sessions.

An overview of the sums of squared differences between GL arrays of different sessions (for all TI values) is given in Table 7-3 for the standard grey matter and the grey-struc masks. Apart from data of the two volunteers above, this Table also includes results for two volunteers of the 4 session study described below in section 7.3. As these are GL inversion data, this analysis is independent from the CBF results described later on.

	volunteer 1	volunteer 2	volunteer 3	volunteer 4	total
grey matter	61.52	15.40	2851	271.0	$3.199 \cdot 10^3$ (100%)
grey-struc mask, 86%	5.704	21.66	2250	130.3	$2.408 \cdot 10^3$ (75%)

Table 7-3 Sum of squared differences ($/10^6$ in a.u.) between GL inversion data (for all TI values) of different sessions for standard grey matter and 86% grey-struc masks.

Overall, the grey-struc masks give a 25% lower sum of squared differences between GL arrays of different sessions. Of course motion will affect all voxels in the imaging slice and the choice of voxel mask has nothing to do with that. However, it might be that the added

information of the segmented structural data helps to make a more robust choice of voxels over the sessions, voxels for which shifts do not change the partial voluming characteristics so dramatically. As variability over sessions is crucial for this longitudinal experiment, the grey-struc mask will be used as well as the standard grey matter mask to look at the data.

7.3 Measuring CBF, inflow delay, BOLD signal and CR over the course of a day

7.3.1 Materials and methods

7.3.1.1 Volunteers and scanning protocol

We successfully studied 6 women, measuring CBF, inflow delay, BOLD signal and CR over the course of a day. In one woman only baseline CBF, inflow delay and BOLD signal were measured. Data of one other volunteer were discarded due to gross movements during the study. The mean age +/- sd of the volunteers was 28 +/- 4. The volunteers' sex and age were deliberately restricted in this way, as CR has been reported to vary with age and sex (Kastrup et al., 1998; Kastrup et al., 1997) and CBF with age (Martin et al., 1991).

All women were healthy, not on any medication and had no history of cerebrovascular disease. The subjects abstained from caffeine containing drinks, alcohol and cigarettes starting the evening prior to the experiment. The activities and eating times throughout the day were similar for all volunteers: between the scanning sessions the volunteers ate and watched videos. Breakfast was after the first scanning session, lunch after the second and snacks were supplied all throughout the day. Before the first scanning session the volunteer was allowed a 20 min nap on the scanner bed, to try to make the first session as close as possible to a true 'just woken up' state.

There were four scanning sessions in a day: from 7.30 – 8.30, 11.30 – 12.30, 15.30 – 16.30 and 19.30 – 20.30. The acquisition order in every session was: Baseline ('rest') state: FAIR and BOLD measurements, Hypercapnia state: FAIR and BOLD measurements. In the first session the inversion efficiency was determined after the baseline and hypercapnia measurements. At the end of the fourth session a T_1 weighted structural was acquired.

The same coral reef video played during all sessions. A baseline task consisted of pressing a mouse button upon recognition of a designated colour (red, yellow, green or pink). The colour was different for each session and randomised over sessions for all subjects.

7.3.1.2 Technical implementation

The volunteer's head was repositioned from session to session using the custom-built repositioning gear and setup described in section 7.2.1. The subject was wearing a loose fitting mask over the nose and mouth. Through this a continuous flow of medical air was maintained of ~30 l/min. End-tidal pCO_2 ($PetCO_2$) was determined from gas continuously sampled via a nasal cannula and analysed using a mass spectrometer. The hypercapnia state consisted of a 8 mm Hg increase in $PetCO_2$ ($\approx$ 4% inspired CO_2) from baseline. A stable $PetCO_2$ was awaited before starting the measurements for each baseline or hypercapnic state. This setup for respiratory gas monitoring and control has been described more extensively in Chapter 6, section 6.2.1.1.

MRI data were acquired on a 2.0 T Siemens Vision MRI scanner. CBF was measured for a single 5 mm slice through the ventricles using FAIR with 6 inversion times (TI=0.3, 0.6, 1.0, 1.2, 1.5, 2.0 s) and 18 acquisitions per inversion point. The inversion efficiency was determined in the first session using the same pulse sequence but with two slice selective inversions, 6 inversion times (TI=0.3, 0.6, 1.0, 1.2, 1.5, 3.0 s) and 36 acquisitions per TI point. For both the slice selective and the FAIR pulse sequences, the in-plane resolution was 4.69·4.69 mm^2, the slice thickness was 5 mm, the inversion slice thickness was 20 mm, the echo time was 42 ms, the b-factor was 5 s/mm^2, and the recovery time after each inversion-readout block was 2.65 s. Whole brain multi-slice BOLD data were acquired at the end of each rest or hypercapnia state, after the CBF measurement: 30 slices of 5 mm centred around the FAIR slice were acquired, with 20 averages of each volume. The voxel size was the same as for the slice selective and FAIR measurements. The echo time was 40 ms. A three-dimensional T_1 weighted magnetization-prepared rapid gradient-echo (MP-RAGE) sequence was run at the end of the day to get structural brain images with a high spatial resolution and high tissue contrast (Deichmann et al., 2002).

7.3.1.3 Data analysis

volunteer movement

The first 8 BOLD acquisitions were discarded from all BOLD data sets to allow for saturation effects. The movements of the volunteer over the course of the day were then assessed by realigning the acquired whole brain BOLD data (two sets for each session) over the 4 sessions — 'inter-realignment'. This procedure and all other realignment, coregistration and reslicing described in this chapter were performed using SPM99 (SPM, 1999).

baseline CBF and inflow delay; cerebrovascular reactivity

The FAIR data were processed following the procedures outlined in section 5.4.7. Standard global and grey matter masks were defined per session according to the criteria listed there. The 86% grey-struc masks were derived for each session by coregistering segmented structural data to the baseline BOLD volume (acquired immediately after the baseline rest CBF measurement), reslicing the segments to the BOLD and FAIR resolution and then taking voxels with grey matter fraction ≥ 0.86. This BOLD volume had only been realigned over its repeat acquisitions, not with respect to other BOLD volumes in the study. This is because these 'intra-realigned' BOLD data should stay as close as possible to the intra-realigned FAIR data for the derived struc-masks to be valid for the FAIR data. This intra-realigned BOLD analysis was performed separately from the *inter*-realigned BOLD realignment over all four sessions as described above and below.

The CR (the difference in CBF between the rest and hypercapnia states divided by the change in $PetCO_2$), baseline CBF and inflow delay over the course of the day were analysed for voxels in the standard grey matter, the 86% grey-struc and the global masks.

baseline BOLD and BOLD relative cerebrovascular reactivity

The inter-realigned BOLD data were used for the BOLD baseline and relative CR (rCR) analyses. The 86% BOLD grey-struc masks were constructed for each session by coregistering segmented structural data to the rest state inter-realigned BOLD data, reslicing the structural segments to the BOLD resolution and then taking voxels with grey matter fraction ≥ 0.86. A global BOLD mask was derived by taking all voxels with CSF

fraction ≤ 0.50 in the coregistered, segmented structural data. A BOLD slice corresponding to the FAIR slice was selected for further analyses. Background voxels were removed with an amplitude mask. Baseline BOLD and BOLD rCR (the difference in BOLD from rest to hypercapnia state, as percentage of the rest state, divided by the change in $PetCO_2$) over the course of the day were analysed for voxels in the BOLD 86% grey-struc and global masks.

7.3.2 Results

7.3.2.1 Volunteer movement

Figure 7-2 gives the BOLD (inter-)realignment results over all sessions for all volunteers, named according to their MRI study numbers. These realignment results are taken as a measure of volunteer movement over the 4 sessions. There are two BOLD data sets of 12 acquisitions for each of the 4 sessions, hence (2*12*4) 96 images. For one volunteer only rest state FAIR and BOLD data were acquired, so this BOLD data set has only 48 images.

One volunteer (M05965) had very large out-of-plane movements (>> 5 mm) and therefore the data for this subject were discarded. There is one other volunteer (M06004) who showed a shift 1-1.5 mm larger than 5 mm during the third session. While the effects of shifts up to 5 mm have been estimated with the study described in section 7.2.2, these shifts are slightly larger. This is something to keep in mind in case her results are dramatically different from the other volunteers'. The other six volunteers have out-of-plane shifts smaller than 5 mm.

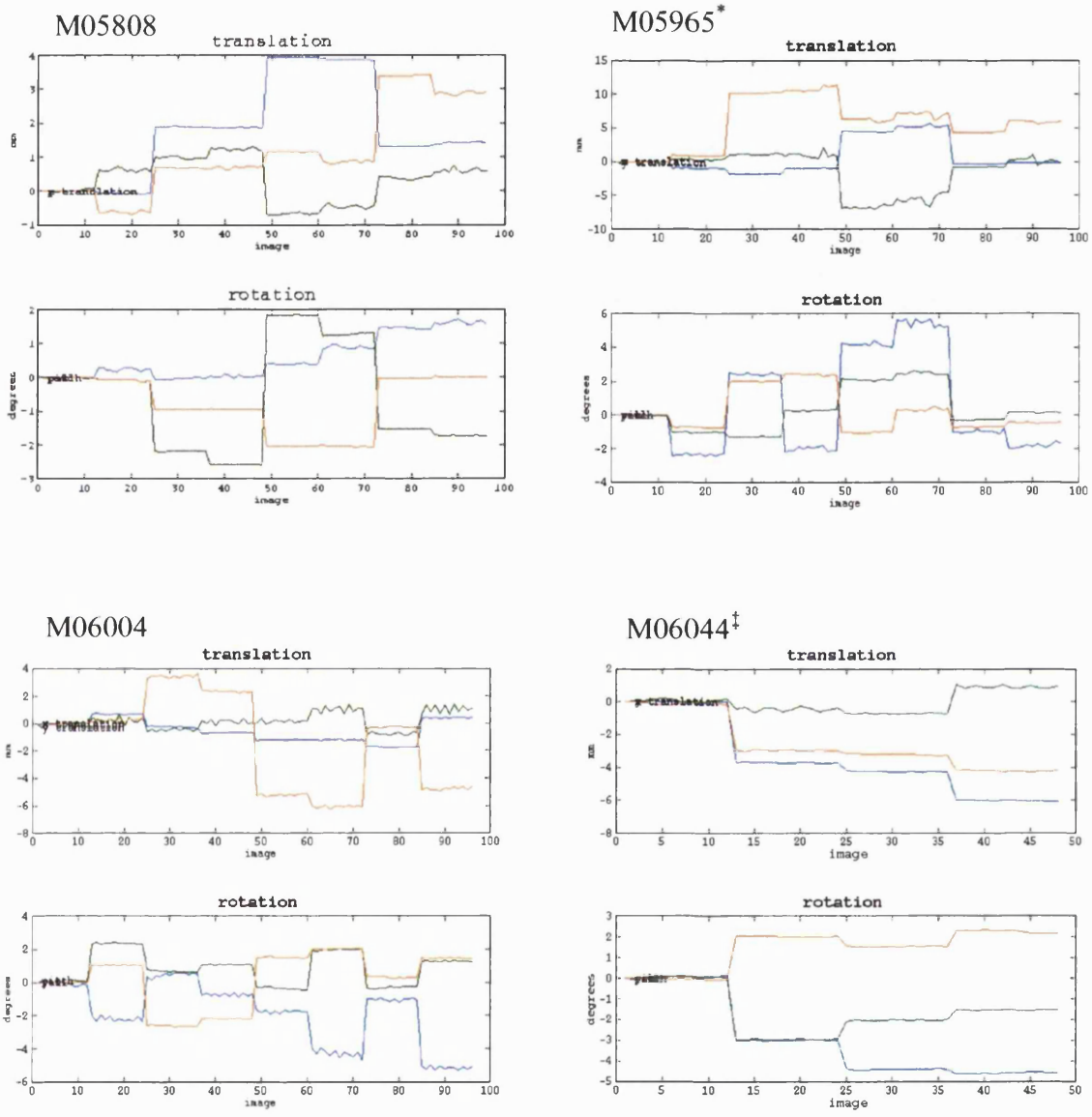

Figure 7-2 Realignment parameters for BOLD inter-realignment, taken as a measure for volunteer movement over all 4 sessions. Each session consists of 2*12 BOLD acquisitions, one BOLD data set for the rest and one for the hypercapnia state. Red: movement in/around z, green: movement in/around y, blue: movement in/around x. Mind the different scales in the plots. Results for first 4 volunteers. Volunteer M05965 – marked by an asterisk – showed such large out-of-plane shifts (i.e. in z) that all her data were discarded. Volunteer M06004 has one session with out-of-plane shifts larger than 5 mm. Volunteer M06044 – marked with ‡ – has only data for rest states, hence only 4*12=48 BOLD acquisitions.

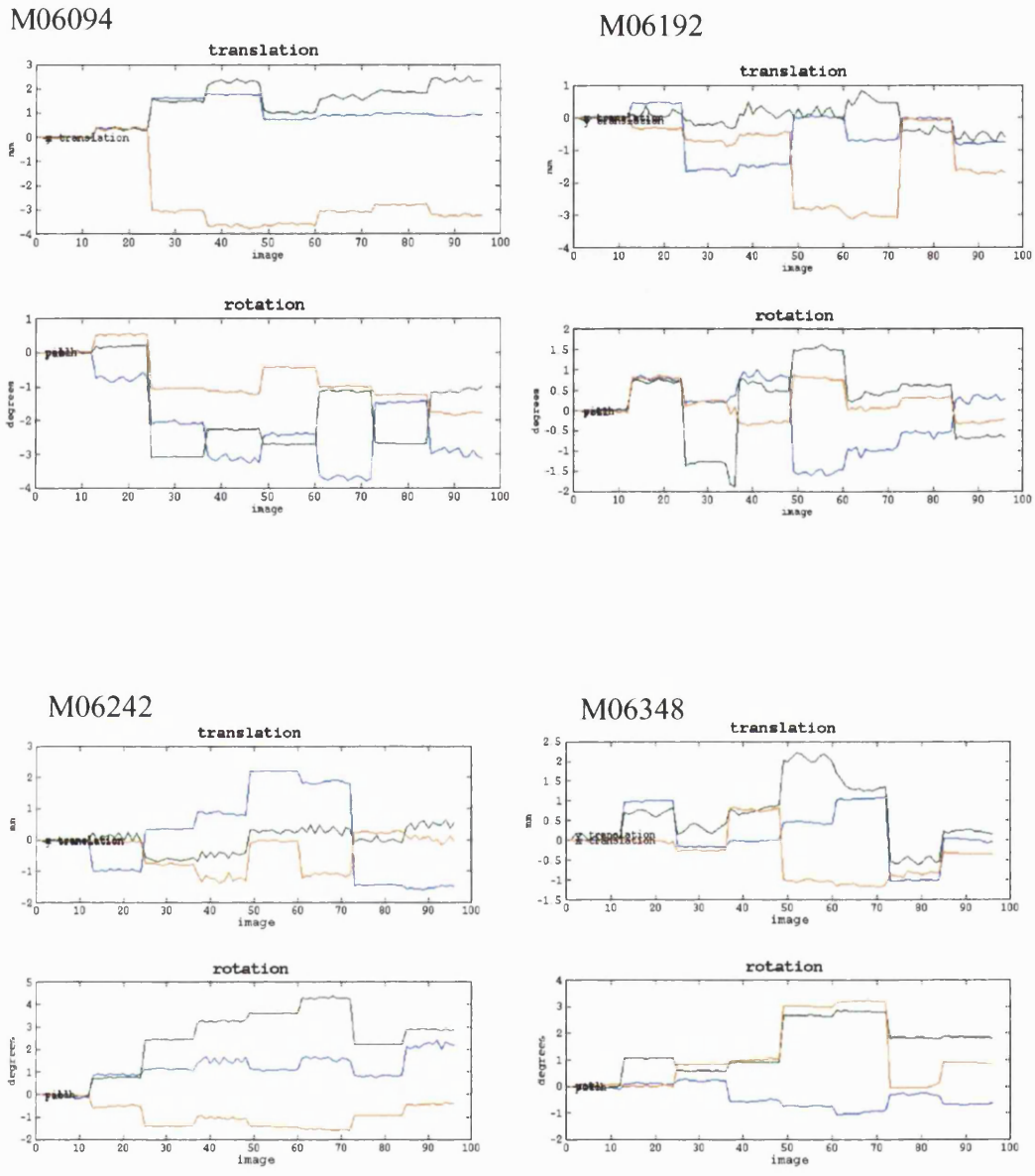

Figure 7-2 (cont.) Realignment parameters for BOLD inter-realignment, taken as a measure for volunteer movement over all 4 sessions. Each session consists of 2*12 BOLD acquisitions, one BOLD data set for the rest and one for the hypercapnia state. Red: movement in/around z, green: movement in/around y, blue: movement in/around x. Mind the different scales in the plots. Results for second 4 volunteers.

7.3.2.2 Baseline CBF and inflow delay over the course of a day

The baseline CBF and inflow delay are given for all volunteers and all masks (standard grey matter mask, 86% grey-struc mask and global mask) in Appendix I. CBF values for all volunteers using the standard grey matter mask are given in Figure 7-3. The CBF averaged over all volunteers is given for all masks in Figure 7-4. This mean CBF and inflow delay over volunteers are also listed in Table 7-4 and Table 7-5 below.

	CBF mean over volunteers +/- standard error, in ml/100g/min			
standard grey matter mask	68.29+/- 3.49(5%)	68.71+/- 4.61(7%)	74.26+/- 4.08(5%)	70.17+/- 4.08(6%)
grey-struc mask	54.24+/- 4.11(8%)	55.90+/- 3.52(6%)	61.37+/- 3.51(6%)	56.42+/- 3.77(7%)
global mask	56.86+/- 2.13(4%)	56.87+/- 2.49(4%)	63.65+/- 2.85(4%)	58.43+/- 2.80(5%)

Table 7-4 Mean CBF +/- standard error, of all volunteers for all 3 masks over the course of a day. The standard error as percentage of the mean is given in brackets.

	inflow delay: mean over volunteers +/- standard error, in ml/100g/min			
standard grey matter mask	0.47+/- 0.03(7%)	0.43+/- 0.02(6%)	0.47+/- 0.02(5%)	0.46+/- 0.02(5%)
grey-struc mask	0.49+/- 0.02(4%)	0.42+/- 0.02(6%)	0.47+/- 0.02(5%)	0.47+/- 0.03(6%)
global mask	0.52+/- 0.03(5%)	0.47+/- 0.02(4%)	0.52+/- 0.03(5%)	0.49+/- 0.02(5%)

Table 7-5 Mean inflow delay +/- standard error, of all volunteers for all 3 masks over the course of a day. The standard error as percentage of the mean is given in brackets.

In the group results there are two trends observable in the mean CBF and inflow delay data: there is a peak in the CBF in the third session and a dip in the inflow delay in the second session. These effects are present for all three masks.

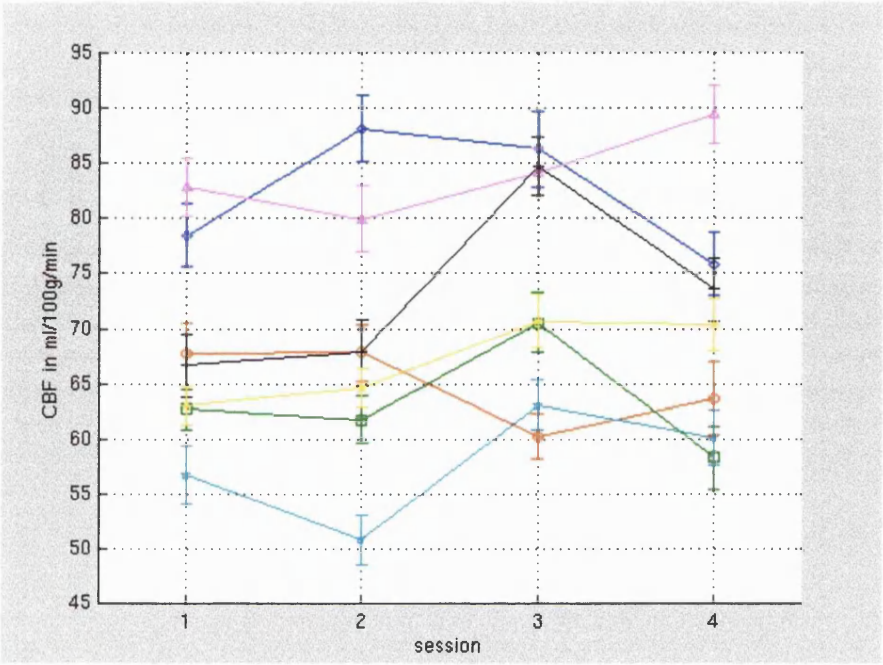

Figure 7-3 Mean +/- se CBF for all volunteers over the course of a day, standard grey matter mask. M05808: red circles; M06004: blue diamonds; M06044: green squares; M06094: magenta triangles; M06192: cyan pentagons, M06242: black crosses; M06348: yellow stars.

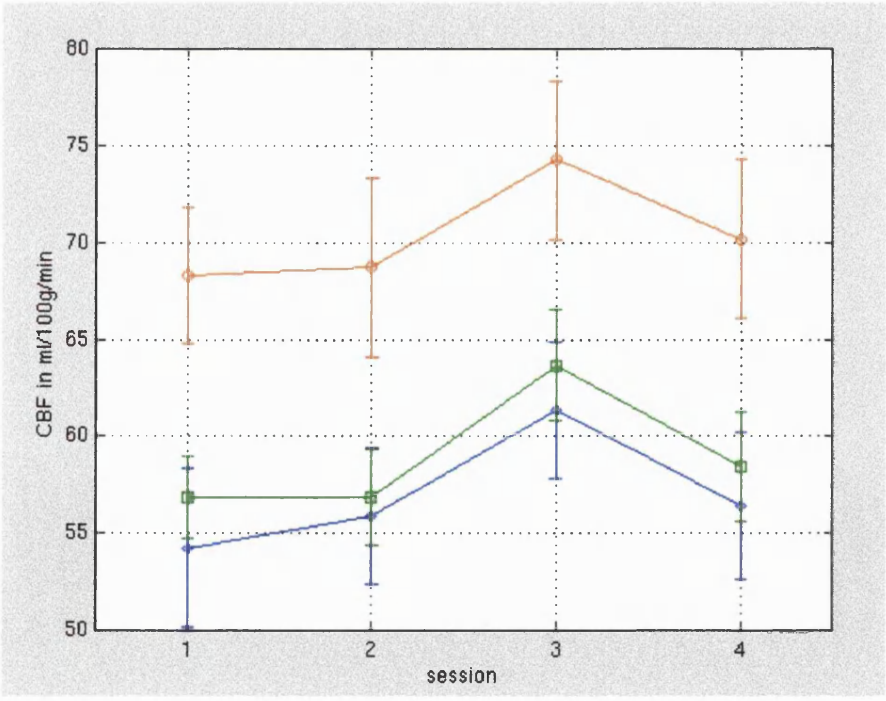

Figure 7-4 Mean +/- se CBF averaged over all volunteers. red circles: standard grey matter mask; blue diamonds: 86% grey-struc mask; green squares: global mask.

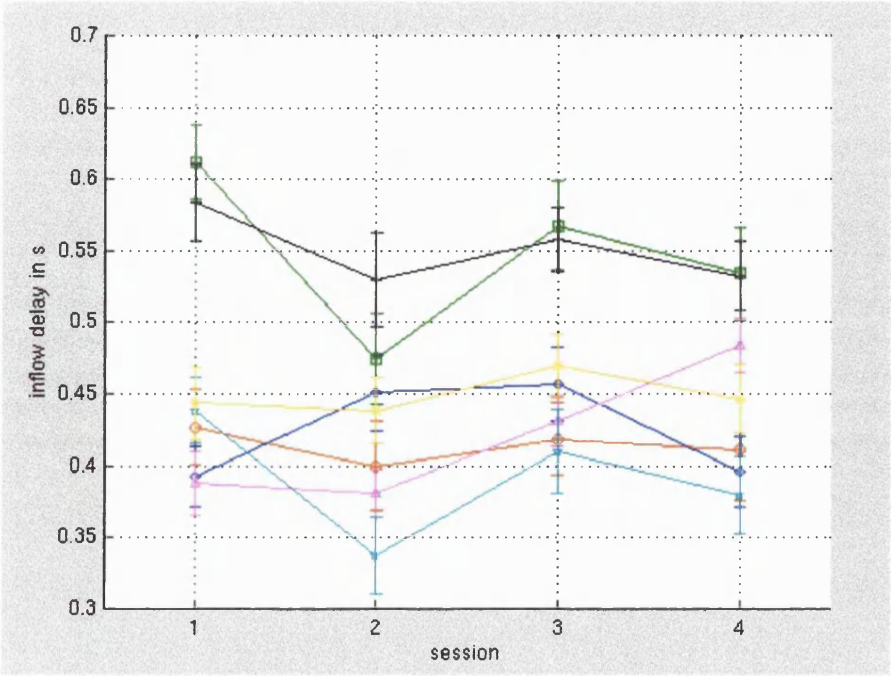

Figure 7-5 Mean +/- se inflow delay for all volunteers over the course of a day, standard grey matter mask. M05808: red circles; M06004: blue diamonds; M06044: green squares; M06094: magenta triangles; M06192: cyan pentagons, M06242: black crosses; M06348: yellow stars.

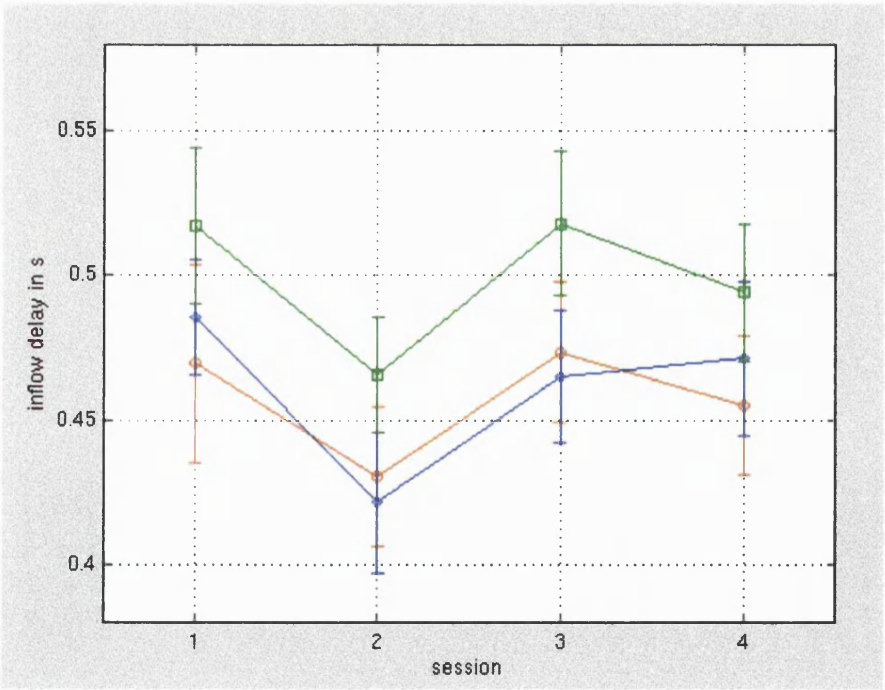

Figure 7-6 Mean +/- se inflow delay averaged over all volunteers. red circles: standard grey matter mask; blue diamonds: 86% grey-struc mask; green squares: global mask.

However, these group trends are not statistically significant: one-way ANOVA analyses give p-values ≥ 0.23. The p-values for the ANOVA analyses are given in Table 7-6 below.

	standard grey matter mask	86% grey-struc mask	global mask
CBF	0.72	0.58	0.23
inflow delay	0.68	0.28	0.38

Table 7-6 P-values for one-way ANOVA test on CBF and inflow delay over the course of a day, when averaged over all volunteers.

Because the ANOVA analyses suggest there is no evidence to consider the group CBF and inflow delay of any of the sessions to be significantly different from other sessions, further analyses of the effects of time of day are superfluous. There are significant differences between sessions for individual volunteers, but these trends all average out over the group. This suggests that it is not necessarily possible to remove time-of-day effects on data by scanning all volunteers at the same time of day. But, as said before, the mean group results will not be influenced by time of day.

It is worthwhile to average over all volunteers and sessions to obtain an overall mean +/- standard error for CBF and inflow delay. The result of this for the 7 volunteers and 4 sessions is given below for the three masks in Table 7-7 and Table 7-8. Most results in this chapter have been listed as mean +/- standard error, as the change of the mean values with time of day was primarily of interest in this experiment. However, in general, the standard deviation of the distributions of CBF and inflow delay that are measured here are also of interest. The standard deviations are therefore listed in the second column.

	mean CBF +/- se in ml/100g/min (28 samples)	sd in ml/100g/min
standard grey matter mask	70.36 +/- 1.98 (3%)	10.47 (15%)
86% grey-struc mask	56.98 +/- 1.83 (3%)	9.70 (17%)
global mask	58.95 +/- 1.33 (2%)	7.05 (12%)

Table 7-7 CBF averaged over volunteers and sessions throughout the day: mean CBF +/- se (se as % mean); sd CBF (sd as % mean)

	mean inflow delay +/- se in s	sd in s
standard grey matter mask	0.46 +/- 0.01 (2%)	0.07 (15%)
86% grey-struc mask	0.46 +/- 0.01 (2%)	0.06 (13%)
global mask	0.50 +/- 0.01 (2%)	0.06 (12%)

Table 7-8 Inflow delay averaged over volunteers and sessions throughout the day: mean inflow delay +/- se (se as % mean); sd inflow delay (sd as % mean)

7.3.2.3 Baseline BOLD over the course of a day

The baseline BOLD signal over the course of a day is given for all volunteers and both masks (BOLD's 86% grey-struc and global masks) in Appendix II. BOLD values for all volunteers using the 86% grey-struc mask are given in Figure 7-7. The BOLD signal averaged over all volunteers is given for both masks in Figure 7-8. The mean BOLD signal over volunteers for the two masks is also listed in Table 7-9 below.

	BOLD signal (/100): mean over volunteers +/- se, in a.u.			
86% grey-struc mask	16.52+/- 0.13(1%)	16.67+/- 0.39(2%)	15.81+/- 0.44(3%)	16.20+/- 0.44(3%)
global mask	16.82 +/- 0.23(1%)	16.90 +/- 0.17(1%)	16.69 +/- 0.23 (1%)	16.62 +/- 0.22 (1%)

Table 7-9 Mean BOLD +/- se (se as % mean), of all volunteers for the 2 masks over the course of a day.

When looking at the group results, there is a trend observable in the mean BOLD data of a dip in the third session for the 86% grey-struc masks. This trend in not visible in the global mask. Performing one-way ANOVA analyses gives p-values of 0.39 and 0.80 for the grey-struc and global mask respectively. Despite the trend, there is therefore no significant change in the measured baseline BOLD signal over the course of the day for this group of volunteers.

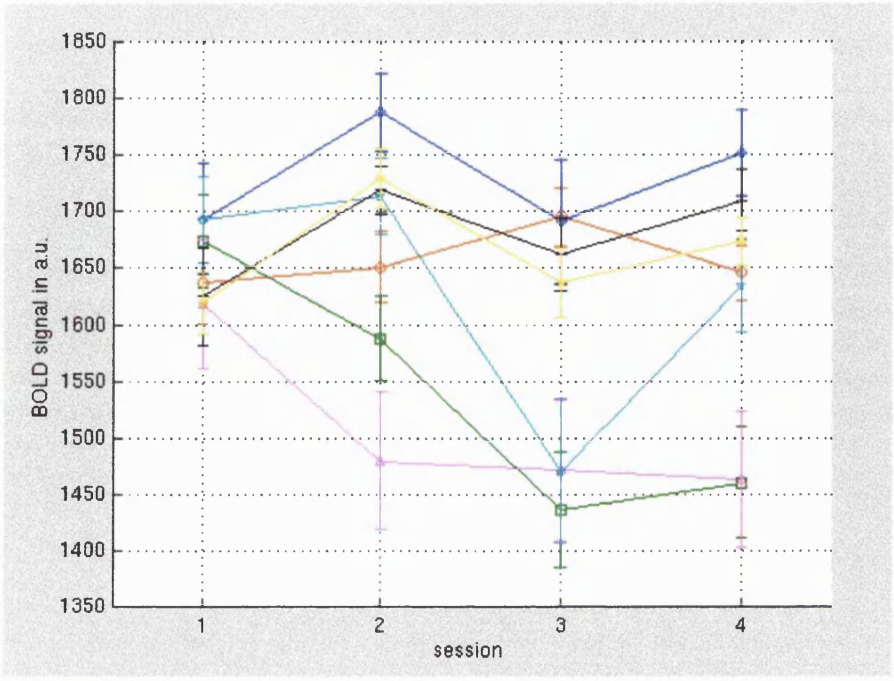

Figure 7-7 Mean +/- se BOLD for all volunteers over the course of a day, standard grey matter mask. M05808: red circles; M06004: blue diamonds; M06044: green squares; M06094: magenta triangles; M06192: cyan pentagons, M06242: black crosses; M06348: yellow stars.

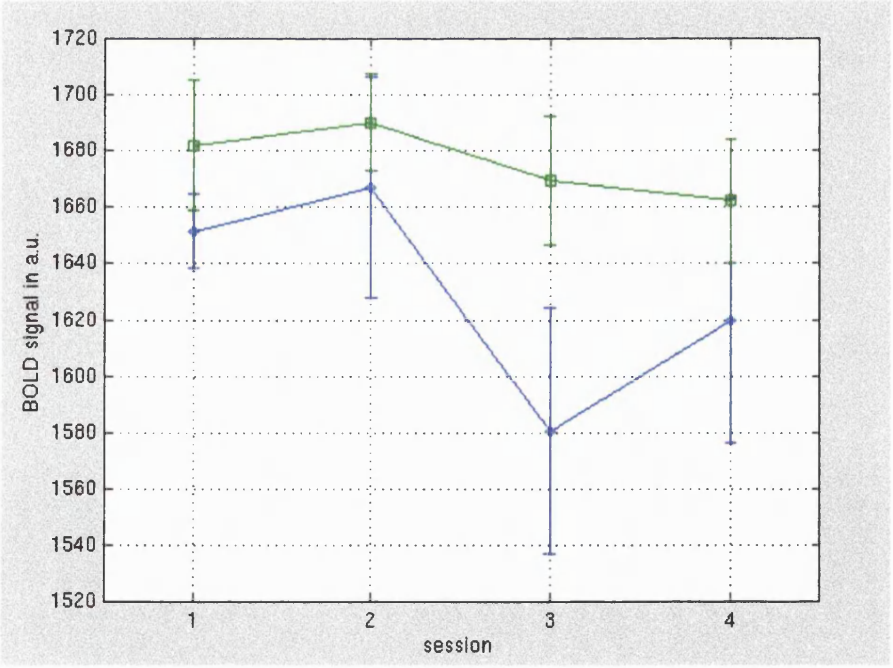

Figure 7-8 Mean +/- se BOLD averaged over all volunteers. blue diamonds: 86% grey-struc mask; green squares: global mask.

The results for averaging over all 7 volunteers and all 4 sessions are given below for the two masks in Table 7-10.

	BOLD signal (/100) mean +/- se in a.u. (28 samples)	sd (/100) in a.u.
86% grey-struc mask	16.30 +/- 0.19 (1%)	0.99 (6%)
global mask	16.76 +/- 0.10 (1%)	0.55 (3%)

Table 7-10 BOLD averaged over volunteers and sessions throughout the day: mean BOLD +/- se (se as % mean); sd BOLD (sd as % mean)

7.3.2.4 Cerebrovascular Reactivity over the course of a day

The cerebrovascular reactivity (CR) is given for all volunteers and all masks (standard grey matter mask, 86% grey-struc mask and global mask) in Appendix III. CR values for all volunteers using the standard grey matter mask are given in Figure 7-9. The CR averaged over all volunteers is given for all masks in Figure 7-10. These mean CR +/- se values over volunteers are also listed in Table 7-11 below.

	mean CR +/- standard error, averaged over all volunteers in ml/100g/min/mm Hg			
	session 1	session 2	session 3	session 4
standard grey	0.77+/- 0.25(32%)	1.20+/- 0.47(39%)	0.40+/-0.44(110%)	0.55+/- 0.42(75%)
86% grey-struc	0.99+/- 0.24(25%)	0.88+/- 0.33(37%)	0.50+/- 0.32(63%)	0.96+/- 0.36(37%)
global mask	1.05+/- 0.24(22%)	1.27+/- 0.30(23%)	0.55+/- 0.29(54%)	0.96+/- 0.22(23%)

Table 7-11 Mean CR +/- standard error, of all volunteers for all 3 masks over the course of a day.

There is a group trend of CR values peaking in the second session and dipping in the third for all three masks. These trends are not statistically significant, however, as the p-values from the one-way ANOVA test are 0.54, 0.68 and 0.30 for the standard grey matter mask, the grey-struc mask and the global mask respectively.

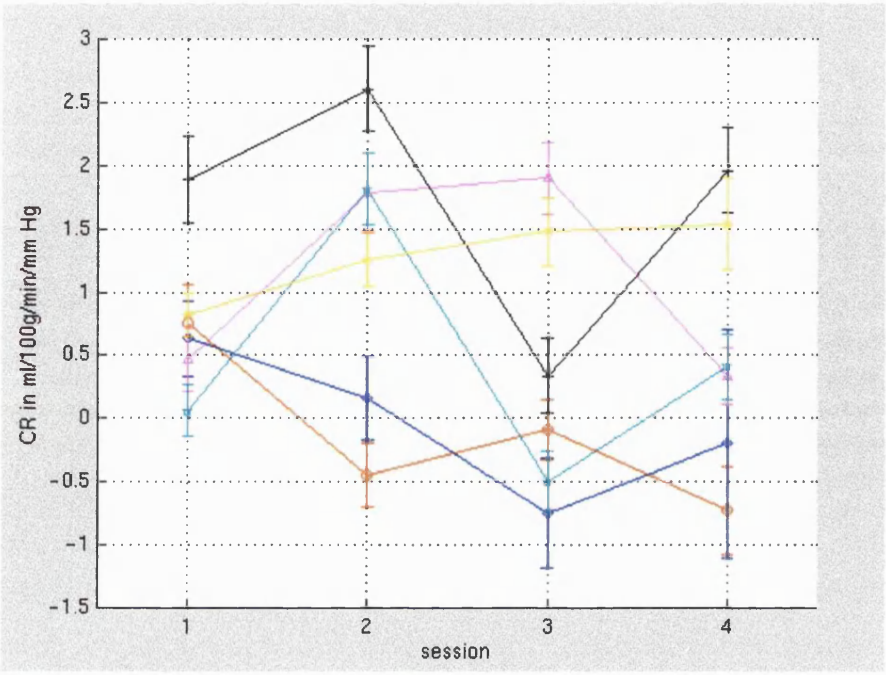

Figure 7-9 Mean +/- se CR for all volunteers over the course of a day, standard grey matter mask. M05808: red circles; M06004: blue diamonds; M06094: magenta triangles; M06192: cyan pentagons, M06242: black crosses; M06348: yellow stars.

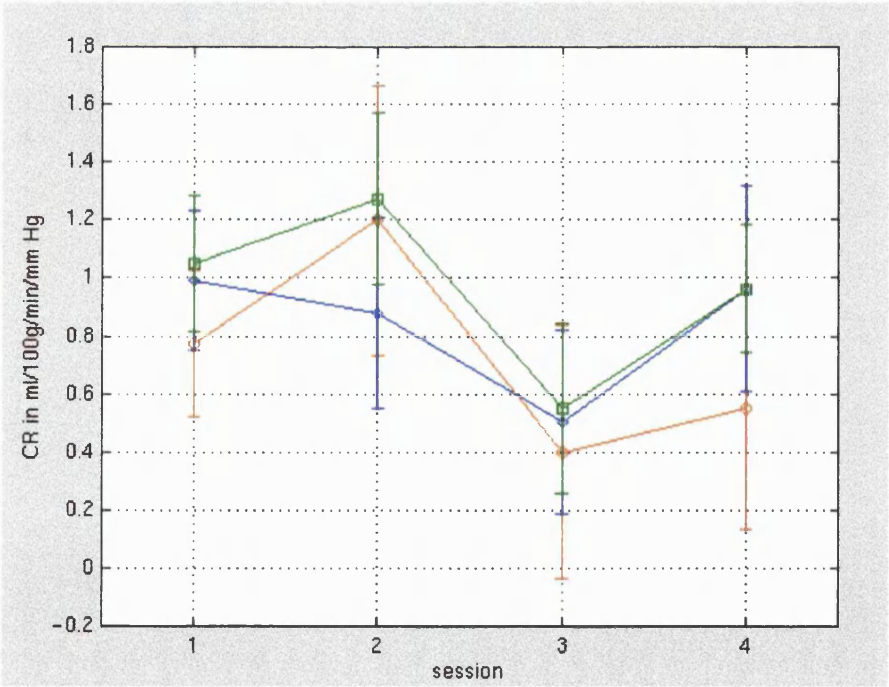

Figure 7-10 Mean +/- se CR averaged over all volunteers. red circles: standard grey matter mask; blue diamonds: 86% grey-struc mask; green squares: global mask.

When averaging the CR over all 6 volunteers and 4 sessions an estimate of the variability of the CR measurement is obtained. This CR +/- se is listed for the three masks below in Table 7-12. The standard deviation of this distribution is listed as well. Obviously the CR measurement is very noisy. Ameriso's morning CR reduction cannot be replicated, either because it is not there, or because this measurement is too noisy to pick it up.

	mean CR +/- se in ml/100g/min/mm Hg (24 samples)	sd in ml/100g/min/mm Hg
standard grey matter mask	0.73 +/- 0.20 (27%)	0.97 (133%)
86% grey-struc mask	0.83 +/- 0.15 (18%)	0.74 (89%)
global mask	0.96 +/- 0.13 (13%)	0.66 (69%)

Table 7-12 CR averaged over volunteers and sessions throughout the day: mean+/- se (se as % of mean); sd (sd as % mean).

7.3.2.5 BOLD relative Cerebrovascular Reactivity over the course of a day

The BOLD relative cerebrovascular reactivity (rCR) is given for all volunteers and both BOLD masks (86% grey-struc mask and global mask) in Appendix IV. A plot of all BOLD rCR values for all volunteers for the BOLD 86% grey-struc mask is given in Figure 7-11. The rCR averaged over all volunteers is given for both masks in Figure 7-12 . These mean rCR +/- se values over volunteers are also listed in Table 7-13 below.

	mean rCR +/- standard error, averaged over all volunteers % BOLD change/mm Hg			
	session 1	session 2	session 3	session 4
86% grey-struc mask	0.27+/- 0.08(29%)	0.21+/- 0.08(37%)	0.25+/- 0.04(17%)	0.30+/- 0.13(42%)
global mask	0.25+/- 0.06(23%)	0.22+/- 0.05(24%)	0.23+/- 0.04(17%)	0.31+/- 0.11(37%)

Table 7-13 BOLD relative CR: mean +/- standard error (se as % mean), of all volunteers for both BOLD masks over the course of a day.

There are no significant changes in BOLD rCR over the course of the day for this group: p-values for the one-way ANOVA are 0.89 and 0.83 for the grey-struc and global masks respectively.

The mean +/- se BOLD rCR and its standard deviation when pooling data of all 6 volunteers and 4 sessions are given below in Table 7-14.

	mean CR +/- se in %BOLD change/mm Hg (24 samples)	sd in %BOLD change/mm Hg
86% grey-struc mask	0.26 +/- 0.04 (16%)	0.20 (77%)
global mask	0.25 +/- 0.03 (13%)	0.17 (66%)

Table 7-14 BOLD relative CR averaged over volunteers and sessions throughout the day: mean+/- se (se as % of mean); sd (sd as % mean).

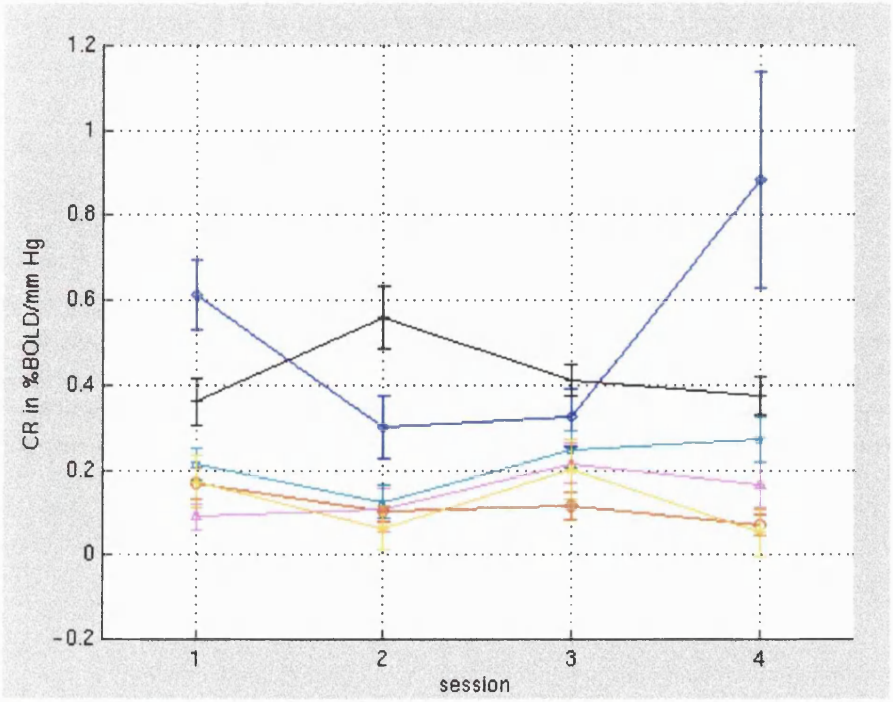

Figure 7-11 Mean +/- se BOLD relative CR for all volunteers over the course of a day, standard grey matter mask. M05808: red circles; M06004: blue diamonds; M06094: magenta triangles; M06192: cyan pentagons, M06242: black crosses; M06348: yellow stars.

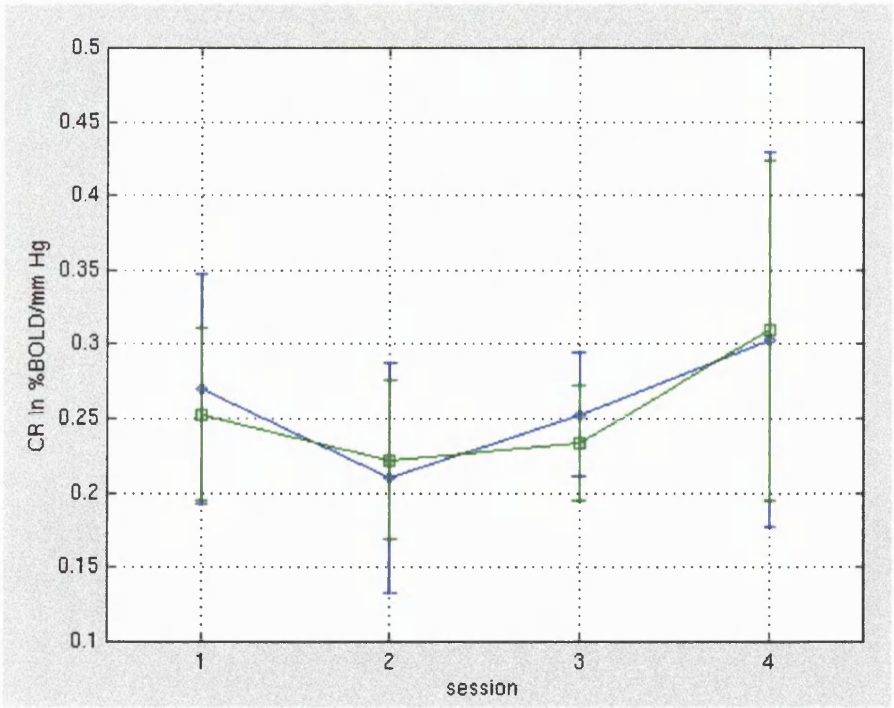

Figure 7-12 Mean +/- se BOLD relative CR averaged over all volunteers. blue diamonds: 86% grey-struc mask; green squares: global mask.

7.3.3 Discussion

To start with the bad news: the CR measurements in this experiment turned out to be very noisy and therefore not very informative. When pooling the data of all volunteers and all sessions, standard deviations of 69%-133% were found for the CR, and 66%-77% for the BOLD rCR. This means that with the current setup (magnetic field strength, number of averages, $PetCO_2$ change) a reliable measurement of the CR is not feasible, using either FAIR or BOLD.

As shown in Chapter 6, the CR can be measured successfully with FAIR and BOLD. That study evoked much larger $PetCO_2$ changes, which did not seem feasible for this multi-session study. For this number of averages the CBF measurement of each rest or hypercapnia state took 20 minutes. It is not desirable to lengthen this time much further. For BOLD, however, only 20 acquisitions were performed lasting 1minute in total, for each rest or hypercapnia state. There is therefore plenty of scope to improve the standard deviation of the BOLD rCR measurement.

Looking at the parameters that could be measured reliably, there was no significant effect found of the time of day on baseline CBF, inflow delay and BOLD signal for the group of volunteers studied. The volunteer sample had deliberately been restricted to women of age 28 +/- 4, to minimise the variability in these parameters over the volunteer sample.

Projecting from these results, this study supports the hypothesis that experiments that look at CBF, inflow delay or BOLD signal over a group will not be confounded by the time of day. However, when studying individuals on their own, care should be taken, as individual data can show significant variations from session to session. This individual variability can have biological (e.g. diurnal rhythms) or experimental (e.g. volunteer motion, machine instability) causes.

The standard deviations on CBF, inflow delay and BOLD signal for the sample of all pooled volunteer and session data are: 12-17% for CBF, 12-15% for inflow delay and 3-6% for BOLD. These variabilities incorporate the aforementioned biological and

experimental contributions, but also the differences in these parameters between individuals.

The standard deviations for CBF and inflow delay are very similar to those predicted for multi-session studies with out-of-plane shifts of 5 mm: 1-10% and 2-19% respectively (section 7.2.2). Most volunteers had out-of-plane shifts of ~3-4 mm; attributing a large part of their variability to inter-session motion seems therefore not unreasonable. After all, in Chapter 6, the standard deviation for these type of masks for each of the 11 volunteers was ~5%. It is also not unlikely, that the whole-brain realigned BOLD data set has a much smaller standard deviation because of its 3D-realignment. It therefore seems advisable to move towards whole-brain FAIR, so 3D-realignment can be used to minimise the effects of inter- and intra-session movements and the standard deviation of CBF and CR measurements can be reduced.

With respect to the feasibility of longitudinal studies: the standard deviation on the CBF measurement (12-17%) is sufficiently small for most activation studies, however, for longitudinal CBF studies, for which quite small changes in CBF are of interest, it is not. Hopefully, with 3D-realignment, the standard deviation of the CBF measurement will be reduced to the order of the standard deviation within a session, i.e. ~ 5%.

Finally, the fact that no significant group effect of time of day was found, puts upper limits on changes in the CBF, inflow delay and BOLD values over the course of a day for the group as a whole: for each parameter, the group mean changed less over the course of a day than, say, 2 ½ times the standard deviation of that parameter over the group within a session. Using the group standard deviations per session listed in section 7.3.2.2 to 7.3.2.5, this means the upper limits of changes in group mean over the course of a day found here are: ~20% for CBF, ~18% for inflow delay and ~8% for the BOLD signal. These values can inform future experimental designs, as they outline the limitations in sensitivity to other physiological or cognitive factors.

7.4 Appendices

Appendix I : baseline CBF and inflow delay values per volunteer

CBF in ml/100g/min for standard grey matter mask				
	session 1	session 2	session 3	session 4
M05808	67.70 +/- 18.23(27%) med. 65.12; se 2.85 # voxels = 41	67.80 +/- 17.80(26%) med. 66.92; se 2.60 # voxels = 47	60.27 +/- 16.20(27%) med. 60.29; se 2.04 # voxels = 63	63.64 +/- 17.65(28%) med. 59.82; se 3.28 # voxels = 29
M06004	78.50 +/- 23.75(30%) med. 75.74; se 2.84 # voxels = 70	88.13 +/- 26.91(31%) med. 84.80; se 3.03 # voxels = 79	86.28 +/- 25.32(29%) med. 86.43; se 3.51 # voxels = 52	75.80 +/- 25.93(34%) med. 74.85; se 2.86 # voxels = 82
M06044	62.72 +/- 18.28(29%) med. 62.47; se 1.82 # voxels = 101	61.75 +/- 17.79(29%) med. 63.15; se 2.14 # voxels = 69	70.56 +/- 26.97(38%) med. 65.47; se 2.71 # voxels = 99	58.30 +/- 25.57(44%) med. 54.52; se 2.84 # voxels = 81
M06094	82.79 +/- 22.64(27%) med. 80.03; se 2.63 # voxels = 74	79.95 +/- 28.32(35%) med. 75.29; se 3.04 # voxels = 87	84.20 +/- 20.90(25%) med. 80.88; se 2.17 # voxels = 93	89.47 +/- 25.01(28%) med. 83.76; se 2.67 # voxels = 88
M06192	56.67 +/- 25.27(45%) med. 48.47; se 2.65 # voxels = 91	50.80 +/- 19.52(38%) med. 49.51; se 2.30 # voxels = 72	63.06 +/- 20.32(32%) med. 62.77; se 2.27 # voxels = 80	60.12 +/- 22.44(37%) med. 56.50; se 2.52 # voxels = 79
M06242	66.65 +/- 29.13(44%) med. 62.14; se 2.88 # voxels = 102	67.82 +/- 25.93(38%) med. 66.15; se 3.01 # voxels = 74	84.72 +/- 27.11(32%) med. 82.99; se 2.68 # voxels = 102	73.52 +/- 28.12(38%) med. 67.50; se 2.92 # voxels = 93
M06348	63.02 +/- 16.68(26%) med. 62.27; se 1.77 # voxels = 89	64.69 +/- 17.65(27%) med. 61.79; se 1.77 # voxels = 99	70.71 +/- 22.67(32%) med. 68.35; se 2.43 # voxels = 87	70.33 +/- 22.73(32%) med. 67.34; se 2.37 # voxels = 92
MEAN +/- se	**68.29+/- 3.49(5%)**	**68.71+/- 4.61(7%)**	**74.26+/- 4.08(5%)**	**70.17+/- 4.08(6%)**

Table 7-15 Baseline CBF results for the standard grey matter mask, for all volunteers. Listed in each cell: mean +/- sd (sd as % mean), median, standard error and number of voxels.

CBF in ml/100g/min for 86% grey-struc mask				
	session 1	session 2	session 3	session 4
M05808	49.81 +/- 20.91(42%) med. 48.81; se 2.32 # voxels = 81	62.00 +/- 25.30(41%) med. 57.12; se 2.78 # voxels = 83	64.96 +/- 19.85(31%) med. 63.56; se 2.26 # voxels = 77	56.92 +/- 21.50(38%) med. 55.35; se 2.43 # voxels = 78
M06004	62.50 +/- 26.24(42%) med. 60.78; se 3.23 # voxels = 66	65.52 +/- 30.58(47%) med. 69.13; se 4.61 # voxels = 44	69.24 +/- 25.45(37%) med. 67.61; se 3.64 # voxels = 49	64.16 +/- 25.02(39%) med. 61.73; se 2.97 # voxels = 71
M06044	40.90 +/- 29.84(73%) med. 47.83; se 3.28 # voxels = 83	40.44 +/- 29.79(74%) med. 47.74; se 3.27 # voxels = 83	46.06 +/- 28.93(63%) med. 50.27; se 2.72 # voxels = 113	39.69 +/- 27.87(70%) med. 41.78; se 2.50 # voxels = 124
M06094	70.63 +/- 26.09(37%) med. 67.94; se 3.03 # voxels = 74	62.15 +/- 23.15(37%) med. 60.04; se 2.73 # voxels = 72	66.56 +/- 25.01(38%) med. 66.74; se 2.93 # voxels = 73	67.35 +/- 27.99(42%) med. 69.28; se 2.93 # voxels = 91
M06192	41.75 +/- 16.56(40%) med. 45.44; se 1.85 # voxels = 80	45.67 +/- 18.49(40%) med. 42.76; se 2.04 # voxels = 82	51.54 +/- 20.31(39%) med. 50.49; se 2.50 # voxels = 66	46.76 +/- 20.32(43%) med. 47.75; se 2.32 # voxels = 77
M06242	56.01 +/- 21.23(38%) med. 55.77; se 2.92 # voxels = 53	58.56 +/- 24.93(43%) med. 55.49; se 2.74 # voxels = 83	70.60 +/- 27.05(38%) med. 68.20; se 2.87 # voxels = 89	63.03 +/- 23.85(38%) med. 62.89; se 2.79 # voxels = 73
M06348	58.11 +/- 18.32(32%) med. 57.72; se 2.10 # voxels = 76	56.91 +/- 17.79(31%) med. 57.79; se 2.14 # voxels = 69	60.62 +/- 24.35(40%) med. 62.11; se 2.91 # voxels = 70	57.04 +/- 20.01(35%) med. 58.75; se 2.39 # voxels = 70
MEAN +/- se	**54.24+/- 4.11(8%)**	**55.90+/- 3.52(6%)**	**61.37+/- 3.51(6%)**	**56.42+/- 3.77(7%)**

Table 7-16 Baseline CBF results for the 86% grey-struc mask, for all volunteers. Listed in each cell: mean +/- sd (sd as % mean), median, standard error and number of voxels.

CBF in ml/100g/min for global mask				
	session 1	session 2	session 3	session 4
M05808	54.52 +/- 22.68(42%) med. 53.49; se 1.22 # voxels = 343	56.84 +/- 20.04(35%) med. 56.36; se 1.06 # voxels = 358	58.27 +/- 21.21(36%) med. 57.22; se 1.10 # voxels = 375	52.44 +/- 20.92(40%) med. 51.61; se 1.16 # voxels = 327
M06004	63.35 +/- 28.82(45%) med. 61.81; se 1.41 # voxels = 416	64.05 +/- 29.11(45%) med. 63.47; se 1.46 # voxels = 396	71.29 +/- 29.48(41%) med. 71.87; se 1.67 # voxels = 311	66.38 +/- 28.31(43%) med. 64.13; se 1.38 # voxels = 418
M06044	52.61 +/- 23.39(44%) med. 52.72; se 1.05 # voxels = 495	53.59 +/- 24.06(45%) med. 52.16; se 1.12 # voxels = 460	56.86 +/- 26.94(47%) med. 53.52; se 1.23 # voxels = 481	50.94 +/- 24.88(49%) med. 48.83; se 1.17 # voxels = 455
M06094	65.36 +/- 31.73(49%) med. 64.58; se 1.57 # voxels = 406	65.50 +/- 31.41(48%) med. 63.31; se 1.46 # voxels = 460	70.40 +/- 27.90(40%) med. 69.37; se 1.32 # voxels = 450	69.50 +/- 34.22(49%) med. 65.38; se 1.61 # voxels = 454
M06192	49.77 +/- 23.57(47%) med. 46.20; se 1.10 # voxels = 456	45.76 +/- 21.03(46%) med. 44.70; se 1.03 # voxels = 419	54.24 +/- 24.63(45%) med. 51.68; se 1.19 # voxels = 428	51.51 +/- 24.19(47%) med. 49.71; se 1.23 # voxels = 384
M06242	56.98 +/- 28.80(51%) med. 54.39; se 1.38 # voxels = 435	56.39 +/- 26.14(46%) med. 54.52; se 1.30 # voxels = 407	72.17 +/- 34.93(48%) med. 68.48; se 1.62 # voxels = 464	60.41 +/- 28.21(47%) med. 57.47; se 1.31 # voxels = 464
M06348	55.43 +/- 21.27(38%) med. 55.36; se 1.04 # voxels = 422	55.97 +/- 23.11(41%) med. 54.53; se 1.12 # voxels = 429	62.31 +/- 26.28(42%) med. 62.05; se 1.27 # voxels = 426	57.85 +/- 25.55(44%) med. 56.99; se 1.25 # voxels = 418
MEAN +/- sd	**56.86+/- 2.13(4%)**	**56.87+/- 2.49(4%)**	**63.65+/- 2.85(4%)**	**58.43+/- 2.80(5%)**

Table 7-17 Baseline CBF results for the global mask, for all volunteers. Listed in each cell: mean +/- sd (sd as % mean), median, standard error and number of voxels.

inflow delay in s for standard grey matter mask				
	session 1	session 2	session 3	session 4
M05808	0.43 +/- 0.17(40%) med. 0.44; se 0.03 # voxels = 41	0.40 +/- 0.21(53%) med. 0.43; se 0.03 # voxels = 47	0.42 +/- 0.20(48%) med. 0.42; se 0.03 # voxels = 63	0.41 +/- 0.19(46%) med. 0.43; se 0.04 # voxels = 29
M06004	0.39 +/- 0.17(44%) med. 0.42; se 0.02 # voxels = 70	0.45 +/- 0.24(53%) med. 0.43; se 0.03 # voxels = 79	0.46 +/- 0.19(41%) med. 0.48; se 0.03 # voxels = 52	0.40 +/- 0.22(56%) med. 0.40; se 0.02 # voxels = 82
M06044	0.61 +/- 0.26(42%) med. 0.55; se 0.03 # voxels = 101	0.47 +/- 0.26(55%) med. 0.45; se 0.03 # voxels = 69	0.57 +/- 0.31(55%) med. 0.51; se 0.03 # voxels = 99	0.53 +/- 0.29(55%) med. 0.48; se 0.03 # voxels = 81
M06094	0.39 +/- 0.19(50%) med. 0.40; se 0.02 # voxels = 74	0.38 +/- 0.15(40%) med. 0.39; se 0.02 # voxels = 87	0.43 +/- 0.17(39%) med. 0.44; se 0.02 # voxels = 93	0.48 +/- 0.18(37%) med. 0.48; se 0.02 # voxels = 88
M06192	0.44 +/- 0.22(50%) med. 0.45; se 0.02 # voxels = 91	0.34 +/- 0.23(68%) med. 0.27; se 0.03 # voxels = 72	0.41 +/- 0.26(63%) med. 0.35; se 0.03 # voxels = 80	0.38 +/- 0.24(63%) med. 0.37; se 0.03 # voxels = 79
M06242	0.58 +/- 0.27(46%) med. 0.54; se 0.03 # voxels = 102	0.53 +/- 0.28(53%) med. 0.49; se 0.03 # voxels = 74	0.56 +/- 0.22(40%) med. 0.53; se 0.02 # voxels = 102	0.53 +/- 0.23(42%) med. 0.51; se 0.02 # voxels = 93
M06348	0.44 +/- 0.24(53%) med. 0.45; se 0.02 # voxels = 89	0.44 +/- 0.22(51%) med. 0.45; se 0.02 # voxels = 99	0.47 +/- 0.21(44%) med. 0.46; se 0.02 # voxels = 87	0.45 +/- 0.23(52%) med. 0.43; se 0.02 # voxels = 92
MEAN +/- se	**0.47+/- 0.03(7%)**	**0.43+/- 0.02(6%)**	**0.47+/- 0.02(5%)**	**0.46+/- 0.02(5%)**

Table 7-18 Baseline inflow delay results for the standard grey matter mask, for all volunteers. Listed in each cell: mean +/- sd (sd as % mean), median, standard error and number of voxels.

inflow delay in s for 86% grey-struc mask				
	session 1	session 2	session 3	session 4
M05808	0.42 +/- 0.28(65%) med. 0.38; se 0.03 # voxels = 81	0.43 +/- 0.26(60%) med. 0.41; se 0.03 # voxels = 83	0.44 +/- 0.24(55%) med. 0.44; se 0.03 # voxels = 77	0.44 +/- 0.23(52%) med. 0.44; se 0.03 # voxels = 78
M06004	0.50 +/- 0.26(52%) med. 0.48; se 0.03 # voxels = 66	0.48 +/- 0.31(64%) med. 0.44; se 0.05 # voxels = 44	0.42 +/- 0.24(57%) med. 0.36; se 0.03 # voxels = 49	0.42 +/- 0.25(59%) med. 0.40; se 0.03 # voxels = 71
M06044	0.47 +/- 0.37(79%) med. 0.52; se 0.04 # voxels = 83	0.36 +/- 0.32(89%) med. 0.36; se 0.04 # voxels = 83	0.44 +/- 0.33(75%) med. 0.44; se 0.03 # voxels = 113	0.45 +/- 0.34(75%) med. 0.45; se 0.03 # voxels = 124
M06094	0.43 +/- 0.26(61%) med. 0.40; se 0.03 # voxels = 74	0.37 +/- 0.23(62%) med. 0.32; se 0.03 # voxels = 72	0.42 +/- 0.24(56%) med. 0.40; se 0.03 # voxels = 73	0.47 +/- 0.25(53%) med. 0.44; se 0.03 # voxels = 91
M06192	0.49 +/- 0.26(52%) med. 0.46; se 0.03 # voxels = 80	0.38 +/- 0.27(72%) med. 0.36; se 0.03 # voxels = 82	0.43 +/- 0.26(61%) med. 0.43; se 0.03 # voxels = 66	0.40 +/- 0.28(70%) med. 0.39; se 0.03 # voxels = 77
M06242	0.58 +/- 0.29(49%) med. 0.55; se 0.04 # voxels = 53	0.53 +/- 0.33(63%) med. 0.52; se 0.04 # voxels = 83	0.58 +/- 0.26(45%) med. 0.54; se 0.03 # voxels = 89	0.61 +/- 0.24(40%) med. 0.55; se 0.03 # voxels = 73
M06348	0.50 +/- 0.26(51%) med. 0.49; se 0.03 # voxels = 76	0.40 +/- 0.20(49%) med. 0.41; se 0.02 # voxels = 69	0.52 +/- 0.21(40%) med. 0.48; se 0.02 # voxels = 70	0.52 +/- 0.28(54%) med. 0.50; se 0.03 # voxels = 70
MEAN +/- se	**0.49+/- 0.02(4%)**	**0.42+/- 0.02(6%)**	**0.47+/- 0.02(5%)**	**0.47+/- 0.03(6%)**

Table 7-19 Baseline inflow delay results for the 86% grey-struc mask, for all volunteers. Listed in each cell: mean +/- sd (sd as % mean), median, standard error and number of voxels.

inflow delay in s for global mask				
	session 1	session 2	session 3	session 4
M05808	0.46 +/- 0.26(56%) med. 0.44; se 0.01 # voxels = 343	0.46 +/- 0.27(60%) med. 0.44; se 0.01 # voxels = 358	0.49 +/- 0.27(55%) med. 0.46; se 0.01 # voxels = 375	0.47 +/- 0.27(56%) med. 0.45; se 0.01 # voxels = 327
M06004	0.47 +/- 0.27(58%) med. 0.45; se 0.01 # voxels = 416	0.44 +/- 0.26(59%) med. 0.42; se 0.01 # voxels = 396	0.46 +/- 0.24(53%) med. 0.45; se 0.01 # voxels = 311	0.43 +/- 0.28(64%) med. 0.41; se 0.01 # voxels = 418
M06044	0.63 +/- 0.29(47%) med. 0.68; se 0.01 # voxels = 495	0.51 +/- 0.29(57%) med. 0.48; se 0.01 # voxels = 460	0.56 +/- 0.31(55%) med. 0.51; se 0.01 # voxels = 481	0.56 +/- 0.30(55%) med. 0.51; se 0.01 # voxels = 455
M06094	0.46 +/- 0.25(53%) med. 0.44; se 0.01 # voxels = 406	0.44 +/- 0.24(54%) med. 0.43; se 0.01 # voxels = 460	0.50 +/- 0.24(49%) med. 0.48; se 0.01 # voxels = 450	0.52 +/- 0.26(50%) med. 0.48; se 0.01 # voxels = 454
M06192	0.48 +/- 0.27(57%) med. 0.46; se 0.01 # voxels = 456	0.38 +/- 0.28(74%) med. 0.34; se 0.01 # voxels = 419	0.44 +/- 0.29(66%) med. 0.40; se 0.01 # voxels = 428	0.41 +/- 0.27(67%) med. 0.39; se 0.01 # voxels = 384
M06242	0.60 +/- 0.30(51%) med. 0.54; se 0.01 # voxels = 435	0.54 +/- 0.31(56%) med. 0.51; se 0.02 # voxels = 407	0.62 +/- 0.28(44%) med. 0.57; se 0.01 # voxels = 464	0.58 +/- 0.27(47%) med. 0.54; se 0.01 # voxels = 464
M06348	0.53 +/- 0.27(52%) med. 0.51; se 0.01 # voxels = 422	0.48 +/- 0.27(57%) med. 0.48; se 0.01 # voxels = 429	0.56 +/- 0.29(52%) med. 0.52; se 0.01 # voxels = 426	0.49 +/- 0.29(59%) med. 0.46; se 0.01 # voxels = 418
MEAN +/- se	**0.52+/- 0.03(5%)**	**0.47+/- 0.02(4%)**	**0.52+/- 0.03(5%)**	**0.49+/- 0.02(5%)**

Table 7-20 Baseline CBF results for the global mask, for all volunteers. Listed in each cell: mean +/- sd (sd as % mean), median, standard error and number of voxels.

Appendix II : baseline BOLD values per volunteer

BOLD signal in a.u. /100, for its 86% grey-struc mask				
	session 1	session 2	session 3	session 4
M05808	16.38+/- 3.80 (23%) med. 17.20; se 0.37 # voxels = 103	16.51 +/- 3.37 (20%) med. 17.18; se 0.31 # voxels = 117	16.96 +/- 2.84 (17%) med. 17.32; se 0.26 # voxels = 118	16.46 +/- 2.67(16%) med. 16.91; se 0.25 # voxels = 116
M06004	16.94 +/- 4.95(29%) med. 18.04; se 0.49 # voxels = 101	17.88 +/- 3.36(19%) med. 18.16; se 0.34 # voxels = 95	16.91 +/- 5.64(33%) med. 18.12; se 0.55 # voxels = 105	17.52 +/- 3.96(23%) med. 18.15; se 0.38 # voxels = 110
M06044	16.74 +/- 3.76(22%) med. 17.39; se 0.41 # voxels = 83	15.88 +/- 4.13(26%) med. 16.63; se 0.37 # voxels = 124	14.37 +/- 5.52(38%) med. 15.66; se 0.52 # voxels = 114	14.61 +/- 5.45(37%) med. 16.05; se 0.49 # voxels = 122
M06094	16.18 +/- 6.03(37%) med. 17.74; se 0.57 # voxels = 111	14.79 +/- 6.23(42%) med. 16.97; se 0.60 # voxels = 106	14.71 +/- 6.66(45%) med. 17.09; se 0.62 # voxels = 114	14.63 +/- 6.60(45%) med. 16.49; se 0.60 # voxels = 121
M06192	16.93 +/- 3.99(24%) med. 17.51; se 0.38 # voxels = 108	17.13 +/- 3.57(21%) med. 17.67; se 0.33 # voxels = 115	14.71 +/- 6.82(46%) med. 17.19; se 0.64 # voxels = 112	16.35 +/- 4.42(27%) med. 17.16; se 0.41 # voxels = 115
M06242	16.25 +/- 4.21(26%) med. 17.17; se 0.43 # voxels = 96	17.19 +/- 2.25(13%) med. 17.44; se 0.21 # voxels = 111	16.62 +/- 3.70(22%) med. 17.37; se 0.33 # voxels = 129	17.10 +/- 2.87(17%) med. 17.63; se 0.27 # voxels = 111
M06348	16.19 +/- 2.56(16%) med. 16.72; se 0.26 # voxels = 94	17.30 +/- 2.50(14%) med. 17.50; se 0.26 # voxels = 90	16.37 +/- 2.81(17%) med. 16.29; se 0.31 # voxels = 84	16.74 +/- 2.00(12%) med. 16.96; se 0.21 # voxels = 87
MEAN +/- se	**16.52+/- 0.13(1%)**	**16.67+/- 0.39(2%)**	**15.81+/- 0.44(3%)**	**16.20+/- 0.44(3%)**

Table 7-21 Baseline BOLD results for BOLD's 86% grey-struc mask, for all volunteers. Listed in each cell: mean +/- sd (sd as % mean), median, standard error and number of voxels.

BOLD signal in a.u. for its global mask				
	session 1	session 2	session 3	session 4
M05808	16.62+/- 2.19 (13%) med. 16.55; se 0.08 # voxels = 730	16.58 +/- 2.20(13%) med. 16.52; se 0.08 # voxels = 726	16.89 +/- 2.18 (13%) med. 16.81; se 0.08 # voxels = 734	16.42 +/- 1.97 (12%) med. 16.37; se 0.07 # voxels = 718
M06004	17.44 +/- 2.10(12%) med. 17.28; se 0.08 # voxels = 695	17.65 +/- 2.21(13%) med. 17.49; se 0.08 # voxels = 720	17.57 +/- 2.28(13%) med. 17.42; se 0.09 # voxels = 695	17.17 +/- 2.13(12%) med. 17.06; se 0.08 # voxels = 703
M06044	16.89 +/- 2.20(13%) med. 16.73; se 0.09 # voxels = 649	16.41 +/- 2.26(14%) med. 16.22; se 0.09 # voxels = 652	16.20 +/- 2.30(14%) med. 15.92; se 0.09 # voxels = 633	15.93 +/- 2.24(14%) med. 15.69; se 0.09 # voxels = 635
M06094	17.63 +/- 2.13(12%) med. 17.56; se 0.09 # voxels = 604	17.28 +/- 2.12(12%) med. 17.00; se 0.09 # voxels = 600	17.10 +/- 2.05(12%) med. 16.78; se 0.09 # voxels = 568	17.27 +/- 2.13(12%) med. 17.02; se 0.09 # voxels = 575
M06192	16.68 +/- 2.33(14%) med. 16.60; se 0.09 # voxels = 690	16.72 +/- 2.26(13%) med. 16.55; se 0.09 # voxels = 698	16.59 +/- 2.34(14%) med. 16.46; se 0.09 # voxels = 664	16.62 +/- 2.24(13%) med. 16.44; se 0.09 # voxels = 693
M06242	16.75 +/- 1.98(12%) med. 16.87; se 0.08 # voxels = 699	17.13 +/- 1.92(11%) med. 17.05; se 0.07 # voxels = 723	16.81 +/- 1.99(12%) med. 16.80; se 0.07 # voxels = 707	17.10 +/- 2.03(12%) med. 17.17; se 0.08 # voxels = 712
M06348	15.74 +/- 2.32(15%) med. 15.69; se 0.09 # voxels = 662	16.56 +/- 2.34(14%) med. 16.62; se 0.09 # voxels = 670	15.71 +/- 2.24(14%) med. 15.59; se 0.09 # voxels = 653	15.85 +/- 2.25(14%) med. 15.75; se 0.09 # voxels = 655
MEAN +/- se	**16.82 +/- 0.23(1%)**	**16.90 +/- 0.17(1%)**	**16.69 +/- 0.23 (1%)**	**16.62 +/- 0.22 (1%)**

Table 7-22 Baseline BOLD results for BOLD's 86% grey-struc mask, for all volunteers. Listed in each cell: mean +/- sd (sd as % mean), median, standard error and number of voxels.

Appendix III : CR values per volunteer

CR in ml/100g/min/mm Hg for standard grey matter mask				
	session 1	session 2	session 3	session 4
M05808	0.75 +/-0.31(41%)	-0.45 +/-0.25(55%)	-0.08 +/- 0.24(284%)	-0.73 +/- 0.35(48%)
M06004	0.63 +/- 0.30(47%)	0.16 +/-0.33(198%)	-0.74 +/- 0.44(59%)	-0.20 +/- 0.91(461%)
M06094	0.47 +/- 0.26(55%)	1.79 +/- 0.31(17%)	1.90 +/- 0.28(15%)	0.33 +/- 0.22(67%)
M06192	0.06 +/- 0.21(327 %)	1.82 +/- 0.28(16 %)	-0.49 +/- 0.23(46%)	0.41 +/- 0.26(64%)
M06242	1.90 +/- 0.34(18%)	2.61 +/- 0.34(13%)	0.34 +/- 0.30(88%)	1.96 +/- 0.34(17%)
M06348	0.82 +/- 0.17(21%)	1.26 +/- 0.22(17%)	1.48 +/- 0.27(19%)	1.54 +/- 0.36(24%)
MEAN +/- se	**0.77+/- 0.25(32%)**	**1.20+/- 0.47(39%)**	**0.40+/-0.44(110%)**	**0.55+/- 0.42(75%)**

Table 7-23 CR results for the standard grey matter mask, for all volunteers. Listed in each cell: mean +/- sd (sd as % mean).

CR in ml/100g/min/mm Hg for 86% grey-struc mask				
	session 1	session 2	session 3	session 4
M05808	1.77 +/- 0.28(16%)	-0.55 +/-0.24(43%)	-0.27 +/-0.24(90%)	-0.02 +/-0.29(1548%)
M06004	1.02 +/- 0.33(32%)	0.55 +/- 0.41(74%)	1.37 +/- 0.39(28%)	2.07 +/- 0.84(40%)
M06094	0.33 +/- 0.26(77%)	1.23 +/- 0.23(19%)	1.36 +/- 0.37(28%)	0.57 +/- 0.26(46%)
M06192	0.27 +/- 0.20(76%)	1.14 +/- 0.20(17%)	0.21 +/-0.36(168%)	0.42 +/- 0.25(59%)
M06242	1.13 +/- 0.33(29%)	1.79 +/- 0.32(18%)	-0.40 +/-0.32(79%)	0.73 +/- 0.32(44%)
M06348	1.42 +/- 0.23(16%)	1.11 +/- 0.26(24%)	0.75 +/- 0.35(46%)	2.01 +/- 0.30(15%)
MEAN +/- se	**0.99+/- 0.24(25%)**	**0.88+/- 0.33(37%)**	**0.50+/- 0.32(63%)**	**0.96+/- 0.36(37%)**

Table 7-24 CR results for the 86% grey-struc mask, for all volunteers. Listed in each cell: mean +/- sd (sd as % mean).

CR in ml/100g/min/mm Hg for global mask				
	session 1	session 2	session 3	session 4
M05808	1.30 +/- 0.15(12%)	0.15 +/- 0.12(79%)	0.02 +/-0.12(667%)	0.20 +/- 0.14(73%)
M06004	1.00 +/- 0.14(14%)	1.05 +/- 0.13(12%)	0.55 +/- 0.18(33%)	1.38 +/- 0.39(28%)
M06094	0.83 +/- 0.14(17%)	1.41 +/- 0.12(8%)	1.80 +/- 0.14(8%)	0.49 +/- 0.11(22%)
M06192	0.09 +/-0.10(119%)	1.30 +/- 0.13(10%)	-0.16 +/-0.11(69%)	0.83 +/- 0.12(14%)
M06242	1.80 +/- 0.18(10%)	2.42 +/- 0.15(6%)	0.21 +/- 0.15(71%)	1.43 +/- 0.14(10%)
M06348	1.29 +/- 0.11(9%)	1.31 +/- 0.13(10%)	0.88 +/- 0.14(16%)	1.44 +/- 0.15(10%)
MEAN +/- se	**1.05+/- 0.24(22%)**	**1.27+/- 0.30(23%)**	**0.55+/- 0.29(54%)**	**0.96+/- 0.22(23%)**

Table 7-25 CR results for the global mask, for all volunteers. Listed in each cell: mean +/- sd (sd as % mean).

Appendix IV : BOLD relative CR values per volunteer

CR in %BOLD change/mm Hg for 86% grey-struc BOLD mask				
	session 1	session 2	session 3	session 4
M05808	0.17 +/- 0.04(22%)	0.10 +/- 0.03(24%)	0.12 +/- 0.03(27%)	0.07 +/- 0.03(37%)
M06004	0.61 +/- 0.08(13%)	0.30 +/- 0.07(24%)	0.32 +/- 0.07(21%)	0.88 +/- 0.25(29%)
M06094	0.09 +/- 0.03(35%)	0.11 +/- 0.05(47%)	0.22 +/- 0.05(22%)	0.17 +/- 0.05(32%)
M06192	0.21 +/- 0.04(18%)	0.13 +/- 0.04(30%)	0.25 +/- 0.04(17%)	0.27 +/- 0.05(20%)
M06242	0.36 +/- 0.06(16%)	0.56 +/- 0.07(13%)	0.41 +/- 0.04(9%)	0.37 +/- 0.05(12%)
M06348	0.17 +/- 0.06(35%)	0.06 +/- 0.05(79%)	0.20 +/- 0.07(35%)	0.05 +/-0.06(106%)
MEAN +/- se	**0.27+/- 0.08(29%)**	**0.21+/- 0.08(37%)**	**0.25+/- 0.04(17%)**	**0.30+/- 0.13(42%)**

Table 7-26 BOLD relative CR results for the 86% grey-struc BOLD mask, for all volunteers. Listed in each cell: mean +/- sd (sd as % mean).

CR in %BOLD change/mm Hg global BOLD mask				
	session 1	session 2	session 3	session 4
M05808	0.12 +/- 0.02(15%)	0.14 +/- 0.01(7%)	0.11 +/- 0.01(13%)	0.08 +/- 0.01(14%)
M06004	0.49 +/- 0.03(7%)	0.19 +/- 0.03(14%)	0.33 +/- 0.03(10%)	0.83 +/- 0.10(13%)
M06094	0.12 +/- 0.02(15%)	0.16 +/- 0.02(13%)	0.16 +/- 0.02(12%)	0.14 +/- 0.02(16%)
M06192	0.19 +/- 0.02(10%)	0.21 +/- 0.02(10%)	0.21 +/- 0.02(11%)	0.25 +/- 0.02(9%)
M06242	0.31 +/- 0.02(7%)	0.49 +/- 0.02(5%)	0.35 +/- 0.02(6%)	0.41 +/- 0.02(5%)
M06348	0.29 +/- 0.03(11%)	0.15 +/- 0.03(17%)	0.25 +/- 0.03(11%)	0.15 +/- 0.03(23%)
MEAN +/- se	**0.25+/- 0.06(23%)**	**0.22+/- 0.05(24%)**	**0.23+/- 0.04(17%)**	**0.31+/- 0.11(37%)**

Table 7-27 BOLD relative CR results for global BOLD mask, for all volunteers. Listed in each cell: mean +/- sd (sd as % mean).

8 Discussion and Conclusions

8.1 The implementation and optimisation of quantitative CBF measurements

In the course of this PhD project, the field of ASL techniques has expanded significantly. The early CBF quantification models as proposed by Kim (Kim et al. 1995) have turned out to be too simple for an accurate CBF quantification: issues such as inversion and readout slice profile interactions (Keilholz-George et al., 2001), the difference between tissue and blood T_1 values (Calamante et al., 1996), the inflow delay (Ye et al., 1997), the finite width of the label bolus (Calamante et al., 1996; Buxton et al., 1998b), macrovascular contributions (Ye et al., 1997) and so forth, have all shown to have an important bearing on the CBF quantification results.

It is therefore not obvious from the literature which approach is best for the CBF quantification of ASL data. I therefore chose to start with a relatively simple model and to evaluate quantification issues one by one to assess whether modifications of the standard model would be beneficial. This optimisation process is described in Chapter 5. Interestingly, I ran into a number of issues so far underrepresented in the literature: firstly, the effects of CSF partial voluming, signalled briefly by Kwong in 1995 (Kwong et al., 1995), which can lead to erroneous results for the slice selective inversion fit. With simulations I systematically characterised this effect and improved the fit model by incorporating a CSF fraction parameter.

The issue of working with subtractions of magnitude data might seem minor, but without due care can lead to a gross distortion of the data. Ironically, this gives CBF and inflow delay values in good accordance with the literature. I have addressed these problems in detail in Chapter 5 and have shown that it is necessary to take the magnitude of the subtracted magnitude data.

Another problem, volunteer movement, had not been described for ASL applications before. However, my multi-session studies in Chapter 7 show significant effects of movement on CBF values, even when using a special repositioning device. In Chapter 5, I proposed and evaluated two realignment methods: an intra-realignment method that only realigns repeat acquisitions for each TI point and an inter-realignment procedure

that uses separately acquired M_0 snapshots to realign the images of different TI points (and therefore different T_1 contrasts) to each other over multiple measurements or sessions. For this single-slice FAIR technique performing intra-realignment was superior. This is probably because the inter-realignment techniques can give spurious results for out-of-plane movement. In the future, however, when whole brain FAIR data become more readily available, the inter-realignment is expected to be the method of choice. Considering that FAIR is a subtraction technique, which makes it extra vulnerable to inter-acquisition variability, and has a low SNR, I think incorporating an inter-realignment protocol in ASL data processing is crucial, maybe even more so than for BOLD fMRI.

The low SNR of the FAIR measurement is another source of concern. For the implementation described in this thesis, white matter CBF analyses had to be abandoned due to the low SNR of the data. Single voxel data are also too noisy to be of great interest, and the data therefore needs to be averaged over a suitably chosen voxel mask. As the CBF measurements described in this thesis were already quite long (~ 20 minutes) it is not really an option to do more averaging over acquisitions. Increasing SNR by using a different readout sequence such as the spiral sequence used by Yang et al. (Yang et al., 1998) might be a good way forward. Alternatively, working at higher magnetic field strengths is also expected to alleviate this problem.

Low SNR is also an issue for the transition from single-slice to multi-slice FAIR. In multi-slice FAIR, a broad slab of the brain is inverted in the slice selective inversion step. All the blood spins flowing within that slab at the time of inversion will be invisible to the FAIR technique. This is expected to lower the SNR of the FAIR measurement even further, which is why the FAIR technique in this thesis was implemented for a single slice.

A way of reducing the complications of a low SNR and a host of quantification issues is to simplify the quantification model or forego quantification all together and work with relative CBF values. I am slightly sceptical of these approaches: in Chapters 5 and 6 I have demonstrated the effects of ignoring inflow delay and discussed the dangers of 'event-related' FAIR applications which assume an unchanged inflow delay for CBF increases. Working with relative CBF values is only safe if the absolute CBF quantification has been well established and replicated by the research community. For PET this is the case, but for ASL, I would argue, not yet.

The validation of quantitative CBF techniques is not straightforward: in animals, the gold-standard is comparison with microsphere techniques; however, as the human brain has much more partial voluming than, for instance, the gerbil, a 100% translation of the validation results to human studies cannot be made. For human CBF measurements, PET is generally regarded as the gold-standard. It was originally planned to validate the CBF technique described in this thesis by comparison with PET data acquired on the same volunteer. However, for practical reasons this was not possible. Instead, the technique was validated by comparison of measured rest CBF with literature values. The well-documented slope of CBF versus $PetCO_2$ increase (the cerebrovascular reactivity) was also measured and compared favourably with other groups' reports. In the last couple of years, there was a validation published of a steady state ASL technique with PET, which showed good correlation between the techniques for grey matter, but an underestimation of white matter CBF for ASL (Ye et al., 2000). The authors proposed that the latter was probably due to an underestimation of the inflow delay with ASL.

Finally, the potential strength of ASL techniques for longitudinal studies has been unexplored in the literature so far. In Chapter 7, a first step in this direction was taken with an experiment of CBF and CR measured at different times over the course of a day. The results for CR were very noisy: volunteer motion and the fact that CR is based on a small difference between two large and noisy CBF values contributed to this. Meaningful longitudinal studies of CR with this technique are therefore still out of reach. Baseline CBF results, however, were much more promising: standard deviations on a CBF measurement of 12-17% put this technique in the realm of functional studies. Hopefully, with 3D-realignment and an increased SNR of the acquisition, longitudinal CBF experiments can be successfully performed.

In conclusion, I will address the original aims for this PhD project:

- to implement a non-invasive, quantitative ASL method for use in cognitive neuroimaging

This aim has been reached. I performed an extensive literature study at the beginning of my project to choose the most promising ASL technique. This is described in Chapter 3. I chose FAIR because of its in-slice labelling (hence minimal transit times) and low rf deposition. The continuing prevalence of FAIR in the literature supports this choice, and the standard deviation on the CBF measurement with FAIR is small enough for functional studies.

- to optimise sequence design for neuroscientific demands

Due to the averaging required, the FAIR technique developed in this project is more suitable for steady state measurements like those performed using PET, than for rapid studies as performed with BOLD fMRI. As mentioned before, there have been event related FAIR studies reported in the literature, but this means inflow delay effects are ignored (Hoge et al, 1999). The fact that the technique implemented here is single-slice, is a major limitation. The reason for this was primarily the SNR reduction that will result from multi-slice ASL.

- to develop an accurate model for CBF quantification

An extensive exploration of CBF quantification issues was performed and improvements on standard acquisition and analysis methods were proposed and implemented.

- to validate CBF results by comparison with another technique and/or literature values

Due to the aforementioned technical limitations, the FAIR technique was only validated by comparison with literature values of baseline CBF and CR.

- to apply the ASL method in a longitudinal neuroscientific experiment

This was reported in Chapter 7. There was no significant effect of time of day on CBF and inflow delay. This finding was used to establish upper limits for diurnal changes in CBF and inflow delay.

8.2 Future Work

On the basis of the work reported in this thesis, the following future research is recommended:

- Implementing whole brain FAIR, so 3D-realignment can be used for multi-session studies

Some of the most interesting applications for these non-invasive CBF measurements are longitudinal studies. My longitudinal study described in Chapter 7 suggests that 3D-realignment is crucial for this.

- Working at higher magnetic field strengths

The measurements described in this thesis were all performed at 2.0 T; however the SNR for the FAIR measurement is quite low. Scanning times for one CBF measurement are already ~ 20 minutes and still the standard deviation on CBF for one voxel (4.69·4.69·5 mm^3) is 25% and for a grey matter mask of 100 voxels it is ~5%. White matter is out of reach for this technique at the moment due to its low SNR. Also, multi-slice FAIR intrinsically has an even lower SNR because a broad band around the slices of interest is being inverted, making all the blood spins inside that band invisible to the CBF measurement. Sensitivity is therefore definitely an issue for this technique and higher magnetic field strengths will help.

- With these technical improvements incorporated, it should be possible to perform longitudinal studies on changes in CBF due to a variety of causes such as learning, aging and treatment with psychopharmaceuticals.

References

Alsop, D.C., Detre, J.A. (1996). Reduced transit-time sensitivity in noninvasive magnetic resonance imaging of human cerebral blood flow. *J. Cereb. Blood Flow Metab.* **16**, 1236-1249

Alsop, D.C., Detre, J.A. (1998). Multisection cerebral blood flow MR imaging with continuous arterial spin labeling. *Radiology* **208**, 410-416

Ameriso, S.F., Mohler, J.G., Suarez, M., Fisher, M. (1994). Morning reduction of cerebral vasomotor reactivity. *Neurology* **44**, 1907-1909.

Axel, L. (1995). Methods using blood pool tracers: part II. In: *Diffusion and Perfusion Magnetic Resonance Imaging.* (Le Bihan, D. ed), New York, Raven Press, 205-211

Barbier, E.L, Lamalle, L., Decorps, M. (2001). Methodology of brain perfusion imaging. *JMRI* **13**, 496-520.

Blamire, A.M. and Styles, P. (2000). Spin Echo Entrapped Perfusion Image (SEEPAGE). A nonsubtraction method for direct imaging of perfusion. *Magn. Reson. Med.* **43**, 701-704

Bottomley, P.A., Hardy, J.C. (1987). Two-dimensional spatially selective spin inversion and spin-echo refocusing with a single nuclear magnetic resonance pulse. *J. Appl. Phys.* **62**, 4284 – 4290

Buxton, R.B., Wong, E.C., Frank, L.R. (1998a). Dynamics of blood flow and oxygenation changes during brain activation: the balloon model. *Magn Reson Med.* **39**, 855-64.

Buxton, R.B., Frank, L.R., Wong, E.C., Siewert, B., Warach, S., Edelman, R.R. (1998b). A general kinetic model for quantitative perfusion imaging with arterial spin labelling. *Magn. Reson. Med.* **40**, 383-396

Calamante, F., Williams, S.R., Van Bruggen, N., Kwong, K.K., Turner, R. (1996). A model for quantification of perfusion in pulsed labelling techniques. *NMR in Biomed.* **8**, 79-83

Calamante, F., Thomas, D.L., Pell, G.S., Wiersma, J., Turner, R. (1999). Measuring cerebral blood flow with magnetic resonance imaging techniques. *J. Cereb. Blood Flow Metab.* **19**,701-735

Chalela, J.A., Alsop, D.C., Gozalez-Atavales, J.B., Maldjian, J.A., Kasner, S.E., Detre, J.A. (2000). Magnetic resonance perfusion imaging in acute ischemic stroke using continuous arterial spin labeling. *Stroke* **31**, 680-687.

Davis, T.L., Kwong, K.K., Weisskoff, R.M., Rosen, B.R. (1998). Calibrated functional MRI: mapping the dynamics of oxidative metabolism. *Proc Natl. Acad.Sci. USA.* **95**, 1834-1839

De Reuck, J., Decoo, D., Marchau, M., Santens, P., Lemahieu, I., Strijckmans, K. (1998). Positron emission tomography in vascular dementia. *Journal of Neurological Sciences* **154**, 55-61

Deichmann, R., Good, C.D, Turner R. (2002). RF inhomogeneity compensation in structural brain imaging. *Magn Reson Med.* **47**, 398-402

Detre, J.A., Leigh, J.S., Williams, D.S., Koretsky, A.P. (1992). Perfusion Imaging. *Magn. Reson. Med.* **23**, 37-45

Dixon, W.T., Su, L.N., Faul, D.D., Gado, M., Rossnick, S. (1986). Projection angiograms of blood labeled by adiabatic fast passage. *Magn. Reson. Med.* **3**, 454-462

Edelman, R.R., Siewert, B., Darby, D.G., Thangaraj, V., Nobre, A.C., Medulam, M.M., Warach, S. (1994). Qualitative mapping of cerebral blood flow and functional localization with echo-planar MR imaging and Signal Targeting with Alternating Radio Frequency. *Neuroradiology* **192**, 513-520

Edelman, R.R., and Chen, Q. (1998). EPISTAR MRI: Multislice mapping of cerebral blood flow. *Magn. Reson. Med.* **40**, 800-805

Feynman, R.P., Leighton, R.B., Sands, M.(1964) The Feynman Lectures on Physics. Addison-Wesley Publishing Company. Reading, Massachusetts.

Fisel C.R., Ackerman, J.L., Buxton, R.B., Garrido L., Belliveau J.W., Rosen B.R. et al. (1991). MR contrast due to microscopically heterogeneous magnetic-susceptibility: numerical simulations and applications to cerebral physiology. *Magn. Reson Med.* **17**, 336-347

Frank, L.R., Wong, E.C., Buxton, R.B. (1997). Slice profile effects in adiabatic inversion: application to multislice perfusion imaging. *Magn. Reson. Med.* **38**, 558-564.

Friston, K.J., Williams, S., Howard, R., Frackowiak, R.S., Turner, R. (1996). Movement-related effects in fMRI time-series. *Magn. Reson. Med.* **35**, 346-355

Gadian, D.G. (1995). NMR and its applications to living systems. 2nd edition. Oxford Science Publications. Oxford.

Gonzalez-Atavales, J.B., Alsop, D.C., Detre, J.A. (2000). Cerebral perfusion and arterial transit time changes during task activation determined with continuous arterial spin labeling. *Magn. Reson. Med.* **43**, 739-746.

Grubb, R.L., Raichle, M.E., Eichling, J.O., Ter-Pogossian, M.M. (1974). The effects of changes in $PaCO_2$ on Cerebral Blood Volume, Blood Flow, and vascular Mean Transit Time. *Stroke* **5**, 630-639

Haase, A., Frahm, J., Matthaei, D., Hanicke, W., Merboldt, K.S. (1986). FLASH imaging. Rapid NMR imaging using low flip-angle pulses. *J. Magn. Res.* **67**, 258

Harper, A.M., and Jennett, S. (1990). Cerebral Blood Flow and Metabolism Manchester University Press, Manchester and New York.

Hajnal, J.V., Myers R., Oatridge, A., Schwieso, J.E., Young, I.R., Bydder, G.M. (1994) Artefacts due to stimulus correlated motion in functional imaging of the brain. *Magn.Reson.Med.* **31**, 283 -291

Hoge, R.D., Atkinson, J., Gill, B. Crelier, G.R., Marrett, S., Pike, G.B. (1999). Investigation of BOLD signal dependence on Cerebral Blood Flow and oxygen consumption: the deoxyhemoglobin dilution model. *Magn. Reson Med.***42**, 849-863.

Hore, P.J. (1995). Nuclear Magnetic Resonance. Oxford University Press. Oxford.

Howell, D. C. (1997). Statistical methods for psychology. Duxbury . 4th ed.

Kastrup, A., Thomas, C., Hartmann, C., Schabet., M. (1997). Sex dependency of cerebrovascular CO_2 reactivity in normal subjects. *Stroke* **28**, 2353-2356.

Kastrup, A., Dichgans, J., Niemeier, M., Schabet, M. (1998). Changes of cerebrovascular CO_2 reactivity during normal aging. *Stroke* **29**, 1311-1314.

Kastrup, A., Krüger, G. Neumann-Haefelin, T., Mosely, M. (2001). Assessment of cerebrovascular reactivity with functional magnetic resonance imaging: comparison of CO_2 and breath holding. *Magn. Reson. Im.* **19**, 13-20.

Keilholz-George, S.D., Knight-Scott, J., Berr S.S. (2001). Theoretical analysis of the effect of imperfect slice profiles on tagging schemes for pulsed arterial spin labeling MRI. *Magn. Reson Med.***46**,141-148

Kim, S-G.(1995). Quantification of relative cerebral blood flow change by flow-sensitive alternating inversion recovery (FAIR) technique: application to functional mapping. *Magn. Reson. Med.* **34**, 293-301

Kim, S-G., Tsekos, N.V., Ashe, J. (1997). Multi-slice perfusion-based functional MRI using the FAIR technique: comparison of CBF and BOLD effects. *NMR in Biomed.* **10**, 191-196.

Kwong, K.K., Belliveau, J.W., Chesler, D.A., Goldberg, I.E., Weisskoff, R.M., Poncelet, B.P., Kennedy, D.N., Hoppel, B.E., Cohen, M.S., Turner R. (1992). Dynamic magnetic resonance imaging of human brain activity during primary sensory stimulation. *Proc Natl Acad Sci U S A.* **89**, 5675-5679

Kwong, K.K., Chesler, D.A., Weisskoff, R.M., Donahue, K.M., Davis, T.L., Ostergaard, L., Campbell, T.A., Rosen, B.R. (1995). MR perfusion studies with T1 weighted echo-planar imaging. *Magn. Reson. Med.* **34**, 878-887

Lauterbur, P.C. (1973). Image formation by induced local interactions: examples employing nuclear magnetic resonance. *Nature* **242**, 190-191

Le Bihan, D., Turner, R. (1992). Magnetic resonance imaging (Stark, D.D. and Bradley, W.G., Eds.) 2nd edition. Mosby, St Louis. 355-371

Lu, W-M., Wong, E.C., Bandettini, P.S., Hyde, J.S. (1999). QUIPSS II with thin slice TI1 periodic saturation: a method for improving accuracy of quantitative perfusion imaging using pulsed arterial spin labeling. *Magn. Reson. Med.* **41**, 1246-1254

Mandeville, J.B., Marota, J.J., Weisskoff, R.W., Rosen, B.R. (1997). An NMR methodology for measuring changes in cmr_{o2} during functional challenge. *Proceedings of the 5th Annual Meeting of ISMRM* 155

Mansfield, P. (1977) Multi-planar image formation using NMR spin echoes. *Journal of Physics C*, L55-L48

Mansfield, P., Morris, P.G. (1982). NMR Imaging in Biomedicine. Academic, New York, 32-114

Martin, A.J., Friston, K.J., Colebatch, J.G., Frackowiak, R.S.J. (1991). Decreases in regional cerebral blood flow with normal aging. *J. Cereb. Blood FLow Metab.* **11**, 684-689

MATLAB, The Math Works, Inc. Natick, MA, USA. http://www.mathworks.com (1994-2001).

Miller, K.L., Luh, W-M., Liu, T.T., Martinez, A., Obata, T. Wong, E.C., Frank, L.R., Buxton, R.B. (2001). Nonlinear temporal dynamics of the Cerebral Blood Flow response. *Hum. Brain Mapp.* **13**(1), 1-12.

Nakane, H., Ibayashi, S., Fujii, K., Sadoshima, S., Irie, K., Kitazono, T. Fujishima, M. (1998). Cerebral blood flow and metabolism in patients with silent brain infarction: occult misery perfusion in the cerebral cortex. *J. Neurol. Neurosurg. Psychiatry* **65**, 317-321.

Ogawa, S., Lee, T.M., Nayak, A.S., Glynn, P. (1990). Oxygenation –sensitive contrast in magnetic resonance image of rodent brain at high magnetic fields. *Magn. Reson. Med.* **14**, 68-78.

Ogawa, S., Menon R., Tank D.W., Kim S.G., Merkle, H., Ellermann, J.M., Ugurbil, K. (1993). Functional brain mapping by blood oxygenation level dependent contrast magnetic resonance imaging. A comparison of signal characteristics with a biophysical model. *Biophys J.* **64**(3), 803-812

Ordidge, R.J., Helpern, J.A., Qing, Z.X., Knight, R.A., Nagesh, V. (1994). Correction of motional artifacts in diffusion-weighted NMR images using navigator echoes. *MRI* **12**, 455-460

Ordidge, R.J., Wylezinska, M., Hugg, J.W., Butterworth, E., Franconi, F. (1996). Frequency Offset Corrected Inversion (FOCI) pulses for use in localized spectroscopy. *Magn. Reson. Med.* **36**, 562-566.

Østergaard, L. Weisskoff R.M., Chesler D.A., Gyldensted C., Rosen B.R. (1996). High resolution measurement of cerebral blood flow using intravascular tracer bolus passages. I. Mathematical approach and statistical analysis. *Magn Reson.Med* **36**, 715-725

Payne, G.S., Leach, M.O. (1997). Implementation and evaluation of frequency offset corrected inversion (FOCI) pulses on a clinical MR system. Magn.Reson.Med. **38**, 828 (1997). [$add other page number]

Pekar, J., Jezzard, P., Roberts, D.A., Leigh, J.S., Frank, J.A., McLaughlin, A.C. (1996). Perfusion Imaging with compensation for asymmetric magnetization transfer effects. *Magn. Reson. Med.* **35**, 70-79

Pell, G.S., Thomas, D.L., Lythgoe, M.F., Calamante, F., Howseman, A.M., Gadian., D.G., Ordidge, R.J. (1999). Implementation of quantitative FAIR perfusion imaging with a short repetition time in time-course studies. *Magn. Reson. Med.* **41**, 829-840

Placidi, F., Diomedi, M., Cupini, L.M., Bernardi, G., Silvestini, M. (1998). Impairment of daytime cerebrovascular reactivity in patients with obstructive sleep apnoea syndrome. *J.Sleep Res.* **7**, 288-292.

Press, W. H, Teukolsky, S.A., Vetterling, W.T., Flannery, B.P. (1992). Numerical Recipes in C. p 660. 2nd edition. Cambridge University Press.

Qureshi, A.I., Winter, C., Bliwise, D.L.(1999). Sleep fragmentation and morning cerebrovasomotor reactivity to hypercapnia. *Am.J.Respir.Crit.Care Med.***160**, 1244-1247.

Rabi, I. I., Millman, S., Kusch, P., Zacharias, J. R. (1939). The molecular beam resonance method for measuring nuclear magnetic moments. The magnetic moments of $_3Li^6$, $_3Li^7$ and $_9F^{19}$. *Phys. Rev.* **55**, 526-535

Reich, T., and Rusinek, H. (1989). Cerebral cortical and white matter reactivity to carbon dioxide. *Stroke* **20**, 453-457.

Rosen, B.R., Belliveau, J.W., Vevea, J.M., Brady, T.J. (1990). Perfusion imaging with NMR contrast agents. *Magn. Reson. Med.* **14**, 249-265

Roy, C.S., Sherrington, C.S. (1890). On the regulation of blood supply of the brain. *J.Physiol.* **11**, 85-108

Schmitt, F., Stehling, M.K., Turner, R. (1998). Echo-Planar Imaging. Theory, Technique and Application. Springer, Berlin.

Silva, A.C., Zhang, W., Williams, D.S., Koretsky, A.P. (1995). Multi-slice MRI of rat brain perfusion during amphetamine stimulation using arterial spin labeling. *Magn. Reson. Med.* **33**, 209-214

Silver, M.S., Joseph, R.I., Hoult, D.I. (1985). Selective spin inversion in nuclear magnetic resonance and coherent optics through an exact solution of the Bloch Riccatti equation. *Physical Review A* **31**, 2753-2755

SPM, Statistical Parametric Mapping data analysis package. (1999). www.fil.ion.ucl.ac.uk/spm.

Stedjskal, E.O. and Tanner, J.E.(1965). Spin diffusion measurements: spin echoes in the presence of time dependent field gradients. *Journal of Chemical Physics* **42**, 288-292

Talairach, J., Tournoux, P. (1988). Co-Planar Stereotaxic Atlas of the Human Brain. Thieme Medical Publishers, Inc. New York.

Thomas, D.L. (1999). Magnetic Resonance Imaging of Diffusion and Perfusion: Techniques and Applications to Cerebral Ischaemia. *PhD thesis, Dept. of Medical Physics and Bioengineering, University College London.*

Turner, R., Le Bihan, D. Moonen, C.T.W., Depres, D., Frank, J.(1991). Echo-planar time course MRI of cat brain oxygenation changes. *Magn.Reson.Med.* **22**, 159-166

Villringer, A., Rosen B.R., Belliveau J.W., Achkerman J.L., Lauffer R.B., Buxton R.B., et al. (1988) Dynamic imaging with lanthanide chelates in normal brain: contrast due to magnetic susceptibility effects. *Magn. Reson. Med* **6**, 164-174

Villringer, A., Dirnagl U. (1995). Coupling of brain activity and cerebral blood flow: basis of functional neuroimaging. *Cerebrovasc. Brain Metab. Rev.* **7**, 240-276

Vymazal, J., Brooks, R.A., Patronas, N., Hajek, M., Bulte, J.W.M., Di Chiro, G. (1995). Magnetic resonance imaging of brain iron in health and disease. *J.Neurol. Sci.***134** (Suppl.) 19-26

Wolff, S.D. and Balaban, R.S. (1989). Magnetization transfer contrast (MTC) and tissue water proton relaxation in vivo. *Magn. Reson. Med.* **10**,135-144

Williams, D.S., Detre, J.A., Leigh, J.S., Koretsky, A.P. (1992). Magnetic resonance imaging of perfusion using spin inversion of arterial water. *Proc. Natl. Acad. Sci. USA* **89**, 212-216

Wong, E.C., Buxton, R.B., Frank, L.R.(1997). Implementation of quantitative perfusion imaging techniques for functional brain mapping using pulsed arterial spin labeling. *NMR in Biomed.* **10**, 237-249

Wong, E.C., Buxton, R.B., Frank, L.R. (1998). Quantitative imaging of perfusion using a single subtraction (QUIPSS and QUIPSS II). *Magn. Reson. Med.* **39**, 702-708

Yang, Y., Frank, J.A., Hou, L., Ye, F.Q., McLaughlin, A.C., Duyn, J.H. (1998). Multislice imaging of quantitative cerebral perfusion with pulsed arterial spin labeling. *Magn. Reson. Med.* **39**, 825-832.

Yang, Y., Engelien, W., Xu, S., Gu, H. Silbersweig, D.A., Stern, E. (2000). Transit time, trailing time, and Cerebral Blood Flow during brain activation: measurement using multislice, pulsed spin-labeling perfusion imaging. *Magn. Reson. Med.* **44**, 680-685.

Ye, F.Q., Mattay, V.S., Jezzard, P., Pekar, J., Frank, J.A., McLaughlin, A.C. (1996). Correction for vascular artifacts in arterial spin tagging techniques. *Proc. ISMRM. 4th Annual Meeting.* 11

Ye, F.Q., Mattay, V.S., Jezzard, J., Frank, J.A., Weinberger, D.R., McLaughlin, A.C. (1997). Correction for vascular artifacts in cerebral blood flow values measured by using arterial spin tagging techniques. *Magn. Reson. Med.* **37**, 226-235

Ye, F.W., Mattay, V.S., Frank, F.A., Weinberger, D.R., McLaughlin, A.C. (1999) Comparison of white and grey matter arterial transit times in spin tagging experiments. *Proc. Intl.Soc.Magn.Reson.Med.* **7**, p1847

Ye, F.W., Berman, K.F., Ellmore, T., Esposito, G., Van Horn, J.D., Yang, Y. Duyn, J. Smith, A.M., Frank, J.A., Weinberger, D.R., McLaughlin, A.C. (2000). $H_2{}^{15}O$ PET validation of steady-state arterial spin tagging cerebral blood flow measurements in humans. *Magn.Reson.Med.* **44**, 450-456.

Yongbi, M.N., Branch, C.A., Helpern, J.A. (1998). Perfusion imaging using FOCI rf pulses. *Magn. Reson. Med.* **40**, 938-943

Yongbi, M.N., Yihong, Y., Frank, J.A., Duyn, J.H. (1999). Multislice perfusion imaging in human brain using the C-FOCI inversion pulse: comparison with Hyperbolic Secant. *Magn. Reson. Med.* **42**,1098-1105

Yongbi, M.N., Tan, C.X. , Frank, J.A., Duyn, J.H. (2000). A protocol for assessing subtraction errors of arterial spin-tagging perfusion techniques in human brain. *Magn. Reson. Med.* **43**, 896-900

Zhou, J., Mori, S.,Van Zijl, P.C.M. (1998). FAIR excluding radiation damping (FAIRER). *Magn. Reson. Med.* **40**, 712-71

Zhou, J., Van Zijl, P.C.M. (1999). Effect of transit times on quantification of cerebral blood flow by the FAIR T_1-difference approach. *Magn. Reson. Med.* **42**, 890-894

Zierler, K.L. (1962). Theoretical basis of indicator-dilation methods for measuring flow and volume. *Circ Res* **10**, 393-40